Science | Science Advances | Science Immunology | Science Signaling | Science Translational Medicine

[ SPECIAL EDITION ]

# IMMUNOLOGY

AAAS

aaas.org/science-journals

# SPECIAL EDITION: Immunology

## Select research published in *Science*, *Science Advances*, *Science Immunology*, *Science Signaling*, and *Science Translational Medicine*

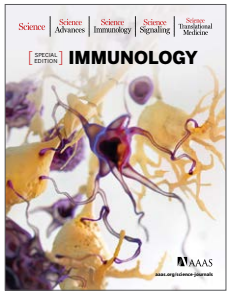


This collection of articles from the *Science* family of journals highlights the latest research on cancer immunotherapy, inflammation, viral infections, allergic responses, and the use of single-cell analyses to determine cell fate.

Image: Valerie Altounian/*Science*

**Editor-in-Chief**
Jeremy Berg, Ph.D.
*Science* family of journals
AAAS, Washington, DC

## Science | AAAS

*Science* is a leading outlet for scientific news, commentary, and cutting-edge research. The journal publishes original peer-reviewed research across the sciences, with articles that consistently rank among the most cited in the world.

**Deputy Editors**
Lisa D. Chong, Ph.D.
Andrew M. Sugden, Ph.D.
Valda J. Vinson, Ph.D.
Jake S. Yeston, Ph.D.

**Immunology Editors**
Priscilla Kelly, Ph.D.
Seth Scanlon, Ph.D.

## Science Advances | AAAS OPEN ACCESS

*Science Advances* is the digital, open access expansion of *Science* magazine. The journal publishes significant, innovative original research that advances the frontiers of science across a broad range of disciplines, from bioscience and medicine to neuroscience, physics, ecology, and material sciences.

**Managing Editor**
Philippa Benson, Ph.D.

**Editorial Team**
Lynden Archer, Ph.D
Aaron Clauset, Ph.D.
Dale Dorsett, Ph.D.
Sarah M. Fortune, M.D.
Kip V. Hodges, Ph.D.
Jeremy Jackson, Ph.D.
Zakya H. Kafafi, Ph.D.
Kevin S. LaBar, Ph.D.
Shahid Naeem, Ph.D.
Ali Shilatifard, Ph.D.
Philip Yeagle, Ph.D.
Warren Warren, Ph.D.

## Science Immunology | AAAS

*Science Immunology* publishes original, peer-reviewed, science-based research articles that report critical advances in all areas of immunological research, including important new tools and techniques.

**Chief Scientific Advisors**
Abul K. Abbas, M.D.
*University of California, San Francisco*
Federica Sallusto, Ph.D.
*Università della Svizzera Italiana*

**Editor**
Ifor Williams, M.D., Ph.D.

**Editorial Team**
Anand Balasubramani, Ph.D.

## Science Signaling | AAAS

*Science Signaling* publishes peer-reviewed, original research investigating cell signaling that underlies physiology and disease, on the molecular, cellular, intercellular and organismal levels.

**Chief Scientific Editor**
Michael B. Yaffe, M.D., Ph.D.
*Massachusetts Institute of Technology*

**Editor**
John F. Foley, Ph.D.

**Editorial Team**
Leslie K. Ferrarelli, Ph.D.
Annalisa M. VanHook, Ph.D.
Erin R. Williams, Ph.D.
Wei Wong, Ph.D.

## Science Translational Medicine | AAAS

*Science Translational Medicine* is an interdisciplinary journal that publishes translational research with impact for human health that fills the knowledge gaps between preclinical studies and clinical applications.

**Chief Scientific Advisors**
Elazer R. Edelman, M.D., Ph.D.
*Massachusetts Institute of Technology*
Garret FitzGerald, M.D.
*University of Pennsylvania*

**Editor**
Orla M. Smith, Ph.D.

**Editorial Team**
Catherine A. Charneski, Ph.D.
Caitlin A. Czajka, Ph.D.
Mattia Maroso, Ph.D.
Yevgeniya Nusinovich, M.D., Ph.D.
Lindsey Pujanandez, Ph.D.

**Learn more and submit your research today: aaas.org/science-journals**

# IN THIS BOOKLET

## *Science*




## *Science Advances*



## *Science Immunology*



## *Science Signaling*



## *Science Translational Medicine*





Publisher/*Science* family of journals: **Bill Moran**
AD/Business Development: **Justin Sawyers**
Marketing Manager: **Shawana Arnold**
Layout/Design: **Kim Huynh**



**Sponsorship Opportunities:**
**Laurie Faraday**, *Science*
lfaraday@aaas.org | +1.508.747.9395
1200 New York Ave NW, Washington DC 20005


**Learn more and submit your research today: aaas.org/science-journals**

CANCER BIOMARKERS

# Mismatch repair deficiency predicts response of solid tumors to PD-1 blockade

**Dung T. Le,[1,2,3] Jennifer N. Durham,[1,2,3]* Kellie N. Smith,[1,3]* Hao Wang,[3]* Bjarne R. Bartlett,[2,4]* Laveet K. Aulakh,[2,4] Steve Lu,[2,4] Holly Kemberling,[3] Cara Wilt,[3] Brandon S. Luber,[3] Fay Wong,[2,4] Nilofer S. Azad,[1,3] Agnieszka A. Rucki,[1,3] Dan Laheru,[3] Ross Donehower,[3] Atif Zaheer,[5] George A. Fisher,[6] Todd S. Crocenzi,[7] James J. Lee,[8] Tim F. Greten,[9] Austin G. Duffy,[9] Kristen K. Ciombor,[10] Aleksandra D. Eyring,[11] Bao H. Lam,[11] Andrew Joe,[11] S. Peter Kang,[11] Matthias Holdhoff,[3] Ludmila Danilova,[1,3] Leslie Cope,[1,3] Christian Meyer,[3] Shibin Zhou,[1,3,4] Richard M. Goldberg,[12] Deborah K. Armstrong,[3] Katherine M. Bever,[3] Amanda N. Fader,[13] Janis Taube,[1,3] Franck Housseau,[1,3] David Spetzler,[14] Nianqing Xiao,[14] Drew M. Pardoll,[1,3] Nickolas Papadopoulos,[3,4] Kenneth W. Kinzler,[3,4] James R. Eshleman,[15] Bert Vogelstein,[1,3,4] Robert A. Anders,[1,3,15] Luis A. Diaz Jr.[1,2,3]†‡**

**The genomes of cancers deficient in mismatch repair contain exceptionally high numbers of somatic mutations. In a proof-of-concept study, we previously showed that colorectal cancers with mismatch repair deficiency were sensitive to immune checkpoint blockade with antibodies to programmed death receptor–1 (PD-1). We have now expanded this study to evaluate the efficacy of PD-1 blockade in patients with advanced mismatch repair–deficient cancers across 12 different tumor types. Objective radiographic responses were observed in 53% of patients, and complete responses were achieved in 21% of patients. Responses were durable, with median progression-free survival and overall survival still not reached. Functional analysis in a responding patient demonstrated rapid in vivo expansion of neoantigen-specific T cell clones that were reactive to mutant neopeptides found in the tumor. These data support the hypothesis that the large proportion of mutant neoantigens in mismatch repair–deficient cancers make them sensitive to immune checkpoint blockade, regardless of the cancers' tissue of origin.**

Therapy with immune checkpoint inhibitors has uncovered a subset of tumors that are highly responsive to an endogenous adaptive immune response (*1*). When the interaction between the checkpoint ligands and their cognate receptors on the effector cells is blocked, a potent and durable antitumor response can be observed, and on occasion this response can be accompanied by severe autoimmunity (*2*–*5*). These findings support the notion that many cancer patients contain in their immune system the capacity to react selectively to their tumors, ostensibly through recognition of tumor-specific antigens.

The molecular determinants that define this subset of tumors are still unclear; however, several markers, including PD-1 ligand (PD-L1) expression, RNA expression signatures, mutational burden, and lymphocytic infiltrates, have been evaluated in specific tumor types (*6*–*10*). Although such markers appear to be helpful in predicting response in specific tumor types, none of them have been evaluated prospectively as a pan-tumor biomarker. Another potential determinant of response is mutation-associated neoantigens (MANAs) that are encoded by cancers (*11*–*14*). Mismatch repair–deficient cancers are predicted to have a very large number of MANAs that might be recognized by the immune system (*15*–*18*). This prediction led us to conduct a small phase 2 study, focused on 11 patients with colorectal cancers, which demonstrated that PD-1 blockade was an effective treatment for many patients with these tumors (*19*). Since the initiation of that trial, other studies have shown that the number of mutations in mismatch repair–deficient colorectal cancers correlates with the response to PD-1 blockade, providing further support for a relationship between mutation burden and treatment response (*20*).

The genomes of mismatch repair–deficient tumors all harbor hundreds to thousands of somatic mutations, regardless of their cell of origin. We therefore sought to investigate the effects of PD-1 blockade (by the anti–PD-1 antibody pembrolizumab) in mismatch repair–deficient tumors independent of the tissue of origin. In the current study, we prospectively evaluated the efficacy of PD-1 blockade in a range of different subtypes of mismatch repair–deficient cancers (ClinicalTrials.gov number NCT01876511).

Eighty-six consecutive patients were enrolled between September 2013 and September 2016 (table S1). The data cutoff was 19 December 2016. All patients received at least one prior therapy and had evidence of progressive disease prior to enrollment. Twelve different cancer types were enrolled in the study (Fig. 1). All enrolled patients had evidence of mismatch repair deficiency as assessed by either polymerase chain reaction or immunohistochemistry. For most cases, germline sequencing of *MSH2*, *MSH6*, *PMS2*, and *MLH1* was performed to determine whether the mismatch repair deficiencies were associated with a germline change in one of these genes (i.e., whether the patients had Lynch syndrome) (table S2). Germline sequence changes diagnostic of Lynch syndrome were noted in 32 cases (48%), with *MSH2* being the most commonly mutated gene. In seven additional cases where germline testing was not performed, the patient reported a family history consistent with a diagnosis of Lynch syndrome.

Adverse events during treatment were manageable and resembled those found in other clinical studies using pembrolizumab (table S3). Although 74% of patients experienced an adverse effect, most were low-grade. Endocrine disorders, mostly hypothyroidism, occurred in 21% of patients and were easily managed with thyroid hormone replacement.

Seventy-eight patients had disease that could be evaluated by Response Evaluation Criteria in Solid Tumors (RECIST) (Table 1). Objective radiographic responses were noted in 46 of the 86 patients [53%; 95% confidence interval (CI), 42 to 64%], with 21% ($n$ = 18) achieving a complete radiographic response. Disease control (measured as partial response + complete response + stable disease) was achieved in 66 of the 86 patients (77%; 95% CI, 66 to 85%). Radiographic responses could be separated into two classes. First, in 12 cases, scans at 20 weeks showed stable disease, which eventually converted to an objective response (measured as tumor size reduction in response to therapy, according to RECIST criteria). Second, in 11 additional cases, we observed

[1]Bloomberg-Kimmel Institute for Cancer Immunotherapy at Johns Hopkins, Baltimore, MD 21287, USA. [2]Swim Across America Laboratory at Johns Hopkins, Baltimore, MD 21287, USA. [3]Sidney Kimmel Comprehensive Cancer Center at Johns Hopkins, Baltimore, MD 21287, USA. [4]Ludwig Center and Howard Hughes Medical Institute at Johns Hopkins, Baltimore, MD 21287, USA. [5]Department of Radiology, Johns Hopkins University School of Medicine, Baltimore, MD 21287, USA. [6]Department of Medicine, Stanford University School of Medicine, Stanford, CA 94305, USA. [7]Providence Cancer Center at Providence Health & Services, Portland, OR 97213, USA. [8]Department of Medicine, University of Pittsburgh Cancer Institute, University of Pittsburgh School of Medicine, Pittsburgh, PA 15232, USA. [9]Gastrointestinal Malignancies Section, Thoracic-GI Oncology Branch, Center for Cancer Research, National Cancer Institute, Bethesda, MD 20892, USA. [10]Division of Medical Oncology, Ohio State University Comprehensive Cancer Center, Columbus, OH 43210, USA. [11]Merck & Co. Inc., Kenilworth, NJ 07033, USA. [12]West Virginia University Cancer Institute, Morgantown, WV 26506, USA. [13]Department of Gynecology and Obstetrics, Johns Hopkins Medicine, Baltimore, MD 21287, USA. [14]Caris Life Sciences, Phoenix, AZ 85040, USA. [15]Department of Pathology, Johns Hopkins University School of Medicine, Baltimore, MD 21287, USA.

*These authors contributed equally to this work. †Present address: Division of Solid Tumor Oncology, Memorial Sloan Kettering Cancer Center, New York, NY 10065, USA.

‡Corresponding author. Email: ldiaz@mskcc.org

an initial partial response or stable disease at the 20-week scan that later converted to a complete response while treatment was continued. The average time to any response was 21 weeks; the average time to complete response was 42 weeks (Fig. 1). Of note, the objective response rate was similar between colorectal cancer and other cancer subtypes. Specifically, we observed objective responses in 52% (95% CI, 36 to 68%) of patients with colorectal cancers and in 54% (95% CI, 39 to 69%) of the patients with cancers originating in other organs (tables S4 and S5). There was also no significant difference in the objective response rate between Lynch syndrome–associated and non–Lynch syndrome–associated tumors [46% (95% CI, 30 to 63%) versus 59% (95% CI, 41 to 76%), respectively; $P = 0.27$].

Neither median progression-free survival (PFS) nor median overall survival (OS) has yet been reached (median follow-up time of 12.5 months; Fig. 1), and the study is ongoing. However, the estimates of PFS at 1 and 2 years were 64% and 53%, respectively. The estimates of OS at 1 and 2 years were 76% and 64%, respectively, which is markedly higher than expected considering the advanced state of disease in this cohort (*21*). The PFS and OS were not significantly different in patients with colorectal cancers relative to those with other cancer types (fig. S1). Neither PFS [hazard ratio (HR) = 1.2 (95% CI, 0.582 to 2.512); $P = 0.61$] or OS [HR = 1.71 (95% CI, 0.697 to 4.196); $P = 0.24$] were influenced by tumors associated with Lynch syndrome.

Eleven patients achieved a complete response and were taken off therapy after 2 years of treatment. No evidence of cancer recurrence has been observed in those patients with an average time off therapy of 8.3 months. Seven other patients had residual disease by imaging, but pembrolizumab was discontinued after reaching the 2-year milestone or because of intolerance to therapy. To date, the average time off

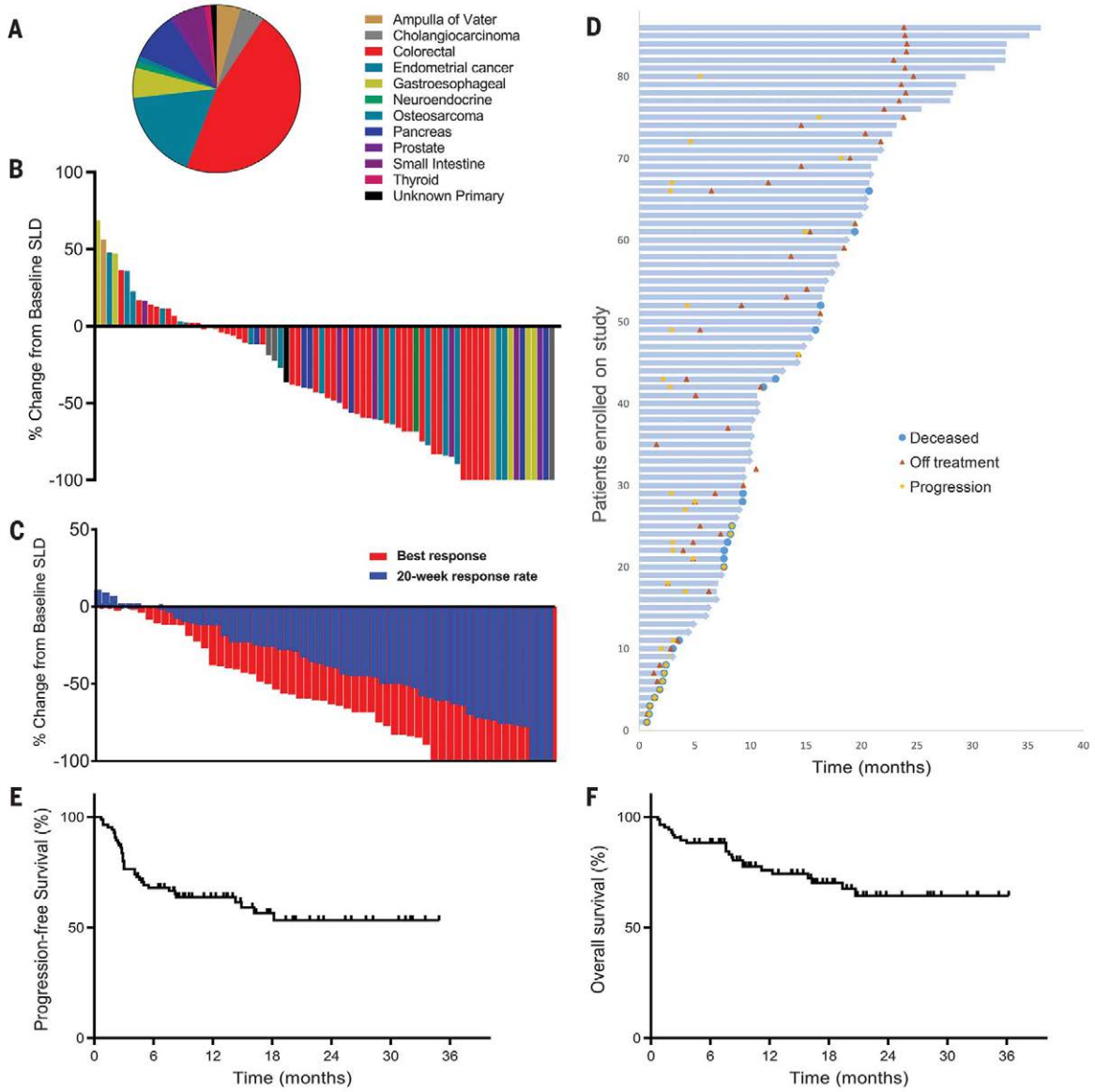


**Fig. 1. Patient survival and clinical response to pembrolizumab across 12 different tumor types with mismatch repair deficiency.** (**A**) Tumor types across 86 patients. (**B**) Waterfall plot of all radiographic responses across 12 different tumor types at 20 weeks. Tumor responses were measured at regular intervals; values show the best fractional change of the sum of longest diameters (SLD) from the baseline measurements of each measurable tumor. (**C**) Confirmed radiographic objective responses at 20 weeks (blue) compared to the best radiographic responses in the same patients (red). The mean time to the best radiographic response was 28 weeks. (**D**) Swimmer plot showing survival for each patient with mismatch repair–deficient tumors, indicating death, progression, and time off therapy. (**E** and **F**) Kaplan-Meier estimates of progression-free survival (E) and overall patient survival (F).

**Table 1. Summary of therapeutic response to pembrolizumab (anti–PD-1) treatment.** Radiographic responses, progression-free survival (PFS), and overall survival (OS) estimates were measured using RECIST v1.1 guidelines. Patients were considered not evaluable if clinical progression precluded a 12-week scan. The rate of disease control was defined as the percentage of patients who had a complete response, partial response, or stable disease for 12 weeks or more. NR, not reached.

| Type of response | Patients (*n* = 86) |
|---|---|
| Complete response | 18 (21%) |
| Partial response | 28 (33%) |
| Stable disease | 20 (23%) |
| Progressive disease | 12 (14%) |
| Not evaluable | 8 (9%) |
| Objective response rate | 53% |
| 95% CI | 42 to 64% |
| Disease control rate | 77% |
| 95% CI | 66 to 85% |
| Median progression-free survival time | NR |
| 95% CI | 14.8 months to NR |
| 2-year progression-free survival rate | 53% |
| 95% CI | 42 to 68% |
| Median overall survival time | NR |
| 95% CI | NR to NR |
| 2-year overall survival rate | 64% |
| 95% CI | 53 to 78% |

therapy for this group was 7.6 months. As of the data cutoff, none of these patients has shown evidence of progression since discontinuation of pembrolizumab.

Twenty patients with measurable radiographic disease underwent percutaneous biopsies between 1 month and 5 months after the initiation of therapy. Twelve of these biopsies demonstrated no evidence of tumor cells and were shown to have varying degrees of inflammation, fibrosis, and mucin, consistent with an ongoing immune response (fig. S2). The other eight cases showed residual tumor cells. The absence of cancer cells in posttreatment biopsies was a strong predictor of PFS [HR for PFS = 0.189 (95% CI, 0.046 to 0.767); $P = 0.012$], with median PFS of 25.9 months versus 2.9 months for biopsies with evidence of residual tumor. Although there was no significant difference in OS between patients whose biopsies were positive or negative for tumor cells, median OS has not yet been reached in patients with negative biopsies (table S6).

Primary clinical resistance to initial therapy with pembrolizumab, as measured by progressive radiographic disease on the first study scan, was noted in 12 patients (14%) (Table 1). After determining the exomic sequences of tumor and matched normal DNA from three of these patients, we compared them to the exomes of 15 primary tumors from patients who had achieved objective responses to the therapy (table S7). The three therapy-insensitive tumors harbored an average of 1413 nonsynonymous mutations, not significantly different from the number in patients with objective responses (1644 nonsynonymous mutations; $P = 0.67$, Student $t$ test). The gene (*B2M*) encoding $\beta_2$-microglobulin, a protein required for antigen presentation (*22*), was not mutated in any of the primary tumors from the resistant group (table S8).

Only five cases of acquired resistance were noted, where patients developed progressive disease after an initial objective response to pembrolizumab. Three of these cases were atypical in that the tumors emerged in occult sites such as the brain (two cases) or bone (one case). All three cases were treated with local therapy (radiation or surgery), and the patients survived and continued treatment with pembrolizumab. However, in accordance with study design, these three patients are listed in Fig. 1 as having progressive disease.

We performed exome sequencing of biopsies of brain metastases from two patients and compared the results with those of their primary tumors (fig. S3 and table S7). In the first case, the primary duodenal tumor and brain metastasis shared 397 nonsynonymous somatic mutations, providing unequivocal evidence that the metastasis was derived from the primary duodenal tumor rather than from an independent tumor. Moreover, the metastasis harbored 1010 nonsynonymous new mutations not present in the primary tumor, while the primary tumor harbored 964 mutations not present in the metastasis (table S9). In the second case, the primary colorectal tumor and brain metastasis shared 848 nonsynonymous somatic mutations, similarly providing unequivocal evidence of a genetic relationship between the two lesions. The brain metastasis harbored 221 nonsynonymous mutations not present in the primary colorectal tumor, while the primary tumor harbored 100 mutations not present in the metastasis (table S10). Of note, the brain metastases from both of these patients contained mutations in the *B2M* gene. In the patient with the colorectal tumor, a truncating mutation (L15Ffs*41) in the *B2M* gene was identified in the metastasis but not in the primary tumor. The primary duodenal tumor harbored a truncating mutation in $\beta_2$-microglobulin (V69Wfs*34), whereas the metastasis retained this mutation and acquired a second *B2M* mutation (12L>P; table S7).

We also evaluated the exomes of three primary tumors from patients who originally had stable disease by RECIST criteria at 20 weeks, but whose disease progressed within 8 months of initiating therapy. The average mutational burden was 1647 for this group, similar to those of the other patients described above. Interestingly, two of these three tumors harbored mutations of *B2M* (table S7).

We next sought to directly test the hypothesis that checkpoint blockade induces peripheral expansion of tumor-specific T cells and that mismatch repair–deficient tumors harbor functional MANA-specific T cells. Deep sequencing of T cell receptor CDR3 regions (TCR-seq) has emerged as a valuable technique to evaluate T cell clonal representation in both tumors and peripheral blood. We performed TCR-seq on tumors from three responding patients (obtained from archival surgical resections) and identified intratumoral clones that were selectively expanded in the periphery (Fig. 2A). These clones were present at very low frequency (often undetectable) in the peripheral blood before pembrolizumab treatment, but many rapidly increased after treatment initiation, followed by a contraction that generally occurred before radiologic responses were observed. To characterize functional T cell clones specific for mutant peptides, we obtained peripheral blood from one of the patients (subject 19). We tested the patient's posttreatment peripheral blood for reactivity against the 15 top candidate MANAs as identified via a neoantigen prediction algorithm [specified by the patient's human leukocyte antigen (HLA) class I alleles; see supplementary materials] with an interferon-γ (IFN-γ) ELISpot assay. Counts of spot-forming cells or cytokine activity analyses revealed T cell responses against 7 of 15 peptides (Fig. 2, B and C). We next interrogated the expanded lymphocyte populations against these seven peptides with TCR-seq. Clonal T cell expansion was noted in response to three of the seven peptides (Fig. 2D), with specificity demonstrated by a lack of expansion in response to any other peptide tested (fig. S4). In the peripheral blood, T cell expansion to these three mutant peptides resulted in 142 unique TCR sequences, seven of which were found in the tumor sample (two from MANA1, three from MANA2, and two from MANA4) (Fig. 2D). Of note, the mutant peptides that scored positive all resulted from frameshift mutations—the type of mutation that is most characteristic of mismatch repair–deficient cancers.

All seven of the MANA-reactive TCRs were detectable in peripheral blood at very low frequency (less than 0.02%) before treatment. However, four of the clones rapidly increased in frequency in the peripheral blood after anti–PD-1 treatment (Fig. 2E). Similar to results from the three patients

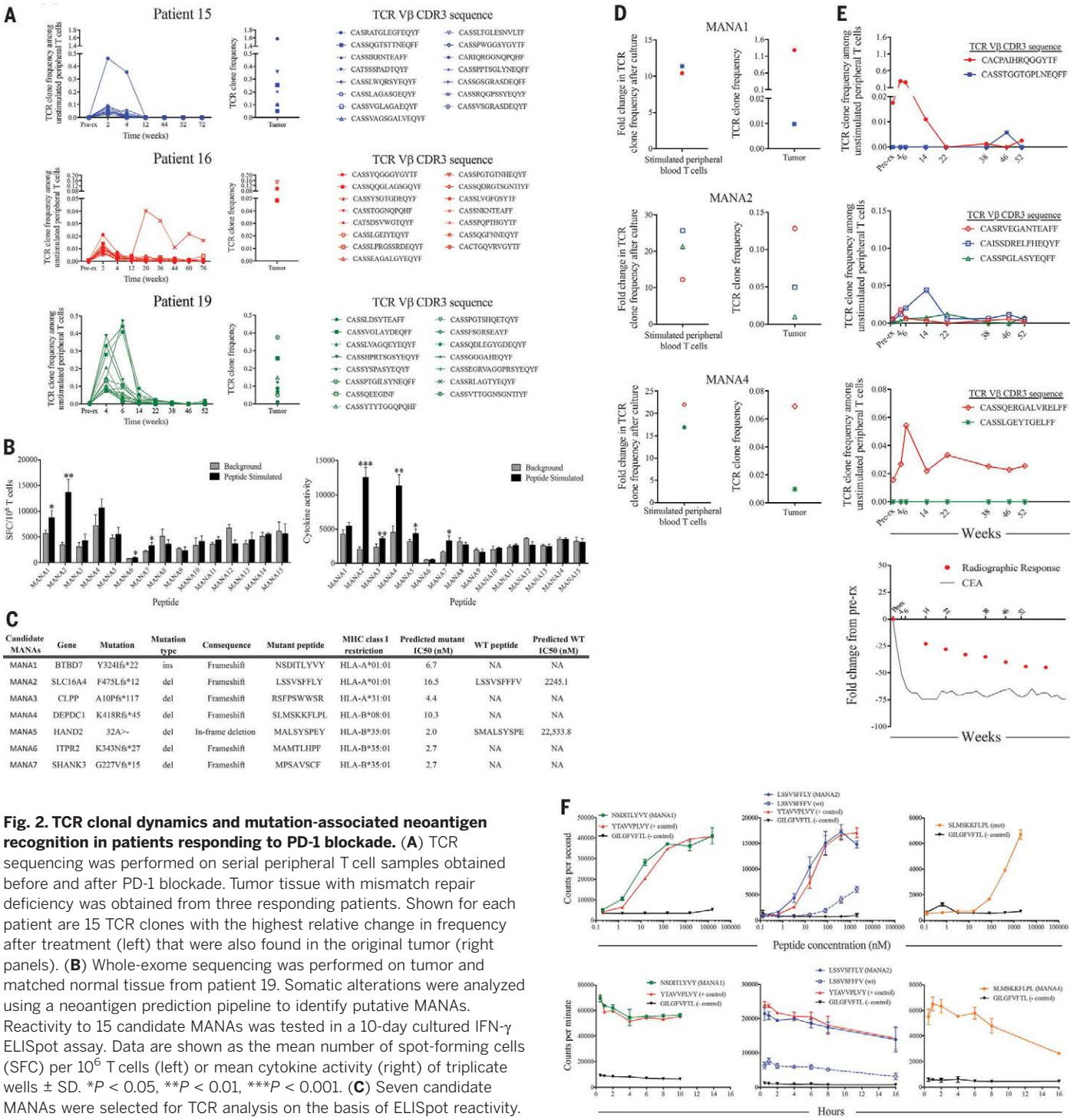


**Fig. 2. TCR clonal dynamics and mutation-associated neoantigen recognition in patients responding to PD-1 blockade.** (**A**) TCR sequencing was performed on serial peripheral T cell samples obtained before and after PD-1 blockade. Tumor tissue with mismatch repair deficiency was obtained from three responding patients. Shown for each patient are 15 TCR clones with the highest relative change in frequency after treatment (left) that were also found in the original tumor (right panels). (**B**) Whole-exome sequencing was performed on tumor and matched normal tissue from patient 19. Somatic alterations were analyzed using a neoantigen prediction pipeline to identify putative MANAs. Reactivity to 15 candidate MANAs was tested in a 10-day cultured IFN-γ ELISpot assay. Data are shown as the mean number of spot-forming cells (SFC) per $10^6$ T cells (left) or mean cytokine activity (right) of triplicate wells ± SD. *$P$ < 0.05, **$P$ < 0.01, ***$P$ < 0.001. (**C**) Seven candidate MANAs were selected for TCR analysis on the basis of ELISpot reactivity. (**D**) MANA-specific T cell responses were identified against three of seven candidate MANAs (MANA1, MANA2, and MANA4) after 10 days of in vitro stimulation (left panels). MANA-specific clones were identified by significant expansion in response to the relevant peptide and no significant expansion in response to any other peptide tested (fig. S3). Data are shown as the relative change in TCR clone frequency compared to the frequency of that clone after identical culture without peptide. These T cell clones were also found in the original tumor biopsy (right panels). (**E**) Frequency of MANA-specific clones, carcinoembryonic antigen (CEA), and radiographic response in the tumor [from (D)] were tracked in the peripheral blood before treatment and at various times after pembrolizumab treatment. Time is shown in weeks after the first pembrolizumab dose. (**F**) In vitro binding and stability assays demonstrate the affinity kinetics of each relevant MANA and the corresponding wild-type peptide (when applicable) for their restricting HLA class I allele. The A*02:01-restricted influenza M GILGFVFTL epitope was used as a negative control for each assay; known HLA-matched epitopes were used as positive controls when available. Data are shown as counts per second with increasing peptide concentration for binding assays (top) or counts per minute over time for stability assays (bottom). Data points indicate the mean of two independent experiments ± SD. Amino acid abbreviations: A, Ala; C, Cys; D, Asp; E, Glu; F, Phe; G, Gly; H, His; I, Ile; K, Lys; L, Leu; M, Met; N, Asn; P, Pro; Q, Gln; R, Arg; S, Ser; T, Thr; V, Val; W, Trp; Y, Tyr.

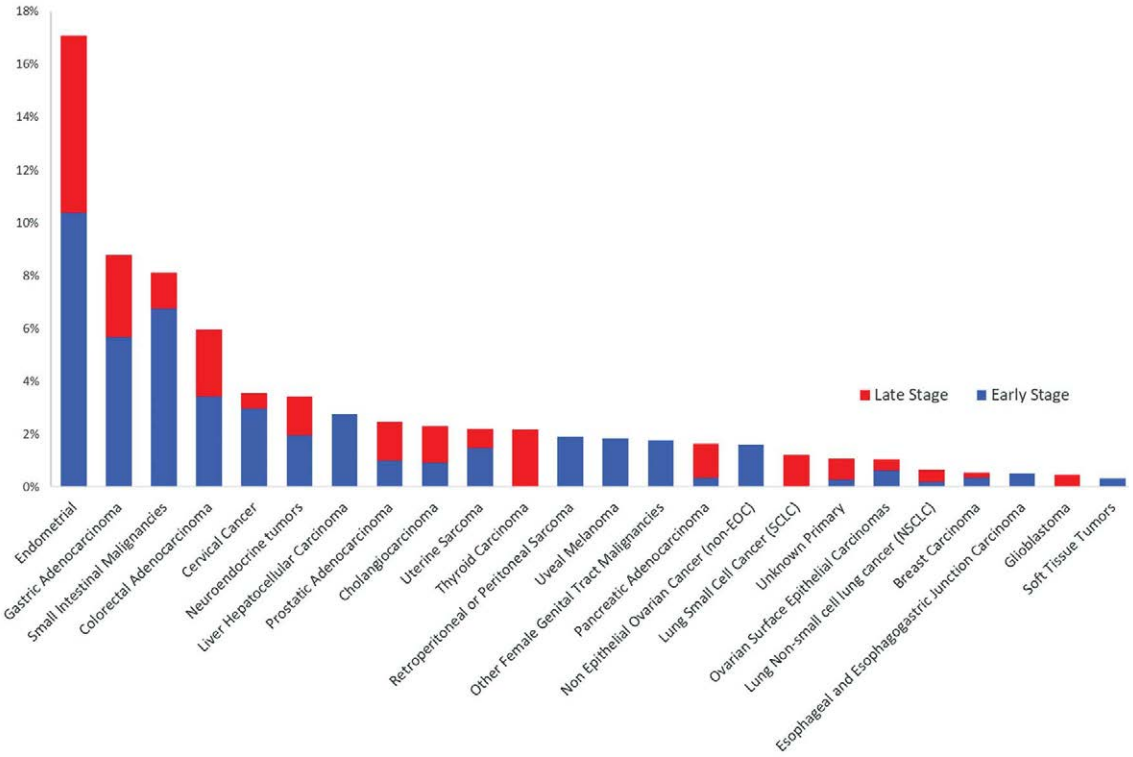


**Fig. 3. Mismatch repair deficiency across 12,019 tumors.** The proportion of mismatch repair–deficient tumors in each cancer subtype is expressed as a percentage. Mismatch repair–deficient tumors were identified in 24 of 32 tumor subtypes tested, more often in early-stage disease (defined as stage < IV).

analyzed above, the frequencies of these functionally validated MANA-specific T cell clones peaked soon after treatment and corresponded with normalization of the systemic tumor marker, predating objective radiographic response by several weeks. This peak in T cell clonal expansion was followed by decreases in frequency, reminiscent of T cell responses to acute viral infections (Fig. 2E). Because all the MANAs were from frameshift mutations, only MANA2 had a similar wild-type counterpart (differing in the two C-terminal amino acids). The corresponding wild-type peptide bound to HLA with less than 1% of the affinity of the mutant peptide counterpart (Fig. 2F), consistent with the mutation conferring enhanced HLA binding.

To estimate the proportion of cancer patients for whom the results of this study might be applicable, we evaluated 12,019 cancers representing 32 distinct tumor types for mismatch repair deficiency using a next-generation sequencing–based approach (Fig. 3). In accordance with a recent independent estimate using a different approach (*23*), we found that >2% of adenocarcinomas of the endometrium, stomach, small intestine, colon and rectum, cervix, prostate, bile duct, and liver, as well as neuroendocrine tumors, uterine sarcomas, and thyroid carcinomas, were mismatch repair–deficient. Across these 11 tumor types, 10% of stage I to stage III cancers and 5% of stage IV cancers were mismatch repair–deficient. This represents roughly 40,000 annual stage I to III diagnoses and 20,000 stage IV diagnoses in the United States alone. Because genetic and immunohistochemical tests for mismatch repair deficiency are already widely available, these results tie immunity, cancer genetics, and therapeutics together in a manner that will likely establish a new standard of care. In the future, testing for mismatch repair deficiency in patients who are refractory to other treatments might be considered in order to identify those who may benefit from PD-1 pathway blockade, regardless of tumor type.

## REFERENCES AND NOTES


1. S. L. Topalian, C. G. Drake, D. M. Pardoll, *Cancer Cell* **27**, 450–461 (2015).
2. P. C. Tumeh *et al.*, *Nature* **515**, 568–571 (2014).
3. D. F. McDermott *et al.*, *J. Clin. Oncol.* **33**, 2013–2020 (2015).
4. S. L. Topalian *et al.*, *J. Clin. Oncol.* **32**, 1020–1030 (2014).
5. S. N. Gettinger *et al.*, *J. Clin. Oncol.* **33**, 2004–2012 (2015).
6. J. M. Taube *et al.*, *Clin. Cancer Res.* **20**, 5064–5074 (2014).
7. N. J. Llosa *et al.*, *Cancer Discov.* **5**, 43–51 (2015).
8. R. S. Herbst *et al.*, *Nature* **515**, 563–567 (2014).
9. N. A. Rizvi *et al.*, *Science* **348**, 124–128 (2015).
10. W. Hugo *et al.*, *Cell* **168**, 542 (2017).
11. N. H. Segal *et al.*, *Cancer Res.* **68**, 889–892 (2008).
12. M. M. Gubin *et al.*, *Nature* **515**, 577–581 (2014).
13. T. N. Schumacher, R. D. Schreiber, *Science* **348**, 69–74 (2015).
14. J. P. Ward, M. M. Gubin, R. D. Schreiber, *Adv. Immunol.* **130**, 25–74 (2016).
15. C. Lengauer, K. W. Kinzler, B. Vogelstein, *Nature* **396**, 643–649 (1998).
16. H. Kim, J. Jen, B. Vogelstein, S. R. Hamilton, *Am. J. Pathol.* **145**, 148–156 (1994).
17. T. C. Smyrk, P. Watson, K. Kaul, H. T. Lynch, *Cancer* **91**, 2417–2422 (2001).
18. R. Dolcetti *et al.*, *Am. J. Pathol.* **154**, 1805–1813 (1999).
19. D. T. Le *et al.*, *N. Engl. J. Med.* **372**, 2509–2520 (2015).
20. M. Overman *et al.*, *J. Clin. Oncol.* **35** (suppl.), 519 (2017).
21. A. Grothey *et al.*, *Lancet* **381**, 303–312 (2013).
22. J. M. Zaretsky *et al.*, *N. Engl. J. Med.* **375**, 819–829 (2016).
23. R. J. Hause, C. C. Pritchard, J. Shendure, S. J. Salipante, *Nat. Med.* **22**, 1342–1350 (2016).


## ACKNOWLEDGMENTS


The data reported are tabulated in the main text and supplementary materials. The raw TCR RNA sequence data have been deposited into the ImmuneACCESS project repository of the Adaptive Biotech database, under the following link: https://clients.adaptivebiotech.com/pub/diaz-2017-science. We thank K. Helwig for administrative support, C. Blair for outstanding technical assistance, and E. H. Rubin, R. Dansey, and R. Perlmutter at Merck & Co. Inc. (Kenilworth, NJ) for supporting this research. Funded by the Swim Across America Laboratory at Johns Hopkins, the Ludwig Center for Cancer Genetics and Therapeutics, the Howard Hughes Medical Institutes, the Bloomberg-Kimmel Institute for Cancer Immunotherapy at Johns Hopkins, the 2017 Stand Up to Cancer Colon Cancer Dream Team, the Commonwealth Fund, the Banyan Gate Foundation, the Lustgarten Foundation for Pancreatic Cancer Research, the Bloomberg Foundation, the Sol Goldman Pancreatic Cancer Research Center, Merck & Co. Inc., Gastrointestinal SPORE grant P50CA062924, and NIH grants P30CA006973, CA163672, CA43460, CA203891, CA67941, CA16058, and CA57345. L.D., D.L., B.V., N.P., and K.W.K. are inventors on a patent application (PCT/US2015/060331 or WO 2016077553 A1) submitted by Johns Hopkins University that covers checkpoint blockade and microsatellite instability. L.D., B.V., N.P., and K.W.K. are founders of PapGene and Personal Genome Diagnostics (PGDx). L.D. is a consultant for Merck, Illumina, PGDx, and Cell Design Labs. PGDx and PapGene, as well as other companies, have licensed technologies from Johns Hopkins University, on which L.D., B.V., N.P., and K.W.K. are inventors. Some of these licenses and relationships are associated with equity or royalty payments. The terms of these arrangements are being managed by Johns Hopkins and Memorial Sloan Kettering in accordance with its conflict-of-interest policies.


## SUPPLEMENTARY MATERIALS

www.sciencemag.org/content/357/6349/409/suppl/DC1
Materials and Methods
Figs. S1 to S4
Tables S1 to S10
References (*24*–*36*)


17 May 2017; accepted 1 June 2017
Published online 8 June 2017
10.1126/science.aan6733

FORCEFORSCIENCE.ORG

# STAND TOGETHER
# Be a Force for Science

**GET THE FACTS**

Understand the science behind the issues that matter.

**FOLLOW AAAS ADVOCACY**

Champion public discussion and evidence-based policy.

**TAKE ACTION**

Learn ways you can become an advocate and stand up for science.

AMERICAN ASSOCIATION FOR THE ADVANCEMENT OF SCIENCE

AAAS

IMMUNOLOGY

# Recurrent infection progressively disables host protection against intestinal inflammation

Won Ho Yang,[1,2,3] Douglas M. Heithoff,[1,3] Peter V. Aziz,[1,2,3] Markus Sperandio,[4] Victor Nizet,[5] Michael J. Mahan,[1,3] Jamey D. Marth[1,2,3]*

**Intestinal inflammation is the central pathological feature of colitis and the inflammatory bowel diseases. These syndromes arise from unidentified environmental factors. We found that recurrent nonlethal gastric infections of Gram-negative *Salmonella enterica* Typhimurium (ST), a major source of human food poisoning, caused inflammation of murine intestinal tissue, predominantly the colon, which persisted after pathogen clearance and irreversibly escalated in severity with repeated infections. ST progressively disabled a host mechanism of protection by inducing endogenous neuraminidase activity, which accelerated the molecular aging and clearance of intestinal alkaline phosphatase (IAP). Disease was linked to a Toll-like receptor 4 (TLR4)–dependent mechanism of IAP desialylation with accumulation of the IAP substrate and TLR4 ligand, lipopolysaccharide-phosphate. The administration of IAP or the antiviral neuraminidase inhibitor zanamivir was therapeutic by maintaining IAP abundance and function.**

Inflammation of the intestinal tract is the defining feature of colitis and the human inflammatory bowel diseases (IBDs), including Crohn's disease and ulcerative colitis (UC). In these syndromes, chronic inflammation disrupts intestinal homeostasis and provokes immune-mediated tissue damage (*1*–*3*). The origins of these diseases remain mysterious and involve one or more environmental factors (*4*). Among multiple human monozygotic twin comparisons, the genetic contribution to the origin of UC is about 20%, whereas in Crohn's disease, genetics may play a larger though often minor role (*5*). Considering the possible environmental origins of disease, pathogenic infection has been studied as a factor in precipitating intestinal inflammation (*6*). Notably, bacterial infections have been linked to seasonal increases in hospital admissions involving intestinal inflammation and IBD (*7*).

Small-inoculum bacterial infections that are brief and self-limited are likely to be the most common infections, and they may frequently go unreported, potentially leading to an underappreciation of the numbers of infections among individuals. We hypothesized that there may be cumulative effects of repeated small-inoculum and subclinical infections, which, if true, may be detected in a model of human food poisoning. We designed a study using recurrent low-titer nonlethal gastrointestinal infection by the bacterium *Salmonella enterica* Typhimurium (ST), a common human pathogen. Nontyphoidal *Salmonella* (NTS) produces a greater human disease burden than any other foodborne bacterial pathogen in the United States, causing more than a million illnesses annually (*8*, *9*). Globally, NTS causes 93.8 million cases and 155,000 deaths each year (*10*) and is responsible for up to 50% of bacteremias in young children from developing countries (*11*, *12*).

## Results

### ST infection elicits intestinal inflammation by diminishing host intestinal alkaline phosphatase levels

Beginning at 8 weeks of age, wild-type C57BL/6J mice were infected by gastric intubation with $2 \times 10^3$ ST colony-forming units (CFU) every 4 weeks for six consecutive months. After infection, ST was detected transiently and predominantly in the small intestine and some lymphoid tissues. The pathogen was cleared by the host to undetectable levels by 21-days post-infection monitoring, which further noted the absence of overt symptoms or mortality among the animals (fig. S1, A and B). The onset of disease required more than a single infection with this low titer, whereas multiple signs of disease were evident among most of the animals before the fourth infection. Phenotypes consistent with the onset of intestinal dysfunction included weight loss, reduced colon length, altered stool consistency (diarrhea), and the presence of fecal blood (Fig. 1, A to D, and fig. S1C). By 20 weeks of age and before the fourth infection, signs of disease were present among most of the animals and further included an epithelial barrier defect (Fig. 1E). At 32 to 48 weeks, rectal prolapse was observed among some animals undergoing recurrent infections (Fig. 1F). The frequency of disease symptoms escalated with successive recurrent infections and persisted for at least 5 months after the cessation of infections.

Reductions in alkaline phosphatase (AP) activity and intestinal AP (IAP) abundance were detected in both the small intestine and intestinal contents, whereas levels of duodenal tissue mRNA encoding IAP were unchanged (Fig. 1, G to I, and fig. S2A). Mammalian IAP is produced exclusively by enterocytes of the duodenum and is released from the cell surface into the lumen where it can dephosphorylate and thereby detoxify the lipopolysaccharide (LPS) endotoxin of Gram-negative bacteria (*13*–*16*). We found that oral supplementation with calf IAP (cIAP) maintained normal AP activity levels in the intestinal tract among animals receiving recurrent ST infections (Fig. 1J). Analysis of LPS isolated from the intestinal tract at 20 weeks of age before the fourth infection and after ST clearance revealed a fourfold increase in endogenous LPS-phosphate levels in the context of a 50% increase in total LPS, both of which were maintained close to normal levels in mice receiving cIAP treatment (Fig. 1K). Augmentation of AP activity by cIAP treatment also protected against the development of disease symptoms encompassing weight loss, colon length, diarrhea, fecal blood, and epithelial barrier function (Fig. 1L).

Inflammatory cytokines associated with intestinal tissue inflammation include chemokine ligand 5 (CCL5), interleukin-1β (IL-1β), tumor necrosis factor–α (TNF-α), and interferon-γ (IFN-γ). Recurrent ST infection progressively increased inflammatory cytokine mRNA expression levels predominantly in the colon, unless cIAP treatment was provided (Fig. 1M). Histopathological changes were also predominantly seen in the colon, including an infiltration of leukocytes into the lamina propria, which included neutrophils, monocytes, and T cells, as well as an erosion of the epithelial barrier, and reduced goblet cell numbers, whereas a much lesser effect was observed in the small intestine and, in addition, only in the ileum (Fig. 1N and figs. S2B and S3). Thus, recurrent nonlethal gastrointestinal infection of ST diminished the expression of host IAP activity that normally confers host protection against intestinal inflammation and tissue damage predominantly in the colon. Studies were further undertaken to identify the mechanisms that regulate IAP function.

### IAP deficiency is linked to an accelerated rate of desialylation and endocytic localization

IAP is synthesized as a glycosylphosphatidylinositol (GPI)–linked glycoprotein residing on the

[1]Center for Nanomedicine, University of California, Santa Barbara, Santa Barbara, CA 93106, USA. [2]Sanford Burnham Prebys Medical Discovery Institute, University of California, Santa Barbara, Santa Barbara, CA 93106, USA. [3]Department of Molecular, Cellular, and Developmental Biology, University of California, Santa Barbara, Santa Barbara, CA 93106, USA. [4]Walter-Brendel-Centre for Experimental Medicine, Ludwig-Maximilians-University, Munich, Germany. [5]Department of Pediatrics and Skaggs School of Pharmacy and Pharmaceutical Sciences, University of California, San Diego, La Jolla, CA 92093, USA.
*Corresponding author. Email: jmarth@sbpdiscovery.com

enterocyte cell surface of the duodenum until it is released into the intestinal lumen by phospholipase activity (*13*, *17*). IAP production was investigated by pulse-chase experiments of ex vivo primary enterocyte cultures derived from small intestinal tissue. Normal rates of IAP synthesis and appearance at the cell surface were observed among all enterocyte cultures regardless of previously cleared infections (Fig. 2A). In contrast, a significant decrease in IAP cell surface half-life with reduced IAP abundance in the culture media was measured among enterocyte samples from mice that had cleared multiple infections (Fig. 2, B and C). Colocalization studies revealed increased colocalization of IAP with markers of early endosomes and lysosomes coincident with reduced cell surface IAP abundance (Fig. 2, D and E).

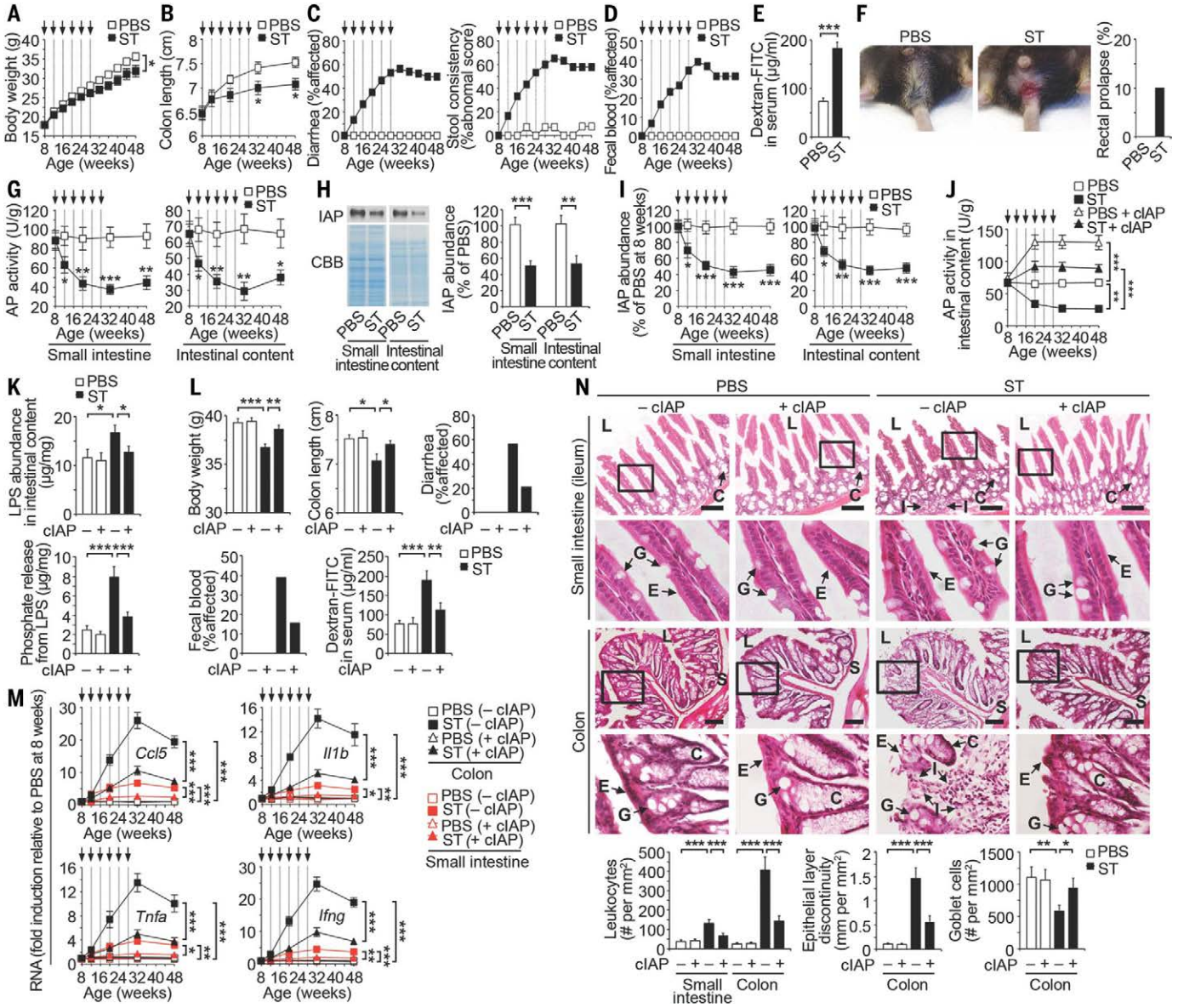


**Fig. 1. Recurrent ST infection diminishes the abundance and protective role of IAP.** Wild-type (WT) mice were analyzed during a course of recurrent ST infection ($2 \times 10^3$ CFU) or uninfected [phosphate-buffered saline (PBS)] at indicated time points (arrows). (**A**) Body weight (ST, $n = 20$; PBS, $n = 19$). (**B**) Colon length ($n = 40$ per condition). (**C**) Diarrhea and stool consistency (ST, $n = 19$; PBS, $n = 13$). (**D**) Fecal blood (ST, $n = 19$; PBS, $n = 13$). (**E**) Intestinal epithelial barrier function ($n = 8$ per condition) at 20 weeks of age before the fourth infection. FITC, fluorescein isothiocyanate. (**F**) Rectal prolapse (ST, $n = 30$; PBS, $n = 20$) at 32 to 48 weeks of age or 4 to 20 weeks after last ST infection (representative image). (**G**) AP activity ($n = 40$ per condition). (**H**) Immunoblot blot analysis of IAP at 20 weeks of age before the fourth infection ($n = 8$ per condition). (**I**) Relative IAP abundance ($n = 40$ per condition). (**J**) AP activity ± cIAP ($n = 40$ per condition). (**K**) LPS abundance and phosphate released from LPS ($n = 8$ per condition) at 20 weeks of age. (**L**) Body weight ($n = 10$ per condition), colon length ($n = 8$ per condition), diarrhea (ST, $n = 23$; PBS, $n = 14$; ST + cIAP, $n = 19$; PBS + cIAP, $n = 15$), fecal blood (ST, $n = 23$; PBS, $n = 14$; ST + cIAP, $n = 19$; PBS + cIAP, $n = 15$) at 48 weeks of age (20 weeks after last ST infection), and intestinal epithelial barrier function ($n = 8$ per condition) at 20 weeks of age before the fourth infection. (**M**) Cytokine mRNA expression ($n = 30$ per condition). (**N**) Hematoxylin and eosin (H&E)–stained intestinal tissues at 48 weeks of age (20 weeks after last ST infection). L, intestinal lumen; E, epithelial layer; C, crypt; G, goblet cell; S, submucosa; I, infiltration of leukocytes. Graphs are representative of 16 fields of view ($n = 4$ per condition). All scale bars, 100 μm. Error bars represent means ± SEM. ***$P < 0.001$, **$P < 0.01$, and *$P < 0.05$; Student's $t$ test (A, B, E, and G to I) or one-way analysis of variance (ANOVA) with Tukey's multiple comparisons test (J to N).

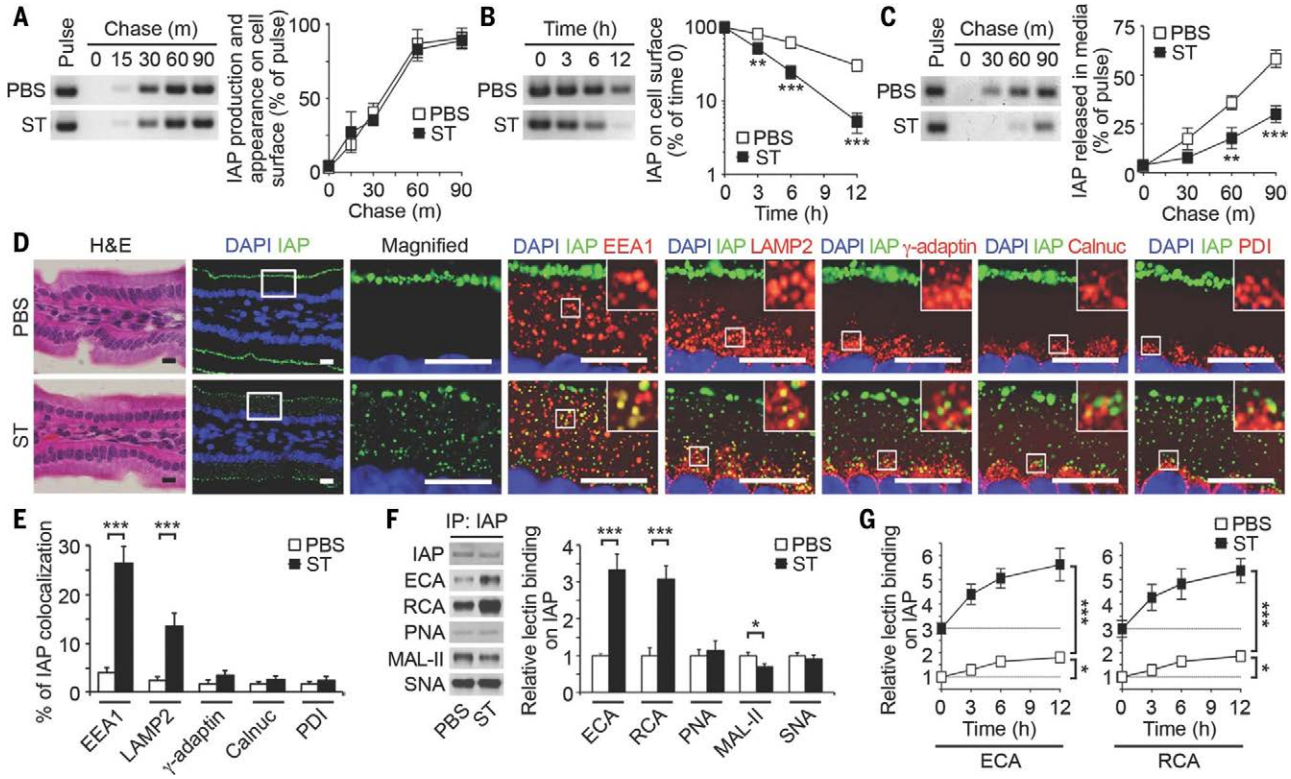


**Fig. 2. Mechanism of IAP regulation during recurrent ST infection.** (**A** to **C**) Pulse-chase analyses of IAP synthesis, trafficking, and cell surface half-life among cultured primary enterocytes isolated from WT mice at 20 weeks of age (before a fourth ST infection). (**D** and **E**) In situ localization and intracellular colocalization of IAP in duodenal sections stained with H&E or with fluorescent antibodies to IAP (green) and intracellular compartment proteins (red), including early endosomes (EEA1), lysosomes (LAMP2), trans-Golgi (γ-adaptin), cis-Golgi (Calnuc), or the endoplasmic reticulum (PDI), depicting the percentage of IAP colocalization (yellow). Graphs are representative of 10 fields of view ($n$ = 4 per condition). Scale bars, 10 μm. DAPI, 4′,6-diamidino-2-phenylindole. (**F**) Lectin blot of IAP from small intestine. (**G**) Lectin binding of IAP on cultured enterocytes after cell surface biotinylation. (A to G) WT mice at 20 weeks of age before fourth infection. (A to C and G) $n$ = 6 per condition. (F) $n$ = 8 per condition. Error bars represent means ± SEM. ***$P$ < 0.001, **$P$ < 0.01, and *$P$ < 0.05; Student's $t$ test (A to C and E and F) or one-way ANOVA with Tukey's multiple comparisons test (G).

IAP is glycosylated during its synthesis in the secretory pathway. We next analyzed the glycan linkages attached to enterocyte IAP using analytical lectins, including the α2-3 sialic acid–specific lectin *Maackia amurensis* lectin II and the galactose-specific lectins *Erythrina cristagalli* agglutinin and *Ricinus communis* agglutinin. These lectins have been validated biochemically and genetically, although their binding does not provide full structural resolution of all glycan types and linkages present. A significant reduction of terminal sialic acid linkages coincident with the exposure of underlying galactose linkages was measured in the context of recurrent infection (Fig. 2F). No comparative changes to other specific glycan linkages were detected, including the sialylation state of core 1 O-glycans, or changes in abundance of α2-6–linked sialic acids, using peanut agglutinin and *Sambucus nigra* lectins, respectively. In the absence of infection, we observed a progressive desialylation of the glycans attached to nascent IAP on the enterocyte cell surface, indicative of a feature of its normal molecular aging. This basal rate of IAP desialylation was significantly increased by recurrent ST infection and was concurrent with increased IAP internalization and degradation in enterocytes (Fig. 2G). Although IAP deficiency appeared to be the predominant factor in disease onset, as indicated by the effects of cIAP treatment, multiple enterocyte cell surface glycoproteins were observed to be desialylated and internalized from the cell surface of endocytes, including sucrase-isomaltase, dipeptidyl peptidase 4, and lactase (fig. S4). These results suggest that the presence of one or more sialyltransferases establishes the normal half-lives (and consequent abundance) of enterocyte cell surface glycoproteins, including IAP.

### *ST3Gal6 is responsible for IAP sialylation in protecting against intestinal inflammation*

The ST3Gal6 sialyltransferase generates α2-3 sialic acid linkages on glycoproteins and is highly expressed in the intestinal tract (*18*, *19*). In mice lacking a functional *St3gal6* gene, we detected a significant reduction in AP activity and IAP abundance, whereas mRNA encoding IAP was unchanged (Fig. 3, A and B, and fig. S5A). Although LPS levels in the intestinal tract were similar at 8 weeks of age, a threefold increase of LPS-phosphate abundance was measured, consistent with reduced AP activity (Fig. 3C). Because of absent ST3Gal6 function, IAP sialic acid linkages were also deficient with increased galactose exposure (Fig. 3D), similar to findings in wild-type mice experiencing recurrent ST infection. Glycan alterations were further detected histologically among small intestinal epithelial cells (fig. S5B). Diminished IAP sialylation in ST3Gal6 deficiency was linked to reduced IAP cell surface residency and increased IAP colocalization with markers of endosomes and lysosomes (Fig. 3, E to I). Thus, IAP sialylation by ST3Gal6 functions to maintain IAP half-life and abundance in the intestinal lumen. The impact of IAP deficiency caused by the absence of ST3Gal6 was further investigated.

Mice aging in the absence of ST3Gal6 was compared with that of wild-type littermates in the presence and absence of recurrent ST infection and cIAP therapy. Spontaneous phenotypes detected in uninfected mice lacking ST3Gal6 included reduced body weight, reduced colon length, diarrhea, the presence of fecal blood, and epithelial barrier dysfunction, all of which were exacerbated by recurrent ST infection. The addition of cIAP to drinking water normalized AP activity levels during adult life and reduced or eliminated signs of disease (Fig. 4, A to C). Similarly, increased LPS-phosphate levels were closely associated with

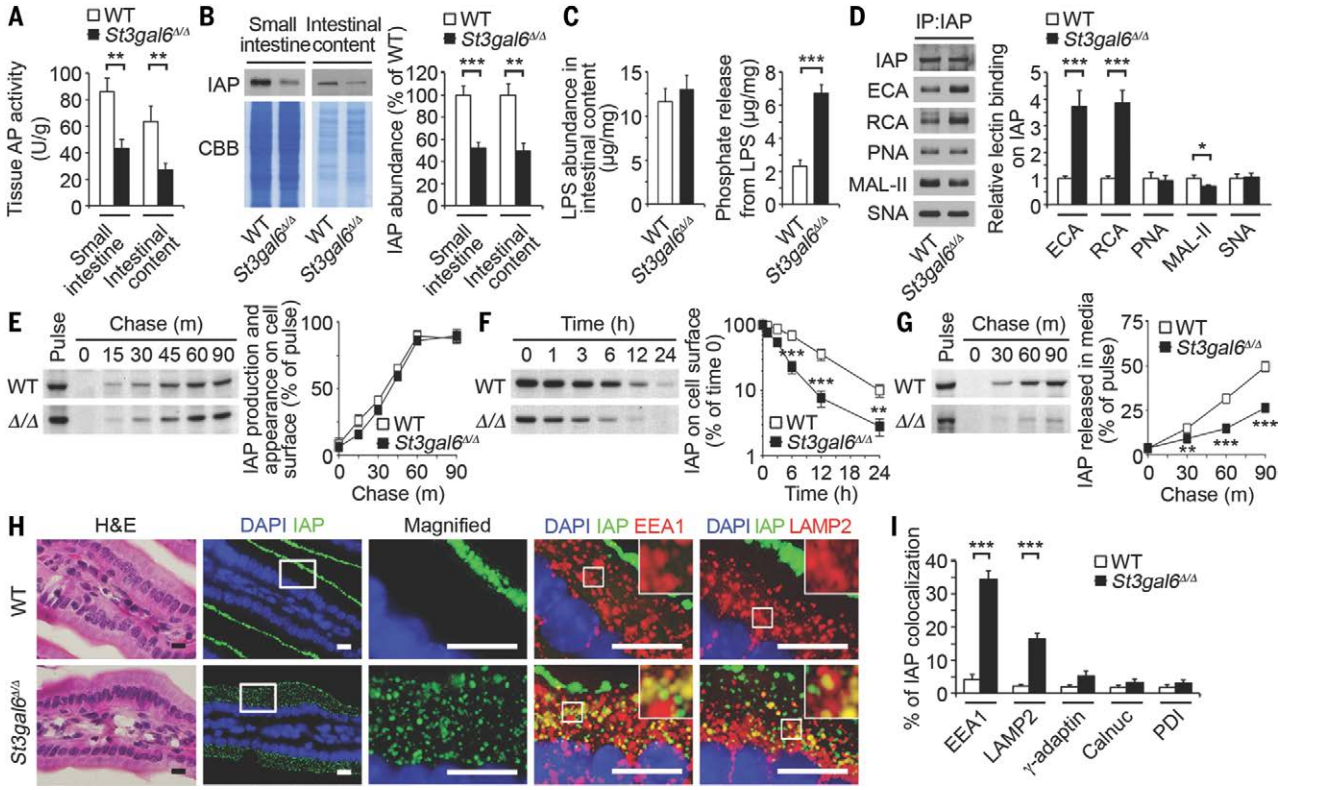


**Fig. 3. Mechanism of IAP regulation by ST3Gal6 sialylation.** (**A**) AP activity. (**B**) IAP protein abundance. (**C**) LPS abundance and phosphate released from LPS of intestinal content. (**D**) Lectin blot of IAP from small intestine. (**E** to **G**) Pulse-chase of IAP synthesis and trafficking and IAP cell surface half-life among cultured primary enterocytes isolated from uninfected ST3Gal6-deficient mice and WT littermates at 8 to 10 weeks of age. (**H** and **I**) In situ localization and intracellular colocalization of IAP in duodenum, depicting the percentage of IAP colocalization (yellow). Graphs are representative of 10 fields of view ($n$ = 4 per genotype). Scale bars, 10 μm. (A to I) *St3Gal6*-deficient mice and WT littermates at 8 to 10 weeks of age, uninfected. (A to D) $n$ = 8 per condition. (E to G) $n$ = 6 per condition. Error bars represent means ± SEM. ***$P$ < 0.001, **$P$ < 0.01, and *$P$ < 0.05; Student's $t$ test (A to G and I).

reduced IAP and the onset of disease symptoms, whereas total LPS increased only modestly in the intestinal contents of infected mice (Fig. 4D). LPS is generated predominantly in the colon by commensal microbes that may serve as markers or effectors of intestinal inflammatory disease (*20*).

A survey of microbiota using 16*S* ribosomal DNA (rDNA) probes revealed a 50% increase of intestinal bacterial load attributed primarily to the Gram-negative Enterobacteriaceae, consistent with the magnitude of increase of total LPS. These findings were present among both uninfected *St3gal6*-null mice and wild-type littermates subjected to recurrent ST infection (Fig. 4E). The temporal acquisition of these microbiota changes observed at 32 weeks was found to emerge progressively among wild-type mice receiving periodic ST infections and was coincident with the emergence and increase in the severity of disease symptoms (fig. S6). These findings are also consistent with reports of altered commensal microbiota populations that can contribute intestinal inflammation and that often include elevated levels of Enterobacteriaceae (*3*, *21*).

ST3Gal6 deficiency spontaneously increased inflammatory cytokines in the intestinal tissues of uninfected animals, and this was further exacerbated by recurrent ST infection (Fig. 4F). Similarly, histopathological findings in the absence of ST3Gal6 correlated with elevated inflammatory marker expression and leukocyte infiltration, epithelial layer discontinuity, and reduced goblet cell numbers, which were also increased in severity by recurrent ST infection (Fig. 4G). These results demonstrated that the ST3Gal6 sialytransferase is essential to support normal IAP sialylation and expression and thereby host protection against spontaneous intestinal inflammation. The cause of IAP desialylation after ST infection was unaccounted for but implicated as a significant trigger of pathogenesis.

### *Disease onset with neuraminidase induction is TLR4-dependent and recapitulated by LPS*

Neuraminidase (Neu) enzymes, also known as sialidases, hydrolyze sialic acids attached to glycan polymers and are encoded in the genomes of diverse organisms, including bacteria, mice, and humans. However, the genome of the ST isolate used in our studies does not encode a Neu (*22*), indicating a host source of the induced Neu activity. Four Neu genes have been identified in mammalian genomes (*Neu1* to *Neu4*), with NEU1 and NEU3 enzymes expressed in multiple compartments, including the cell surface, and in the blood (*23*, *24*). An increase in Neu activity occurred in the small intestine because of ST infection. Studies of Toll-like receptor 4 (*Tlr4*)–null mice revealed that this induction of host Neu activity was dependent on TLR4 function (Fig. 5A). Among mammalian Neu isozymes, only NEU3 abundance and *Neu3* RNA expression correlated with TLR4-dependent induction of Neu activity (Fig. 5, B and C). The absence of *Neu3* induction due to TLR4 deficiency resulted in normal IAP expression at the enterocyte cell surface (Fig. 5D). This was coincident with normal levels of sialic acid linkages on IAP and among apical glycoproteins of the small intestinal epithelium (fig. S5, C and D). AP activity and IAP abundance also remained normal in TLR4 deficiency, and LPS-phosphate levels did not increase significantly after ST infections (Fig. 5, E to G). The induction of inflammatory cytokines caused by recurrent ST infection was also blocked by TLR4 deficiency, and signs of disease were reduced or eliminated with the maintenance of epithelial barrier function (Fig. 5, H and I).

TLR4 is activated by binding to its LPS ligand (*25*, *26*). The LPS bacterial endotoxin is found predominantly in the colon (*27*, *28*), where it can initiate proinflammatory signaling to engage immune

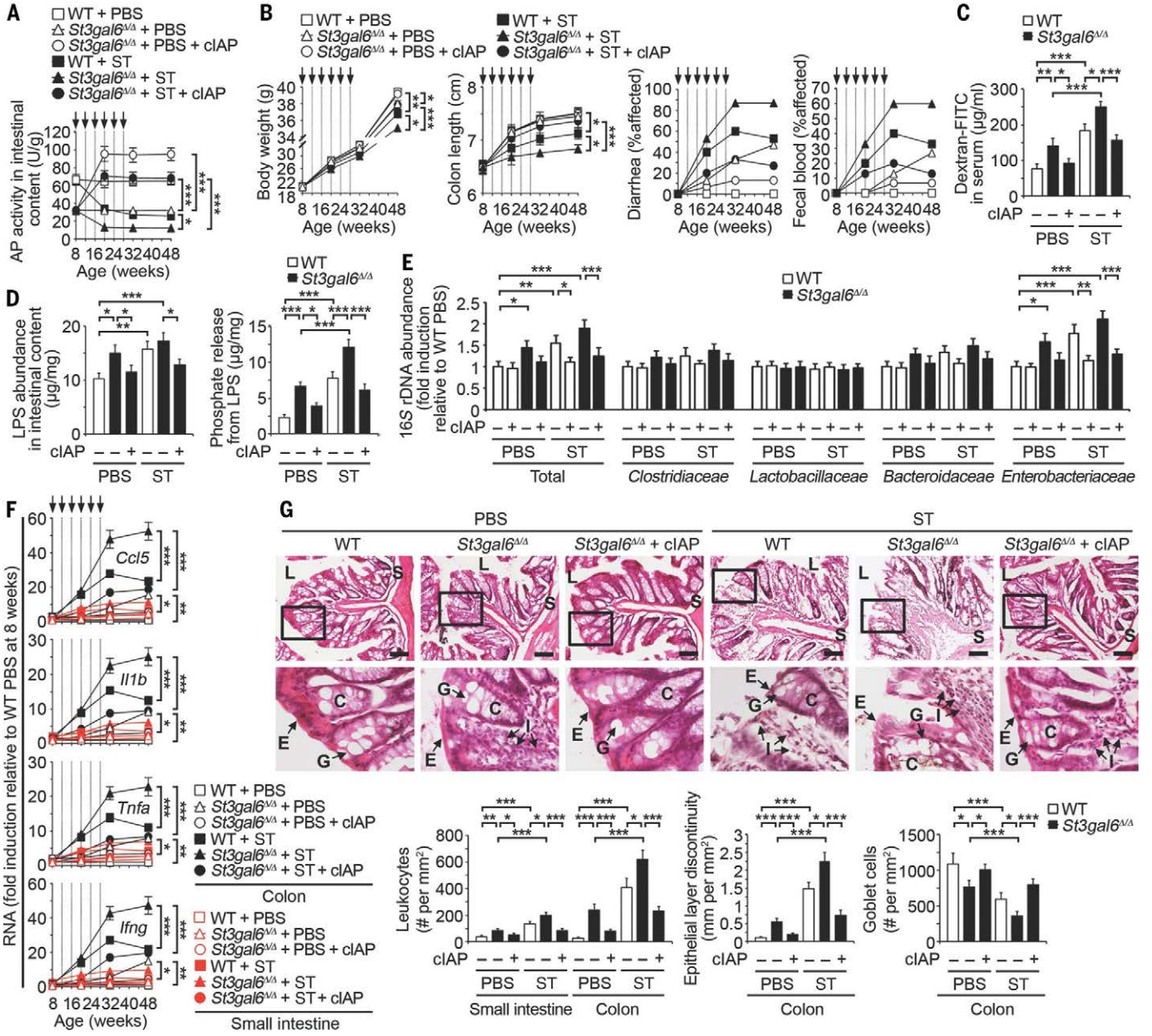


**Fig. 4. ST3Gal6 sialylation of IAP prevents intestinal inflammation.** Indicated genotypes after ST reinfection (arrows) were analyzed in the absence or presence of cIAP. (**A**) AP activity ($n$ = 32 per condition). (**B**) Body weight ($n$ = 10 per condition), colon length ($n$ = 32 per condition), diarrhea ($n$ = 30 per condition), and fecal blood ($n$ = 30 per condition). (**C**) Intestinal epithelial barrier function. (**D**) LPS abundance and phosphate released from LPS of intestinal content. (**E**) Commensal microbiome 16S rDNA in intestinal content ($n$ = 10 per condition). (**F**) Inflammatory cytokine RNA in colon and small intestine ($n$ = 24 per condition). (**G**) H&E-stained colon sections. Graphs are representative of 10 fields of view ($n$ = 4 per condition). Scale bars, 100 µm. (C and D) Data were acquired from mice 20 weeks of age before fourth infection. (E to G) Data were acquired from mice 32 weeks of age and 4 weeks after the last infection. (C and D) $n$ = 8 per condition. Error bars represent means ± SEM. ***$P$ < 0.001, **$P$ < 0.01, and *$P$ < 0.05; one-way ANOVA with Tukey's multiple comparisons test (A to G).

cells in the onset and development of disease (*29*, *30*). We investigated whether LPS was itself sufficient for Neu induction, IAP deficiency, and concurrent elevations of inflammatory cytokines. Dose-response analyses using commercially obtained LPS were undertaken to determine minimal dosage and timing for further study (fig. S7, A and B). We found that gastric intubation of LPS induced Neu activity, NEU3 abundance, and *Neu3* RNA levels with reductions in AP activity and IAP abundance, all of which were dependent on TLR4 function (Fig. 6, A to F). The induction of Neu activity by LPS resulted in TLR4-dependent reductions of sialic acid linkages with galactose exposure on isolated IAP and among apical cell surface glycoproteins of the small intestinal epithelium (fig. S7, C and D). LPS increased the internalization and colocalization of IAP with endocytic markers coincident with reduced IAP expression at the cell surface (fig. S7E). Normal IAP levels were retained after LPS administration in TLR4 deficiency with relatively low abundance of LPS-phosphate (Fig. 6G). The induction of LPS-induced inflammatory cytokines was also blocked by TLR4 deficiency with the retention of epithelial barrier function (Fig. 6, H and I). Thus, LPS/TLR4 signaling resulting from recurrent low-titer ST infection is linked to the induction of host NEU3 and increased Neu activity, resulting in IAP desialylation and its subsequent

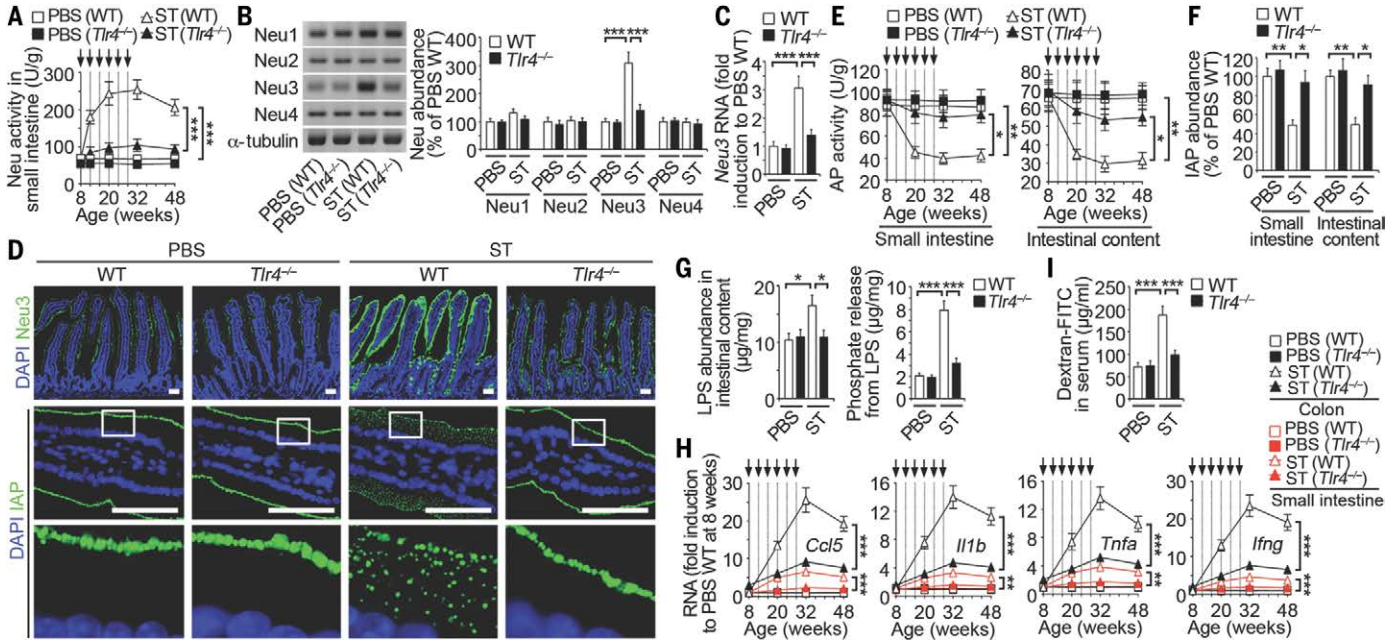


**Fig. 5. Host Neu is induced by TLR4 during recurrent ST infection.** WT and *Tlr4*-deficient mice were analyzed after recurrent ST infections (arrows). (**A**) Neu activity ($n$ = 30 per condition). (**B**) NEU1 to NEU4 protein abundance in the small intestine. (**C**) *Neu3* mRNA expression in small intestine. (**D**) In situ localization of NEU3 and IAP in duodenum. Images are representative of 10 fields of view ($n$ = 4 per condition). Scale bars, 50 μm. (**E**) AP activity ($n$ = 24 per condition). (**F**) IAP protein abundance. (**G**) LPS abundance and phosphate released from LPS of intestinal content. (**H**) Inflammatory cytokine RNA abundance ($n$ = 16 per condition). (**I**) Intestinal epithelial barrier function. (B, C, F, G, and I) $n$ = 6 per condition. (B, C, F, G, and I) Animals were 20 weeks of age before the fourth infection. Error bars represent means ± SEM. ***$P$ < 0.001, **$P$ < 0.01, and *$P$ < 0.05; one-way ANOVA with Tukey's multiple comparisons test (A to I).

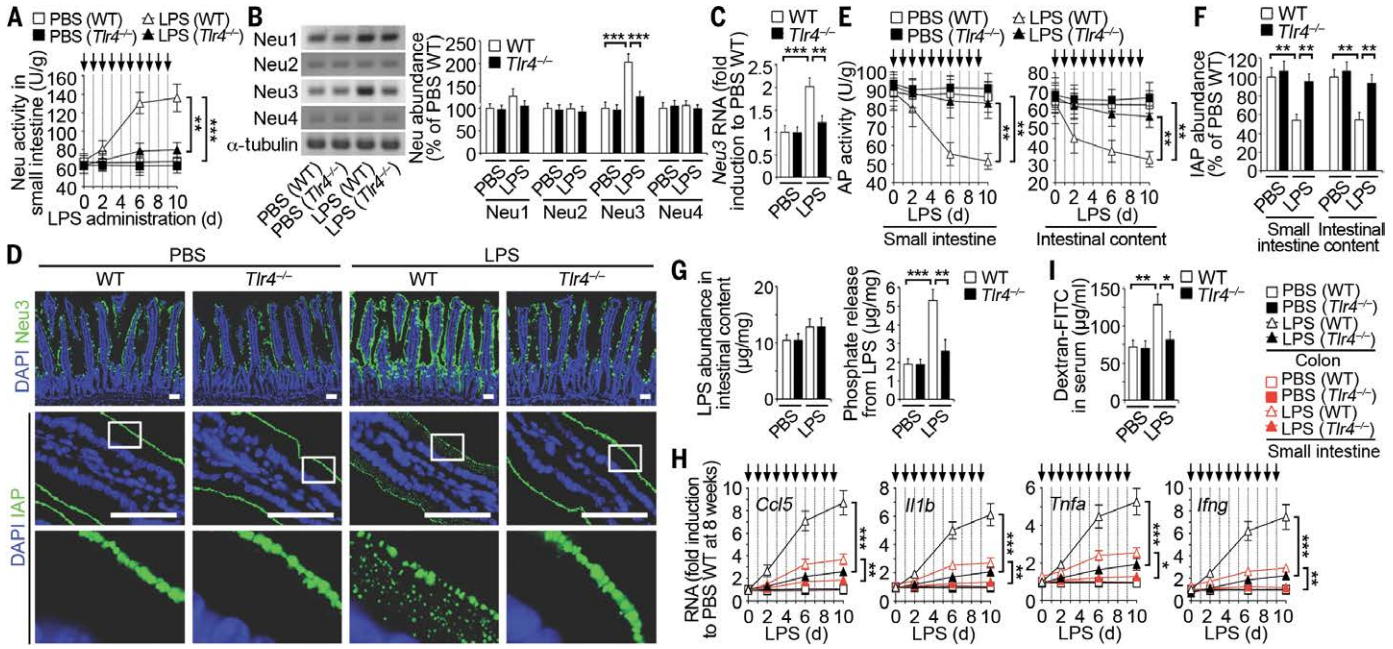


**Fig. 6. Host Neu is induced by TLR4 and LPS.** (**A**) Neu activity in mice at 8 weeks of age before repeated LPS administrations (arrows). (**B** and **C**) Neu protein abundance and *Neu3* RNA expression in small intestine. (**D**) In situ localization of NEU3 and IAP in duodenum sections, representative of 10 fields of view ($n$ = 4 per condition). Scale bars, 50 μm. (**E**) AP activity before repeated LPS administrations (arrows). (**F**) IAP protein abundance. (**G** to **I**) Phosphate released from LPS of intestinal content, inflammatory cytokine RNA abundance, and intestinal epithelial barrier function. (A and E) $n$ = 24 per condition. (B, C, F, G, and I) $n$ = 6 per condition. (H) $n$ = 16 per condition. (B, C, F, G, and I) Mice on day 6 after LPS administration. Error bars represent means ± SEM. ***$P$ < 0.001, **$P$ < 0.01, and *$P$ < 0.05; one-way ANOVA with Tukey's multiple comparisons test (A to I).

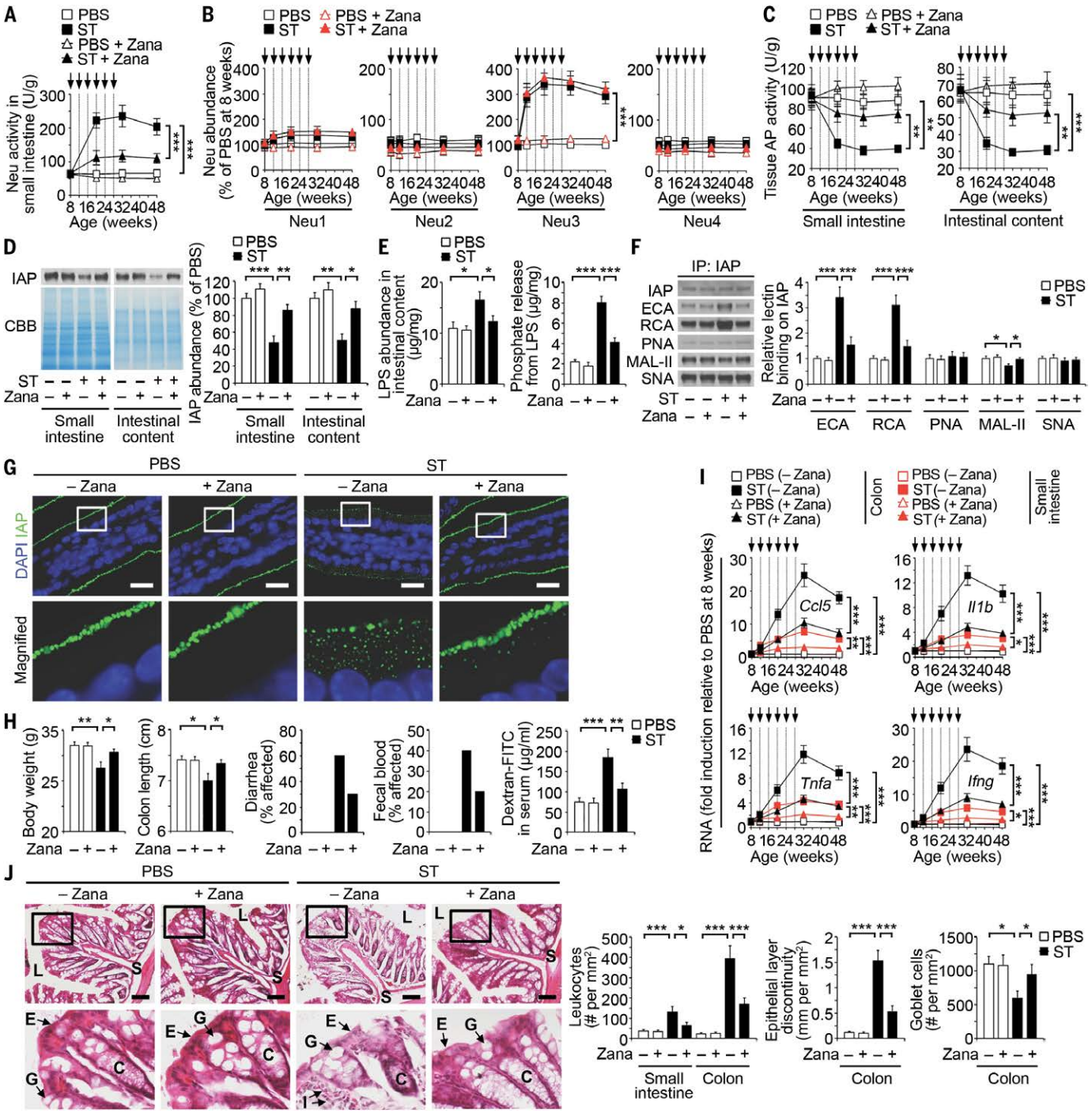


**Fig. 7. Effects of the Neu inhibitor zanamivir on intestinal inflammation.** WT mice were analyzed at indicated ages before ST reinfection (arrows) in the absence or presence of zanamivir (Zana) (0.5 mg/ml) provided in drinking water immediately after first infection. (**A**) Neu activity. (**B**) NEU1 to NEU4 protein abundance in small intestine. (**C**) AP activity. (**D**) IAP protein abundance. (**E**) LPS abundance and phosphate released from LPS of intestinal content. (**F**) Lectin blotting of IAP protein from small intestine. (**G**) In situ localization of IAP in duodenum, representative of 10 fields of view ($n$ = 4 per condition). Scale bars, 20 μm. (**H**) Body weight ($n$ = 10 per condition), colon length ($n$ = 8 per condition), diarrhea ($n$ = 10 per condition) and fecal blood ($n$ = 10 per condition) at 32 weeks of age, and intestinal epithelial barrier function ($n$ = 8 per condition) at 20 weeks of age. (**I**) Inflammatory cytokine RNA abundance. (**J**) H&E-stained colon sections at 32 weeks of age. Graphs are representative of 10 fields of view ($n$ = 4 mice per condition). Scale bars, 100 μm. (D to G) Mice at 20 weeks of age. (A and C) $n$ = 32 per condition. (B and I) $n$ = 30 per condition. (D to F) $n$ = 6 per condition. Error bars represent means ± SEM. ***$P$ < 0.001, **$P$ < 0.01, and *$P$ < 0.05; one-way ANOVA with Tukey's multiple comparisons test (A to J).

pathogenic deficiency. Thus, Neu inhibition may be therapeutic in the context of recurrent ST infection.

### *Therapeutic effect of zanamivir entails the maintenance of IAP abundance and function*

The marketed antiviral drug zanamivir inhibits influenza Neu activity (*31*) and has been used in research on mammalian Neu isozymes (*24*, *32*, *33*). At pharmacological dosages, zanamivir inhibits NEU2, NEU3, and NEU4 but not NEU1 (*32*, *33*). We found that oral treatment with zanamivir maintained normal Neu activity levels in animals experiencing recurrent ST infections (Fig. 7A). Zanamivir did not block the physical induction of NEU3, which persisted for at least 20 weeks after the last ST infection (Fig. 7B). However, the inhibition of Neu activity by zanamivir maintained host AP activity, IAP abundance, and normal lectin-binding patterns among apical glycoproteins of the small intestinal epithelium (Fig. 7, C and D, and fig. S8). The maintenance of IAP expression and activity was linked to the retention of relatively low LPS-phosphate levels that were otherwise elevated by ST infection (Fig. 7E). Zanamivir inhibited IAP desialylation coincident with normal IAP expression at the enterocyte cell surface (Fig. 7, F and G). Zanamivir also inhibited the induction of inflammatory cytokines and reduced the appearance of disease markers of intestinal inflammation, including alterations of commensal microbiota and barrier dysfunction (Fig. 7, H to J, and fig. S9). In contrast, for acute and chronic models of chemically induced colitis using dextran sodium sulfate (DSS) (*34*, *35*), zanamivir had no effect, whereas ST3Gal6 deficiency exacerbated signs of disease, consistent with the presence of different inflammatory mechanisms that may be responsive to IAP treatment (fig. S10). Our findings together indicate a disease mechanism of environmental and pathogen origin, which encompasses the different locations and functions of the small intestine and colon (Fig. 8).

## Discussion

An increasingly severe colitis developed from recurrent low-titer nonlethal transient gastric infections of the Gram-negative pathogen ST. In this mouse model of repeated human food poisoning, the host rapidly cleared the pathogen. Nevertheless, subsequent recurrent infections progressively disabled a mechanism in the host that normally protects against spontaneous intestinal inflammation. This anti-inflammatory mechanism operates primarily in the colon but is dependent on IAP production and release from duodenal enterocytes of the small intestine. ST infection targeted this protective mechanism by activating host TLR4 function in the duodenum, inducing host Neu activity with elevated NEU3 expression at the luminal surface of the enterocyte. Neu induction accelerated the rate of nascent IAP aging by desialylation on the enterocyte cell surface, reducing IAP half-life, inducing IAP internalization and degradation, and resulting in a downstream IAP deficiency in the colon. IAP deficiency was linked to the deficient dephosphorylation of LPS molecules produced by commensal microbiota. This TLR4-dependent disease manifested primarily in the colon with IBD-like symptoms closer to UC than Crohn's disease, and was linked to increases in the proinflammatory TLR4 ligand LPS-phosphate. Similarly, the genetic disruption of ST3Gal6-dependent sialic acid linkage formation during IAP synthesis caused IAP deficiency, resulting in a spontaneous colitis, which increased in severity with age and was exacerbated by recurrent ST infections. In both cases, diminished glycoprotein sialylation among enterocytes resulted in reduced IAP half-life, leading to IAP deficiency with markedly elevated LPS-phosphate abundance in the colon. Consistent with a TLR4-dependent mechanism, LPS administration alone recapitulated NEU3 induction and IAP deficiency, bypassing the requirement for IAP deficiency to increase colonic LPS-phosphate levels in provoking inflammation.

Intestinal inflammation failed to resolve after the discontinuation of periodic recurrent infections and persisted for months afterward as a lasting outcome. The degree of this persistence may be determined in part by initial infection titers and the time between recurrent infections and may result from multiple mechanisms. One possibility is the generation of epigenetic modifications to inflammatory gene promoters regulated by TLR4 function that result in the persistence of inflammatory cytokine expression, and may explain observations of the slow resolution of inflammatory processes (*36*, *37*). The enterocyte *Neu3* allele is perhaps regulated in this way because its expression remained induced long after periodic ST infections were discontinued. It is also possible that the escalating inflammation resulting from increased recruitment and activation of innate and adaptive immune cells reaches a point wherein the degree of immunological activation and damage to the epithelium is not easily reversed or attenuated. Disease persistence was also coincident with microbiota alterations that we found emerged concurrently with signs of disease and endured after the discontinuation of recurrent infections. In this regard, acute enteric infections with *Yersinia* can trigger gut microbiota dysbiosis and chronic inflammation after pathogen clearance in *Tlr1*-deficient mice (*38*). In addition, the microbiota alterations that we observed predominantly involved Enterobacteriaceae, which are frequently imbalanced in studies of intestinal inflammatory disease (*21*, *38*).

Neu enzymes function in a variety of processes, including pathogen virulence, glycan catabolism, and biological signaling (*39*–*41*) and may differ among isozymes and origins, such as indicated from cecal sources in contributing to DSS-induced colitis (*34*). Mammalian *Neu3* includes presumptive binding sites for transcriptional factors STAT3, RREB1, MYOD, Ik2, PAX2, Aml1a, HOXA9, and MEIS1 and may use alternate promoters controlled by Sp1/Sp3 transcription factors (*42*). Indeed, STAT3 and Sp1 transcription factors are

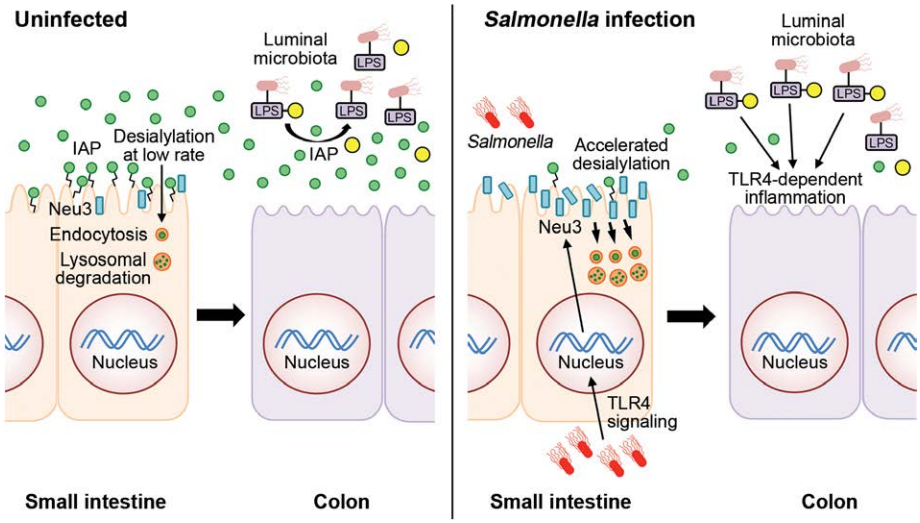


**Fig. 8. Model of intestinal inflammation due to recurrent Gram-negative ST infection.** In the absence of infection of the small intestine, the anti-inflammatory GPI-linked IAP glycoprotein (green circles) is highly expressed on the enterocyte cell surface. IAP is eventually released into the lumen and travels through the intestinal tract to the colon where it detoxifies LPS-phosphate produced by Gram-negative and commensal bacteria via dephosphorylation (yellow circles). Nascent IAP at the enterocyte cell surface undergoes a low rate of desialylation linked to the rate of internalization and degradation involving a normal mechanism of IAP aging and turnover. Enterocytes of the small intestine respond to LPS-phosphate and ST infection by activating TLR4 function, which induces host NEU3 Neu (blue bars) on the enterocyte surface. Increased Neu activity accelerates the rate of IAP desialylation and internalization (orange circles), reducing IAP abundance and resulting in increased levels of LPS-phosphate in the colon where TLR4 activation elicits inflammation and disease.

activated by LPS (*43*, *44*). The transcriptional activation of *Neu3* may further underlie NEU3 induction in cancers of colon, renal, and prostate tissues, whereas mice lacking NEU3 exhibited fewer colitis-associated colonic tumors (*45*–*47*). Our studies of an ST isolate lacking an annotated and demonstrable Neu gene have further linked *Neu3* RNA induction with the elevation of host Neu activity, supporting the view that host NEU3 is involved in the desialylation of the IAP glycoprotein, which results in IAP internalization and deficiency. However, it remains possible that the Neu activity that we have measured comes from an unannotated Neu enzyme or the endogenous microbiota, neither of which can be resolved until *Neu3*-deficient mice are further studied. Although NEU3 activity is primarily active toward gangliosides, studies have shown significant but lesser activity toward glycoprotein substrates (*48*). It is also possible that NEU3 may act indirectly via the desialylation of its canonical ganglioside substrates. Nevertheless, NEU3 has been reported to desialylate the epidermal growth factor receptor glycoprotein (*49*). Moreover, data similar to our present findings have further implicated NEU3 in the desialylation of circulating glycoproteins in the blood linked to a mechanism that determines the various half-lives of plasma proteins (*24*).

The regulation of enterocyte IAP trafficking by sialylation extends this recently discovered mechanism of secreted protein aging and turnover to include the determination of protein half-lives at the cell surface. Although ST infection resulted in the desialylation and internalization of multiple enterocyte glycoproteins expressed at the cell surface, the disease phenotype was largely due to IAP deficiency. This represents an example of a specific glycan linkage that is commonly found on secreted and cell surface proteins having a biological purpose more restrictively associated with one or a few such glycoproteins (*50*–*52*). This can be explained, in part, by the presence of multiple sialyltransferases operating in the intestinal tract, which are responsible for the sialylation of different subsets of bioactive glycoproteins and which function in different biological processes. For example, the present findings involving ST3Gal6 deficiency should be compared with other studies of ST3Gal4 deficiency (*34*). Additional factors that may influence IAP expression and disease onset include mutations of glycan acceptor sites of IAP and transcriptional or mutagenic modifications to relevant glycosyltransferase and glycosidase genes, each of which can contribute to glycoprotein function (*53*). The control of IAP half-life via the increased internalization and degradation of desialylated IAP implies the possible presence of a sialic acid–binding lectin analogous to the mammalian siglecs of leukocytes (*54*). Such lectins may normally bind nascent sialylated IAP on the enterocyte surface to inhibit premature IAP endocytosis, enabling the subsequent release of IAP into the lumen. Alternatively, the exposure of underlying galactose may unmask cryptic ligands for galactose-binding lectins, such as the galectins, which modulate glycoprotein endocytosis (*50*, *55*).

Diminished AP activity has been described in patients with colitis and celiac disease, and oral AP supplementation is under investigation for the treatment of inflammatory diseases, including the IBDs (*56*–*59*). Moreover, NEU3 protein abundance and activity is reportedly increased in human IBD patients (*60*). In animal studies, IAP deficiency contributes to colitis and allows increased bacterial transit from the intestinal lumen to the mesenteric lymph nodes (*16*, *35*, *56*, *61*). We have found that IAP is highly regulated and that ST infection disables IAP function in host protection while progressively eroding microbial barriers by successive rounds of what might otherwise be considered unproductive infections. Environmental Gram-negative pathogens that access and infect the small intestine may have a similar strategy toward misappropriating host TLR4 function to diminish IAP activity and increase colonic LPS-phosphate levels, provoking intestinal inflammation. This further emphasizes the dual nature of host TLR4 function, which may be either advantageous or disadvantageous perhaps depending on the context of exposure and the severity of infection. Although the link that we identified between host TLR4 function and NEU3 induction appears to favor the pathogen, advantageous features of TLR4 signaling may become evident with high *Salmonella* titers that engender extended pathogen colonization of the intestinal tract. Nevertheless, IAP augmentation and Neu inhibition represent candidate therapies for preventing the onset and progression of an escalating colitis that originates from recurrent low-titer *Salmonella* infections, as may occur in common cases of human food poisoning.

## Materials and methods

### *Laboratory animals*

Inbred C57BL/6J mice were used (Jackson Laboratory). *St3gal6*-deficient mice (*19*) were backcrossed six or more generations into the C57BL/6J background prior to study. *TLR4*$^{-/-}$ mice (B6(Cg)-Tlr4$^{tm1.2Karp}$/J) were purchased from the Jackson Laboratory. Littermates bearing normal alleles were used as controls. All mice analyzed were provided sterile pellet food and water ad libitum. Institutional Animal Care and Use Committees of the University of California Santa Barbara and the Sanford Burnham Prebys Medical Discovery Institute approved studies undertaken herein.

### *Bacterial strains and infection protocols*

*Salmonella enterica* subsp. *enterica* serovar Typhimurium reference strain ATCC 14028 (CDC 6516-60) was used as previously described (*62*). For the induction of chronic colitis, 8-week-old mice were infected with *ST* ($2 \times 10^3$ cfu) via gastric intubation up to five times at 4-week intervals after the initial infection. For monitoring the development of colitis, mice were weighed biweekly and assessed for colitis-associated symptoms, including the presence of diarrhea, stool consistency (0, normal; 2, loose stools; 4, diarrhea), fecal blood (occult fecal blood positive, Beckman Coulter), and rectal prolapse as previously described (*63*).

### *Histology*

Mouse tissues were fixed in 10% buffered formalin (Sigma-Aldrich), transferred to 30% sucrose/PBS, and embedded in Tissue-Tek OCT compound (Sakura Finetek). Three-micron frozen serial sections were stained with hematoxylin and eosin (H & E; Sigma-Aldrich) or incubated with 1 μg/ml of antibodies to one or more molecules including CD3ε (M-20, Santa Cruz Biotechnology), Gr-1 (M-66, Santa Cruz Biotechnology), F4/80 (M-300, Santa Cruz Biotechnology), TNFα (M-18, Santa Cruz Biotechnology), EEA1 (C-15, Santa Cruz Biotechnology), LAMP2 (C-20, Santa Cruz Biotechnology), γ-adaptin (I-19, Santa Cruz Biotechnology), Calnuc (V-18, Santa Cruz Biotechnology), protein disulfide isomerase PDI (G-20, Santa Cruz Biotechnology), Neu3 (M-50, Santa Cruz Biotechnology), sucrase-isomaltase (A-17, Santa Cruz Biotechnology), dipeptidyl peptidase 4 (H-270, Santa Cruz Biotechnology), lactase (T-14, Santa Cruz Biotechnology), or 1:1000 dilution of IAP specific antiserum kindly provided by Dr. Jose Millan (*64*), or 5 μg/ml of biotinylated lectins including *Erythrina cristagalli* (ECA), *Ricinus Communis* Agglutinin-I (RCA), Peanut Agglutinin (PNA), *Maackia amurensis*-II (MAL-II), or *Sambucus nigra* (SNA) (Vector Laboratories). CD3ε, TNFα, sucrase-isomaltase, and lactase were visualized with 0.4 μg/ml of FITC-conjugated rabbit anti-goat IgG (Santa Cruz Biotechnology); Gr-1, F4/80, IAP, Neu3, and dipeptidyl peptidase 4 were visualized with FITC-conjugated goat 0.4 μg/ml of anti-rabbit IgG (Santa Cruz Biotechnology); EEA1, LAMP2, γ-adaptin, Calnuc, and PDI were visualized with 0.4 μg/ml of Texas Red-conjugated rabbit anti-goat IgG (Santa Cruz Biotechnology) and biotinylated lectins were visualized with 1 μg/ml of FITC-conjugated streptavidin (Vector Laboratories). These primary antibody or lectin incubations were performed at 4°C overnight and secondary antibody or streptavidin incubations were performed at room temperature for 1 h. All microscopic work was performed using a TissueGnostics microscopy workstation equipped with Zeiss AxioImager Z1 microscope system, Hamamatsu C13440-20C camera, PixeLINK PL-D673CU camera, and Lumen Dynamics X-Cite XLED1 illuminator. All microscopic images were obtained and histopathological studies including quantification of cells, cell boundaries, and marker expression were performed with TissueFAXS (Version 3.5), TissueQuest (Version 4.0), and HistoQuest software (Version 4.0) (TissueGnostics USA Ltd.). Colocalization was further quantified by MetaMorph software (Version 7.0) (Universal Imaging Corporation) (*65*). Yellow signals in merged images of IAP (green) and intracellular compartments (red) indicate colocalization, and the threshold intensity value of 12 (intensity range, 0–255) and size of 0.026 $\mu m^2$ were used as the cut-off.

### *mRNA preparation and quantification by real-time PCR*

Total RNA was isolated from tissues using Trizol (Invitrogen) and subjected to reverse transcription (RT) using SuperScript III (Invitrogen). Quantitative real-time PCR was performed using Brilliant SYBR Green Reagents with the Mx3000P

QPCR System (Stratagene). Primers used for real-time PCR in the mouse were: CCL5-RT-F (5′-TCGTGTTTGTCACTCGAAGG-3′), CCL5-RT-R (5′-CTAGCTCATCTCCAAATAGT-3′), IL-1b-RT-F (5′-GCCCATCCTCTGTGACTCAT-3′), IL-1b-RT-R (5′-AGGCCACAGGTATTTTGTCG-3′), TNFa-RT-F (5′-CATCTTCTCAAAATTCGAGT-3′), TNFa-RT-R (5′-TTTGAGATCCATGCCGTTGG-3′), IFNg-RT-F (5′-ACTGGCAAAAGGATGGTGAC-3′), IFNg-RT-R (5′-GTTGCTGATGGCCTGATTGT-3′), Neu3-RT-F (5′-CTCAGTCAGAGATGAGGATGCT-3′), Neu3-RT-R (5′-GTGAGACATAGTAGGCATAGGC-3′), IAP-RT-F (5′- CTCATCTCCAACATGGAC-3′), IAP-RT-R (5′-TGCTTAGCACTTTCACGG-3′), GAPDH-RT-F (5′-TGGTGAAGGTCGGTGTGAAC-3′) and GAPDH-RT-R (5′-AGTGATGGCATGGACTGTGG-3′). Relative mRNA levels were normalized to expression of GAPDH RNA.

### Immunoprecipitation, immunoblotting, and lectin blotting

Tissue samples were homogenized in radioimmunoprecipitation assay (RIPA) buffer (50 mM Tris-HCl (pH 7.6), 150 mM NaCl, 1 mM EDTA, 1% NP-40, 1% sodium deoxycholate, and 0.1% SDS) supplemented with complete protease inhibitor cocktail per instructions (Roche) and incubated overnight at 4°C on a rotating wheel with 1:100 dilution of IAP-specific antiserum (*64*) or 2 μg/ml of antibodies to sucrase-isomaltase (A-17, Santa Cruz Biotechnology), dipeptidyl peptidase 4 (H-270, Santa Cruz Biotechnology), or lactase (T-14, Santa Cruz Biotechnology), followed by 2 h of incubation in the presence of protein A/G PLUS agarose (Santa Cruz Biotechnology). Immunoprecipitates were washed five times with RIPA buffer and eluted with SDS sample buffer. Protein samples eluted were subjected to SDS-PAGE, transferred to nitrocellulose membranes and incubated with 2% BSA in Tris-buffered saline (TBS). They were then analyzed by immunoblotting using either 1 μg/ml of antibodies to Neu1 (H-300, Santa Cruz Biotechnology), Neu2 (M-13, Santa Cruz Biotechnology), Neu3 (M-50, Santa Cruz Biotechnology), Neu4 (N-14, Santa Cruz Biotechnology), sucrase-isomaltase (A-17, Santa Cruz Biotechnology), dipeptidyl peptidase 4 (H-270, Santa Cruz Biotechnology), lactase (T-14, Santa Cruz Biotechnology), α-Tubulin (H-300, Santa Cruz Biotechnology), or 1:1000 dilution of anti-IAP antiserum, or by lectin blotting with HRP-conjugated ECA (0.5 μg/ml), RCA (0.1 μg/ml), PNA (1 μg/ml), MAL-II (0.2 μg/ml), or SNA (0.1 μg/ml) (EY Laboratories). Signals detected by chemiluminescence (GE Healthcare) were analyzed by integrated optical density using Labworks software (UVP Bioimaging Systems). Parallel protein samples were visualized with Coomassie brilliant blue G250 staining (Bio-Rad).

### Neuraminidase activity and inhibition

Neuraminidase activity was measured in tissue extracts in RIPA buffer using the Amplex Red Neuraminidase Assay Kit according to the manufacturers' instructions (Molecular Probes). For inhibition of neuraminidase activity in the small intestine and colon, zanamivir (0.5 mg/ml; Sigma-Aldrich) was provided in the drinking water immediately following the initial *ST* infection at 8 weeks of age, and continued for the duration of study as indicated.

### ELISA

Enzyme-linked immunosorbent assay (ELISA) plates (Nunc) were coated with 2 μg/ml of antibodies to either Neu1 (H-300, Santa Cruz Biotechnology), Neu2 (M-13, Santa Cruz Biotechnology), Neu3 (M-50, Santa Cruz Biotechnology), Neu4 (N-14, Santa Cruz Biotechnology), sucrase-isomaltase (A-17, Santa Cruz Biotechnology), dipeptidyl peptidase 4 (H-270, Santa Cruz Biotechnology), or lactase (T-14, Santa Cruz Biotechnology), or 1:1000 dilution of IAP antiserum, and blocked with BSA before incubation with serial dilutions of mouse tissue extracts that were biotinylated using 1 mg/ml of N-hydroxysuccinimide-biotin (Pierce). Antigens were detected following the addition of 1:1000 dilution of HRP-streptavidin (BD Biosciences) and 3,3′,5,5′ tetramethylbenzidine (TMB, Sigma-Aldrich). Lectin binding was determined in parallel by the addition of HRP-conjugated ECA (0.5 μg/ml), RCA (0.1 μg/ml), PNA (1 μg/ml), MAL-II (0.2 μg/ml), or SNA (0.1 μg/ml) (EY Laboratories), followed by TMB, and changes in glycan linkages were detected by comparing lectin binding among identical amounts of biotinylated IAP, sucrase-isomaltase, dipeptidyl peptidase 4, or lactase antigen calculated as described (*66*). Alkaline phosphatase activity was measured using the *p*-nitrophenyl phosphate substrate (pNPP; Sigma-Aldrich) as previously described (*61*).

### LPS phosphorylation

To determine LPS content in the intestinal contents, LPS was isolated as previously described (*67*) by the hot phenol–water method with minor modifications. Briefly, the intestinal contents were weighed, diluted ten-fold weight to volume in Tris-buffered saline (TBS), and homogenized. The extract solution of intestinal contents was added to same volume of 99% phenol (Ambion), preheated to 65°C and incubated for 15 min at 65°C. After cooling on ice, the samples were centrifuged at 10,000 × *g* for 10 min. The aqueous phase was acquired and residual phenol was removed by extracting with diethyl ether (Sigma-Aldrich). The diethyl ether phase was discarded and the water phase containing the LPS was placed in a hood for 1 h to allow the remaining diethyl ether to evaporate. The above steps were repeated after treatment with proteinase K (Promega), RNase (Invitrogen) and DNase (Invitrogen). LPS preparations from indicated sources were quantified by the purpald assay as described previously (*68*). LPS preparations for comparative studies were indistinguishable by chromatography and silver staining (Bio-Rad). To compare the abundance of phosphate linked to LPS, phosphate release was measured by the malachite green phosphate assay (*61*). Briefly, purified calf intestinal alkaline phosphatase (10 U; Invitrogen) was incubated at pH 8.0 for 3 h at 37°C with 1 mg of LPS isolated from intestinal contents. Free phosphate released was measured as a colored complex of phosphomolybdate and malachite green at 620 nm according to the manufacturer's instructions (BioAssay Systems).

### Pulse–chase analysis and cell-surface half-life

Techniques as previously described (*50*) were used for pulse–chase measurements of IAP synthesis and trafficking among cultured primary enterocytes. Mouse enterocytes were isolated from the duodenum as previously described (*69*). The proximal duodenum was removed and flushed through with solution A (1.5 mM KCl, 96 mM NaCl, 27 mM sodium citrate, 8 mM $KH_2PO_4$, 5.6 mM $Na_2HPO_4$) at room temperature. The duodenum was minced in an enzyme cocktail (333 U/ml collagenase, 2.5 U/ml elastase, and 10 μg/ml DNAse) in HEPES-buffered Krebs Ringer solution (5 mM HEPES (4-(2-hydroxyethyl)-1-piperazineethanesulfonic acid, pH 7.4), 120 mM NaCl, 24 mM $NaHCO_3$, 4.8 mM KCl, 1.2 mM $MgSO_4$, 1.2 mM $KH_2PO_4$, 20 mM glucose, 1 mM $CaCl_2$) and incubated while shaking at 37°C for 30 minutes. Cells were filtered through a 70-μm filter and washed twice in Dulbecco's modified Eagle's medium (DMEM) supplemented with 10% fetal calf serum, 1% β-mercaptoethanol, and 1% L-asparagine. Isolated enterocytes were washed twice with Hank's balanced salt solution (HBSS), then incubated with DMEM depleted of methionine (Gibco) with 10% fetal calf serum for 2 h at 37°C. Pulse labeling was performed with 400 μCi/ml [$^{35}$S]methionine for 10 min at 37°C, and cells were then washed twice in ice-cold HBSS. Cells were lysed or returned to new media of above culture conditions containing 2 mM methionine for 15, 30, 45, 60, or 90 min. Media used in chase samples were harvested at each time point. Cells used in chase samples were washed twice with ice-cold PBS and incubated with 1 mg/ml of sulfo-NHS-LC-biotin (Pierce Chemical) at 4°C for 30 min. Biotinylation was stopped by three washes with 15 mM glycine in ice-cold PBS. Cells were homogenized in RIPA buffer, and biotinylated proteins were purified using immobilized monomeric avidin gel (Pierce). Eluates isolated in the presence of D-biotin (Pierce) or media samples for chase were incubated with IAP-specific antiserum. Immunoprecipitates were subjected to SDS-PAGE, and gels were fixed before drying and autoradiography at −70°C for 3–7 days. For cell-surface half-life analysis, primary enterocytes were washed twice with ice-cold PBS and biotinylated with sulfo-NHS-LC-biotin as described above. Cells were further cultured at the indicated times, and then homogenized in RIPA buffer, followed by immunoprecipitation using the IAP-specific antiserum. IAP immunoprecipitates were subjected to SDS-PAGE, transferred to nitrocellulose membranes, and visualized with HRP-conjugated streptavidin. To determine IAP glycosylation on enterocyte surface, primary enterocytes were washed twice with ice-cold PBS and biotinylated with sulfo-NHS-LC-biotin as described above. Cells were further cultured at the indicated times, and then homogenized in RIPA buffer. Biotinylated proteins were purified

using immobilized monomeric avidin gel and incubated on ELISA plates (Nunc) coated with IAP antiserum. Lectin binding was determined in parallel by the addition of HRP-conjugated ECA, RCA, PNA, MAL-II or SNA, followed by TMB, and changes in glycan linkages were detected by comparing lectin binding among identical amounts of biotinylated IAP antigen calculated as described (*66*).

### Calf intestinal alkaline phosphatase (cIAP) treatment and LPS administration

cIAP (20 U/ml; Lee Biosolutions) was provided immediately in drinking water from the time of the initial *ST* infection. For LPS administration, 8-week-old mice were orally administered LPS (100 mg/kg; *E. coli* 0111:B4) via gastrointubation and challenged at 24-h intervals after the initial administration of 10 days.

### In vivo intestinal barrier function

Dextran-FITC (Sigma) was administered via oral gavage (600 mg/kg), blood was collected from anesthetized animals into Microtainer Serum Separator Tubes (BD Biosciences) at 4 h with no anticoagulant, and allowed to clot for 30 minutes at room temperature. Serum was collected after centrifugation at 10,000 × *g* for 10 min. The amount of FITC in each sample was measured by using a Spectra Max Gemini EM fluorescent plate reader (Molecular Devices) at 490 and 530 nm for the excitation and emission wavelengths, respectively.

### Comparative studies of intestinal microbiota

DNA from intestinal content was isolated with a QIAamp DNA Mini Kit according to the manufacturer's instructions (Qiagen). Commensal microbiota was analyzed by quantitative real-time PCR using Brilliant SYBR Green Reagents with the Mx3000P QPCR System (Stratagene) with specific primers for bacteria (*70*) (Total-F-5′-GTGCCAGCMGCCGCGGTAA-3′, Total-R-5′-GACTACCAGGGTATCTAAT-3′; Clostridiaceae-F-5′-TTAACACAATAAGTWATCCACCTGG-3′, Clostridiaceae -R-5′-ACCTTCCTCCGTTTTGTCAAC-3′; Lactobacillaceae-F-5′-AGCAGTAGGGAATCTTCC-3′, Lactobacillaceae-R-5′-CGCCACTGGTGTTCYTCCATATA-3′; Bacteroidaceae-F-5′-CCAATGTGGGGGACCTTC-3′, Bacteroidaceae-R-5′-AACGCTAGCTACAGGCTT-3′; Enterobacteriaceae-F-5′-CATTGACGTTACCCGCAGAAGAAGC-3′, Enterobacteriaceae-R-5′-CTCTACGAGACTCAAGCTTGC-3′). Relative bacterial DNA levels were related to the amount of total isolated DNA from intestinal content.

### DSS-induced acute and chronic colitis

For survival studies in acute colitis, 12-week-old mice were administered drinking water containing 4% dextran sodium sulfate (DSS; molecular weight, 40,000 to 50,000; USB Corp.) ad libitum for 5 days and then returned to normal drinking water without DSS until the end of the experiment (day 14). For other experiments in acute colitis, mice were administered 2% DSS solution in drinking water for 5 days. DSS-induced chronic colitis was induced as previously described (*35*). Briefly, 12-week-old mice were administered 2% DSS solution in drinking water with four cycles of DSS given ad libitum for 7 days followed by a 7-day DSS-free interval. Zanamivir (0.5 mg/ml; Sigma-Aldrich) was provided in the drinking water immediately following the administration of DSS and continued for the duration of study as indicated. Body weight, stool consistency, and the presence of occult blood were determined. Stool scores were determined as follows: 0, well-formed pellets; 1, semiformed stools that did not adhere to the anus; 2, semiformed stools that adhered to the anus; 3, liquid stools that adhered to the anus. Bleeding scores were determined as follows: 0, no blood as tested with hemoccult (Beckman Coulter); 1, positive hemoccult; 2, blood traces in stool visible; 3, gross rectal bleeding as previously described (*71*).

### Statistical analysis

All data were analyzed as mean ± SEM unless otherwise indicated. Student's unpaired *t* test, one-way ANOVA with Tukey's multiple comparisons test, log-rank test, or Kruskal-Wallis test with Dunn's multiple comparisons test with GraphPad Prism software (Version 7.0) were used to determine statistical significance among multiple studies. *P* values of less than 0.05 were considered significant. Statistical significance was denoted by $*P < 0.05$, $**P < 0.01$, or $***P < 0.001$.

## REFERENCES AND NOTES


1. B. Khor, A. Gardet, R. J. Xavier, Genetics and pathogenesis of inflammatory bowel disease. *Nature* **474**, 307–317 (2011). doi: 10.1038/nature10209; pmid: 21677747
2. A. Kaser, S. Zeissig, R. S. Blumberg, Inflammatory bowel disease. *Annu. Rev. Immunol.* **28**, 573–621 (2010). doi: 10.1146/annurev-immunol-030409-101225; pmid: 20192811
3. P. J. Sansonetti, War and peace at mucosal surfaces. *Nat. Rev. Immunol.* **4**, 953–964 (2004). doi: 10.1038/nri1499; pmid: 15573130
4. D. Knights, K. G. Lassen, R. J. Xavier, Advances in inflammatory bowel disease pathogenesis: Linking host genetics and the microbiome. *Gut* **62**, 1505–1510 (2013). doi: 10.1136/gutjnl-2012-303954; pmid: 24037875
5. J. Halfvarson, Genetics in twins with Crohn's disease: Less pronounced than previously believed? *Inflamm. Bowel Dis.* **17**, 6–12 (2011). doi: 10.1002/ibd.21295; pmid: 20848478
6. L. Eckmann, Animal models of inflammatory bowel disease: Lessons from enteric infections. *Ann. N. Y. Acad. Sci.* **1072**, 28–38 (2006). doi: 10.1196/annals.1326.008; pmid: 17057188
7. A. Sonnenberg, Seasonal variation of enteric infections and inflammatory bowel disease. *Inflamm. Bowel Dis.* **14**, 955–959 (2008). doi: 10.1002/ibd.20408; pmid: 18302273
8. Centers for Disease Control and Prevention (CDC), Vital signs: Incidence and trends of infection with pathogens transmitted commonly through food—Foodborne Diseases Active Surveillance Network, 10 U.S. sites, 1996–2010. *MMWR Morb. Mortal. Wkly. Rep.* **60**, 749–755 (2011). pmid: 21659984
9. E. Scallan *et al*., Foodborne illness acquired in the United States—Major pathogens. *Emerg. Infect. Dis.* **17**, 7–15 (2011). doi: 10.3201/eid1701.P11101; pmid: 21192848
10. S. E. Majowicz *et al*.,The global burden of nontyphoidal *Salmonella* gastroenteritis. *Clin. Infect. Dis.* **50**, 882–889 (2010). doi: 10.1086/650733; pmid: 20158401
11. H. K. de Jong, C. M. Parry, T. van der Poll, W. J. Wiersinga, Host-pathogen interaction in invasive Salmonellosis. *PLOS Pathog.* **10**, e1002933 (2012). doi: 10.1371/journal.ppat.1002933; pmid: 23055923
12. N. A. Feasey, G. Dougan, R. A. Kingsley, R. S. Heyderman, M. A. Gordon, Invasive non-typhoidal salmonella disease: An emerging and neglected tropical disease in Africa. *Lancet* **379**, 2489–2499 (2012). doi: 10.1016/S0140-6736(11)61752-2; pmid: 22587967
13. B. F. Hinnebusch *et al*., Enterocyte differentiation marker intestinal alkaline phosphatase is a target gene of the gut-enriched Krüppel-like factor. *Am. J. Physiol. Gastrointest. Liver Physiol.* **286**, G23–G30 (2004). doi: 10.1152/ajpgi.00203.2003; pmid: 12919939
14. K. Poelstra, W. W. Bakker, P. A. Klok, M. J. Hardonk, D. K. Meijer, A physiologic function for alkaline phosphatase: Endotoxin detoxification. *Lab. Invest.* **76**, 319–327 (1997). pmid: 9121115
15. I. Koyama, T. Matsunaga, T. Harada, S. Hokari, T. Komoda, Alkaline phosphatases reduce toxicity of lipopolysaccharides *in vivo* and *in vitro* through dephosphorylation. *Clin. Biochem.* **35**, 455–461 (2002). doi: 10.1016/S0009-9120(02)00330-2; pmid: 12413606
16. J. M. Bates, J. Akerlund, E. Mittge, K. Guillemin, Intestinal alkaline phosphatase detoxifies lipopolysaccharide and prevents inflammation in zebrafish in response to the gut microbiota. *Cell Host Microbe* **2**, 371–382 (2007). doi: 10.1016/j.chom.2007.10.010; pmid: 18078689
17. N. L. Sussman *et al*., Intestinal alkaline phosphatase is secreted bidirectionally from villous enterocytes. *Am. J. Physiol.* **257**, G14–G23 (1989). pmid: 2546440
18. L. G. Ellies *et al*., Sialyltransferase specificity in selectin ligand formation. *Blood* **100**, 3618–3625 (2002). doi: 10.1182/blood-2002-04-1007; pmid: 12393657
19. W. H. Yang, C. Nussbaum, P. K. Grewal, J. D. Marth, M. Sperandio, Coordinated roles of ST3Gal-VI and ST3Gal-IV sialyltransferases in the synthesis of selectin ligands. *Blood* **120**, 1015–1026 (2012). doi: 10.1182/blood-2012-04-424366; pmid: 22700726
20. N. Kamada, S. U. Seo, G. Y. Chen, G. Nunez, Role of the gut microbiota in immunity and inflammatory disease. *Nat. Rev. Immunol.* **13**, 321–335 (2013). doi: 10.1038/nri3430; pmid: 23618829
21. N. A. Nagalingam, S. V. Lynch, Role of the microbiota in inflammatory bowel diseases. *Inflamm. Bowel Dis.* **18**, 968–984 (2012). doi: 10.1002/ibd.21866; pmid: 21936031
22. N. Figueroa-Bossi, S. Uzzau, D. Maloriol, L. Bossi, Variable assortment of prophages provides a transferable repertoire of pathogenic determinants in *Salmonella*. *Mol. Microbiol.* **39**, 260–271 (2001). doi: 10.1046/j.1365-2958.2001.02234.x; pmid: 11136448
23. E. Monti *et al*., Sialidases in vertebrates: A family of enzymes tailored for several cell functions. *Adv. Carbohydr. Chem. Biochem.* **64**, 403–479 (2010). doi: 10.1016/S0065-2318(10)64007-3; pmid: 20837202
24. W. H. Yang *et al*., An intrinsic mechanism of secreted protein aging and turnover. *Proc. Natl. Acad. Sci. U.S.A.* **112**, 13657–13662 (2015). doi: 10.1073/pnas.1515464112; pmid: 26489654
25. A. Poltorak *et al*., Defective LPS signaling in C3H/HeJ and C57BL/10ScCr mice: Mutations in *Tlr4* gene. *Science* **282**, 2085–2088 (1998). doi: 10.1126/science.282.5396.2085; pmid: 9851930
26. B. Beutler, Endotoxin, toll-like receptor 4, and the afferent limb of innate immunity. *Curr. Opin. Microbiol.* **3**, 23–28 (2000). doi: 10.1016/S1369-5274(99)00046-6; pmid: 10679425
27. M. T. Abreu, Toll-like receptor signalling in the intestinal epithelium: How bacterial recognition shapes intestinal function. *Nat. Rev. Immunol.* **10**, 131–144 (2010). doi: 10.1038/nri2707; pmid: 20098461
28. H. Huhta *et al*., The expression of Toll-like receptors in normal human and murine gastrointestinal organs and the effect of microbiome and cancer. *J. Histochem. Cytochem.* **64**, 470–482 (2016). doi: 10.1369/0022155416656154; pmid: 27370795
29. R. Dheer *et al*., Intestinal epithelial Toll-like receptor 4 signaling affects epithelial function and colonic microbiota and promotes a risk for transmissible colitis. *Infect. Immun.* **84**, 798–810 (2016). doi: 10.1128/IAI.01374-15; pmid: 26755160
30. C. L. Leaphart *et al*., A critical role for TLR4 in the pathogenesis of necrotizing enterocolitis by modulating intestinal injury and repair. *J. Immunol.* **179**, 4808–4820 (2007). doi: 10.4049/jimmunol.179.7.4808; pmid: 17878380
31. A. Moscona, Neuraminidase inhibitors for influenza. *N. Engl. J. Med.* **353**, 1363–1373 (2005). doi: 10.1056/NEJMra050740; pmid: 16192481
32. K. Hata *et al*., Limited inhibitory effects of oseltamivir and zanamivir on human sialidases. *Antimicrob. Agents Chemother.* **52**, 3484–3491 (2008). doi: 10.1128/AAC.00344-08; pmid: 18694948
33. N. M. Stamatos *et al*., LPS-induced cytokine production in human dendritic cells is regulated by sialidase activity. *J. Leukoc. Biol.* **88**, 1227–1239 (2010). doi: 10.1189/jlb.1209776; pmid: 20826611

34. Y.-L. Huang, C. Chassard, M. Hausmann, M. von Itzstein, T. Hennet, Sialic acid catabolism drives intestinal inflammation and microbial dysbiosis in mice. *Nat. Commun.* **6**, 8141 (2015). doi: 10.1038/ncomms9141; pmid: 26303108
35. S. Ramasamy *et al*., Intestinal alkaline phosphatase has beneficial effects in mouse models of chronic colitis. *Inflamm. Bowel Dis.* **17**, 532–542 (2011). doi: 10.1002/ibd.21377; pmid: 20645323
36. T. Dolowschiak *et al*., IFN-γ hinders recovery from mucosal inflammation during antibiotic therapy for *Salmonella* gut infection. *Cell Host Microbe* **20**, 238–249 (2016). doi: 10.1016/j.chom.2016.06.008; pmid: 27453483
37. S. L. Foster, R. Medzhitov, Gene-specific control of the TLR-induced inflammatory response. *Clin. Immunol.* **130**, 7–15 (2009). doi: 10.1016/j.clim.2008.08.015; pmid: 18964303
38. K. Kamdar *et al*., Genetic and metabolic signals during acute enteric bacterial infection alter the microbiota and drive progression to chronic inflammatory disease. *Cell Host Microbe* **19**, 21–31 (2016). doi: 10.1016/j.chom.2015.12.006; pmid: 26764594
39. S. Manco *et al*., Pneumococcal neuraminidases A and B both have essential roles during infection of the respiratory tract and sepsis. *Infect. Immun.* **74**, 4014–4020 (2006). doi: 10.1128/IAI.01237-05; pmid: 16790774
40. S. M. Schwerdtfeger, M. F. Melzig, Sialidases in biological systems. *Pharmazie* **65**, 551–561 (2010). pmid: 20824954
41. A. Varki, P. Gagneux, Multifarious roles of sialic acids in immunity. *Ann. N. Y. Acad. Sci.* **1253**, 16–36 (2012). doi: 10.1111/j.1749-6632.2012.06517.x; pmid: 22524423
42. K. Yamaguchi *et al*., Regulation of plasma-membrane-associated sialidase *NEU3* gene by Sp1/Sp3 transcription factors. *Biochem. J.* **430**, 107–117 (2010). doi: 10.1042/BJ20100350; pmid: 20518744
43. W. Ma *et al*., The p38 mitogen-activated kinase pathway regulates the human interleukin-10 promoter via the activation of Sp1 transcription factor in lipopolysaccharide-stimulated human macrophages. *J. Biol. Chem.* **276**, 13664–13674 (2001). doi: 10.1074/jbc.M011157200; pmid: 11278848
44. V. S. Carl, J. K. Gautam, L. D. Comeau, M. F. Smith Jr., Role of endogenous IL-10 in LPS-induced STAT3 activation and IL-1 receptor antagonist gene expression. *J. Leukoc. Biol.* **76**, 735–742 (2004). doi: 10.1189/jlb.1003526; pmid: 15218058
45. Y. Kakugawa *et al*., Up-regulation of plasma membrane-associated ganglioside sialidase (Neu3) in human colon cancer and its involvement in apoptosis suppression. *Proc. Natl. Acad. Sci. U.S.A.* **99**, 10718–10723 (2002). doi: 10.1073/pnas.152597199; pmid: 12149448
46. S. Kawamura *et al*., Plasma membrane-associated sialidase (NEU3) regulates progression of prostate cancer to androgen-independent growth through modulation of androgen receptor signaling. *Cell Death Differ.* **19**, 170–179 (2012). doi: 10.1038/cdd.2011.83; pmid: 21681193
47. K. Yamaguchi *et al*., Reduced susceptibility to colitis-associated colon carcinogenesis in mice lacking plasma membrane-associated sialidase. *PLOS ONE* **7**, e41132 (2012). doi: 10.1371/journal.pone.0041132; pmid: 22815940
48. T. Wada *et al*., Cloning, expression, and chromosomal mapping of a human ganglioside sialidase. *Biochem. Biophys. Res. Commun.* **261**, 21–27 (1999). doi: 1006/bbrc.1999.0973; pmid: 10405317
49. A. Mozzi *et al*., NEU3 activity enhances EGFR activation without affecting EGFR expression and acts on its sialylation levels. *Glycobiology* **25**, 855–868 (2015). doi: 10.1093/glycob/cwv026; pmid: 25922362
50. K. Ohtsubo *et al*., Dietary and genetic control of glucose transporter 2 glycosylation promotes insulin secretion in suppressing diabetes. *Cell* **123**, 1307–1321 (2005). doi: 10.1016/j.cell.2005.09.041; pmid: 16377570
51. B. Weinhold *et al*., Genetic ablation of polysialic acid causes severe neurodevelopmental defects rescued by deletion of the neural cell adhesion molecule. *J. Biol. Chem.* **280**, 42971–42977 (2005). doi: 10.1074/jbc.M511097200; pmid: 16267048
52. P. K. Grewal *et al*., ST6Gal-I restrains CD22-dependent antigen receptor endocytosis and Shp-1 recruitment in normal and pathogenic immune signaling. *Mol. Cell. Biol.* **26**, 4970–4981 (2006). doi: 10.1128/MCB.00308-06; pmid: 16782884
53. K. Ohtsubo, J. D. Marth, Glycosylation in cellular mechanisms of health and disease. *Cell* **126**, 855–867 (2006). doi: 10.1016/j.cell.2006.08.019; pmid: 16959566
54. P. R. Crocker, J. C. Paulson, A. Varki, Siglecs and their roles in the immune system. *Nat. Rev. Immunol.* **7**, 255–266 (2007). doi: 10.1038/nri2056; pmid: 17380156
55. F.-T. Liu, G. A. Rabinovich, Galectins: Regulators of acute and chronic inflammation. *Ann. N. Y. Acad. Sci.* **1183**, 158–182 (2010). doi: 10.1111/j.1749-6632.2009.05131.x; pmid: 20146714
56. A. Tuin *et al*., Role of alkaline phosphatase in colitis in man and rats. *Gut* **58**, 379–387 (2009). doi: 10.1136/gut.2007.128868; pmid: 18852260
57. M. Lukas *et al*., Exogenous alkaline phosphatase for the treatment of patients with moderate to severe ulcerative colitis. *Inflamm. Bowel Dis.* **16**, 1180–1186 (2010). doi: 10.1002/ibd.21161; pmid: 19885903
58. K. Molnár *et al*., Intestinal alkaline phosphatase in the colonic mucosa of children with inflammatory bowel disease. *World J. Gastroenterol.* **18**, 3254–3259 (2012). doi: 10.3748/wjg.v18.i25.3254; pmid: 22783049
59. S. N. Alam *et al*., Intestinal alkaline phosphatase prevents antibiotic-induced susceptibility to enteric pathogens. *Ann. Surg.* **259**, 715–722 (2014). doi: 10.1097/SLA.0b013e31828fae14; pmid: 23598380
60. J. J. Miklavcic *et al*., Increased catabolism and decreased unsaturation of ganglioside in patients with inflammatory bowel disease. *World J. Gastroenterol.* **21**, 10080–10090 (2015). doi: 10.3748/wjg.v21.i35.10080; pmid: 26401073
61. R. F. Goldberg *et al*., Intestinal alkaline phosphatase is a gut mucosal defense factor maintained by enteral nutrition. *Proc. Natl. Acad. Sci. U.S.A.*. **105**, 3551–3556 (2008). doi: 10.1073/pnas.0712140105; pmid: 18292227
62. D. M. Heithoff *et al*., Intraspecies variation in the emergence of hyperinfectious bacterial strains in nature. *PLOS Pathog.* **8**, e1002647 (2012). doi: 10.1371/journal.ppat.1002647; pmid: 22511871
63. J. Fu *et al*., Loss of intestinal core 1-derived *O*-glycans causes spontaneous colitis in mice. *J. Clin. Invest.* **121**, 1657–1666 (2011). doi: 10.1172/JCI45538; pmid: 21383503
64. S. Narisawa *et al*., Accelerated fat absorption in intestinal alkaline phosphatase knockout mice. *Mol. Cell. Biol.* **23**, 7525–7530 (2003). doi: 10.1128/MCB.23.21.7525-7530.2003; pmid: 14560000
65. K. Ohtsubo, M. Z. Chen, J. M. Olefsky, J. D. Marth, Pathway to diabetes through attenuation of pancreatic beta cell glycosylation and glucose transport. *Nat. Med.* **17**, 1067–1075 (2011). doi: 10.1038/nm.2414; pmid: 21841783
66. L. G. Ellies *et al*., Sialyltransferase ST3Gal-IV operates as a dominant modifier of hemostasis by concealing asialoglycoprotein receptor ligands. *Proc. Natl. Acad. Sci. U.S.A.* **99**, 10042–10047 (2002). doi: 10.1073/pnas.142005099; pmid: 12097641
67. M. R. Davis Jr., J. B. Goldberg, Purification and visualization of lipopolysaccharide from Gram-negative bacteria by hot aqueous-phenol extraction. *J. Vis. Exp.* **2012**, 3916 (2012). doi: 10.3791/3916; pmid: 22688346
68. C.-H. Lee, C.-M. Tsai, Quantification of bacterial lipopolysaccharides by the purpald assay: Measuring formaldehyde generated from 2-keto-3-deoxyoctonate and heptose at the inner core by periodate oxidation. *Anal. Biochem.* **267**, 161–168 (1999). doi: 10.1006/abio.1998.2961; pmid: 9918668
69. N. J. Foot *et al*., *Ndfip1*–deficient mice have impaired DMT1 regulation and iron homeostasis. *Blood* **117**, 638–646 (2011). doi: 10.1182/blood-2010-07-295287; pmid: 20959604.
70. A. Fuhrer *et al*., Milk sialyllactose influences colitis in mice through selective intestinal bacterial colonization. *J. Exp. Med.* **207**, 2843–2854 (2010). doi: 10.1084/jem.20101098; pmid: 21098096
71. M. H. Zaki *et al*., The NLRP3 inflammasome protects against loss of epithelial integrity and mortality during experimental colitis. *Immunity* **32**, 379–391 (2010). doi: 10.1016/j.immuni.2010.03.003; pmid: 20303296



## ACKNOWLEDGMENTS

This research was funded by NIH grants HL125352 (J.D.M. and V.N.) and HL131474 (J.D.M., M.J.M., and V.N.). Additional support was provided by the Wille Family Foundation (J.D.M.) and by SFB914 from the German Research Foundation (M.S.). The data presented in this study are in the main text and in the Supplementary Materials. W.H.Y., D.M.H., P.V.A., M.J.M., and J.D.M. designed the experimental strategies. J.D.M. and M.J.M. supervised the project. W.H.Y., D.M.H., and P.V.A. performed the experiments and acquired data. All authors contributed to data analysis and manuscript preparation. The authors declare that they have no competing interests.


## SUPPLEMENTARY MATERIALS

www.sciencemag.org/content/358/6370/eaao5610/suppl/DC1
Figs. S1 to S10

4 August 2017; accepted 13 November 2017
10.1126/science.aao5610

HEALTH AND MEDICINE

# Zika virus causes testicular atrophy

Ryuta Uraki,[1] Jesse Hwang,[1] Kellie Ann Jurado,[2] Sarah Householder,[1] Laura J. Yockey,[2] Andrew K. Hastings,[1] Robert J. Homer,[3,4] Akiko Iwasaki,[2,5] Erol Fikrig[1,5]*



**Zika virus (ZIKV) is an emerging mosquito-borne flavivirus that has recently been found to cause fetal infection and neonatal abnormalities, including microcephaly and neurological dysfunction. ZIKV persists in the semen months after the acute viremic phase in humans. To further understand the consequences of ZIKV persistence in males, we infected *Ifnar1*$^{-/-}$ mice via subcutaneous injection of a pathogenic but nonlethal ZIKV strain. ZIKV replication persists within the testes even after clearance from the blood, with interstitial, testosterone-producing Leydig cells supporting virus replication. We found high levels of viral RNA and antigen within the epididymal lumen, where sperm is stored, and within surrounding epithelial cells. Unexpectedly, at 21 days post-infection, the testes of the ZIKV-infected mice were significantly smaller compared to those of mock-infected mice, indicating progressive testicular atrophy. ZIKV infection caused a reduction in serum testosterone, suggesting that male fertility can be affected. Our findings have important implications for nonvector-borne vertical transmission, as well as long-term potential reproductive deficiencies, in ZIKV-infected males.**

## INTRODUCTION

Zika virus (ZIKV), a positive-stranded RNA virus belonging to the Flavivirus family, has recently been associated with several unexpected viral characteristics (*1*, *2*). Although the main mode of ZIKV transmission is thought to be mosquito-mediated, as in other flaviviruses (*3*, *4*), ZIKV has additionally been found to use both maternal-fetal (*5*) and sexual transmission (*6*) as a means of virus spread. Upon systemic infection, virus replication can be detected in most organs; it has also been found within several immune-privileged sites, including the brain (*7*–*18*), placenta (*19*, *20*), eyes (*21*), ovaries (*22*), and testes (*23*, *24*). In humans, persistent shedding of infectious virus has been found in vaginal secretions (*25*) and semen (*26*–*33*) at times well past the acute viremic and symptomatic stage of virus infection.

## RESULTS

To understand the pathology associated with persistence of ZIKV shedding within the testes, we used a murine infection model that leads to high levels of systemic virus replication but does not ultimately result in death (*Ifnar1*$^{-/-}$ mice challenged with ZIKV$^{MEX}$). ZIKV$^{MEX}$-infected *Ifnar1*$^{-/-}$ mice demonstrated relatively mild body weight loss (Fig. 1A) and developed peak viremia at 5 days post-infection (dpi) (Fig. 1B). We were surprised to find that the ZIKV$^{MEX}$ strain, which has not yet been published in mouse models, did not result in the lethal pathology of previous strains (*22*, *24*). This allowed us to monitor the effects of ZIKV infection of a pandemic strain at later time points of infection. Consistent with these findings, mice sacrificed at 5 dpi were found to have high levels of viral RNA (Fig. 1C) and infectious virus (Fig. 1D) within the brain, testes, and blood. At 9 dpi, ZIKV was essentially cleared from the bloodstream and was undetectable at 21 dpi (Fig. 1B).

To decipher the cellular tropism within the testes, we performed immunohistochemistry (IHC) using a mouse monoclonal antibody recognizing ZIKV NS1 antigen on testes and epididymis of ZIKV$^{MEX}$-infected *Ifnar1*$^{-/-}$ mice at 5 dpi. As shown in Fig. 2A, viral antigens were mainly detected within the interstitial cells of the testes. These regions are mainly composed of Leydig cells, a testicular cell type that supports sperm production through the generation of testosterone (*34*). We did not detect ZIKV within the seminiferous tubules in ZIKV$^{MEX}$-infected *Ifnar1*$^{-/-}$ mice at 5 dpi (Fig. 2A, a and b). Because the epididymis is a highly convoluted tube that stores and carries sperm (*35*), we also examined epididymal tissue of ZIKV$^{MEX}$-infected *Ifnar1*$^{-/-}$ mice for ZIKV antigen and found an overwhelming amount of antigen associated with the sperm mass within the epididymal duct lumen (Fig. 2A, d). In addition, we also observed several epithelial cells lining the lumen that were positive for viral antigen (red arrows in Fig. 2A, d). In further support of ZIKV infection of testes, RNA analysis of several cytokines indicated that an innate immune response was elicited at 5 dpi (Fig. 2B).

Because IHC analysis suggested that Leydig cells, which are responsible for the supply of testosterone in testes, are targets for ZIKV infection, we next determined the expression level of several genes related to testosterone synthesis (*36*) in ZIKV$^{MEX}$-infected *Ifnar1*$^{-/-}$ mice testes and found a consistent reduction among all genes tested as compared in testes of ZIKV$^{MEX}$-infected *Ifnar1*$^{-/-}$mice (Fig. 2C). To confirm the susceptibility of Leydig cells to ZIKV, we infected isolated WT or *Ifnar1*$^{-/-}$ Leydig cells with ZIKV$^{MEX}$ in vitro. As shown in Fig. 2D, Leydig cells were able to productively support ZIKV replication, indicating that Leydig cells could serve as a target and a reservoir cell type for ZIKV within the testes.

Strikingly and rather unexpectedly, at 21 dpi, the testes of ZIKV$^{MEX}$-infected *Ifnar1*$^{-/-}$ mice were significantly reduced in size as compared to those of uninfected mice (Fig. 3A), as determined by both weight (Fig. 3B) and length (Fig. 3C). These findings suggest that persistent ZIKV infection may lead to hypofertility. Because IHC, in vitro infection, and the decreased expression of genes related with testosterone synthesis indicated Leydig cells as putative targets for ZIKV infection within the testes, we next set to determine whether atrophy could occur as the result of decreased testosterone levels in ZIKV-infected mice. We examined levels of testosterone within serum from ZIKV$^{MEX}$-infected *Ifnar1*$^{-/-}$ mice at 5 and 21 dpi as compared with mock-infected *Ifnar1*$^{-/-}$ mice and found a significant decrease in testosterone at 5 dpi with a consistent reduction at 21 dpi (Fig. 3D). Notably, the testosterone levels

[1]Section of Infectious Diseases, Department of Internal Medicine, Yale University School of Medicine, New Haven, CT 06520, USA. [2]Department of Immunobiology, Yale University School of Medicine, New Haven, CT 06520, USA. [3]Department of Pathology, Yale University School of Medicine, New Haven, CT 06520, USA. [4]U.S. Department of Veterans Affairs Connecticut Healthcare System Pathology and Laboratory Medicine Service, West Haven, CT 06516, USA. [5]Howard Hughes Medical Institute, Chevy Chase, MD 20815, USA.
*Corresponding author. Email: erol.fikrig@yale.edu

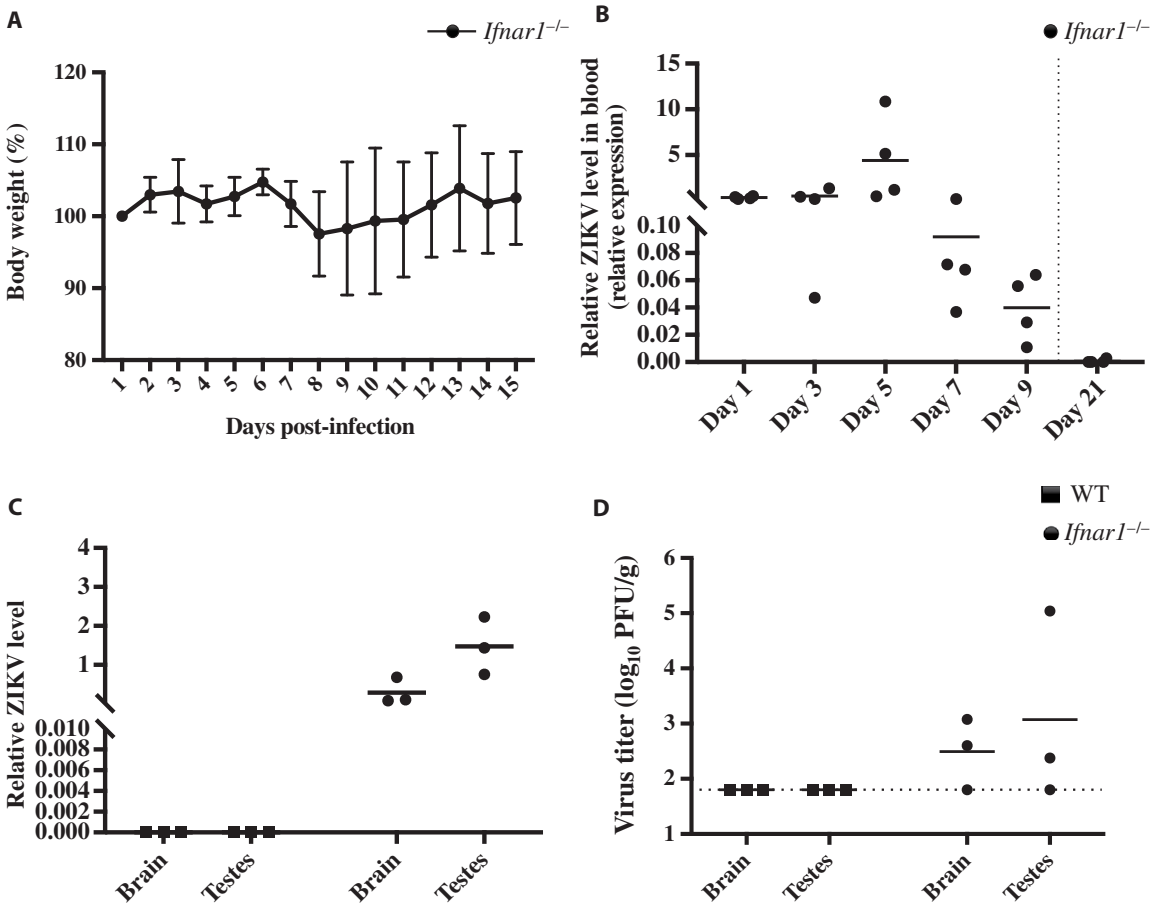


**Fig. 1. Characterization of ZIKV in mice.** *Ifnar1*$^{-/-}$ mice ($n$ = 4) were infected with $10^5$ plaque-forming units (PFU) of ZIKV$^{MEX}$ via subcutaneous route. (**A**) Weights were monitored for 15 days after virus infection. The values represent average scores of body weight compared with initial body weight ± SD from four mice. (**B**) Blood samples were collected at 1, 3, 5, 7, 9, and 21 dpi, and the virus loads were examined by quantitative reverse transcription polymerase chain reaction (qRT-PCR). Three wild-type (WT) and *Ifnar1*$^{-/-}$ mice were infected subcutaneously with $10^5$ PFU of ZIKV$^{MEX}$. Multiple organs were collected from mice ($n$ = 3) after challenge on day 5 and subjected to virus loads by qRT-PCR (**C**) and by plaque assays in Vero cells (**D**). The results are expressed as the mean titers. The detection limit of plaque assays is 1.8 $\log_{10}$ PFU/g.

at 5 dpi (six of seven mice) and at 21 dpi (two of seven mice) were lower than the assay detection limit. These findings support other data documenting ZIKV infection of Leydig cells (Fig. 2, A and D) and suggest a potential mechanism for ZIKV-induced testicular atrophy. Viral RNA was noticeably higher in the epididymis compared to testes (Fig. 3E), consistent with the copious amount of viral antigen detected by IHC within the epididymal lumen (Fig. 2A). It remains conceivable that multiple cell types within the reproductive tract produce virus, and the cell-free virus becomes stored and concentrated in the epididymis before physical expulsion upon sexual activity.

## DISCUSSION

Because humans with a fully functioning immune system also demonstrate persistent ZIKV infection of the testes, these findings have major implications for the fertility of men who have been exposed to ZIKV. It will be important to monitor the fertility of men who have been infected with ZIKV to better understand the impact in humans. We hypothesize that active infection of Leydig cells within the interstitial regions of the testes could cause decreased testosterone production, which ultimately results in testicular atrophy. There is precedence for deleterious effects on the production of testosterone and spermatogenesis caused by infection with mumps virus, which also targets Leydig cells as a site of replication within the testes (*37*–*39*). Alternatively, or in conjunction, because inflammation is known to also lead to testicular atrophy, the phenotype may be caused indirectly, or enhanced by, the immune response to detection of ZIKV. Because all experiments were carried out in *Ifnar1*$^{-/-}$ mice, our data rule out the possibility of type I interferon signaling in testicular atrophy caused by ZIKV.

RNA analysis of testes samples of ZIKV$^{MEX}$-infected *Ifnar1*$^{-/-}$ mice found ZIKV to be present within the testes and epididymis at 5 dpi in all mice and at 21 dpi in most mice. Because there is no detectable ZIKV RNA within the blood of ZIKV$^{MEX}$-infected *Ifnar1*$^{-/-}$ mice at 21 dpi (Fig. 1B), this observation recapitulates the human presentation of persistent ZIKV replication within the testes. For ZIKV$^{MEX}$-infected *Ifnar1*$^{-/-}$ mice sacrificed at 35 dpi, when the epididymis was measured to be ZIKV-negative, some of the testes were still reduced in size (15 to 45% shorter in length) as compared to testes of mock-infected mice. Determination of the possibility of recovery from testicular atrophy over greater time periods is warranted. Recently, two other groups also reported that ZIKV can cause long-term testicular damage; however, the infected cell types found in these studies (spermatogonia, primary spermatocytes, Sertoli cells, and/or peritubular myoid cells) differ from those reported here, indicating that further

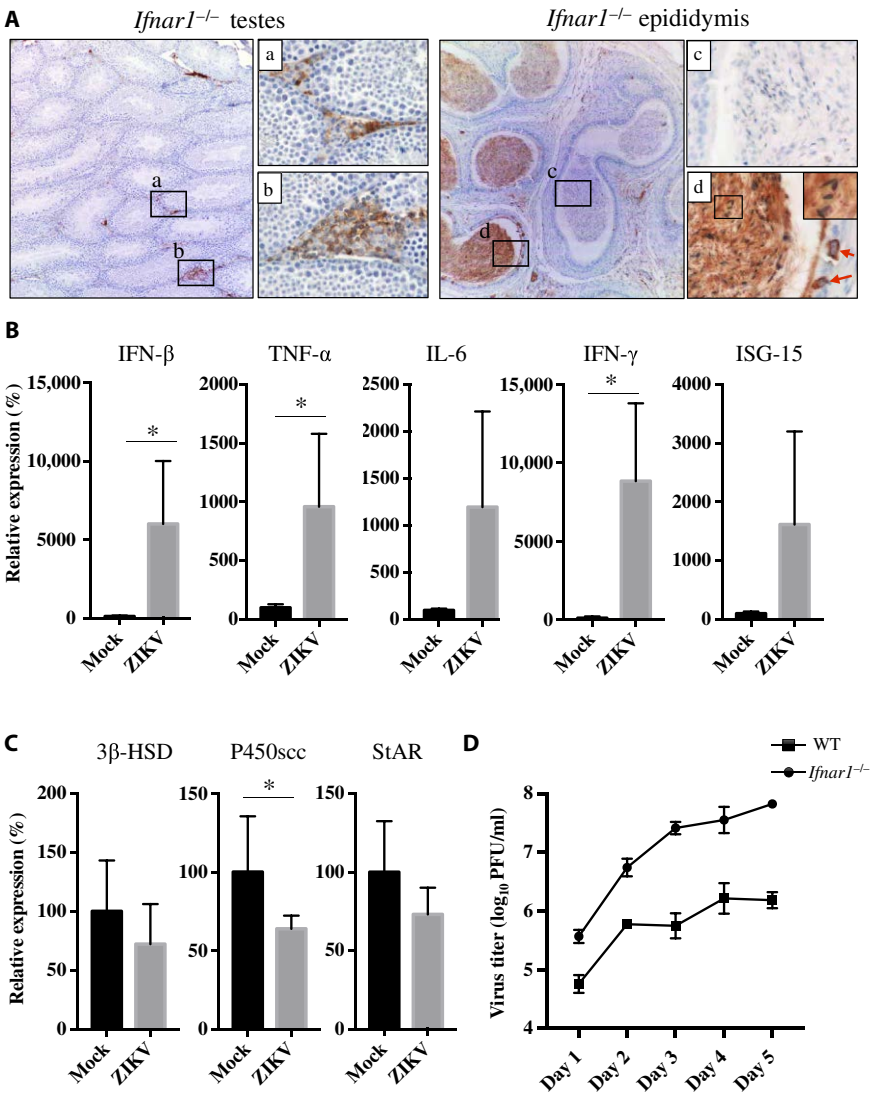


**Fig. 2. ZIKV infection in testes and epididymis.** *Ifnar1*$^{-/-}$ mice were infected with $10^5$ PFU of ZIKV$^{MEX}$ via subcutaneous route. (**A**) IHC was performed using an anti-ZIKV NS1 antibody. Left panels (low magnification) show insets shown on the right (higher magnification). Red arrowheads indicate infected epithelial cells. (**B** and **C**) At 5 dpi, testes were collected, and total RNA was extracted for qRT-PCR of interferon-β (IFN-β), tumor necrosis factor–α (TNF-α), interleukin-6 (IL-6), IFN-γ, and interferon-stimulated gene 15 (ISG-15) (B). The testicular mRNA expression levels of testosterone-synthetic genes [steroidogenic acute regulatory factor (StAR), cytochrome P-450 side-chain cleavage enzyme (P450scc), and 3β-hydroxysteroid dehydrogenase (3β-HSD)] were examined by qRT-PCR (C). Data are normalized to mouse β-actin (*$P < 0.05$). (**D**) Isolated Leydig cells from WT and *Ifnar1*$^{-/-}$ mice were infected with ZIKV at a multiplicity of infection of 10. At the indicated times after infection, virus titers in the supernatant were determined with Vero cells. The reported values are means ± SD.

studies are required to examine the temporal and molecular details of ZIKV tropism within the reproductive tract (*40*, *41*). In addition, further work is necessary to assess the relative contributions of the innate immune response and/or testosterone reduction in ZIKV-induced testicular atrophy. Regardless, the hypofertility implications of testicular atrophy call for an urgent global need to develop vaccines and antiviral therapeutics.

## MATERIALS AND METHODS

### Ethics statement

This study was performed in accordance with the recommendations in the *Guide for the Care and Use of Laboratory Animals* of the National Institutes of Health. The protocols were approved by the Institutional Animal Care and Use Committee at the Yale University School of Medicine.

### Cells

C6/36 *Aedes albopictus* cells were grown in Dulbecco's modified Eagle's medium (DMEM) with 10% fetal calf serum (FCS) and 1% tryptose phosphate broth at 30°C in 5% $CO_2$. Vero cells (African green monkey kidney epithelial cells) were maintained in DMEM with 10% FCS at 37°C in 5% $CO_2$. C6/36 cells were used for generating ZIKV stocks, and Vero cells were used for plaque assays, as described below.

### Virus

An American-derived ZIKV (MEX2-81 strain, referred to as ZIKV$^{MEX}$) isolated in 2016 was used in this study (*19*, *42*). C6/36 cells were infected with ZIKV$^{MEX}$ and maintained up to 10 days. Cell-free supernatants were collected and stored at −80°C.

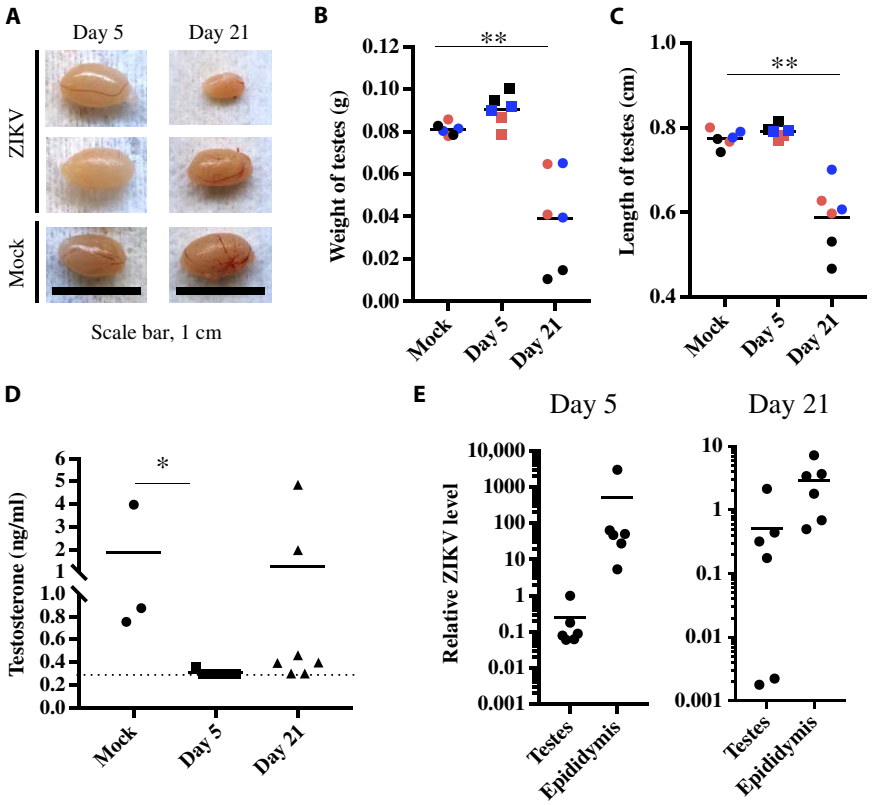


**Fig. 3. Testicular abnormalities after ZIKV infection.** The testes of *Ifnar1*$^{-/-}$ mice infected with $10^5$ PFU of ZIKV$^{MEX}$ via subcutaneous route and of mock-infected mice were harvested at 5 and 21 dpi. (**A**) The pictures compare the testes of infected mice. Scale bar, 1 cm. (**B** and **C**) Weight and length of whole testes from infected animals were measured ($n = 6$ testes comprising three mice; $^{**}P < 0.01$). Same color indicates the same mice. (**D**) The levels of testosterone in blood of infected mice were investigated by enzyme-linked immunosorbent assay ($^{*}P < 0.05$). The detection limit is 0.3 ng/ml. (**E**) The relative viral RNA levels in testes and epididymis at 5 and 21 dpi were examined by qRT-PCR. Data are normalized to mouse β-actin.

### Plaque assays

Vero cells were seeded in 12-well plates 24 hours before infection. Serial-diluted ZIKV was incubated for 1 hour at 37°C in 5% $CO_2$. Then, cells were overlaid with 2% agarose and 2× medium. At 3 to 4 dpi, cells were fixed by 10% formalin and stained with 0.005% amido black, and PFU were counted.

### Mouse experiments

Four- to six-week-old *Ifnar1*$^{-/-}$ (C57BL/6 background) and WT C57BL/6 mice were analyzed in this study. Mice were bred in a specific pathogen–free facility at Yale University or purchased from The Jackson Laboratory (WT C57BL/6). Mice were inoculated with ZIKV via subcutaneous injection (footpad; a volume of 50 μl) with $10^5$ PFU of ZIKV. Survivals and weights were monitored every day up to 15 dpi. Mice exhibiting a weight loss of >20% of initial body weight or neurological disease were euthanized. To examine the viremia, we collected blood samples at 1, 3, 5, 7, 9, and 21 dpi and performed real-time PCR. To assess virus growth or host responses in organs, we euthanized three mice at 5 or 21 dpi, and their organs were collected, homogenized with DMEM with 10% FCS or TRIzol, and titrated using plaque assays or real-time PCR.

### RNA extraction, real-time PCR, and PCR

The homogenized organ and blood samples from ZIKV-infected mice were transferred to a fresh 1.5-ml tube to which chloroform was added. The tubes were vortexed well and centrifuged for 10 min at 14,000 rpm at 4°C. The aqueous layers were mixed with 100% ethanol and then subjected to RNA extraction using RNeasy Mini Kit (Qiagen) according to the manufacturer's instructions. Extracted RNA was reverse-transcribed using iScript cDNA Synthesis Kit (Bio-Rad) according to the manufacturer's protocol. Gene expressions of samples were queried using iQ SYBR Green Supermix. ZIKV RNA or target gene mRNA levels were normalized to mouse β-actin RNA levels according to the $2^{-\Delta\Delta Ct}$ calculations. The qRT-PCR primer sequences are available upon request.

### Detection of testosterone in serum

The concentration of testosterone in serum of ZIKV-infected *Ifnar1*$^{-/-}$ mice was performed by using the Mouse Testosterone ELISA Kit (Abcam) according to the manufacturer's instructions.

### Isolation of Leydig cells

Leydig cells were isolated from WT and *Ifnar1*$^{-/-}$ mice according to previous studies (*36*, *43*). In brief, the testes of two mice were decapsulated and incubated with collagenase (0.5 mg/ml) in F12/DMEM (Life Technologies) supplemented with 10% FCS at room temperature for 15 min with gentle inverting. The suspensions were filtered through 70-μm mesh to separate the interstitial cells from seminiferous tubules. The interstitial cells were cultured in F12/DMEM supplemented with FCS. After 24 hours, Leydig cells were detached by 0.125% trypsin treatment for 5 min and resuspended to dish.

### Histopathological analysis

The testes of mice were preserved in 4% paraformaldehyde/phosphate-buffered saline for pathological examination. The fixed samples were processed for paraffin embedding. Sections were processed for immunohistological staining with an anti-ZIKV NS1 antibody.

### Data analysis

Data analysis was performed using GraphPad Prism and Microsoft Excel. One-tailed Student's *t* test was used to determine the significance of qRT-PCR values for host responses. One-way analysis of variance (ANOVA) was used to compare the weight and length of testes and testosterone levels.

## REFERENCES AND NOTES


1. H. M. Lazear, M. S. Diamond, Zika virus: New clinical syndromes and its emergence in the Western Hemisphere. *J. Virol.* **90**, 4864–4875 (2016).
2. G. S. Campos, A. C. Bandeira, S. I. Sardi, Zika virus outbreak, Bahia, Brazil. *Emerg. Infect. Dis.* **21**, 1885–1886 (2015).
3. V. Richard, T. Paoaafaite, V.-M. Cao-Lormeau, Vector competence of French Polynesian *Aedes aegypti* and *Aedes polynesiensis* for Zika virus. *PLOS Negl. Trop. Dis.* **10**, e0005024 (2016).
4. J. P. Boorman, J. S. Porterfield, A simple technique for infection of mosquitoes with viruses; transmission of Zika virus. *Trans. R. Soc. Trop. Med. Hyg.* **50**, 238–242 (1956).
5. L. J. Yockey, L. Varela, T. Rakib, W. Khoury-Hanold, S. L. Fink, B. Stutz, K. Szigeti-Buck, A. Van den Pol, B. D. Lindenbach, T. L. Horvath, A. Iwasaki, Vaginal exposure to Zika virus during pregnancy leads to fetal brain infection. *Cell* **166**, 1247–1256.e4 (2016).
6. F. C. Coelho, B. Durovni, V. Saraceni, C. Lemos, C. T. Codeco, S. Camargo, L. M. Carvalho, L. Bastos, D. Arduini, D. A. M. Villela, M. Armstrong, Higher incidence of Zika in adult women in Rio de Janeiro suggests a significant contribution of sexual transmission from men to women. *Int. J. Infect. Dis.* **51**, 128–132 (2016).
7. K.-Y. Wu, G.-L. Zuo, X.-F. Li, Q. Ye, Y.-Q. Deng, X.-Y. Huang, W.-C. Cao, C.-F. Qin, Z.-G. Luo, Vertical transmission of Zika virus targeting the radial glial cells affects cortex development of offspring mice. *Cell Res.* **26**, 645–654 (2016).
8. J.-B. Brault, C. Khou, J. Basset, L. Coquand, V. Fraisier, M.-P. Frenkiel, B. Goud, J.-C. Manuguerra, N. Pardigon, A. D. Baffet, Comparative analysis between flaviviruses reveals specific neural stem cell tropism for Zika virus in the mouse developing neocortex. *EBioMedicine* **10**, 71–76 (2016).
9. F. R. Cugola, I. R. Fernandes, F. B. Russo, B. C. Freitas, J. L. M. Dias, K. P. Guimarães, C. Benazzato, N. Almeida, G. C. Pignatari, S. Romero, C. M. Polonio, I. Cunha, C. L. Freitas, W. N. Brandão, C. Rossato, D. G. Andrade, D. de Paula Faria, A. T. Garcez, C. A. Buchpigel, C. T. Braconi, E. Mendes, A. A. Sall, P. M. de Andrade Zanotto, J. P. S. Peron, A. R. Muotri, P. C. B. Beltrão-Braga, The Brazilian Zika virus strain causes birth defects in experimental models. *Nature* **534**, 267–271 (2016).
10. J. Dang, S. K. Tiwari, G. Lichinchi, Y. Qin, V. S. Patil, A. M. Eroshkin, T. M. Rana, Zika virus depletes neural progenitors in human cerebral organoids through activation of the innate immune receptor TLR3. *Cell Stem Cell* **19**, 258–265 (2016).
11. P. P. Garcez, E. C. Loiola, R. Madeiro da Costa, L. M. Higa, P. Trindade, R. Delvecchio, J. M. Nascimento, R. Brindeiro, A. Tanuri, S. K. Rehen, Zika virus impairs growth in human neurospheres and brain organoids. *Science* **352**, 816–818 (2016).
12. N. W. Hanners, J. L. Eitson, N. Usui, R. B. Richardson, E. M. Wexler, G. Konopka, J. W. Schoggins, Western Zika virus in human fetal neural progenitors persists long term with partial cytopathic and limited immunogenic effects. *Cell Rep.* **15**, 2315–2322 (2016).
13. C. Li, D. Xu, Q. Ye, S. Hong, Y. Jiang, X. Liu, N. Zhang, L. Shi, C.-F. Qin, Z. Xu, Zika virus disrupts neural progenitor development and leads to microcephaly in mice. *Cell Stem Cell* **19**, 120–126 (2016).
14. H. Li, L. Saucedo-Cuevas, J. A. Regla-Nava, G. Chai, N. Sheets, W. Tang, A. V. Terskikh, S. Shresta, J. G. Gleeson, Zika Virus infects neural progenitors in the adult mouse brain and alters proliferation. *Cell Stem Cell* **19**, 593–598 (2016).
15. M. Onorati, Z. Li, F. Liu, A. M. M. Sousa, N. Nakagawa, M. Li, M. T. Dell'Anno, F. O. Gulden, S. Pochareddy, A. T. N. Tebbenkamp, W. Han, M. Pletikos, T. Gao, Y. Zhu, C. Bichsel, L. Varela, K. Szigeti-Buck, S. Lisgo, Y. Zhang, A. Testen, X.-B. Gao, J. Mlakar, M. Popovic, M. Flamand, S. M. Strittmatter, L. K. Kaczmarek, E. S. Anton, T. L. Horvath, B. D. Lindenbach, N. Sestan, Zika virus disrupts phospho-TBK1 localization and mitosis in human neuroepithelial stem cells and radial glia. *Cell Rep.* **16**, 2576–2592 (2016).
16. X. Qian, H. N. Nguyen, M. M. Song, C. Hadiono, S. C. Ogden, C. Hammack, B. Yao, G. R. Hamersky, F. Jacob, C. Zhong, K.-y. Yoon, W. Jeang, L. Lin, Y. Li, J. Thakor, D. A. Berg, C. Zhang, E. Kang, M. Chickering, D. Nauen, C.-Y. Ho, Z. Wen, K. M. Christian, P.-Y. Shi, B. J. Maher, H. Wu, P. Jin, H. Tang, H. Song, G.-l. Ming, Brain-region-specific organoids using mini-bioreactors for modeling ZIKV exposure. *Cell* **165**, 1238–1254 (2016).
17. H. Tang, C. Hammack, S. C. Ogden, Z. Wen, X. Qian, Y. Li, B. Yao, J. Shin, F. Zhang, E. M. Lee, K. M. Christian, R. A. Didier, P. Jin, H. Song, G.-l. Ming, Zika virus infects human cortical neural progenitors and attenuates their growth. *Cell Stem Cell* **18**, 587–590 (2016).
18. F. Zhang, C. Hammack, S. C. Ogden, Y. Cheng, E. M. Lee, Z. Wen, X. Qian, H. N. Nguyen, Y. Li, B. Yao, M. Xu, T. Xu, L. Chen, Z. Wang, H. Feng, W.-K. Huang, K.-j. Yoon, C. Shan, L. Huang, Z. Qin, K. M. Christian, P.-Y. Shi, M. Xia, W. Zheng, H. Wu, H. Song, H. Tang, G.-L. Ming, P. Jin, Molecular signatures associated with ZIKV exposure in human cortical neural progenitors. *Nucleic Acids Res.* **44**, 8610–8620 (2016).
19. K. A. Jurado, M. K. Simoni, Z. Tang, R. Uraki, J. Hwang, S. Householder, M. Wu, B. D. Lindenbach, V. M. Abrahams, S. Guller, E. Fikrig, Zika virus productively infects primary human placenta-specific macrophages. *JCI Insight* **1**, e88461 (2016).
20. K. M. Quicke, J. R. Bowen, E. L. Johnson, C. E. McDonald, H. Ma, J. T. O'Neal, A. Rajakumar, J. Wrammert, B. H. Rimawi, B. Pulendran, R. F. Schinazi, R. Chakraborty, M. S. Suthar, Zika virus infects human placental macrophages. *Cell Host Microbe* **20**, 83–90 (2016).
21. J. J. Miner, A. Sene, J. M. Richner, A. M. Smith, A. Santeford, N. Ban, J. Weger-Lucarelli, F. Manzella, C. Rückert, J. Govero, K. K. Noguchi, G. D. Ebel, M. S. Diamond, R. S. Apte, Zika virus infection in mice causes panuveitis with shedding of virus in tears. *Cell Rep.* **16**, 3208–3218 (2016).
22. S. D. Dowall, V. A. Graham, E. Rayner, B. Atkinson, G. Hall, R. J. Watson, A. Bosworth, L. C. Bonney, S. Kitchen, R. Hewson, A susceptible mouse model for Zika virus infection. *PLOS Negl. Trop. Dis.* **10**, e0004658 (2016).
23. S. L. Rossi, R. B. Tesh, S. R. Azar, A. E. Muruato, K. A. Hanley, A. J. Auguste, R. M. Langsjoen, S. Paessler, N. Vasilakis, S. C. Weaver, Characterization of a novel murine model to study Zika virus. *Am. J. Trop. Med. Hyg.* **94**, 1362–1369 (2016).
24. H. M. Lazear, J. Govero, A. M. Smith, D. J. Platt, E. Fernandez, J. J. Miner, M. S. Diamond, A mouse model of Zika virus pathogenesis. *Cell Host Microbe* **19**, 720–730 (2016).
25. K. O. Murray, R. Gorchakov, A. R. Carlson, R. Berry, L. Lai, M. Natrajan, M. N. Garcia, A. Correa, S. M. Patel, K. Aagaard, M. J. Mulligan, Prolonged detection of Zika virus in vaginal secretions and whole blood. *Emerg. Infect. Dis.* **23**, 99–101 (2017).
26. E. D'Ortenzio, S. Matheron, Y. Yazdanpanah, X. de Lamballerie, B. Hubert, G. Piorkowski, M. Maquart, D. Descamps, F. Damond, I. Leparc-Goffart, Evidence of sexual transmission of Zika virus. *N. Engl. J. Med.* **374**, 2195–2198 (2016).
27. C. Frank, D. Cadar, A. Schlaphof, N. Neddersen, S. Günther, J. Schmidt-Chanasit, D. Tappe, Sexual transmission of Zika virus in Germany, April 2016. *Euro Surveill.* **21**, 10.2807/1560-7917.ES.2016.21.23.30252 (2016).
28. T. Fréour, S. Mirallié, B. Hubert, C. Splingart, P. Barriere, M. Maquart, I. Leparc-Goffart, Sexual transmission of Zika virus in an entirely asymptomatic couple returning from a Zika epidemic area, France, April 2016. *Euro Surveill.* **21**, 10.2807/1560-7917.ES.2016.21.23.30254 (2016).
29. J. Harrower, T. Kiedrzynski, S. Baker, A. Upton, F. Rahnama, J. Sherwood, Q. S. Huang, A. Todd, D. Pulford, Sexual transmission of Zika virus and persistence in Semen, New Zealand, 2016. *Emerg. Infect. Dis.* **22**, 1855–1857 (2016).
30. E. Nicastri, C. Castilletti, G. Liuzzi, M. Iannetta, M. R. Capobianchi, G. Ippolito, Persistent detection of Zika virus RNA in semen for six months after symptom onset in a traveller returning from Haiti to Italy, February 2016. *Euro Surveill.* **21**, 10.2807/1560-7917.ES.2016.21.32.30314 (2016).
31. J. M. Turmel, P. Abgueguen, B. Hubert, Y. M. Vandamme, M. Maquart, H. Le Guillou-Guillemette, I. Leparc-Goffart, Late sexual transmission of Zika virus related to persistence in the semen. *Lancet* **387**, 2501 (2016).
32. S. L. Hills, K. Russell, M. Hennessey, C. Williams, A. M. Oster, M. Fischer, P. Mead, Transmission of Zika virus through sexual contact with travelers to areas of ongoing transmission—Continental United States, 2016. *MMWR Morb. Mortal. Wkly Rep.* **65**, 215–216 (2016).
33. M. Arsuaga, S. G. Bujalance, M. Diaz-Menendez, A. Vazquez, J. R. Arribas, Probable sexual transmission of Zika virus from a vasectomised man. *Lancet Infect. Dis.* **16**, 1107 (2016).
34. T. O. Abney, The potential roles of estrogens in regulating Leydig cell development and function: A review. *Steroids* **64**, 610–617 (1999).
35. R. C. Jones, To store or mature spermatozoa? The primary role of the epididymis. *Int. J. Androl.* **22**, 57–67 (1999).
36. H. Wu, L. Shi, Q. Wang, L. Cheng, X. Zhao, Q. Chen, Q. Jiang, M. Feng, Q. Li, D. Han, Mumps virus-induced innate immune responses in mouse Sertoli and Leydig cells. *Sci. Rep.* **6**, 19507 (2016).
37. A. Le Tortorec, H. Denis, A. P. Satie, J. J. Patard, A. Ruffault, B. Jégou, N. Dejucq-Rainsford, Antiviral responses of human Leydig cells to mumps virus infection or poly I:C stimulation. *Hum. Reprod.* **23**, 2095–2103 (2008).
38. R. Le Goffic, T. Mouchel, A. Ruffault, J. J. Patard, B. Jégou, M. Samson, Mumps virus decreases testosterone production and gamma interferon-induced protein 10 secretion by human Leydig cells. *J. Virol.* **77**, 3297–3300 (2003).

39. N. Dejucq, B. Jégou, Viruses in the mammalian male genital tract and their effects on the reproductive system. *Microbiol. Mol. Biol. Rev.* **65**, 208–231 (2001).
40. J. Govero, P. Esakky, S. M. Scheaffer, E. Fernandez, A. Drury, D. J. Platt, M. J. Gorman, J. M. Richner, E. A. Caine, V. Salazar, K. H. Moley, M. S. Diamond, Zika virus infection damages the testes in mice. *Nature* **540**, 438–442 (2016).
41. W. Ma, S. Li, S. Ma, L. Jia, F. Zhang, Y. Zhang, J. Zhang, G. Wong, S. Zhang, X. Lu, M. Liu, J. Yan, W. Li, C. Qin, D. Han, N. Wang, X. Li, G. F. Gao, Zika virus causes testis damage and leads to male infertility in mice. *Cell* **167**, 1511–1524.e10 (2016).
42. J. Song, M. G. Mauk, B. A. Hackett, S. Cherry, H. H. Bau, C. Liu, Instrument-free point-of-care molecular detection of Zika virus. *Anal. Chem.* **88**, 7289–7294 (2016).
43. W. Zhu, Q. Chen, K. Yan, Z. Liu, N. Li, X. Zhang, L. Yu, Y. Chen, D. Han, *RIG-I*-like receptors mediate innate antiviral response in mouse testis. *Mol. Endocrinol.* **27**, 1455–1467 (2013).

**Acknowledgments:** We thank M. Flamand (Institut Pasteur) and B. Lindenbach (Yale University) for contributing the NS1 mouse monoclonal antibody. E.F. and A.I. are investigators at the Howard Hughes Medical Institute. **Funding:** This work was supported by NIH grants 5T32 AI007019-40 (to K.A.J.), 4T32HL007974-15 (to J.H.), and T32 GM007205 (to L.J.Y.). **Author contributions:** R.U., J.H., K.A.J., and E.F. conceived the study. R.U., J.H., K.A.J., and E.F. designed the experiments. R.U., J.H., K.A.J., L.J.Y., S.H., and A.K.H. performed the experiments and analyzed the data. R.J.H. and A.I. provided intellectual guidance in the analysis and interpretation of data. R.U., J.H., K.A.J., A.I., and E.F. wrote the manuscript with contributions from all coauthors. **Competing interests:** The authors declare that they have no competing interests. **Data and materials availability:** All data needed to evaluate the conclusions in the paper are present in the paper. Additional data related to this paper may be requested from the authors.

Submitted 20 November 2016
Accepted 20 December 2016
Published 22 February 2017
10.1126/sciadv.1602899

**Citation:** R. Uraki, J. Hwang, K. A. Jurado, S. Householder, L. J. Yockey, A. K. Hastings, R. J. Homer, A. Iwasaki, E. Fikrig, Zika virus causes testicular atrophy. *Sci. Adv.* **3**, e1602899 (2017).

MICROBIOLOGY

# Walls talk: Microbial biogeography of homes spanning urbanization


10.1126/sciadv.1501061

**Jean F. Ruiz-Calderon,[1]* Humberto Cavallin,[2]* Se Jin Song,[3]* Atila Novoselac,[4] Luis R. Pericchi,[5] Jean N. Hernandez,[1] Rafael Rios,[6] Oralee H. Branch,[7] Henrique Pereira,[8] Luciana C. Paulino,[9] Martin J. Blaser,[10] Rob Knight,[11] Maria G. Dominguez-Bello[1,10†]**

**Westernization has propelled changes in urbanization and architecture, altering our exposure to the outdoor environment from that experienced during most of human evolution. These changes might affect the developmental exposure of infants to bacteria, immune development, and human microbiome diversity. Contemporary urban humans spend most of their time indoors, and little is known about the microbes associated with different designs of the built environment and their interaction with the human immune system. This study addresses the associations between architectural design and the microbial biogeography of households across a gradient of urbanization in South America. Urbanization was associated with households' increased isolation from outdoor environments, with additional indoor space isolation by walls. Microbes from house walls and floors segregate by location, and urban indoor walls contain human bacterial markers of space use. Urbanized spaces uniquely increase the content of human-associated microbes—which could increase transmission of potential pathogens—and decrease exposure to the environmental microbes with which humans have coevolved.**

## INTRODUCTION

Urbanization of traditional villages—the villages developing in more urban form, and historical villagers migrating to towns and cities—is occurring concurrently with a global convergence toward a more Westernized urban plan and life-style (*1*). This process occurs as human societies integrate from hunter-gatherers into first rural and then urban life-styles. Urbanization also involves more people spending most of their lives in indoor built environments (*2*, *3*).

A large proportion of the microbes found in the built environment are shed by humans (*4*–*7*) or animals (*8*), and with natural ventilation, microbes can also be transported from outdoors (*5*, *6*, *9*). Understanding the consequences of architectural changes on environmental exposures, including microbial exposures, is therefore important in improving home design and ultimately human health. Here, we determine the changes in architectural design and the resulting microbial communities of houses spanning a range of modernization within the Amazon River basin. We measured community demographics and architectural parameters, and characterized the microbial communities of 10 houses and their inhabitants from each of four locations: a traditional jungle village of hunter-gatherers near the border between Peru and Ecuador, a rural village further east along a similar latitude, the large Peruvian town of Iquitos, and, finally, the modern Brazilian city of Manaus (Fig. 1A).

[1]Department of Biology, University of Puerto Rico, Rio Piedras Campus, San Juan 00931, Puerto Rico. [2]School of Architecture, University of Puerto Rico, Rio Piedras Campus, San Juan 00931, Puerto Rico. [3]Department of Ecology and Evolutionary Biology, University of Colorado at Boulder, Boulder, CO 80309, USA. [4]Department of Civil, Architectural and Environmental Engineering, University of Texas at Austin, Austin, TX 78712, USA. [5]Department of Mathematics, University of Puerto Rico, Rio Piedras Campus, San Juan 00931, Puerto Rico. [6]Department of Environmental Sciences, University of Puerto Rico, Rio Piedras Campus, San Juan 00931, Puerto Rico. [7]Department of Microbiology, New York University Langone Medical Center, New York, NY 10016, USA. [8]Federal University of Amazonas, Manaus, AM 66077-000, Brazil. [9]Center for Natural Sciences and Humanities, Federal University of ABC, Santo André, SP 09210, Brazil. [10]Department of Medicine, New York University Langone Medical Center, New York, NY 10016, USA. [11]Departments of Pediatrics and Computer Science & Engineering, University of California at San Diego, La Jolla, CA 92093, USA.
*These authors contributed equally to this work.
†Corresponding author. E-mail: maria.dominguez-bello@nyumc.org

## RESULTS

The jungle village of Checherta is a 21-house Achuar community of hunter-gatherers (tables S1 and S2, and fig. S1, A and B). Homes are organized around a central area, including a communal building. This community design is retained in the 25-house rural village of Puerto Almendras, with the homes surrounding a soccer field (fig. S1C and table S1). Iquitos has 0.4 million inhabitants and is the largest urban population in the world not accessible by roads (fig. S1C and tables S1 and S2). Manaus, the capital of Amazonas State in Brazil, is a contemporary Western city with 1.8 million inhabitants (fig. S1D and tables S1 and S2).

Although no significant environmental differences were found across the urbanization gradient, large architectural changes were observed (Fig. 1). No significant differences were found across the studied locations in outdoor temperature (mean variation, <2°C; table S3) or relative humidity, and all locations had high ventilation rates (air exchange rates of 25 to 100 $h^{-1}$ in the jungle village, 7 to 20 $h^{-1}$ in the rural village, 4 to 17 $h^{-1}$ in the town, and 0.8 to 15 $h^{-1}$ in the city). The jungle village homes of Checherta are open huts made of wood and reeds, and are generally single open-plan spaces composed of two functional areas (Fig. 1, A and B, and fig. S2): a dormitory containing one platform bed per family, and a fire area for cooking and socializing. Up to six core families, among extended family members, share a home. As urbanization increases, a progressive separation of the indoor environment from the outdoor occurs first, followed by internal division of home spaces and the use of a wider variety of building materials (table S4). In the rural village, a toilet appears as an external latrine, which in the town and city becomes a piped indoor bathroom. Town and city houses typically have additional spaces differentiated by functional purpose (living room, kitchen, and bathroom) and segregated by walls (Fig. 1B).

Houses in the most urbanized conditions are more variable in design, but in general, there is an urbanization-associated increase in the number of rooms per person (privacy index) (Fig. 1C, fig. S3, and table S4), house area, and its variance ($P < 0.005$; Fig. 1C and table S4). The average

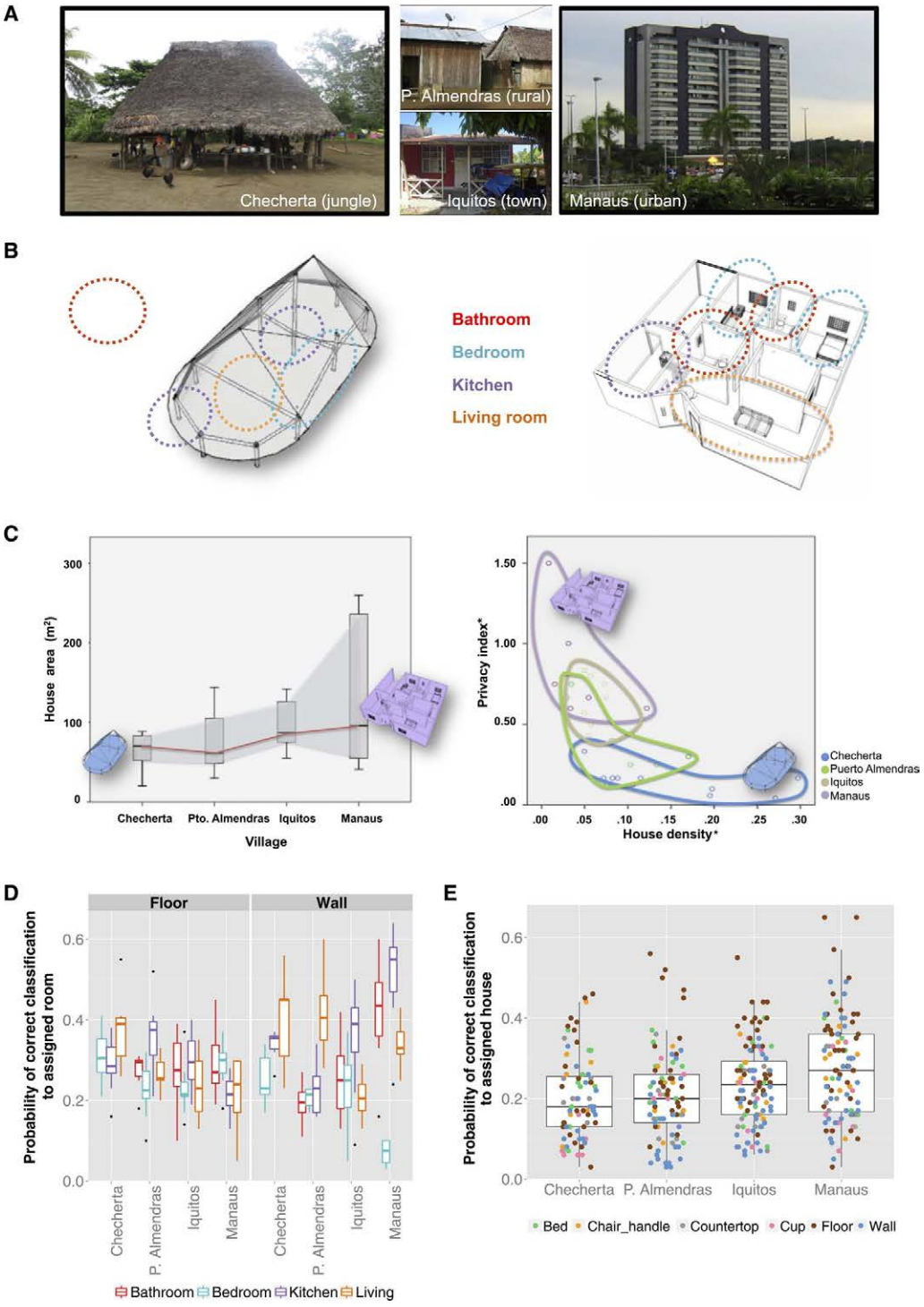


**Fig. 1. Architecture and space use covary with key structural features such as house partitioning, area, and occupant density across the four locations; differences in space use are reflected in the microbial communities of the walls, but not floors, which contribute to the microbial signatures of the homes.** (**A**) Photos of the typical structures found across the four communities along this urbanization gradient [Checherta (jungle), Puerto Almendras (rural), Iquitos (town), and Manaus (city)]. (**B**) Typical floor plans of houses in Checherta and Manaus (left and right, respectively). (**C**) Distribution of house area (left) and mean privacy index *(privacy index = number of rooms/number of people) according to occupant density (occupant density = number of people/square meters) (right) by location. (**D**) Classification probability of correct assignment to a sample's true location using a random forest classifier. The probability of being able to predict a functional space using the microbial community of the walls increases with increased partitioning of spaces by use in the urban areas (for example, bathrooms and kitchens in separate walled-off spaces). Floor microbial communities, on the other hand, are not as discriminatory among rooms. (**E**) Classification probability of correct assignment of a given sample to the correct house.

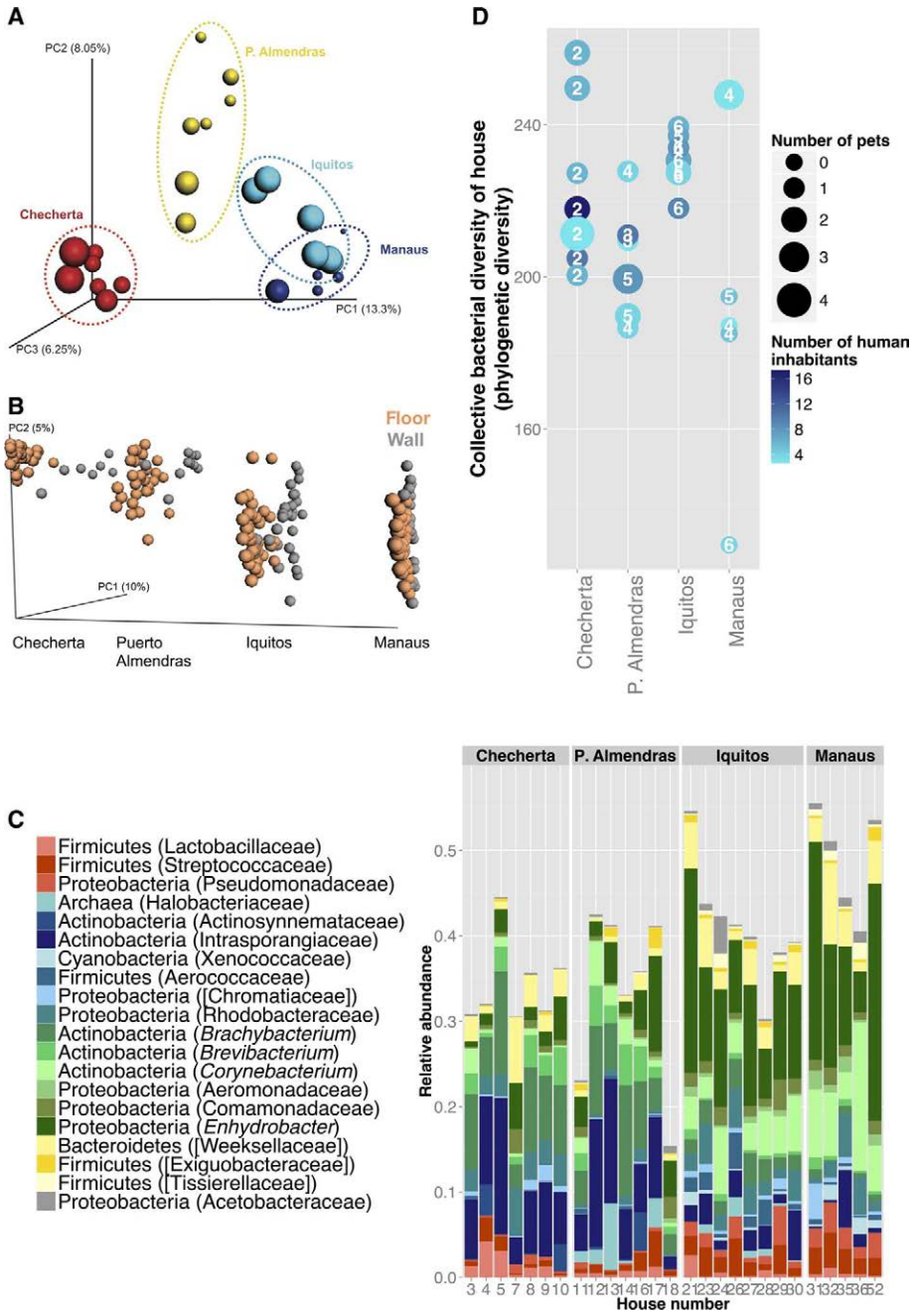


**Fig. 2. Microbial community structure in houses differs significantly across the urbanization gradient.** Seven sites that were common to all houses (living room, bedroom, kitchen floors, beds, chair handles, countertops, and living room walls) were collapsed into one sample to obtain a total measure of diversity for each home. (**A**) Principal coordinates analysis (PCoA) of the seven collapsed samples for each home shows tight clustering of the samples by community ($P < 0.01$, analysis of similarities). Point size shows the $\alpha$ diversity level, measured as phylogenetic diversity (PD) (smallest, <150; largest, >250). (**B**) PCoA plot of unweighted UniFrac distances of wall and floor bacterial communities by village. Floor samples are clustered very tightly in the jungle community, but not wall samples. This indicates that floor microbial communities resemble more to each other than wall samples. This clustering of floor samples decreases with urbanization, and microbial communities of walls and floors merge in urban locations, meaning that urban locations have similar microbes on the walls and floors, whereas in rural locations, floors have very different microbial communities. (**C**) Top 20 feature taxa of high relative abundance (>0.1%) that allowed for correct prediction of a sample's source community; these include taxa commonly associated with humans (for example, Streptococcaceae, Lactobacillaceae, and Pseudomonadaceae) (shown in red hues) and taxa commonly associated with the environment (for example, Intrasporangiaceae and Rhodobacteraceae) (shown in blue hues). Taxa shown in the literature to be associated with both the environment and the human body are shown in green hues. (**D**) Distribution of the collective $\alpha$ diversity (PD) of each home, colored by the number of human inhabitants residing in the home. Numbers inside the points indicate the number of different material types that are represented by the seven samples, and the size corresponds to the total number of pets in the home (dog, cat, monkey, chicken, turtle, or parrot).

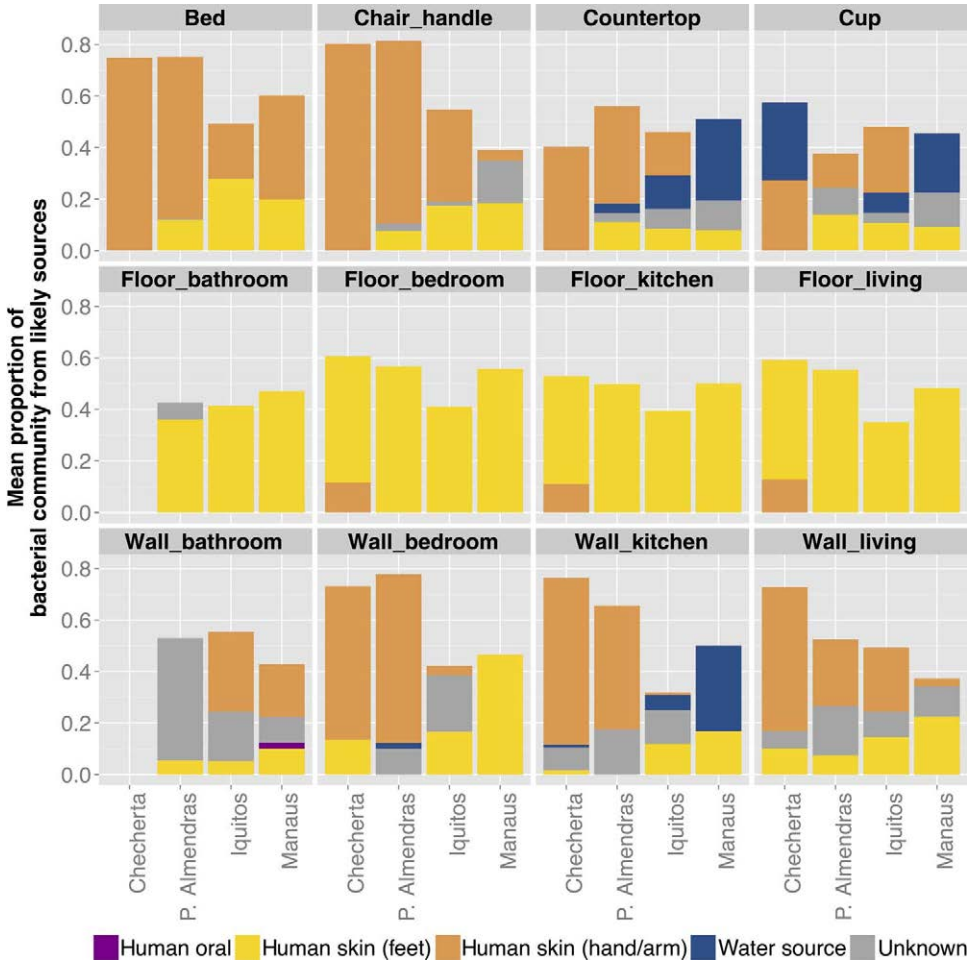


**Fig. 3. Source tracking indicates home sample's bacteria reflecting typical use.** For each home, the human oral and skin samples as well as a water source, such as a water bucket or faucet, were input as potential sources of microbes found in sites around the home. Values shown represent likely contributions from each of these sources, averaged across the homes in each community. All sites contain at least a considerable proportion of taxa that are also found on the skin of the home's inhabitants, with floors showing the highest levels of similarity.

house occupancy (persons per square meter) decreases with urbanization ($P < 0.005$; Fig. 1C and table S4), which is consistent with higher area and smaller families.

Remarkably, classification of house functional spaces using microbes was possible (Fig. 1D and fig. S4), and the probability of correct assignment given the wall bacterial composition increased with urbanization (Fig. 1E). We tested for differences in the types and diversity of household bacteria across locations. Microbial richness (α diversity) did not change with urbanization (Fig. 2 and figs. S5 and S6), but bacterial composition was markedly different (Fig. 2, A and B, and figs. S7 and S8) with houses becoming more microbially distinct along the gradient. Bacterial community structure in samples from floor and walls converged with urbanization (Fig. 2B). At the jungle end of the gradient, floors were made of dirt and people walked barefoot, and walls were wood columns; at the city end, floors and walls were made of synthetic materials, and people walked with shoes (in all but one house). Moreover, wall microbes better differentiated the kitchen and bathroom functional spaces in urban than in rural houses (Fig. 1D and fig. S9). The 10 most important operational taxonomic units (OTUs) that help discriminate among rooms in Manaus comprise several taxa normally associated with the human oral cavity, including *Streptococcus*, *Neisseria*, *Actinomyces*, and *Veillonella dispar*, as well as taxa normally associated with the human gut such as Enterobacteriaceae.

Despite lower occupant density in urban houses, "humanization" of the houses occurred with increased urbanization (Fig. 2D), associated with home enclosure—isolation from the outdoor environment—especially in dwellings sealed for air conditioning. Human bacteria were enriched in the town and city houses, with *Prevotella*, *Verrucomicrobia*, and *Serratia* on the walls (figs. S7 and S10), and skin taxa on the floors, consistent with human shedding (*7*, *10*–*12*) and with the isolation of homes from bacterial sources from outdoor environments. Environmental bacteria were proportionally higher in the jungle and rural village house floors and included soil bacteria [for example, *Mesorhizobium* and *Luteimonas* from water sources and *Rickettsiella* from arthropods (figs. S7 and S10)]. The environmental bacterium found in walls included *Acidobacteriales*, *Bradyrhizobium*, *Dactylosporangium*, *Actinomycetospora*, *Actinoalloteichus*, *Saccharopolyspora*, *Pedomicrobium*, and *Rickettsiella* (figs. S7 and S10). As we move from the rural to the urban locations, there is a shift within Actinobacteria,

from *Brachybacterium* and *Brevibacterium* commonly found in the environment to *Corynebacterium*, common in human skin (Fig. 2B).

A Bayesian approach called SourceTracker allowed the estimation of proportion of each community (that is, sample) that are likely to originate from each of a specified set of source environments (*9*). This analysis further confirmed the presence of a partially oral-like community on the urban bathroom walls (Fig. 3); these traces of human oral microbes from bathrooms and traces of water-associated microbes on kitchen countertops and walls likely contribute to the increased ability to identify both the houses and the indoor functional spaces.

We found no systematic association between the bacterial communities and many other parameters measured in the study including the structural materials in the households, number of people living in the house, number of pets (Fig. 2C), temperature variations, light incidence, frequency of cleaning, number of outsiders at sampling time, date of last rain, and time of day samples were collected ($P > 0.05$ in all cases). In particular, consistent with recent studies (*11*, *13*), we find that samples within a house with different materials are more similar to one another than samples from the same material across different houses and that, in all communities, the inhabitants of each house are a major source of bacteria (Fig. 3).

## DISCUSSION

Our findings indicate that the bacteria from the surfaces of house walls are informative of level of urbanization based on architectural design. Floors are the most informative of the commonalities found in individual houses across urbanization levels, whereas walls, less perturbed reservoirs of microbes accumulated through room usage, provide an indicator of room function.

Ventilation, described as a key factor for microbial community composition in urban settings (*14*–*16*), was very high in all of the houses of our study and does not explain differences in home microbial composition with urbanization. Instead, we propose that the presence of walls dividing functional spaces acquires function-dependent microbes, mostly of human origin.

The current study is limited to one geographical region of the world and is a small pilot study, and thus, results may not be generalizable. Further research should identify mechanistic explanations for these phenomena. Insights into the chemical signals that bacteria provide in different sites within the home are also needed. These remarkable changes in house microbial content across urbanization might translate into differences in microbial exposure that may have developmental health implications for humans (*17*), according to several related hypotheses [the "hygiene" hypothesis (*18*), the "Old Friends" hypothesis (*19*), and the "Disappearing microbiota" hypothesis (*20*)], suggesting that the reduced pattern of microbial exposure leads to immune and metabolic disorders that have become the new disease paradigm in the industrialized world.

## MATERIALS AND METHODS

### Design of the study

We selected four communities at the same latitude in the Amazon Basin, with different degrees of urbanization (fig. S1): an isolated jungle village, a rural community, an urban town, and an urban city. The specific locations were selected to represent four significantly different urbanization levels with similar climate. Ten houses from each location were sampled in four sites to characterize architectural and microbiological profiles of house walls and floors. The sample size of $n = 40$ per location was based on estimations using a two-sided test, for significant differences in the microbial composition, with a Cohen's $d = 0.63$, power of 80%, and $\alpha = 0.05$.

### Communities' description

Four human settings were studied in this work, spanning urbanization. Three of them were in Peru, and one in Brazil.

The Peruvian rural community of Checherta is a traditional, native, hunter-gatherer, Amerindian village in the border between Peru and Ecuador (fig. S1). It is inhabited by approximately 300 inhabitants, living in open huts, with the exception of one house that was enclosed from the outside by walls (fig. S11), made of natural materials (Fig. 1A and fig. S2). It has a recently made school consisting of one classroom and three adjacent latrines, which remain unused by the locals. Checherta has no electricity or potable water services; water is obtained from the nearest river, and the village is highly inaccessible, requiring travel by a plane that can land on an improvised landing field in Nuevo Andoas and then taking a 2-day trip on small river boats (table S1).

The second Peruvian community, Puerto Almendras, is a rural setting located at ~1-hour drive (12 km) west from Iquitos. It has ~250 inhabitants that live in houses with external walls, made out of both natural and industrial materials. Most of the houses were not internally subdivided, and those spaces that were remained connected with adjacent areas because the walls did not reach the roof. Puerto Almendras has a water reservoir (however, no potable water service), electricity service, a school, and a health care center within walking distance. Houses are distributed around a soccer field.

The third Peruvian community was the town of Iquitos, the world's biggest populated center that is inaccessible by road—it is accessible only by plane or boat (table S1). This town has 371,000 inhabitants, an international airport, paved roads, municipally treated piped water, and electricity. All houses are enclosed in external walls that separate them from the outdoor environment and are made of industrial materials. Walls that divide the inner house do not always reach the roof.

The fourth location was Manaus in Brazil, the biggest city in the Amazon region, with a population of 1.8 million, accessible by roads, boats, and planes. Sampled houses were completely separated from the environment and internally divided by walls. Unlike the Peruvian communities, this city has enormous social differences, and we sampled homes from middle class families.

### Architectural determinations

Sketches of the houses were created with measurements collected in the field, with photographs of each household (Fig. 1A and figs. S2 and S11), that provided the basis for estimations of floor area/surface, volume, openness (proportion of apertures, location in floor plans, and orientation), human density (number of people per square meter), and privacy index for each household. Additionally, this information sets the basis for modeling using a building modeling program (Autodesk Revit) to produce three-dimensional representations of each sampled house.

Environmental variables of temperature and relative humidity were collected. A HOBO Micro Station Data Logger (H21-002) was used to record 2-min interval data of temperature and relative humidity.

Analysis of qualitative data from both architecture and environmental variables was made using the SPSS version 20 program to compare variations in architecture and environment between locations.

### Bacterial community structure determinations

Microbial samples were collected (using sterile swabs) from floors and walls of living rooms, kitchens, bedrooms, and bathrooms—or equivalent functional spaces in jungle houses—of each household. Metadata information from each sample was recorded, including surface material, sample height (walls), cleaning frequency, presence of pets in the home, light, surface temperature, and whether people wore shoes. Shoes were worn in 36% of family members in Checherta, 75% in Puerto Almendras, and 100% in Iquitos and Manaus.

Cryovial-containing samples were frozen in a dry shipper and stored at −80°C until DNA was extracted using the MoBio PowerSoil Kit (following the manufacturer's instructions). The V3-V4 regions of the *16S rRNA* gene were sequenced using the HiSeq Illumina platform. Sequences were analyzed using the Qiime pipeline. Sequences were trimmed at 100 base pairs, and open-reference OTU picking (*21*) was performed at a 97% identity to assign taxonomy using Greengenes version 13_8 (*22*) and to characterize novel taxa. α Diversity was estimated using PD whole tree (*23*) on rarefied tables at 10,000 sequences per sample for floors and 2500 sequences per sample for walls. β Diversity was measured using unweighted UniFrac (*24*) on the rarefied tables. Finally, the Bayesian approach SourceTracker was used to identify possible sources of contamination (*9*).

## SUPPLEMENTARY MATERIALS

Supplementary material for this article is available at http://advances.sciencemag.org/cgi/content/full/2/2/e1501061/DC1

Fig. S1. Satellite view and urban plan of the communities selected for this study in the South American Amazonas.
Fig. S2. Typical house in the jungle community of Checherta.
Fig. S3. Distribution of privacy index on each location.
Fig. S4. UniFrac-based PCoA of microbial communities in the floors (A and B) and walls (C and D), colored by village (A and C) and by room (B and D).
Fig. S5. Bacterial α diversity calculated with the PD whole tree metric on floor and wall samples by location.
Fig. S6. Bacterial α diversity calculated with the PD whole tree metric on floor and wall samples by home site in each location.
Fig. S7. Taxonomic composition of floor and wall samples from each location.
Fig. S8. UniFrac distances of the microbial communities in floors and walls, and between and within locations.
Fig. S9. UniFrac-based PCoA of microbial communities in the walls of jungle (Checherta) and city (Manaus).
Fig. S10. Discriminative bacteria from each location based on an LDA effective size (LEfSe) analysis on floor and walls from all villages.
Fig. S11. Blueprint of a closed, segregated house from Checherta.
Table S1. Urban parameters of the four sampling sites for this study.
Table S2. Architectural qualitative descriptions of the studied settlements.
Table S3. Summary statistics for indoor temperature and relative humidity on the four locations at 1-min intervals.
Table S4. Architectural parameters for the studied settlements (averages and SDs).

## REFERENCES AND NOTES


1. J. N. Pieterse, *Globalization and Culture: Global Mélange* (Rowman & Littlefield, Lanham, MD, 2015).
2. P. Höppe, I. Martinac, Indoor climate and air quality—Review of current and future topics in the field of ISB study group 10. *Int. J. Biometeorol.* **42**, 1–7 (1998).
3. N. E. Klepeis, W. C. Nelson, W. R. Ott, J. P. Robinson, A. M. Tsang, P. Switzer, J. V. Behar, S. C. Hern, W. H. Engelmann, The National Human Activity Pattern Survey (NHAPS): A resource for assessing exposure to environmental pollutants. *J. Expo. Anal. Environ. Epidemiol.* **11**, 231–252 (2001).
4. G. E. Flores, S. T. Bates, J. G. Caporaso, C. L. Lauber, J. W. Leff, R. Knight, N. Fierer, Diversity, distribution and sources of bacteria in residential kitchens. *Environ. Microbiol.* **15**, 588–596 (2012).
5. G. E. Flores, S. T. Bates, D. Knights, C. L. Lauber, J. Stombaugh, R. Knight, N. Fierer, Microbial biogeography of public restroom surfaces. *PLOS One* **6**, e28132 (2011).
6. K. M. Hewitt, C. P. Gerba, S. L. Maxwell, S. T. Kelley, Office space bacterial abundance and diversity in three metropolitan areas. *PLOS One* **7**, e37849 (2012).
7. J. F. Meadow, S. W. Kembel, M. Moriyama, T. K. O'Connor, A. M. Womack, G. Z. Brown, J. L. Green, B. J. M. Bohannan, Bacterial communities on classroom surfaces vary with human contact. *Microbiome* **2**, 7 (2014).
8. K. E. Fujimura, C. C. Johnson, D. R. Ownby, M. J. Cox, E. L. Brodie, L. Havstad, E. M. Zoratti, K. J. Woodcroft, K. R. Bobbitt, G. Wegienka, H. A. Boushey, S. V. Lynch, Man's best friend? The effect of pet ownership on house dust microbial communities. *J. Allergy Clin. Immunol.* **126**, 410–412.e3 (2010).
9. D. Knights, J. Kuczynski, E. S. Charlson, J. Zaneveld, M. C. Mozer, R. G. Collman, F. D. Bushman, R. Knight, S. T. Kelley, Bayesian community-wide culture-independent microbial source tracking. *Nat. Methods* **8**, 761–763 (2011).
10. S. W. Kembel, J. F. Meadow, T. K. O'Connor, G. Mhuireach, D. Northcutt, J. Kline, M. Moriyama, G. Z. Brown, B. J. M. Bohannan, J. L. Green, Architectural design drives the biogeography of indoor bacterial communities. *PLOS One* **9**, e87093 (2014).
11. S. Lax, D. P. Smith, J. Hampton-Marcell, S. M. Owens, K. M. Handley, N. M. Scott, S. M. Gibbons, P. Larsen, B. D. Shogan, S. Weiss, J. L. Metcalf, L. K. Ursell, Y. Vázquez-Baeza, W. Van Treuren, N. A. Hasan, M. K. Gibson, R. Colwell, G. Dantas, R. Knight, J. A. Gilbert, Longitudinal analysis of microbial interaction between humans and the indoor environment. *Science* **345**, 1048–1052 (2014).
12. J. F. Meadow, A. E. Altrichter, A. C. Bateman, J. Stenson, G. Z. Brown, J. L. Green, B. J. M. Bohannan, Humans differ in their personal microbial cloud. *PeerJ* **3**, e1258 (2015).
13. R. R. Dunn, N. Fierer, J. B. Henley, J. W. Leff, H. L. Menninger, Home life: Factors structuring the bacterial diversity found within and between homes. *PLOS One* **8**, e64133 (2013).
14. M. Frankel, G. Bekö, M. Timm, S. Gustavsen, E. W. Hansen, A. M. Madsena, Seasonal variations of indoor microbial exposures and their relation to temperature, relative humidity, and air exchange rate. *Appl. Environ. Microbiol.* **78**, 8289–8297 (2012).
15. J. F. Meadow, A. E. Altrichter, S. W. Kembel, J. Kline, G. Mhuiraech, M. Moriyama, D. Northcutt, T. K. O'Connor, A. M. Womack, G. Z. Brown, J. L. Green, B. J. M. Bohannan, Indoor airborne bacterial communities are influenced by ventilation, occupancy, and outdoor air source. *Indoor Air* **24**, 41–48 (2014).
16. S. W. Kembel, E. Jones, J. Kline, D. Northcutt, J. Stenson, A. M. Womack, B. J. M. Bohannan, G. Z. Brown, J. L. Green, Architectural design influences the diversity and structure of the built environment microbiome. *ISME J.* **6**, 1469–1479 (2012).
17. J. C. Clemente, E. C. Pehrsson, M. J. Blaser, K. Sandhu, Z. Gao, B. Wang, M. Magris, G. Hidalgo, M. Contreras, Ó. Noya-Alarcón, O. Lander, J. McDonald, M. Cox, J. Walter, P. L. Oh, J. F. Ruiz, S. Rodriguez, N. Shen, S. J. Song, J. Metcalf, R. Knight, G. Dantas, M. G. Dominguez-Bello, The microbiome of uncontacted Amerindians. *Sci. Adv.* **1**, e1500183 (2015).
18. D. P. Strachan, Hay fever, hygiene, and household size. *BMJ* **299**, 1259–1260 (1989).
19. G. A. W. Rook, Review series on helminths, immune modulation and the hygiene hypothesis: The broader implications of the hygiene hypothesis. *Immunology* **126**, 3–11 (2009).
20. M. J. Blaser, S. Falkow, What are the consequences of the disappearing human microbiota? *Nat. Rev. Microbiol.* **7**, 887–894 (2009).
21. J. R. Rideout, Y. He, J. A. Navas-Molina, W. A. Walters, L. K. Ursell, S. M. Gibbons, J. Chase, D. McDonald, A. Gonzalez, A. Robbins-Pianka, J. C. Clemente, J. A. Gilbert, S. M. Huse, H.-W. Zhou, R. Knight, J. G. Caporaso, Subsampled open-reference clustering creates consistent, comprehensive OTU definitions and scales to billions of sequences. *PeerJ* **2**, e545 (2014).
22. D. McDonald, M. N. Price, J. Goodrich, E. P. Nawrocki, T. Z. DeSantis, A. Probst, G. L. Andersen, R. Knight, P. Hugenholtz, An improved Greengenes taxonomy with explicit ranks for ecological and evolutionary analyses of bacteria and archaea. *ISME J.* **6**, 610–618 (2012).
23. D. P. Faith, A. M. Baker, Phylogenetic diversity (PD) and biodiversity conservation: Some bioinformatics challenges. *Evol. Bioinform. Online* **2**, 121–128 (2006).
24. C. Lozupone, R. Knight, UniFrac: A new phylogenetic method for comparing microbial communities. *Appl. Environ. Microbiol.* **71**, 8228–8235 (2005).


**Acknowledgments:** We acknowledge the collaborators in Peru, the interpreter J. J. Semu, and the late Father Luigi for being a source of information and inspiration. In Manaus, we had the valuable help of A. Vasconcelos and J. Machado with the fieldwork. **Funding:** This work was supported by the Sloan Foundation, the C&D Fund, and the Emch Fund for Microbial Diversity (to M.G.D.-B.). Partial support was also provided by the NIH Research Initiative for Scientific

Enhancement Program 2R25GM061151-13 (to J.F.R.-C.). **Author contributions:** M.G.D.-B. and R.K. designed the study. J.F.R.-C., H.C., A.N., J.N.H., R.R., O.H.B., H.P., L.C.P., M.J.B., and M.G.D.-B. collected the data and processed the specimens. J.F.R.-C., S.J.S., R.K., H.C., L.R.P., and M.G.D.-B. analyzed the data. M.G.D.B., J.F.R.-C., H.C., S.J.S., and R.K. drafted the manuscript. All authors reviewed the final manuscript. **Competing interests:** The authors declare that they have no competing interests. **Data and materials availability:** All data needed to evaluate the conclusions in the paper are present in the paper and/or the Supplementary Materials. Additional data related to this paper may be requested from the authors and/or http://qiita.ucsd.edu/study/description/10333.

Submitted 7 August 2015
Accepted 29 November 2015
Published 12 February 2016
10.1126/sciadv.1501061

**Citation:** J. F. Ruiz-Calderon, H. Cavallin, S. J. Song, A. Novoselac, L. R. Pericchi, J. N. Hernandez, R. Rios, O. H. Branch, H. Pereira, L. C. Paulino, M. J. Blaser, R. Knight, M. G. Dominguez-Bello, Walls talk: Microbial biogeography of homes spanning urbanization. *Sci. Adv.* **2**, e1501061 (2016).

MALARIA

# Single-cell RNA-seq and computational analysis using temporal mixture modeling resolves $T_H1/T_{FH}$ fate bifurcation in malaria



Tapio Lönnberg,[1,2]* Valentine Svensson,[1]* Kylie R. James,[3]* Daniel Fernandez-Ruiz,[4] Ismail Sebina,[3] Ruddy Montandon,[2] Megan S. F. Soon,[3] Lily G. Fogg,[3] Arya Sheela Nair,[3] Urijah N. Liligeto,[3] Michael J. T. Stubbington,[1,2] Lam-Ha Ly,[2] Frederik Otzen Bagger,[1,2,5,6] Max Zwiessele,[7] Neil D. Lawrence,[7] Fernando Souza-Fonseca-Guimaraes,[3] Patrick T. Bunn,[3] Christian R. Engwerda,[3] William R. Heath,[4,8] Oliver Billker,[2] Oliver Stegle,[1†‡] Ashraful Haque,[3†‡] Sarah A. Teichmann[1,2†‡]

**Differentiation of naïve $CD4^+$ T cells into functionally distinct T helper ($T_H$) subsets is crucial for the orchestration of immune responses. Because of extensive heterogeneity and multiple overlapping transcriptional programs in differentiating T cell populations, this process has remained a challenge for systematic dissection in vivo. By using single-cell transcriptomics and computational analysis with a temporal mixtures of Gaussian processes model, termed GPfates, we reconstructed the developmental trajectories of $T_H1$ and $T_{FH}$ (T follicular helper) cells during blood-stage *Plasmodium* infection in mice. By tracking clonality using endogenous T cell receptor sequences, we first demonstrated that $T_H1/T_{FH}$ bifurcation had occurred at both population and single-clone levels. Next, we identified genes whose expression was associated with $T_H1$ or $T_{FH}$ fates and demonstrated a T cell–intrinsic role for Galectin-1 in supporting $T_H1$ differentiation. We also revealed the close molecular relationship between $T_H1$ and interleukin-10–producing Tr1 cells in this infection. $T_H1$ and $T_{FH}$ fates emerged from a highly proliferative precursor that up-regulated aerobic glycolysis and accelerated cell cycling as cytokine expression began. Dynamic gene expression of chemokine receptors around bifurcation predicted roles for cell-cell interaction in driving $T_H1/T_{FH}$ fates. In particular, we found that precursor $T_H$ cells were coached toward a $T_H1$ but not a $T_{FH}$ fate by inflammatory monocytes. Thus, by integrating genomic and computational approaches, our study has provided two unique resources: a database, www.PlasmoTH.org, which facilitates discovery of novel factors controlling $T_H1/T_{FH}$ fate commitment, and, more generally, GPfates, a modeling framework for characterizing cell differentiation toward multiple fates.**

## INTRODUCTION

$CD4^+$ T cells are key instructors of the immune system. They can display extensive phenotypic and functional diversity by differentiating into a range of T helper ($T_H$) subsets, including $T_H1$, $T_H2$, $T_H17$, $T_{FH}$ (T follicular helper), $T_H22$, $T_{reg}$ (T regulatory), and $T_H9$ cells, that are distinguished mainly by cytokine and transcription factor expression profiles. Because $T_H$ cells can control infections and drive immune-mediated diseases, there remains tremendous interest in the molecular mechanisms that mediate their in vivo differentiation.

Malaria, caused by the protozoan parasite *Plasmodium*, afflicted 212 million humans in 2015 (*1*). Both $T_H1$ responses (*2*) and $T_{FH}$-dependent antibody responses (*3*) can independently protect against malaria and are elicited simultaneously in malaria-infected individuals (*4*), as well as in mice challenged with rodent-infective strains, such as *Plasmodium chabaudi chabaudi* AS (*Pc*AS) (*5*). However, the molecular relationships between $T_H1$ and $T_{FH}$ cells remain unclear during *Plasmodium* infection and, more generally, during any immune challenge. A recent study has demonstrated that the unique T cell receptor (TCR) of a naïve $CD4^+$ T cell imparted a strong preference for either a $T_H1$ or a $T_{FH}$ fate (*6*). Nevertheless, for many clones, both fates could still emerge, implying that other mechanisms, such as internal stochasticity and cell-extrinsic factors, also govern fate choices in vivo. Transcription factors including T-bet, Gata3, RORγT, and Bcl6 have been reported to drive and stabilize $T_H$ fates, leading to their characterization as "lineage-defining" molecules. This has tended to present $T_H$ differentiation as a choice between mutually exclusive linear pathways. However, transient coexpression of these transcription factors (for example, of Bcl6/T-bet and Foxp3/RORγT) suggests that overlapping intermediate $T_H$ states also exist in vivo. Moreover, substantial heterogeneity occurs in the kinetics of $CD4^+$ T cell responses, resulting in a complex mixture of intermediate states during differentiation, which is not easily resolved via assessment of a small number of molecules.

Conventional dendritic cells (cDCs) are the dominant initial source of antigenic signaling to naïve $CD4^+$ T cells in secondary lymphoid tissues, for example, in the spleens of *Plasmodium*-infected mice (*7*). In other models, it was shown that cDCs made long-lasting stable contacts with naïve $CD4^+$ T cells to initiate priming (*8*). Once activated, $CD4^+$ T cells regained motility, permitting further cellular interactions. Consistent with this observation, activated $CD4^+$ T cells required further

[1]European Molecular Biology Laboratory, European Bioinformatics Institute, Wellcome Genome Campus, Hinxton, Cambridge, U.K. [2]Wellcome Trust Sanger Institute, Wellcome Genome Campus, Hinxton, Cambridge, U.K. [3]QIMR Berghofer Medical Research Institute, Herston, Brisbane, Queensland, Australia. [4]Department of Microbiology and Immunology, Peter Doherty Institute, University of Melbourne, Parkville, Victoria, Australia. [5]Department of Haematology, University of Cambridge, Cambridge Biomedical Campus, Cambridge, U.K. [6]National Health Service Blood and Transplant, Cambridge Biomedical Campus, Long Road, Cambridge, U.K. [7]Department of Computer Science, University of Sheffield, Sheffield, U.K. [8]Australian Research Council Centre of Excellence in Advanced Molecular Imaging, University of Melbourne, Parkville, Victoria, Australia.
*These authors contributed equally to this work.
†These authors contributed equally to this work.
‡Corresponding author. Email: st9@sanger.ac.uk (S.A.T.); ashraful.haque@qimrberghofer.edu.au (A.H.); stegle@ebi.ac.uk (O.S.)

antigenic stimulation to optimize clonal expansion and $T_H$ differentiation (*9*); cDCs were considered the most likely candidates (*8*, *10*), with other cell types remaining less explored. Studies of mice with altered monocytic responses suggested roles for these cells in $CD4^+$ T cell priming, specifically in tissues with few cDCs (*11*). Other reports used cDC deficiency to illustrate that monocytes could activate naive $CD4^+$ T cells (*12*). However, few in vivo studies have explored roles for monocytes in $T_H$ differentiation, where cDC responses remain intact.

Here, we used single-cell RNA sequencing (scRNA-seq) to study *Plasmodium*-specific TCR transgenic $CD4^+$ T (PbTII) cells during blood-stage *Pc*AS infection in mice. We then used a computational modeling strategy to reconstruct the molecular trajectories of $T_H1$ and $T_{FH}$ cells. Last, we investigated cell-cell interactions based on dynamic expression of chemokines and their receptors, and examined roles for inflammatory monocytes in supporting activated $CD4^+$ T cells toward a $T_H$ fate.

## RESULTS

### scRNA-seq resolves $T_H1$ and $T_{FH}$ cell fates during *Plasmodium* infection in mice

We used scRNA-seq to elucidate the development and heterogeneity of $T_H1$ and $T_{FH}$ cells during *Pc*AS infection (Fig. 1A and fig. S1). We transferred naïve, proliferative dye-labeled PbTII cells into congenic wild-type mice and recovered them at days 2, 3, 4, and 7 after infection by cell-sorting those expressing the early activation marker CD69 or displaying dilution of the proliferative dye (fig. S2). Flow cytometric measurements of the canonical $T_H1$ markers T-bet (coded by *Tbx21*) and interferon-γ (IFNγ) and $T_{FH}$ markers CXCR5 and Bcl6 indicated that these subsets emerged in parallel by day 7 after infection (Fig. 1, B to D, and fig. S3) (*13*, *14*). Notably, markers of $T_H2$, $T_H17$, or $T_{reg}$ subsets were not up-regulated by PbTII cells (fig. S4).

Initially, we used principal components analysis (PCA) to explore the overall transcriptomic landscape of the PbTII cells (fig. S5A). The top principal components were strongly associated with the number of detected unique transcripts [reflective of mRNA content and proliferative status (fig. S5B)] and differentiation (figs. S5C to S7 and table S1). As expected, the variability related to previously established $T_H1$ and $T_{FH}$ gene expression signatures became more prominent with time, separating two subpopulations at day 7 (Fig. 1, E and F) (*15*). Together, these results suggested a progressive commitment to

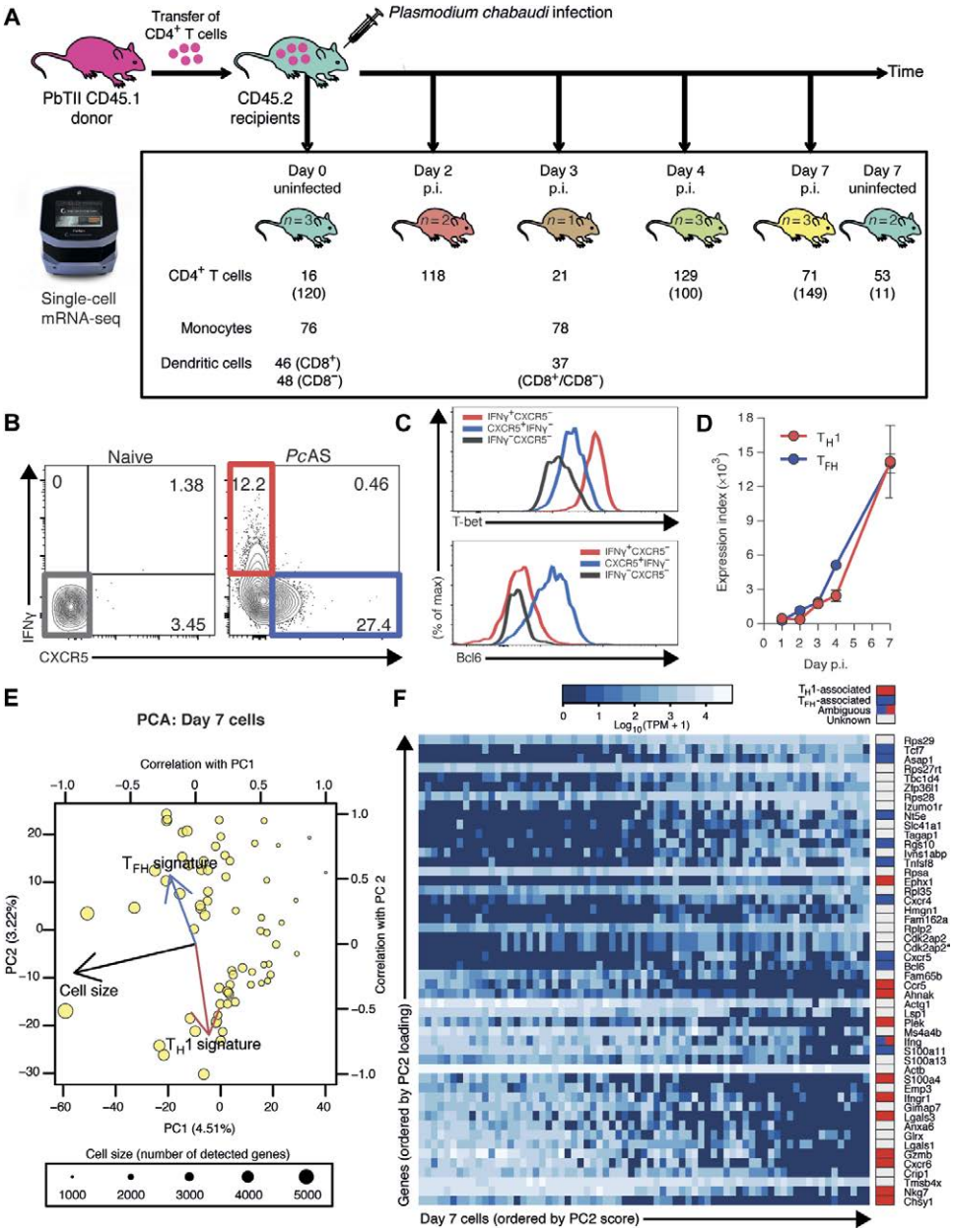


**Fig. 1. Single-cell mRNA sequencing of PbTII cells.** (**A**) PbTII cells were transferred from a single donor to multiple recipients. The numbers denote single cells from which mRNA-sequencing (mRNA-seq) data were successfully recorded. Numbers in parentheses refer to the replicate experiment presented in fig. S12. (**B** and **C**) Representative fluorescence-activated cell sorting (FACS) plots showing bifurcation of splenic $T_H1$ ($T\text{-bet}^+IFN\gamma^+$) and $T_{FH}$ ($Bcl6^+CXCR5^+$) PbTII $CD4^+$ T cells at day 7 post-infection (p.i.) with *Pc*AS. (**D**) Flow cytometry data indicate concurrent differentiation of $T_H1$ ($IFN\gamma^+$) and $T_{FH}$ ($CXCR5^+$) PbTII $CD4^+$ T cells within the spleen of *Pc*AS-infected mice ($n = 4$). Index expression is the product of mean fluorescence intensity and proportion $IFN\gamma^+$ or $CXCR5^+$. Data are representative of two independent experiments. (**E**) PCA of single PbTII cells at day 7 after infection with *Pc*AS. The arrows represent Pearson correlation with PC1 and PC2. Cell size refers to the number of detected genes. "$T_H1$ signature" and "$T_{FH}$ signature" refer to cumulative expression of genes associated with $T_H1$ or $T_{FH}$ phenotypes [total transcripts per million (TPM) of all genes in the set] (*15*). (**F**) Expression levels of the leading 50 genes with the largest PC2 loadings at day 7 (D). Genes were annotated as either $T_H1$- or $T_{FH}$-associated on the basis of public data sets (*15*, *37*, *44*, *47*). **Cdk2ap2* appears twice because two alternative genomic annotations exist.

$T_H1$ and $T_{FH}$ fates, and indicated that single-cell transcriptomes could be used for estimating both proliferative states and degrees of differentiation of individual cells.

### Delineation of $T_H1$ and $T_{FH}$ trajectories using a Mixture of Gaussian Processes model

The results from the PCA suggested that variation in PbTII transcriptomes could be used to reconstruct the transcriptional programs that are underlying the $T_H1$ and $T_{FH}$ differentiation. To more explicitly model the temporal dynamics of this differentiation process, we developed GPfates, a temporal mixture model that builds on the Gaussian Process Latent Variable Model (*16*) and Overlapping Mixtures of Gaussian Processes (OMGP) (*17*). Briefly, this approach is based on first reconstructing the differentiation trajectory from the observed data ("pseudotime," Fig. 2, A and B), thereby establishing an order for the cells. Although our model uses the sample time as prior information, the inferred orderings did not strictly adhere to the experimental time points (fig. S8). For example, cells from day 4 after infection were mixed with some of the cells from days 3 and 7 at either end of the day 4 pseudotime distribution. This result is consistent with the idea that bulk assessments of cells at specific time points fail to account for the heterogeneity and differential kinetics of responses made by single cells. To assess the robustness of the established ordering, we repeated this analysis without supplying the experimental sampling times to the model, finding overall consistent results (Comp. Supp. Fig. 8).

In a second step, GPfates uses the inferred temporal orders as input for a nonparametric time series mixture model [OMGP (*17*)]. This approach revealed two simultaneous trends emerging during pseudotime (Fig. 2, C and D), which separated from each other, indicating that a developmental bifurcation occurred.

In a third step, GPfates uses a change point model (section 4.2 of Supplementary Computational Methods), thereby facilitating to annotate pseudotime after bifurcation. The cell fate split appeared to initiate among early day 4 post-infection cells (in pseudotime; Fig. 2, C and D), an inference that was robust when using bootstrapped subsets of cells (section 6.2 of Supplementary Computational Methods).

We found that differentially expressed genes between the identified trajectories agreed with known $T_H1/T_{FH}$ signature genes (Fig. 3, A and B, and fig. S9) (*15*), strongly suggesting that the fitted mixture components corresponded to cells with $T_H1$ and $T_{FH}$ phenotypes. Notably, these bifurcation trends could not be identified by other published methods for reconstructing bifurcating single-cell trajectories (Comp. Supp. Fig. 14) (*18*–*22*). We also successfully applied GPfates to resolve bifurcation events in other published data sets (Comp. Supp. Figs. 11 and 12) (*23*, *24*), suggesting that our approach is more generally applicable for studying cellular differentiation using scRNA-seq data.

### Lineage barcoding using endogenous TCR sequences reveals $T_H1/T_{FH}$ bifurcation from single $CD4^+$ T cells

Although the TCR transgenic approach used in this study minimized the influence of TCR sequence variability on cell fate determination (*6*), the strain was *Rag*-sufficient, thus retaining potential for expression of diverse endogenous TCR chains, in addition to the transgenic TCR. Sequence analysis of TCR transcripts in single PbTII cells confirmed universal expression of the PbTII Vα2 and Vβ12 chains (tables S2 and S3), as well as highly diverse, though lower, levels of expression of endogenous TCRα chains in many cells (fig. S10). *Rag*-sufficient PbTII cells differentiated as effectively as $Rag1^{-/-}$ PbTII cells into both $T_H1$ and $T_{FH}$ cells (fig. S11), indicating that endogenous TCR sequences had not influenced $T_H$ fate bifurcation.

Given the vast combinatorial diversity of the endogenous TCR sequences, we used these as unique molecular barcodes to identify ancestrally related PbTII clones. We identified six clones comprising multiple sibling cells. Of these, two consisted of sibling cells that mapped close to the bifurcation point. For the remaining four clones, siblings exhibited highly diverging patterns of differentiation, with three sibling pairs falling at the extremities of the $T_H1$-$T_{FH}$ phenotype spectrum (Fig. 3C). These results demonstrated that $T_H1/T_{FH}$ bifurcation had occurred at both population and single-clone levels in our system, with the progeny of a single cell populating both $T_H1$ and $T_{FH}$ compartments.

### Transcriptional signatures associated with bifurcation of $T_H1$ and $T_{FH}$ fates

Next, we sought to identify genes whose expression differed between the $T_H1$ and $T_{FH}$ branches. We derived a bifurcation statistic to estimate the concordance with bifurcation for individual genes (see section 4.2 of Supplementary Computational Methods for details and Fig. 3D). Among the highest-ranking genes, the most common pattern was up-regulation along the $T_H1$ branch (Fig. 3D). This suggested that $T_{FH}$ cells were developmentally closer to the shared progenitor state than $T_H1$ cells, because the $T_H1$ fate involved up-regulation of numerous genes not expressed in either the progenitor or $T_{FH}$ states.

To validate the robustness of these gene signatures and the timing of the bifurcation, we repeated the infection and, at days 0, 4, and 7, sequenced additional PbTII cells using the Smart-seq2 protocol (Fig. 1A and fig. S12A). A nonlinear dimensionality reduction indicated that the single cells from both experiments populated similar transcriptional landscapes (fig. S12B) and that the subset characteristic coexpression patterns of the bifurcating genes identified by GPfates emerged by day 7 (fig. S12C). Notably, the day 7 cells from each mouse could be separated into distinct $T_H1$ and $T_{FH}$ subpopulations using the top bifurcating genes (fig. S12D). These results indicated that the bifurcation-associated gene expression patterns were reproducible across experiments and sequencing platforms.

The highest-ranking transcription factors for the bifurcation included *Tcf7* for the $T_{FH}$ fate and *Id2* for the $T_H1$ fate (Fig. 3, D and E). *Tcf7* is required for T cell development and has been recently shown to be instrumental for $T_{FH}$ differentiation (*25*, *26*). It also represented one of the rare genes defined by a decrease in expression when moving toward the $T_H1$ fate. *Id2* is an antagonist of *Tcf7* and was recently identified as a key driver of $T_H1$ responses (*27*). As expected, the hallmark $T_{FH}$ transcription factor *Bcl6* was also strongly associated with the $T_{FH}$ fate. In $T_H1$ cells, many bifurcating genes encoded immune-related receptors (Fig. 3, D and E), such as *Cxcr6* (fig. S13, A and B), *Ifngr1*, and *S1pr1*, which mediate egress from secondary lymphoid organs. This was consistent with the notion that $T_H1$ cells can migrate to peripheral tissues and remain receptive to external signals. In contrast, the only bifurcating chemokine receptor associated with a $T_{FH}$ fate was *Cxcr5*, which is important for trafficking into B cell follicles (*28*).

Many of the bifurcating genes had no known role in $T_H$ differentiation. For example, *lgals1* (encoding Galectin-1), a molecule generally implicated in cDC (*29*) and $T_{reg}$ function (*30*), was unexpectedly up-regulated in PbTII cells around bifurcation and maintained along the $T_H1$ but not the $T_{FH}$ trajectory (fig. S14A). This observation was confirmed at the protein level (fig. S14B). Next, comparison of $T_H1/T_{FH}$ fates in cotransferred wild-type and $lgals1^{-/-}$ PbTII cells during *Pc*AS infection (fig. S14C) revealed a specific role for Galectin-1 in supporting

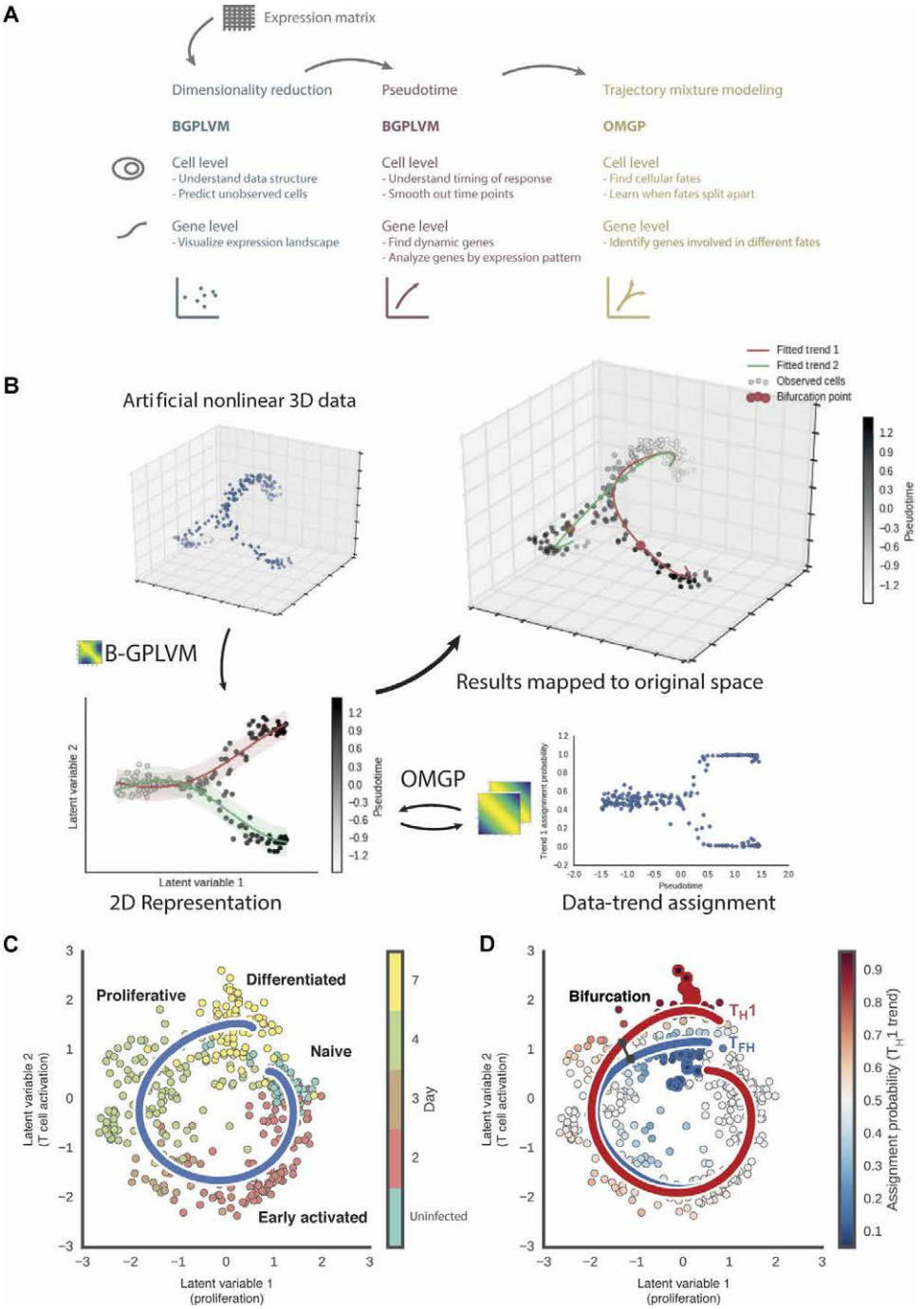


**Fig. 2. GPfates modeling of bifurcation processes using scRNA-seq data.** (**A**) Overview of the analysis workflow that underlies GPfates, consisting of dimensionality reduction of high-dimensional single-cell transcriptomes (left), inference of a pseudotemporal ordering of the cells (middle), and the reconstruction of trajectories using temporal mixture modeling (right). These individual steps build on models derived using the Gaussian process framework. Once fitted, GPfates enables for different downstream analyses, including cell orderings, bifurcation time point estimates, and inference of the genes that drive bifurcation events. (**B**) Illustration of intermediate results obtained from GPfates. Left: A low-dimensional representation, as well as a pseudotemporal ordering of the cells, is inferred using a nonlinear dimensionality reduction (Gaussian Process Latent Variable Model). Temporal trajectories and bifurcations are then reconstructed using a temporal mixture model (Overlapping Mixture of Gaussian Processes), with data-trend assignments per cell. B-GPLVM, Bayesian Gaussian Process Latent Variable Model; 3D, three-dimensional. (**C**) Low-dimensional representation (2D) of the complete data sets (408 single-cell transcriptomes). The blue line depicts the inferred progression of pseudotime. Text labels illustrate features typical of cells in the corresponding pseudotime region. (**D**) Inference of two simultaneous trends based on the pseudotime using the temporal mixture model.

$T_H1$ but not $T_{FH}$ fate (fig. S14D). Together, these data illustrate the potential for the GPfates model to enable identification of factors controlling $T_H1$ and $T_{FH}$ fates. Further examination of bifurcating genes is facilitated by an online database (www.PlasmoTH.org) accompanying this paper (Fig. 3F).

Coinciding with $T_H1/T_{FH}$ differentiation, we also noted up-regulation of *Il10* particularly in the $T_H1$ branch (fig. S15A). Most of the *Il10*-expressing cells also expressed *Ifng* at equal or higher levels as those expressing *Ifng* alone (fig. S15, B and C). These data revealed the development of Tr1 cells, defined as interleukin-10 (IL-10)/IFNγ–coexpressing $CD4^+$ T cells. Given that *Il10* expression was associated with the $T_H1$ branch, this suggested that Tr1 cells were developmentally related to $T_H1$ cells. Unexpectedly, we found that aside from *Il10*, only two genes, *Trib2* and *BC017643*, were differentially expressed between *Il10*/*Ifng*-coexpressing Tr1 cells and *Ifng*-expressing $T_H1$ cells (fig. S15D). Furthermore, a comparison of gene expression frequencies between Tr1 and $T_H1$ cells revealed a substantial degree of similarity across the genome (fig. S15E). Together, these data strongly suggest that Tr1 cells derive directly from $T_H1$ cells during blood-stage *Plasmodium* infection.

## Pseudotemporal relationships between cell cycling, aerobic glycolysis, and cytokine expression

Clonal expansion, increased aerobic glycolysis, and cytokine expression are hallmarks of $T_H$ cell development whose temporal relationships with each other remain to be fully resolved in vivo. We noted that PbTII cells became highly proliferative around bifurcation, as shown by the up-regulation of *Mki67* (Fig. 4, A and B, and fig. S16A) and other known proliferation marker genes (fig. S16B) (*31*). This correlated with cell cycle activity, as inferred from the scRNA-seq data using the Cyclone tool, and confirmed by flow cytometric measurements of DNA content and cell size (Fig. 4, C and D, and fig. S16C). On day 4 after infection, the cells also increased expression of genes associated with aerobic glycolysis but not oxidative phosphorylation (Fig. 4F), an indication of increased metabolic requirements being met by glucose metabolism and increased mammalian target of rapamycin complex 1 (mTORC1) activity. Consistent with this was the observed

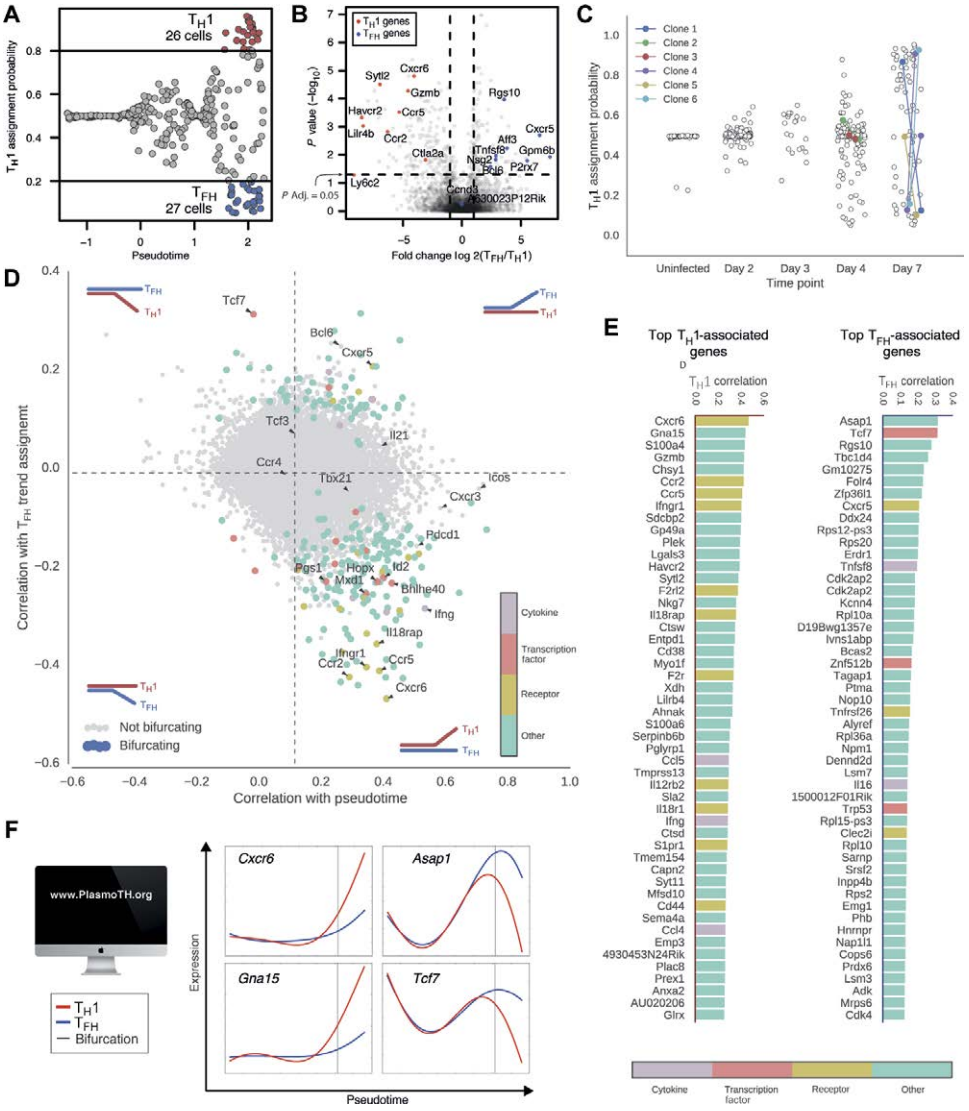


**Fig. 3. The relationship of known $T_H1$ and $T_{FH}$ transcriptomic signatures and the GPfates trajectories.** (**A**) $T_H1$ and $T_{FH}$ assignment probabilities of individual cells. For differential expression analysis (B), $T_H1$ and $T_{FH}$ were defined as cells with assignment probability of ≥0.8 for the respective trend. (**B**) Differential expression patterns between cells assigned to $T_H1$ and $T_{FH}$ states. Fold differences (*x* axis) and the corresponding adjusted *P* value (*y* axis) of differential expression for expressed genes (in at least 20% of cells) are shown. Statistical significance was determined using Wilcoxon rank sum test, with Benjamini and Hochberg correction for multiple testing. The horizontal and vertical dashed lines denote adjusted *P* value of 0.05 and twofold change, respectively. (**C**) Parallel $T_H1$ and $T_{FH}$ differentiation within cells of a single $CD4^+$ T cell clone. Colors correspond to individual clones determined by sequence analysis of endogenous TCR genes (tables S2 and S3). (**D**) Identification of genes associated with $T_H1$ and $T_{FH}$ trajectories. For each gene, the expression correlation with pseudotime (*x* axis) versus the correlation with the $T_{FH}$ trend assignment (*y* axis) is shown. Gene relevance was determined using the bifurcation statistic (Materials and Methods, fig. S9C). The top 248 bifurcating genes, with bifurcation statistic >49, are represented in colors according to the functional classification of the genes (Supplementary Materials and Methods and table S4). (**E**) Genes with the strongest association with $T_H1$ or $T_{FH}$ differentiation, filtered using the bifurcation score as in (D). The genes are ranked in descending order of association with the respective trend. *Cdk2ap2* appears twice because of alternative genomic annotations. (**F**) Web address for GPfates database, where the expression kinetics of genes of interest can be visualized. Examples illustrate the top-ranking bifurcating genes from (E).

elevated levels of ribosomal protein S6 phosphorylation on day 4 after infection (Fig. 4E).

By day 4 after infection, PbTII cells had gone through several rounds of cell division with differing kinetics and with some cells expressing IFNγ. By comparing *Ifng*-expressing and nonexpressing cells on day 4 after infection, we noted that early *Ifng*-expressing cells cycled faster and expressed aerobic glycolysis genes more highly than non–cytokine-expressing counterparts (Fig. 4G). Together, our data suggest that around bifurcation, PbTII cells exhibited a highly proliferative and metabolically active state, with those cells cycling fastest and exhibiting most glycolytic activity being the first to acquire the capacity to secrete IFNγ.

## Gene dynamics identifies potential decision-making molecules

To elucidate how PbTII cells transitioned from the proliferative precursor state to $T_H1$ and $T_{FH}$ fates, we sought to resolve the hierarchy of gene expression before and during cell fate bifurcation. In addition to genes directly following the bifurcation trend, we reasoned that expression of genes encoding key decision-making molecules might also be likely to be dynamic and peak before the bifurcation. First, to identify these, we selected those genes displaying interesting nonlinear trends in their expression patterns over pseudotime by Gaussian Process regression. This was achieved via a *D* statistic (model likelihood ratio), where each gene's expression pattern over pseudotime was tested for variation unexplained by random noise (*32*). On the basis of the *D* statistic (>50.0, Fig. 5C), we identified 2061 dynamic genes (Fig. 5A). Second, we ordered these genes according to their peak expression time to provide a temporal overview (Fig. 5A) and noted that a substantial fraction of them peaked around bifurcation. These included the $T_H1$-driving genes *Tbx21*, *Il2ra*, and *Il2rb*, supporting our initial hypothesis. Moreover, cells around bifurcation also transcribed the highest number of genes compared with those at all other points in pseudotime (Fig. 5B).

This model also infers the length-scale of the dynamic model, namely, the degree of fast-acting behavior over pseudotime (Fig. 5C). Using this additional feature, we noted roughly equivalent dynamics for *Tbx21*, *Il2ra*, and *Il2rb*. Furthermore, we noted similar dynamics, though with slightly later peak times, for the chemokine receptors *Cxcr5* and *Cxcr3*. Closer examination of all chemokine receptor genes also revealed peak expression around bifurcation for *Ccr4* but not others (fig. S17). Given that *Cxcr5* and *Cxcr3* have been associated with $T_{FH}$ and $T_H1$ cells, respectively (*10*, *33*, *34*), and because they exhibited similar dynamics, we hypothesized that these were competing receptors that directly influenced

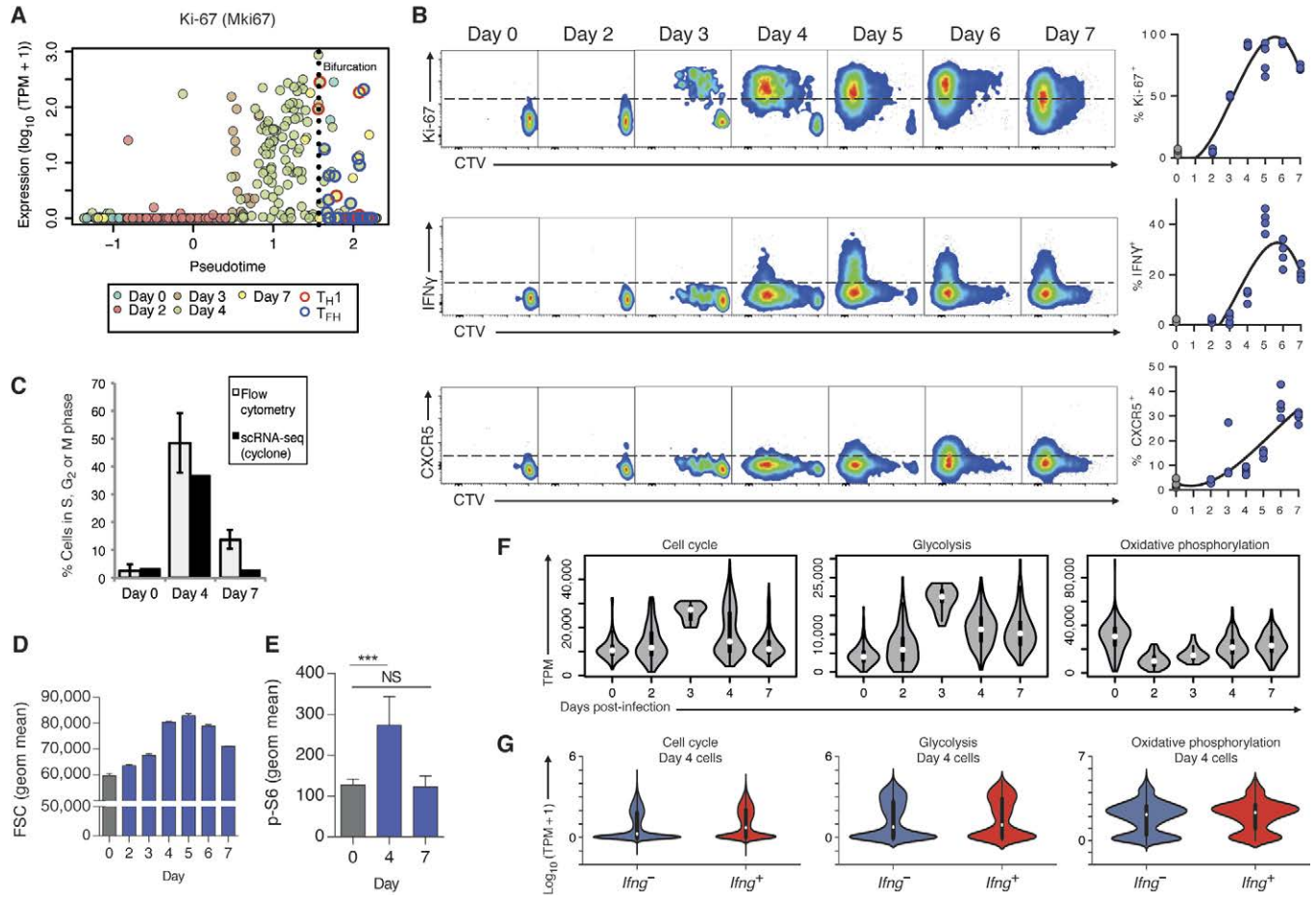


**Fig. 4. The bifurcation of T cell fates is accompanied by changes in transcription, proliferation, and metabolism.** (**A**) Expression kinetics of *Mki67*, encoding the proliferative marker Ki-67, as a function of pseudotime. (**B**) Representative FACS plots showing kinetics of CellTrace Violet (CTV) dilution and Ki-67, IFNγ, or CXCR5 expression, with summary graphs showing % of PbTII cells expressing these (after $10^6$ PbTII cells transferred) in uninfected (day 0) and *Pc*AS-infected mice at indicated days after infection ($n = 4$ mice per time point, with data from individual mice shown in summary graphs; solid line in summary graphs indicates temporal trends fit using a third-order polynomial regression). Data are representative of two independent experiments. (**C**) Relative cell cycle speed of PbTII cells, determined by measuring the fraction of cells in S, $G_2$, or M phase. Results when allocating cells to cell cycle phases using flow cytometry (fig. S16C) or computational assignments on the basis of the scRNA-seq data are shown. (**D**) Cell size estimation using forward scatter (FSC) measurements of PbTII cells. (**E**) Cellular metabolic activity of PbTII cells in naive mice ($n = 3$) and at days 4 and 7 after infection ($n = 6$), as determined by flow cytometric assessment of ribosomal protein S6 phosphorylation (p-S6). Histogram and proportions are representative of two independent experiments. ***$P < 0.001$, one-way analysis of variance (ANOVA) and Tukey's multiple comparisons tests. (**F**) Expression kinetics of genes associated with the cell cycle [251 genes derived from Cyclebase (*48*)], glycolysis (41 genes, GO:0006096), and oxidative phosphorylation (30 genes, GO:0006119) during *Pc*AS infection. Cumulative expression levels of genes in the respective categories per single cell are shown. Data from all cells and mice (Fig.1A) were pooled. (**G**) Differential expression analysis comparing the experiment-corrected expression of genes associated with cell cycle ($P < 10^{-103}$), glycolysis ($P < 10^{-4}$), and oxidative phosphorylation ($P < 10^{-5}$) (F) in *Ifng*-positive (≥10 TPM) and *Ifng*-negative cells (<10 TPM) at day 4 after infection with *Pc*AS from both experiments combined.

$T_H1/T_{FH}$ fate (Fig. 5D). Assessment of *Cxcr3*/*Cxcr5* coexpression around bifurcation revealed a substantial portion of cells expressing both receptors (fig. S18). Thus, our examination of gene expression dynamics revealed large numbers of genes being expressed and peaking around bifurcation, including not only those associated with clonal expansion but also numerous sequentially expressed transcription factors and receptors with potential to influence $T_H$ fate.

## Monocytes support activated PbTII cells toward a $T_H1$ but not a $T_{FH}$ fate

Given similar dynamics and peak expression times for *Cxcr3* and *Cxcr5*, and peak expression around bifurcation for *Ccr4* (fig. S17), we reasoned that cell-cell interactions via these receptors controlled $T_H1/T_{FH}$ fate. Hence, we considered cell types that could control $T_H$ fate, specifically around bifurcation. Because B cells supported a $T_{FH}$ fate (fig. S19), we hypothesized that coordinated action by myeloid cells provided competing signals to support a $T_H1$ fate.

To study this, we examined splenic cDCs and inflammatory monocytes before PbTII bifurcation. We sorted $CD8\alpha^+$ and $CD11b^+$ cDCs and $Ly6C^{hi}$ monocytes from naïve and infected mice (fig. S20) and performed scRNA-seq. PCA of cDCs distinguished the two naïve cell types along PC2 (Fig. 6A and fig. S21) with an efficiency consistent with recent data (*35*) and further highlighted a number of expected and previously unknown cDC subset-specific genes (fig. S22). We next compared naïve cDCs with those from infection (Fig. 6A and fig. S21) and separated these along PC6 (Fig. 6A). Analysis of differential gene expression in cDCs due to infection identified 30 genes, 29 of which were up-regulated (Fig. 6B and fig. S23), including transcription factors *Stat1* and *Irf1* and

Science Immunology

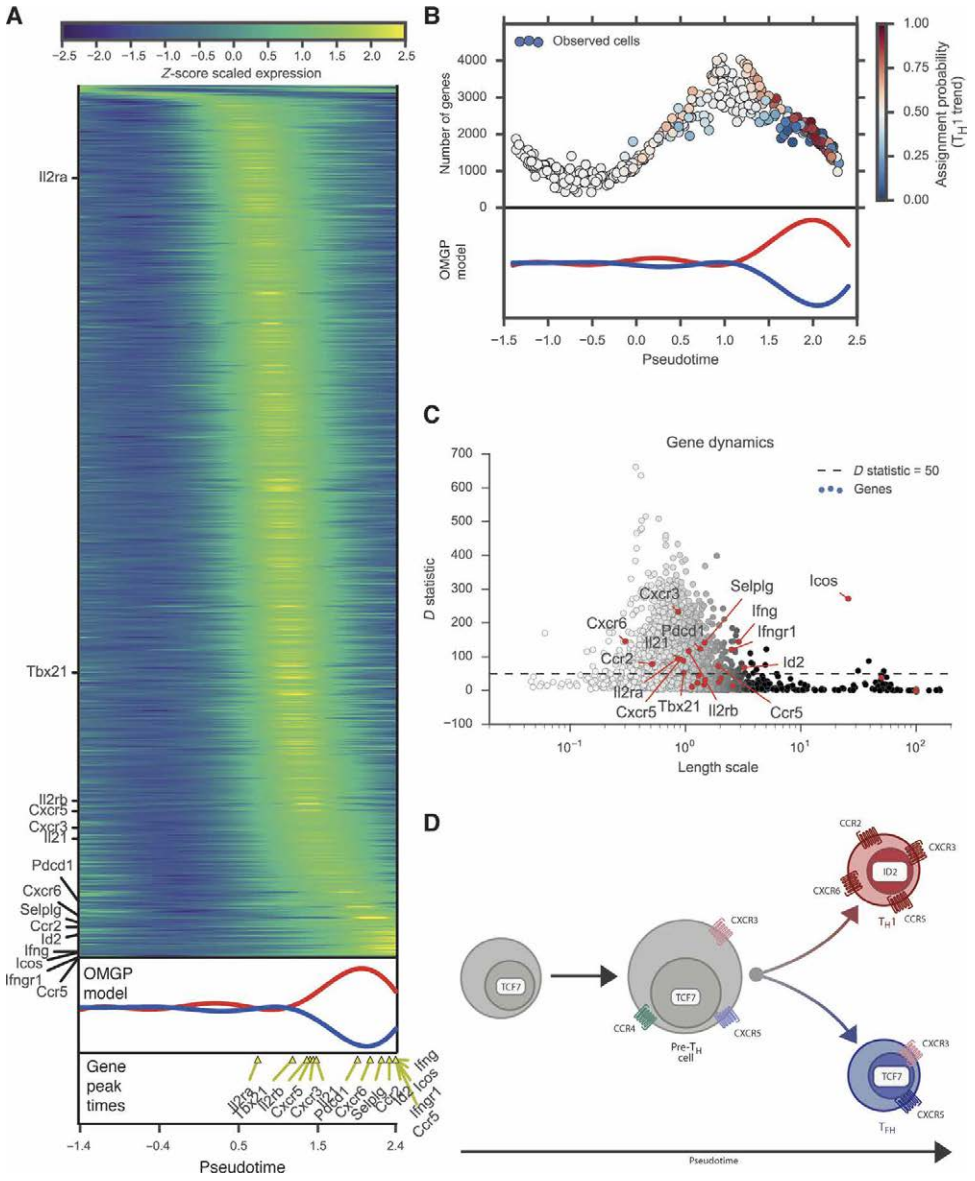


**Fig. 5. Temporal gene expression dynamics during *Pc*AS infection.** (**A**) Expression patterns over pseudotime shown for top 2061 dynamic genes (defined by *D* statistic >50). Genes are ordered per peak expression time. $T_H1$ and $T_{FH}$ probability trajectories from the GPfates OMGP model presented at the bottom to depict bifurcation and provide temporal context between the gene expressions and cellular fates. Various dynamically expressed immune receptors, transcription factors, and secreted molecules are annotated. (**B**) Relationship of transcriptional activity and divergence of $T_H1$ and $T_{FH}$ fates. The number of detected genes per cell is shown across pseudotime. The color of the data points represents trend assignment probability (Fig.2). $T_H1$ and $T_{FH}$ trajectories from the GPfates OMGP model presented to depict relation to the bifurcating behavior. (**C**) Gene expression dynamics assessed using *D* statistic and optimal squared exponential kernel length-scales. Genes with a *D* statistic of >50 selected as displaying nonlinear expression patterns over pseudotime. The optimal length-scales of the squared exponential kernels of the Gaussian Processes plotted on *x* axis, where small values indicate that some rapid changes in expression over pseudotime occur. (**D**) Model summarizing the expression patterns of key chemokine receptors and the transcription factors *Id2* and *Tcf7* during $T_H1$-$T_{FH}$ cell fate determination. The size of the cell represents proliferative capacity (Fig.4, A to F).

CXCR3-attractant chemokines *Cxcl9* and *Cxcl10*. Notably, gene expression patterns among individual cDCs varied according to the gene. For example, *Stat1* and *Irf1* were expressed by several naïve cDCs and further up-regulated during infection (Fig. 6C). This was similar for *Cxcl9*, which was expressed by CD8α$^+$ cDCs in naive mice, whereas *Cxcl10* was induced only upon infection (Fig. 6C). These data suggested interactions between cDCs and uncommitted CXCR3$^+$ PbTII cells, consistent with a recent study (*10*). Next, PCA of Ly6C$^{hi}$ monocytes from naïve and infected mice distinguished them from each other along PC2 (Fig. 6D and fig. S24). Differential gene expression analysis between naïve and infected groups uncovered ~100 genes, both up-regulated and down-regulated during infection (Fig. 6E and fig. S25). A high proportion (~40%) of genes up-regulated in cDCs were also induced in Ly6C$^{hi}$ monocytes, including *Stat1*, *Irf1*, and *Cxcl10* (Fig. 6, E and F), suggesting possible overlapping functionality. In addition, monocytes expressed other chemokines, including *Cxcl2*, *Ccl2*, and *Ccl3* (Fig. 6, E and F). Furthermore, specific examination of all immune cellular interaction genes (fig. S26) revealed emerging variable expression of *Tnf*, *Cd40*, *Pdl1*, *Ccl4*, *Ccl5*, *Cxcl16*, *Cxcl9*, and *Cxcl11* in monocytes, thus suggesting complex cell-cell interactions for Ly6C$^{hi}$ monocytes during infection.

Because *Cxcl9*, *Cxcl10*, *Cxcl11*, *Ccl2*, *Ccl3*, and *Ccl5* signal through *Cxcr3* or *Ccr4*, which were expressed by activated PbTII cells, we next hypothesized that Ly6C$^{hi}$ monocytes, in addition to cDCs (*10*), interacted with PbTII cells and influenced $T_H1/T_{FH}$ fate. To test this, we first assessed chemokine expression at the protein level by Ly6C$^{hi}$ monocytes (Fig. 6G). Kinetics of CXCL9 production was similar in cDCs and Ly6C$^{hi}$ monocytes. Next, we used *LysMCre* × *iDTR* mice, in which Ly6C$^{hi}$ monocytes were depleted after PbTII cell activation but before bifurcation (Fig. 6H and fig. S27). We noted a modest reduction in CD68$^+$ splenic macrophages using this approach (fig. S27B). Using this approach, we found that monocytes/macrophages supported a $T_H1$ but not a $T_{FH}$ fate (Fig. 6H). Together, our data support a model in which activated PbTII cells are supported toward either a $T_{FH}$ fate by B cells (fig. S19) or a $T_H1$ fate by chemokine-expressing myeloid cells, including Ly6C$^{hi}$ inflammatory monocytes.

## DISCUSSION

By capturing single CD4$^+$ T cell transcriptomes during an experimental malaria infection, and computationally reconstructing the course of events, we have resolved the bifurcation of naïve CD4$^+$ T cells into $T_H1$ and $T_{FH}$ cells at a molecular level. GPfates modeling

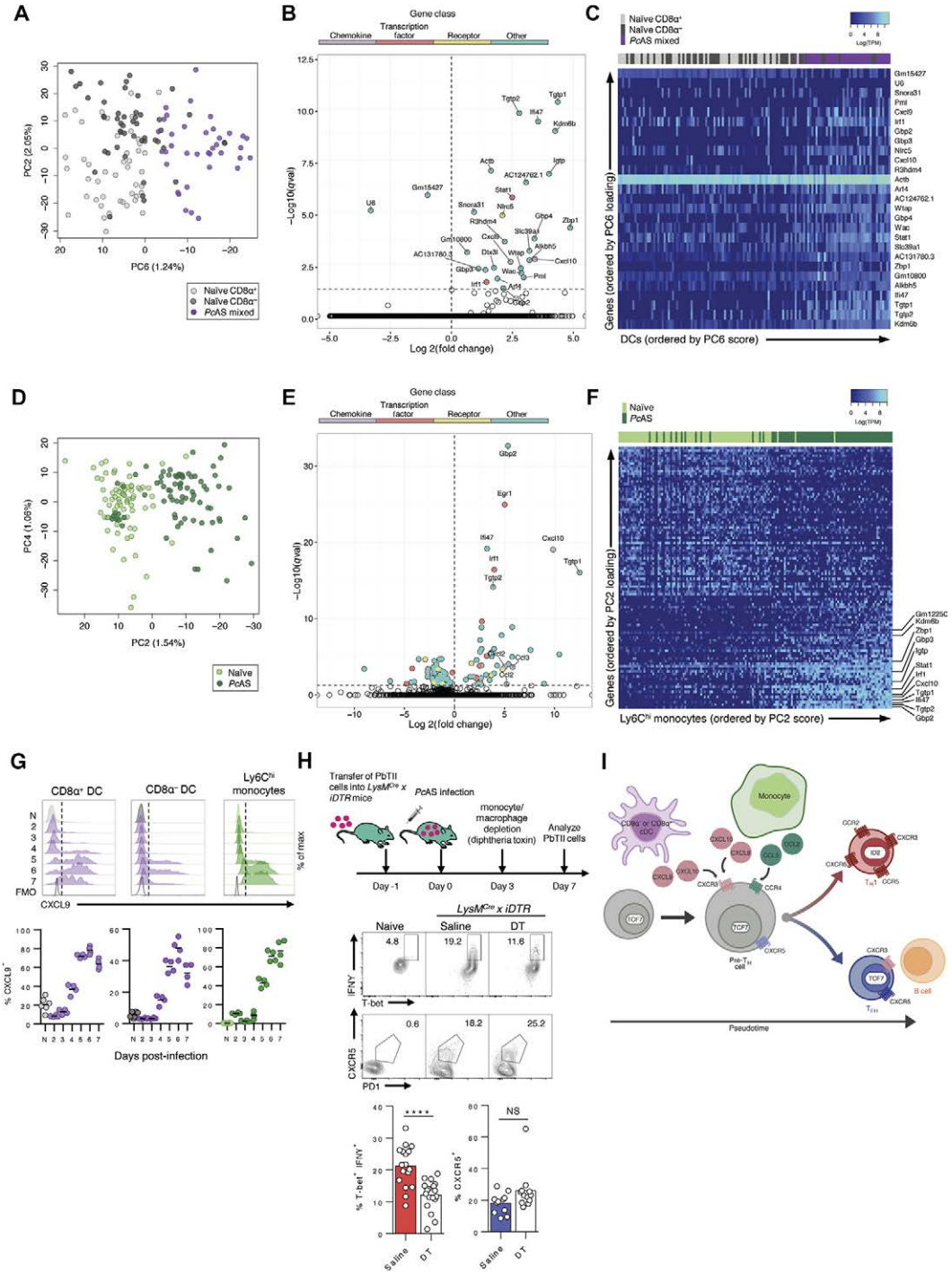


**Fig. 6. Myeloid cells influence $T_H$ bifurcation in uncommitted PbTII cells.** (**A** to **C**) Splenic CD8$\alpha^+$ and CD11b$^+$ CD8$\alpha^-$ cDCs from a naïve mouse, mixed cDCs from an infected mouse, and (**D** to **F**) Ly6C$^{hi}$ monocytes from naïve and infected mice were analyzed by scRNA-seq, with mRNA reads filtered by minimum expression of 100 TPM in at least two cells. (A and D) PCA showing clustering of (A) cDCs or (D) monocytes. (B and E) Fold change and confidence for differentially expressed genes (*19*) between infected and naive (B) cDCs or (E) monocytes; genes were filtered on expression in >10 cells; genes satisfying $q < 0.05$ are colored per function. (C and F) Differentially expressed genes ($q < 0.05$) in (C) cDCs and (F) monocytes, between naive and infected mice: Cells and genes are ordered according to PC score and loading, respectively. Common genes between heat maps are annotated in (F). (**G**) Representative FACS histograms and proportions of splenic CD8$\alpha^+$ cDCs, CD8$\alpha^-$ cDCs, and Ly6C$^{hi}$ monocytes expressing CXCL9 in naive and infected mice; data show individual mice with line at mean and are representative of two independent experiments ($n = 4$ mice per time point per experiment). (**H**) PbTII cells were transferred into *LysMCre* × *iDTR* mice 1 day before infection. At 3 days after infection, mice were treated with diphtheria toxin (DT) or saline. Proportions of $T_H1$ (T-bet$^{hi}$ IFN$\gamma^+$) and $T_{FH}$ (CXCR5$^+$) PbTII cells at 7 days after infection; data pooled from three independent experiments ($n = 5$ to 6 per experiment). ****$P < 0.0001$, Mann-Whitney $U$ test; NS, not significant. (**I**) Summary model proposes that chemokine interactions between nonbifurcated PbTII cells and myeloid cells support a $T_H1$ fate, whereas B cells support a $T_{FH}$ fate.

of scRNA-seq data is not limited to immune cells or single bifurcation events. This model can also be combined with existing computational workflows, including alternative methods to estimate pseudotemporal dynamics (see section 6.2 of Supplementary Computational Methods) (*19*, *36*). The GPfates approach permits analysis of cellular differentiation toward two fates (Comp. Supp. Fig. 11) and, in principle, toward multiple fates (Comp. Supp. Fig. 12). However, GPfates exhibits some limitations. Most notably, the ability to identify and pinpoint bifurcation events is linked to changes in the transcriptome that reflect these cellular decisions. In particular, because scRNA-seq profiles are subject to high levels of noise, this means that changes will only be detectable with some lag time (Supplementary Computational Methods). The processed expression data and the GPfates model presented in this study can be accessed at www.plasmoTH.org, where users can visualize their genes of interest.

Our data provide the framework for revealing molecular insights into the early stages of $T_H$ cell differentiation and describe the sequence of transcriptional events before and after the bifurcation of $T_H1$ and $T_{FH}$ fates. Transcriptomic profiling previously suggested developmental similarities between $T_{FH}$ and $T_H1$ cells (*37*). However, highly immunogenic viral or bacterial infections induced $CD4^+$ T cells to segregate into $Bcl6^+$ ($T_{FH}$) or $Blimp\text{-}1^+$ ($T_H1$) subpopulations within 2 days (*38*, *39*). In our parasitic model, single $CD4^+$ T cell transcriptomes remained remarkably similar until 4 days of infection. Although it is difficult to directly compare infection models, we speculate that *Plasmodium* infection in mice may not drive $T_H$ bifurcation as early as observed with highly immunogenic viruses or bacteria, particularly given evidence of immunosuppression (*40*).

IL-10–producing Tr1 cells can suppress immune responses, which could aid the treatment of immune-mediated disorders (*41*) or be detrimental for chronic infections (*42*). Despite this, their relationship to $T_H1$ cells is not clear (*43*). In our model, Tr1 cells emerged from the $T_H1$ trajectory. This observation, coupled with similar transcriptomes for $T_H1$ and Tr1 cells, provides evidence that Tr1 cells are highly related to, and derive directly from, $T_H1$ cells in this model. Thus, our modeling of scRNA-seq data revealed molecular relationships between $T_H1$, Tr1, and $T_{FH}$ cells and showed that a single naïve $CD4^+$ T cell can simultaneously give rise to more than one cell fate during experimental malaria.

Activated $CD4^+$ T cells may experience different microenvironments within secondary lymphoid tissue. The observation that bifurcation toward $T_H1$ and $T_{FH}$ fates was preceded by up-regulation of chemokine receptors prompted us to investigate possible cell-cell interactions with chemokine-expressing myeloid cells. Previous studies have highlighted the potential for cDCs in lymph nodes to produce $T_H1$-associated chemokines (*10*). Our study, which focused on the spleen, further implicated inflammatory monocytes in $T_H1$ support. However, because our transgenic approach for depleting monocytes also removed a small portion of splenic red pulp macrophages, we cannot fully discount the possibility that they may partly contribute to a $T_H1$ fate. Nevertheless, we propose that splenic monocytes/macrophages influence bifurcation by supporting a $T_H1$ fate during *Plasmodium* infection. Our studies emphasize that although cDCs are key for initiating $CD4^+$ T cell activation in the spleen, other myeloid cells can also promote a $T_H1$ fate in the presence of cDCs. In contrast, given that CXCR5 was the only chemokine receptor notably associated with bifurcation toward a $T_{FH}$ fate, cellular interaction with B cell follicles may be the primary mechanism for supporting a $T_{FH}$ fate. Our model proposes that activated, uncommitted $CD4^+$ T cells become receptive to competing chemoattractant signals from different zones of the spleen, and suggests intercellular communication as a major driver of bifurcation. However, upstream of these processes, internal stochasticity in uncommitted $CD4^+$ T cells may control the balance of chemokine receptor expression. Future experiments combining our integrated single-cell genomics and computational modeling with in vivo positional and trafficking data may reveal molecular relationships between internal stochasticity, migratory behavior, and $T_H$ cell fate.

## MATERIALS AND METHODS

### Study design

The goal of this study was to use scRNA-seq to capture the transcriptomes of individual splenic PbTII cells at various time points during the first week of a blood-stage *Pc*AS infection. Multiple mice were used for most time points to test for possible batch effects, with an independent experimental repeat performed on a different scRNA-seq platform. scRNA-seq data were modeled using Gaussian processes, with statistical testing for significance of both genes and cells associated with the Gaussian processes.

### Experimental mice and infections

Wild-type and transgenic inbred mouse strains were housed and used in blood-stage *Plasmodium* infections, as described in Supplementary Materials and Methods.

### Flow cytometry

Splenocytes were isolated and assessed by flow cytometry as described in Supplementary Materials and Methods.

### Single-cell mRNA sequencing

Single-cell capture and processing, as well as quality control analysis of scRNA-seq data, were performed as described in Supplementary Materials and Methods.

### Statistics

Statistical analyses were conducted using R, Python, or GraphPad Prism. The types of statistical tests and significance levels are described in respective figure legends.

## SUPPLEMENTARY MATERIALS

immunology.sciencemag.org/cgi/content/full/2/9/eaal2192/DC1

Materials and Methods

Fig. S1. Enrichment of PbTII cells for adoptive transfer.

Fig. S2. Sorting strategy for PbTII cells.

Fig. S3. Flow cytometric assessment of $T_H1/T_{FH}$ responses during *Pc*AS infection.

Fig. S4. Expression of subset-specific marker genes in PbTII cells.

Fig. S5. Heterogeneity of activated PbTII cells and variability associated with cell size and differentiation.

Fig. S6. Heterogeneity of $T_H1/T_{FH}$ signature gene expression in activated PbTII cells.

Fig. S7. Heterogeneity of the entire PbTII time series and the contribution of $T_H1$ and $T_{FH}$ signature genes to the overall variability.

Fig. S8. The relationship of pseudotime with time points and with the $T_H1$ assignment probability.

Fig. S9. Correlation of GPfates trends with $T_H1$ and $T_{FH}$ signature genes.

Fig. S10. Expression of transgenic and endogenous TCRs.

Fig. S11. Expression of endogenous TCRs does not influence PbTII cell $T_H1/T_{FH}$ differentiation.

Fig. S12. Robustness of top bifurcating genes across experiments.

Fig. S13. Flow cytometric validation of CXCR6 expression in PbTII cells before and after bifurcation.

Fig. S14. T cell–intrinsic Galectin-1 supports $T_H1$ fate commitment.

Fig. S15. IL-10– and IFNγ-coproducing Tr1 cells derive from $T_H1$ cells.

Fig. S16. Proliferative burst of activated PbTII cells.

Fig. S17. Kinetics of chemokine receptor expression during *Pc*AS infection according to the GPfates model.

Fig. S18. Coexpression of chemokine receptors at single-cell level during *Pc*AS infection.
Fig. S19. B cells are essential for $T_{FH}$ responses in PbTII cells during *Pc*AS infection.
Fig. S20. Sorting strategy for myeloid cells.
Fig. S21. PCA of cDCs from naïve and infected mice.
Fig. S22. Differential gene expression between single splenic CD8$\alpha^+$ and CD8$\alpha^-$ cDCs.
Fig. S23. Differentially expressed genes between single naïve and day 3 *Pc*AS-infected cDCs.
Fig. S24. PCA of Ly6C$^{hi}$ monocytes from naïve and infected mice.
Fig. S25. Differentially expressed genes between single Ly6C$^{hi}$ monocytes from naïve and day 3 *Pc*AS-infected mice.
Fig. S26. Expression of immune signaling genes by cDCs and monocytes.
Fig. S27. Myeloid cell depletion in *LysMCre* × *iDTR* mice.
Table S1. The expression data from day 7 after infection with functional annotations for genes (*15*, *37*, *44*–*46*) (external file).
Table S2. TraCeR detection statistics for the original data set (external file).
Table S3. TraCeR detection statistics for the replicate data set (external file).
Table S4. Annotation of receptors, cytokines, and transcription factors.
Supplementary Computational Methods—The GPfates model (external file)
References (*49*–*64*)

## REFERENCES AND NOTES


1. *World Malaria Report 2016* (World Health Organization, 2016).
2. A. Pinzon-Charry, V. McPhun, V. Kienzle, C. Hirunpetcharat, C. Engwerda, J. McCarthy, M. F. Good, Low doses of killed parasite in CpG elicit vigorous CD4+ T cell responses against blood-stage malaria in mice. *J. Clin. Invest.* **120**, 2967–2978 (2010).
3. M. J. Boyle, L. Reiling, G. Feng, C. Langer, F. H. Osier, H. Aspeling-Jones, Y. S. Cheng, J. Stubbs, K. K. A. Tetteh, D. J. Conway, J. S. McCarthy, I. Muller, K. Marsh, R. F. Anders, J. G. Beeson, Human antibodies fix complement to inhibit *Plasmodium falciparum* invasion of erythrocytes and are associated with protection against malaria. *Immunity* **42**, 580–590 (2015).
4. N. Obeng-Adjei, S. Portugal, T. M. Tran, T. B. Yazew, J. Skinner, S. Li, A. Jain, P. L. Felgner, O. K. Doumbo, K. Kayentao, A. Ongoiba, B. Traore, P. D. Crompton, Circulating Th1-cell-type Tfh cells that exhibit impaired B cell help are preferentially activated during acute malaria in children. *Cell Rep.* **13**, 425–439 (2015).
5. D. Perez-Mazliah, J. Langhorne, CD4 T-cell subsets in malaria: TH1/TH2 revisited. *Front. Immunol.* **5**, 671 (2015).
6. N. J. Tubo, A. J. Pagán, J. J. Taylor, R. W. Nelson, J. L. Linehan, J. M. Ertelt, E. S. Huseby, S. S. Way, M. K. Jenkins, Single naive CD4$^+$ T cells from a diverse repertoire produce different effector cell types during infection. *Cell* **153**, 785–796 (2013).
7. S. deWalick, F. H. Amante, K. A. McSweeney, L. M. Randall, A. C. Stanley, A. Haque, R. D. Kuns, K. P. A. MacDonald, G. R. Hill, C. R. Engwerda, Cutting edge: Conventional dendritic cells are the critical APC required for the induction of experimental cerebral malaria. *J. Immunol.* **178**, 6033–6037 (2007).
8. S. Celli, F. Lemaître, P. Bousso, Real-time manipulation of T cell-dendritic cell interactions in vivo reveals the importance of prolonged contacts for CD4$^+$ T cell activation. *Immunity* **27**, 625–634 (2007).
9. M. Bajénoff, O. Wurtz, S. Guerder, Repeated antigen exposure is necessary for the differentiation, but not the initial proliferation, of naive CD4$^+$ T cells. *J. Immunol.* **168**, 1723–1729 (2002).
10. J. R. Groom, J. Richmond, T. T. Murooka, E. W. Sorensen, J. H. Sung, K. Bankert, U. H. von Andrian, J. J. Moon, T. R. Mempel, A. D. Luster, CXCR3 chemokine receptor-ligand interactions in the lymph node optimize CD4$^+$ T helper 1 cell differentiation. *Immunity* **37**, 1091–1103 (2012).
11. T. M. Hohl, A. Rivera, L. Lipuma, A. Gallegos, C. Shi, M. Mack, E. G. Pamer, Inflammatory monocytes facilitate adaptive CD4 T cell responses during respiratory fungal infection. *Cell Host Microbe* **6**, 470–481 (2009).
12. H. Nakano, K. L. Lin, M. Yanagita, C. Charbonneau, D. N. Cook, T. Kakiuchi, M. D. Gunn, Blood-derived inflammatory dendritic cells in lymph nodes stimulate acute T helper type 1 immune responses. *Nat. Immunol.* **10**, 394–402 (2009).
13. R. J. Johnston, A. C. Poholek, D. DiToro, I. Yusuf, D. Eto, B. Barnett, A. L. Dent, J. Craft, S. Crotty, Bcl6 and Blimp-1 are reciprocal and antagonistic regulators of T follicular helper cell differentiation. *Science* **325**, 1006–1010 (2009).
14. S. J. Szabo, S. T. Kim, G. L. Costa, X. Zhang, C. G. Fathman, L. H. Glimcher, A novel transcription factor, T-bet, directs Th1 lineage commitment. *Cell* **100**, 655–669 (2000).
15. J. S. Hale, B. Youngblood, D. R. Latner, A. U. R. Mohammed, L. Ye, R. S. Akondy, T. Wu, S. S. Iyer, R. Ahmed, Distinct memory CD4$^+$ T cells with commitment to T follicular helper- and T helper 1-cell lineages are generated after acute viral infection. *Immunity* **38**, 805–817 (2013).
16. N. D. Lawrence, "The Gaussian process latent variable model" (Technical Report CS-06-03, University of Sheffield, 2006).
17. M. Lazaro-Gredilla, S. Van Vaerenbergh, N. D. Lawrence, Overlapping mixtures of Gaussian processes for the data association problem. *Pattern Recogn.* **45**, 1386–1395 (2012).
18. E. Marco, R. L. Karp, G. Guo, P. Robson, A. H. Harte, L. Trippa, G.-C. Yuan, Bifurcation analysis of single-cell gene expression data reveals epigenetic landscape. *Proc. Natl. Acad. Sci. U.S.A.* **111**, E5643–E5650 (2014).
19. C. Trapnell, D. Cacchiarelli, J. Grimsby, P. Pokharel, S. Li, M. Morse, N. J. Lennon, K. J. Livak, T. S. Mikkelsen, J. L. Rinn, The dynamics and regulators of cell fate decisions are revealed by pseudotemporal ordering of single cells. *Nat. Biotechnol.* **32**, 381–386 (2014).
20. J. Chen, A. Schlitzer, S. Chakarov, F. Ginhoux, M. Poidinger, Mpath maps multi-branching single-cell trajectories revealing progenitor cell progression during development. *Nat. Commun.* **7**, 11988 (2016).
21. L. Haghverdi, M. Büttner, F. A. Wolf, F. Buettner, F. J. Theis, Diffusion pseudotime robustly reconstructs lineage branching. *Nat. Methods* **13**, 845–848 (2016).
22. M. Setty, M. D. Tadmor, S. Reich-Zeliger, O. Angel, T. M. Salame, P. Kathail, K. Choi, S. Bendall, N. Friedman, D. Pe'er, Wishbone identifies bifurcating developmental trajectories from single-cell data. *Nat. Biotechnol.* **34**, 637–645 (2016).
23. B. Treutlein, D. G. Brownfield, A. R. Wu, N. F. Neff, G. L. Mantalas, F. H. Espinoza, T. J. Desai, M. A. Krasnow, S. R. Quake, Reconstructing lineage hierarchies of the distal lung epithelium using single-cell RNA-seq. *Nature* **509**, 371–375 (2014).
24. F. Guo, L. Yan, H. Guo, L. Li, B. Hu, Y. Zhao, J. Yong, Y. Hu, X. Wang, Y. Wei, W. Wang, R. Li, J. Yan, X. Zhi, Y. Zhang, H. Jin, W. Zhang, Y. Hou, P. Zhu, J. Li, L. Zhang, S. Liu, Y. Ren, X. Zhu, L. Wen, Y. Q. Gao, F. Tang, J. Qiao, The transcriptome and DNA methylome landscapes of human primordial germ cells. *Cell* **161**, 1437–1452 (2015).
25. Y. S. Choi, J. A. Gullicksrud, S. Xing, Z. Zeng, Q. Shan, F. Li, P. E. Love, W. Peng, H.-H. Xue, S. Crotty, LEF-1 and TCF-1 orchestrate $T_{FH}$ differentiation by regulating differentiation circuits upstream of the transcriptional repressor Bcl6. *Nat. Immunol.* **16**, 980–990 (2015).
26. L. Xu, Y. Cao, Z. Xie, Q. Huang, Q. Bai, X. Yang, R. He, Y. Hao, H. Wang, T. Zhao, Z. Fan, A. Qin, J. Ye, X. Zhou, L. Ye, Y. Wu, The transcription factor TCF-1 initiates the differentiation of $T_{FH}$ cells during acute viral infection. *Nat. Immunol.* **16**, 991–999 (2015).
27. L. A. Shaw, S. Bélanger, K. D. Omilusik, S. Cho, J. P. Scott-Browne, J. P. Nance, J. Goulding, A. Lasorella, L.-F. Lu, S. Crotty, A. W. Goldrath, Id2 reinforces $T_H1$ differentiation and inhibits E2A to repress $T_{FH}$ differentiation. *Nat. Immunol.* **17**, 834–843 (2016).
28. S. Hardtke, L. Ohl, R. Förster, Balanced expression of CXCR5 and CCR7 on follicular T helper cells determines their transient positioning to lymph node follicles and is essential for efficient B-cell help. *Blood* **106**, 1924–1931 (2005).
29. C. V. Poncini, J. M. Ilarregui, E. I. Batalla, S. Engels, J. P. Cerliani, M. A. Cucher, Y. van Kooyk, S. M. González-Cappa, G. A. Rabinovich, *Trypanosoma cruzi* infection imparts a regulatory program in dendritic cells and T cells via galectin-1–dependent mechanisms. *J. Immunol.* **195**, 3311–3324 (2015).
30. M. I. Garín, C.-C. Chu, D. Golshayan, E. Cernuda-Morollón, R. Wait, R. I. Lechler, Galectin-1: A key effector of regulation mediated by CD4$^+$CD25$^+$ T cells. *Blood* **109**, 2058–2065 (2006).
31. M. L. Whitfield, L. K. George, G. D. Grant, C. M. Perou, Common markers of proliferation. *Nat. Rev. Cancer* **6**, 99–106 (2006).
32. I. C. Macaulay, V. Svensson, C. Labalette, L. Ferreira, F. Hamey, T. Voet, S. A. Teichmann, A. Cvejic, Single-cell RNA-sequencing reveals a continuous spectrum of differentiation in hematopoietic cells. *Cell Rep.* **14**, 966–977 (2016).
33. D. Breitfeld, L. Ohl, E. Kremmer, J. Ellwart, F. Sallusto, M. Lipp, R. Förster, Follicular B helper T cells express CXC chemokine receptor 5, localize to B cell follicles, and support immunoglobulin production. *J. Exp. Med.* **192**, 1545–1552 (2000).
34. P. Schaerli, K. Willimann, A. B. Lang, M. Lipp, P. Loetscher, B. Moser, CXC chemokine receptor 5 expression defines follicular homing T cells with B cell helper function. *J. Exp. Med.* **192**, 1553–1562 (2000).
35. D. A. Jaitin, E. Kenigsberg, H. Keren-Shaul, N. Elefant, F. Paul, I. Zaretsky, A. Mildner, N. Cohen, S. Jung, A. Tanay, I. Amit, Massively parallel single-cell RNA-seq for marker-free decomposition of tissues into cell types. *Science* **343**, 776–779 (2014).
36. S. C. Bendall, K. L. Davis, E.-a. D. Amir, M. D. Tadmor, E. F. Simonds, T. J. Chen, D. K. Shenfeld, G. P. Nolan, D. Pe'er, Single-cell trajectory detection uncovers progression and regulatory coordination in human B cell development. *Cell* **157**, 714–725 (2014).
37. X. Liu, X. Yan, B. Zhong, R. I. Nurieva, A. Wang, X. Wang, N. Martin-Orozco, Y. Wang, S. H. Chang, E. Esplugues, R. A. Flavell, Q. Tian, C. Dong, Bcl6 expression specifies the T follicular helper cell program in vivo. *J. Exp. Med.* **209**, 1841–1852 (2012).
38. Y. S. Choi, R. Kageyama, D. Eto, T. C. Escobar, R. J. Johnston, L. Monticelli, C. Lao, S. Crotty, ICOS receptor instructs T follicular helper cell versus effector cell differentiation via induction of the transcriptional repressor Bcl6. *Immunity* **34**, 932–946 (2011).
39. M. Pepper, A. J. Pagán, B. Z. Igyártó, J. J. Taylor, M. K. Jenkins, Opposing signals from the Bcl6 transcription factor and the interleukin-2 receptor generate T helper 1 central and effector memory cells. *Immunity* **35**, 583–595 (2011).
40. A. Haque, S. E. Best, M. Montes de Oca, K. R. James, A. Ammerdorffer, C. L. Edwards, F. de Labastida Rivera, F. H. Amante, P. T. Bunn, M. Sheel, I. Sebina, M. Koyama, A. Varelias, P. J. Hertzog, U. Kalinke, S. Y. Gun, L. Rénia, C. Ruedl, K. P. A. MacDonald, G. R. Hill, C. R. Engwerda, Type I IFN signaling in CD8- DCs impairs Th1-dependent malaria immunity. *J. Clin. Invest.* **124**, 2483–2496 (2014).
41. X. Clemente-Casares, J. Blanco, P. Ambalavanan, J. Yamanouchi, S. Singha, C. Fandos, S. Tsai, J. Wang, N. Garabatos, C. Izquierdo, S. Agrawal, M. B. Keough, V. W. Yong, E. James,

A. Moore, Y. Yang, T. Stratmann, P. Serra, P. Santamaria, Expanding antigen-specific regulatory networks to treat autoimmunity. *Nature* **530**, 434–440 (2016).
42. K. N. Couper, D. G. Blount, M. S. Wilson, J. C. Hafalla, Y. Belkaid, M. Kamanaka, R. A. Flavell, J. B. de Souza, E. M. Riley, IL-10 from $CD4^+CD25^-Foxp3^-CD127^-$ adaptive regulatory T cells modulates parasite clearance and pathology during malaria infection. *PLOS Pathog.* **4**, e1000004 (2008).
43. L. Apetoh, F. J. Quintana, C. Pot, N. Joller, S. Xiao, D. Kumar, E. J. Burns, D. H. Sherr, H. L. Weiner, V. K. Kuchroo, The aryl hydrocarbon receptor interacts with c-Maf to promote the differentiation of type 1 regulatory T cells induced by IL-27. *Nat. Immunol.* **11**, 854–861 (2010).
44. H. D. Marshall, A. Chandele, Y. Woo Jung, H. Meng, A. C. Poholek, I. A. Parish, R. Rutishauser, W. Cui, S. H. Kleinstein, J. Craft, S. M. Kaech, Differential expression of Ly6C and T-bet distinguish effector and memory Th1 $CD4^+$ cell properties during viral infection. *Immunity* **35**, 633–646 (2011).
45. A. Flores-Langarica, J. L. Marshall, S. Bobat, E. Mohr, J. Hitchcock, E. A. Ross, R. E. Coughlan, M. Khan, N. Van Rooijen, I. R. Henderson, I. C. Maclennan, A. F. Cunningham, T-zone localized monocyte-derived dendritic cells promote Th1 priming to *Salmonella*. *Eur. J. Immunol.* **41**, 2654–2665 (2011).
46. A. Crawford, J. M. Angelosanto, C. Kao, T. A. Doering, P. M. Odorizzi, B. E. Barnett, E. John Wherry, Molecular and transcriptional basis of $CD4^+$ T cell dysfunction during chronic infection. *Immunity* **40**, 289–302 (2014).
47. M. J. Stubbington, B. Mahata, V. Svensson, A. Deonarine, J. K. Nissen, A. G. Betz, S. A. Teichmann, An atlas of mouse $CD4^+$ T cell transcriptomes. *Biol. Direct* **10**, 14 (2015).
48. A. Santos, R. Wernersson, L. J. Jensen, Cyclebase 3.0: A multi-organism database on cell-cycle regulation and phenotypes. *Nucleic Acids Res.* **43**, D1140–D1144 (2015).
49. C. E. Rasmussen, C. K. I. Williams, *Gaussian Processes for Machine Learning* (MIT Press, 2006).
50. M. K. Titsias, N. D. Lawrence, Bayesian Gaussian process latent variable model, in *Proceedings of the Thirteenth International Workshop on Artificial Intelligence and Statistics*, Y. W. Teh, D. M. Titterington, Eds. (2010), pp. 844–851.
51. J. E. Reid, L. Wernisch, Pseudotime estimation: Deconfounding single cell time series. *Bioinformatics* **32**, 2973–2980 (2016).
52. J. Hensman, M. Rattray, N. D. Lawrence, Fast nonparametric clustering of structured time-series. *IEEE Trans. Pattern Anal. Mach. Intell.* **37**, 383–393 (2015).
53. J. Hensman, M. Rattray, N. D. Lawrence, in *Advances in Neural Information Processing Systems 25*, F. Pereira, C. J. C. Burges, L. Bottou, K. Q. Weinberger, Eds. (Curran Associates Inc., 2012), pp. 2888–2896.
54. P. V. Kharchenko, L. Silberstein, D. T. Scadden, Bayesian approach to single-cell differential expression analysis. *Nat. Methods* **11**, 740–742 (2014).
55. L. Haghverdi, F. Buettner, F. J. Theis, Diffusion maps for high-dimensional single-cell analysis of differentiation data. *Bioinformatics* **31**, 2989–2998 (2015).
56. K. Campbell, C. Yau, http://biorxiv.org/content/early/2015/09/15/026872 (2015).
57. P. Diaconis, S. Goel, S. Holmes, Horseshoes in multidimensional scaling and local kernel methods. *Ann. Appl. Stat.* **2**, 777–807 (2008).
58. L. Van der Maaten, G. Hinton, Visualizing data using t-SNE. *J. Mach. Learn. Res.* **9**, 2579–2605 (2008).
59. O. Stegle, K. J. Denby, E. J. Cooke, D. L. Wild, Z. Ghahramani, K. M. Borgwardt, A robust Bayesian two-sample test for detecting intervals of differential gene expression in microarray time series. *J. Comput. Biol.* **17**, 355–367 (2010).
60. J. Yang, C. A. Penfold, M. R. Grant, M. Rattray, Inferring the perturbation time from biological time course data. *Bioinformatics* **32**, 2956–2964 (2016).
61. A.-I. Niu, Y.-q. Wang, H. Zhang, C.-h. Liao, J.-k. Wang, R. Zhang, J. Che, B. Su, Rapid evolution and copy number variation of primate *RHOXF2*, an X-linked homeobox gene involved in male reproduction and possibly brain function. *BMC Evol. Biol.* **11**, 298 (2011).
62. T. Sasaki, A. Shiohama, S. Minoshima, N. Shimizu, Identification of eight members of the Argonaute family in the human genome. *Genomics* **82**, 323–330 (2003).
63. N. D. Owens, I. L. Blitz, M. A. Lane, I. Patrushev, J. D. Overton, M. J. Gilchrist, M. J. Gilchrist, K. W. Y. Cho, Measuring absolute RNA copy numbers at high temporal resolution reveals transcriptome kinetics in development. *Cell Rep.* **14**, 632–647 (2016).
64. M. J. T. Stubbington, T. Lönnberg, V. Proserpio, S. Clare, A. O. Speak, G. Dougan, S. A. Teichmann, T cell fate and clonality inference from single-cell transcriptomes. *Nat. Methods* **13**, 329–332 (2016).

**Acknowledgments:** We thank the Wellcome Trust Sanger Institute Sequencing Facility for performing Illumina sequencing, Wellcome Trust Sanger Institute Single Cell Genomics Core Facility for single-cell sample processing, and the Wellcome Trust Sanger Institute Research Support Facility for care of the mice used in these studies. We thank QIMR Berghofer Flow Cytometry and Animal Facilities for expert advice and care of wild-type and transgenic mice. We acknowledge S. Lorenz, J. Cartwright, and T. Metcalf for expert technical assistance. We thank G. Emerton for constructing the database and the interface for accessing the data. We thank M. Raymond for work in defining cytokines and cell surface receptors. S. Ng is acknowledged for assistance with graphic design. **Funding:** This work was supported by Wellcome Trust (no. WT098051), European Research Council grant ThSWITCH (no. 260507), Australian National Health and Medical Research Council Project grant (number 1028641), and Career Development Fellowship (no. 1028643), University of Queensland; Australian Infectious Diseases Research Centre grants; and the Lister Institute for Preventive Medicine. K.R.J. was supported by grants from European Molecular Biology Laboratory Australia and OzEMalaR. F.O.B. was supported by the Lundbeck Foundation. M.Z. was supported by the Marie Curie Initial Training Networks grant "Machine Learning for Personalized Medicine" (EU FP7-PEOPLE Project Ref 316861, MLPM2012). **Author contributions:** T.L. and K.R.J. performed the scRNA-seq experiments. V.S. developed the GPfates model in collaboration with M.Z., N.D.L., O.S., and S.A.T. D.F.-R. and W.R.H. generated the PbTII mouse model. K.R.J., R.M., I.S., M.S.F.S., L.G.F., A.S.N., U.N.L., F.S.-F.-G., P.T.B., and C.R.E. performed the mouse experiments. T.L., V.S., K.R.J., L.-H.L., and F.O.B. analyzed the data and interpreted the results M.J.T.S. performed the TCR clonality analysis. T.L., K.R.J., R.M., O.B., A.H., and S.A.T. designed the experiments. O.S., A.H., and S.A.T. cosupervised the study. T.L., V.S., K.R.J., O.S., A.H., and S.A.T. wrote the manuscript. All authors have read and approved the manuscript. **Competing interests:** The authors declare that they have no competing interests. **Data and materials availability:** The data presented in this paper are publicly available in the ArrayExpress database with accession number E-MTAB-4388.

Submitted 14 October 2016
Accepted 23 January 2017
Published 3 March 2017
10.1126/sciimmunol.aal2192

**Citation:** T. Lönnberg, V. Svensson, K. R. James, D. Fernandez-Ruiz, I. Sebina, R. Montandon, M. S. F. Soon, L. G. Fogg, A. S. Nair, U. N. Liligeto, M. J. T. Stubbington, L.-H. Ly, F. O. Bagger, M. Zwiessele, N. D. Lawrence, F. Souza-Fonseca-Guimaraes, P. T. Bunn, C. R. Engwerda, W. R. Heath, O. Billker, O. Stegle, A. Haque, S. A. Teichmann, Single-cell RNA-seq and computational analysis using temporal mixture modeling resolves $T_H1/T_{FH}$ fate bifurcation in malaria. *Sci. Immunol.* **2**, eaal2192 (2017).

ANTIVIRAL IMMUNITY

# Type I interferons instigate fetal demise after Zika virus infection

Laura J. Yockey,[1] Kellie A. Jurado,[1] Nitin Arora,[2] Alon Millet,[1] Tasfia Rakib,[1] Kristin M. Milano,[3] Andrew K. Hastings,[4] Erol Fikrig,[4,5] Yong Kong,[6] Tamas L. Horvath,[7] Scott Weatherbee,[8] Harvey J. Kliman,[3] Carolyn B. Coyne,[2,9] Akiko Iwasaki[1,5]*



**Zika virus (ZIKV) infection during pregnancy is associated with adverse fetal outcomes, including microcephaly, growth restriction, and fetal demise. Type I interferons (IFNs) are essential for host resistance against ZIKV, and IFN-α/β receptor (IFNAR)–deficient mice are highly susceptible to ZIKV infection. Severe fetal growth restriction with placental damage and fetal resorption is observed after ZIKV infection of type I IFN receptor knockout (*Ifnar1*$^{-/-}$) dams mated with wild-type sires, resulting in fetuses with functional type I IFN signaling. The role of type I IFNs in limiting or mediating ZIKV disease within this congenital infection model remains unknown. In this study, we challenged *Ifnar1*$^{-/-}$ dams mated with *Ifnar1*$^{+/-}$ sires with ZIKV. This breeding scheme enabled us to examine pregnant dams that carry a mixture of fetuses that express (*Ifnar1*$^{+/-}$) or do not express IFNAR (*Ifnar1*$^{-/-}$) within the same uterus. Virus replicated to a higher titer in the placenta of *Ifnar1*$^{-/-}$ than within the *Ifnar1*$^{+/-}$ concepti. Yet, rather unexpectedly, we found that only *Ifnar1*$^{+/-}$ fetuses were resorbed after ZIKV infection during early pregnancy, whereas their *Ifnar1*$^{-/-}$ littermates continue to develop. Analyses of the fetus and placenta revealed that, after ZIKV infection, IFNAR signaling in the conceptus inhibits development of the placental labyrinth, resulting in abnormal architecture of the maternal-fetal barrier. Exposure of midgestation human chorionic villous explants to type I IFN, but not type III IFNs, altered placental morphology and induced cytoskeletal rearrangements within the villous core. Our results implicate type I IFNs as a possible mediator of pregnancy complications, including spontaneous abortions and growth restriction, in the context of congenital viral infections.**

## INTRODUCTION

Zika virus (ZIKV), an emerging mosquito-borne flavivirus, infected more than 500,000 individuals in 2015 and 2016 as it spread across the Americas and is now present in 62 countries across the world (*1*, *2*). Symptoms in healthy individuals are mostly mild, including fever, rash, and conjunctivitis, with most infections remaining asymptomatic. However, the recent outbreak has led to a worldwide concern over the ability of the virus to cause birth defects, including microcephaly, in infected pregnant women. In addition to microcephaly, ZIKV causes a range of other pregnancy complications, including intrauterine growth restriction (IUGR), spontaneous abortion, and stillbirth (*3*). Although ZIKV is primarily transmitted through the mosquito *Aedes aegypti*, increasing evidence supports sexual transmission as a route of infection: ZIKV RNA persists in semen for up to 6 months after infection, and there are a number of reports of ZIKV transmission among sexual partners in areas where mosquito transmission has not been reported (*4*, *5*). However, it is unknown whether the mechanisms of ZIKV-induced fetal pathology after mosquito-borne and sexually transmitted infection are similar.

The type I interferons (IFNs), including IFN-β and multiple subtypes of IFN-α, are key antiviral factors that mount a rapid and potent innate defense against viruses (*6*). Production of type I IFN is initiated through recognition of pathogen-associated molecular patterns, generated during viral infection (*7*, *8*). Type I IFNs bind to their receptor, IFNAR (IFN-α/β receptor), to induce an antiviral state through transcription of IFN-stimulated genes (ISGs), which restrict viral replication through a broad range of antiviral mechanisms (*6*, *9*). In addition to inducing cell-intrinsic antiviral effects, IFNs have an extensive range of biological activities, including activating adaptive immune responses (*10*), blocking cell proliferation, and inducing apoptosis (*11*). Thus, in addition to restricting viral infection, IFNs also have the potential to contribute to pathogenesis.

Multiple mouse models of ZIKV infection have demonstrated adverse pregnancy outcomes (*12*–*16*). Because ZIKV is unable to suppress the mouse IFNAR signaling as successfully as it suppresses human IFNAR signaling (*17*, *18*), many mouse models of ZIKV infection require blockade of IFNAR using an antibody, use of *Ifnar1*-deficient mice, or the use of high levels of virus to induce pathology (*12*, *14*, *19*). Pregnancy studies of ZIKV have used a model in which *Ifnar1*$^{-/-}$ females are crossed to wild-type (WT) males, creating *Ifnar1*$^{+/-}$ fetuses with an intact IFN response (*13*, *14*, *20*). In these models, fetuses develop severe growth restriction when pregnant dams are infected subcutaneously or intravaginally after embryonic day 7.5 (E7.5). If mice are infected earlier, between E4.5 and E6.5, most fetuses are resorbed. ZIKV infection in this model induces severe pathology of the placenta and abnormal placental architecture (*13*).

The placenta supports fetal development by facilitating exchange of nutrients and gases between the maternal and fetal blood. In addition, it serves as a barrier by preventing transfer of pathogens from the mother to the fetus (*3*, *21*). It is known that inflammation and infection can disrupt the function and development of the placenta, leading to IUGR, preeclampsia, preterm birth, and fetal demise, as demonstrated in humans and animal models (*22*, *23*). Others have

[1]Department of Immunobiology, Yale University School of Medicine, New Haven, CT 06520, USA. [2]Department of Pediatrics, University of Pittsburgh School of Medicine, Pittsburgh, PA 15224, USA. [3]Department of Obstetrics, Gynecology, and Reproductive Sciences, Yale University School of Medicine, New Haven, CT 06520, USA. [4]Section of Infectious Diseases, Department of Internal Medicine, Yale University School of Medicine, New Haven, CT 06520, USA. [5]Howard Hughes Medical Institute, Chevy Chase, MD 20815, USA. [6]Yale School of Public Health, New Haven, CT 06520, USA. [7]Program in Integrative Cell Signaling and Neurobiology of Metabolism, Section of Comparative Medicine New Haven, CT 06520, USA. [8]Department of Genetics, Yale University School of Medicine, New Haven, CT 06520, USA. [9]Center for Microbial Pathogenesis, Children's Hospital of Pittsburgh of UPMC (University of Pittsburgh Medical Center), Pittsburgh, PA 15224, USA.
*Corresponding author. Email: akiko.iwasaki@yale.edu

also suggested that the immune response to ZIKV at the maternal-fetal interface may be responsible for ZIKV-associated birth defects (*24*). In addition, type I IFNs have been shown to mediate preterm birth in mouse models (*25*). On the other hand, IFNs are known to have important roles in supporting normal pregnancy and protecting the fetus from viral infections (*26*). For example, ISGs are up-regulated during implantation in mice and humans (*27*), and human syncytiotrophoblasts constitutively express type III IFNs (IFN-λs), making them resistant to infection by viruses (*28*, *29*). In addition, type III IFNs play a role in restricting ZIKV vertical transmission in mice (*20*).

In this study, we interrogate the effect of type I IFN signaling on fetal development using a mouse model of ZIKV infection. Vaginal or subcutaneous ZIKV infection of *Ifnar1*$^{-/-}$ dams crossed with *Ifnar1*$^{+/-}$ sires enabled us to investigate the role of IFNAR signaling in antiviral protection and disease. Paradoxically, our results revealed a detrimental role of fetal IFNAR signaling in mediating IUGR and fetal resorption by causing abnormal placental development.

## RESULTS

### Fetal IFNAR signaling instigates fetal demise despite controlling ZIKV replication

In our previous studies, we observed that vaginal infection of mice lacking the transcription factors upstream of type I IFN, *Irf3*$^{-/-}$ *Irf7*$^{-/-}$ dams crossed to *Irf3*$^{-/-}$ *Irf7*$^{-/-}$ sires, had higher levels of ZIKV in the placenta but had minimal growth restriction compared with fetuses from *Ifnar*$^{-/-}$ dams crossed to WT sires (*14*). Although the *Irf3*$^{-/-}$ *Irf7*$^{-/-}$ mice are capable of responding to IFN, we hypothesize that the lack of pathology in this model, despite high levels of virus, is due to the lack of IFN induction in the first place. Consistent with this, we observed that the ISGs were induced in *Ifnar*$^{+/-}$ fetuses and placenta, but they were absent in the *Irf3*$^{-/-}$ *Irf7*$^{-/-}$ matings, correlating with the level of pathology (fig. S1, A to F). These findings led us to hypothesize that IFN signaling, rather than the levels of virus, mediates fetal pathology after ZIKV infection.

To directly test the role of type I IFNs in antiviral defense and fetal development after ZIKV infection, we crossed *Ifnar1*$^{-/-}$ females with *Ifnar1*$^{+/-}$ males, producing a mixture of *Ifnar1*$^{-/-}$ and *Ifnar1*$^{+/-}$ fetuses in the same litter (Fig. 1A). Pregnant dams were infected intravaginally with $1.5 \times 10^5$ plaque-forming units (PFU) of Cambodian strain of ZIKV on either E5.5 or E.8.5, corresponding to the mid and late first trimester in humans (*30*), respectively. Fetuses were harvested on E17.5, close to term. We observed resorption of all fetuses of the *Ifnar1*$^{+/-}$ genotype when dams were infected with ZIKV on E5.5 (Fig. 1, B and C). However, all *Ifnar1*$^{-/-}$ littermates continued to develop after infection on E5.5, indicating that a functional copy of *Ifnar1* is required to mediate fetal demise after early ZIKV infection of pregnant dams (Fig. 1, B and C). When dams were challenged with ZIKV on E8.5, *Ifnar1*$^{+/-}$ fetuses were not resorbed but showed more severe growth restriction compared with their *Ifnar1*$^{-/-}$ littermates (Fig. 1, B and C). Analysis of viral RNA showed that, after E8.5 infection, there was more viral RNA detected in the placentas of the *Ifnar1*$^{-/-}$ littermates compared with their *Ifnar1*$^{+/-}$ littermates on E17.5 [9 days postinfection (dpi)] (Fig. 1D). Plaque assays revealed 1000-fold higher levels of infectious virus in the *Ifnar*$^{-/-}$ placentas compared with *Ifnar*$^{+/-}$ placentas (fig. S2A). After infection at E5.5, there were comparable levels of virus in the *Ifnar1*$^{-/-}$ placenta and the resorbed *Ifnar1*$^{+/-}$ conceptus, and these levels were lower than what was observed for the E8.5 *Ifnar1*$^{-/-}$ placentas on E17.5 (12 dpi) (Fig. 1D). In the fetus, viral RNA was present but at low levels in both genotypes and at both time points of infection (Fig. 1E), and infectious virus was below the limit of detection for most fetuses after infection at E8.5 (fig. S2B). These results indicated that IFNAR signaling in the conceptus, despite controlling ZIKV replication in the placenta, leads to fetal demise after congenital infection.

To understand how and when development is blocked in the *Ifnar1*$^{+/-}$ conceptus, we harvested fetuses at various days after infection of dams on E5.5. Gross examination of the *Ifnar1*$^{+/-}$ fetuses revealed no overt differences with *Ifnar1*$^{-/-}$ fetuses or with uninfected counterparts on E9.5 (Fig. 2, A and B). On E10.5, there was a modest reduction in size of the *Ifnar1*$^{+/-}$ fetuses, and in 1 of 6 litters, all *Ifnar1*$^{+/-}$ fetuses were resorbed (3 of 17), but fetuses otherwise appeared grossly normal (Fig. 2, A and B). However, by E11.5, the majority of *Ifnar1*$^{+/-}$ fetuses (7 of 11) were dead, and by E12.5, all *Ifnar1*$^{+/-}$ fetuses were resorbed (Fig. 2, A and B). Thus, IFNAR-dependent fetal demise after early ZIKV infection occurs between E10.5 and E12.5.

### Placental labyrinth architecture is abnormal in IFNAR-competent concepti

Postimplantation death between E5.5 and E12.5 is typically caused by defects in the fetal red blood cells (RBCs), vasculature, heart, or the placenta (*31*). Thus, we focused on analysis of the placenta, which develops between E8.5 and E10.5 (*32*, *33*). Global transcriptional analysis by RNA sequencing (RNA-seq) of placentas at E10.5 demonstrated evidence of active IFNAR signaling in the *Ifnar1*$^{+/-}$ placenta, with robust induction of hundreds of ISGs (fig. S3 and table S2). To determine which cells are infected by ZIKV, we stained the E10.5 placenta and decidua for ZIKV antigen. The decidua is the maternally derived endometrial lining of the uterus, and the fetus-derived placenta is composed of the junctional zone and labyrinth zone, where nutrient exchange occurs between the maternal and fetal blood (Fig. 3A) (*21*, *32*). We detected rare ZIKV-infected leukocytes (CD45$^+$ cells) in both the *Ifnar1*$^{+/-}$ and *Ifnar1*$^{-/-}$ decidua but not in the underlying placenta (fig. S4). These cells likely represent decidual macrophages or dendritic cells, and this is consistent with a report showing ZIKV RNA in leukocytes of maternal tissue surrounding the placenta in an infected patient (*34*, *35*). These results suggest that ZIKV infects maternal cells in the decidua, which may be a source of type I IFNs that act on fetal cells of the underlying junctional zone or labyrinth layer to induce robust ISGs.

Next, we performed histological analysis of the developing placenta and decidua to determine the impact of ISG expression. At E9.5, the placenta and decidua were grossly normal in all groups: They showed normal decidualization, a layer of trophoblast giant cells, and a labyrinth with both maternal blood spaces, containing anucleated maternal RBCs, and fetal blood spaces, containing nucleated fetal RBCs (fig. S5). By E10.5, we observed marked abnormality in the labyrinth of the ZIKV-infected *Ifnar1*$^{+/-}$, but not *Ifnar1*$^{-/-}$, placentas (Fig. 3B). Specifically, the labyrinth appeared to have denser cellularity, with decreased vascular spaces and minimal fetal blood cell content (Fig. 3B, arrows). In addition, there were abnormal spheroid structures (Fig. 3B, asterisk), likely composed of trophoblasts. The decidua and trophoblast giant cells were comparable between all groups. Although the labyrinth of the infected *Ifnar1*$^{-/-}$ placentas looked more disorganized with increased cellularity compared with the uninfected controls, there were still abundant fetal RBCs within the fetal blood space (Fig. 3B). By E11.5, when most ZIKV-infected *Ifnar1*$^{+/-}$ fetuses were resorbed, the labyrinth appeared disorganized with reduced fetal blood vessels and abundant spheroid structures, and by E12.5, *Ifnar1*$^{+/-}$ placentas show almost no maternal or fetal blood vessels (fig. S5). In contrast, the labyrinths of *Ifnar1*$^{-/-}$ placentas on E11.5 and E12.5 were

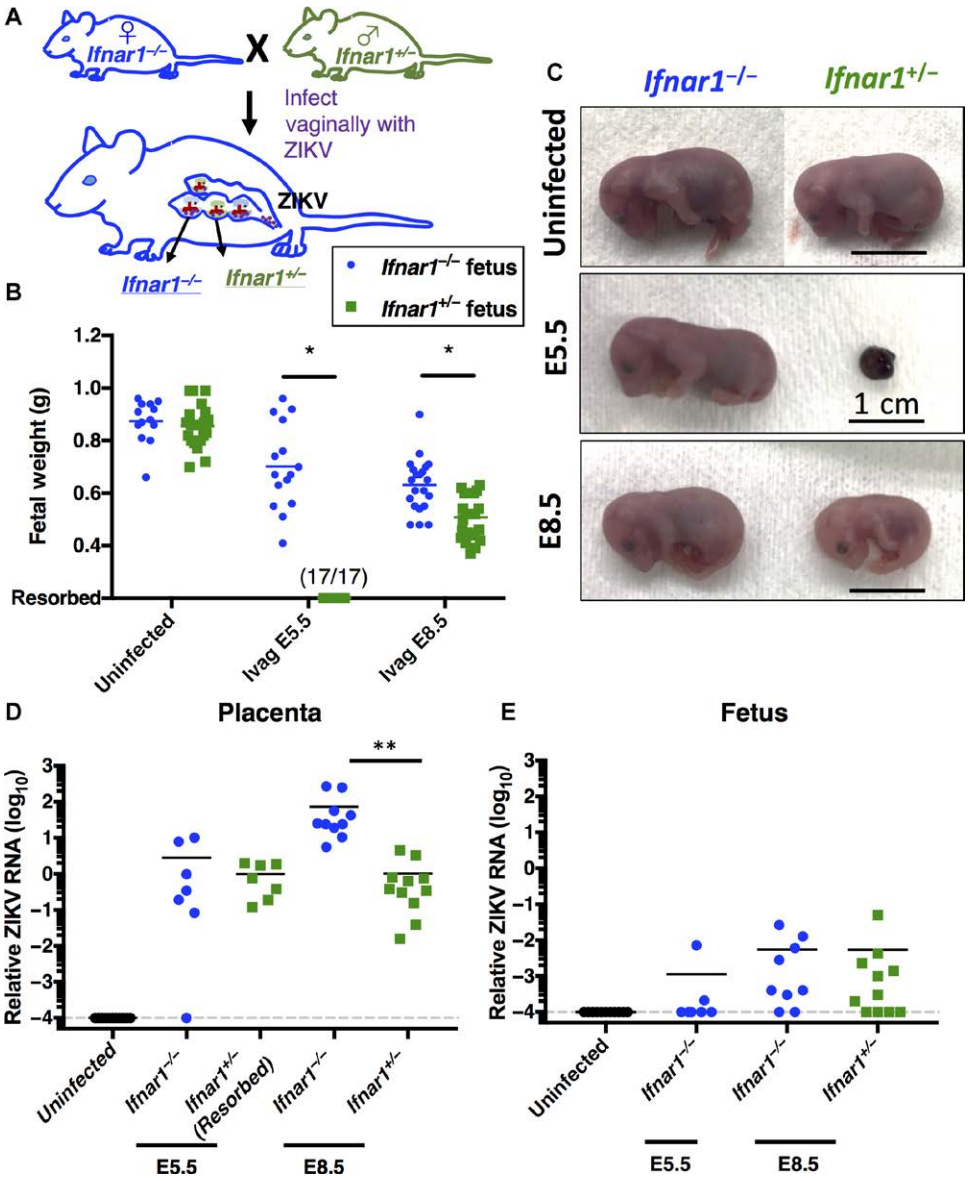


**Fig. 1. Fetal IFN signaling leads to severe IUGR and resorption after ZIKV infection.** *Ifnar1*$^{-/-}$ females mated to *Ifnar1*$^{+/-}$ males were infected intravaginally (Ivag) with $1.5 \times 10^5$ PFU Cambodian ZIKV on E5.5 or E8.5 and harvested on E17.5. (**A**) Schematic showing mating strategy. Fetal weights were measured (**B**), and fetuses were visually inspected (**C**). RNA was isolated from the placenta or resorbed conceptus (**D**) or fetus (**E**) to determine ZIKV levels. Relative ZIKV levels were determined by normalization to *Hprt*. Individual data points with mean are shown. For fetal weights, ZIKV E5.5 ($n = 15$ *Ifnar1*$^{-/-}$ and $n = 17$ *Ifnar1*$^{+/-}$ from four litters); ZIKV E8.5 ($n = 21$ *Ifnar1*$^{-/-}$ and $n = 22$ *Ifnar1*$^{+/-}$ from six litters); and uninfected ($n = 13$ *Ifnar1*$^{-/-}$ and $n = 21$ *Ifnar1*$^{+/-}$ from four litters). For ZIKV RNA, ZIKV E5.5 ($n = 7$ *Ifnar1*$^{-/-}$ and $n = 7$ *Ifnar1*$^{+/-}$ from three litters); ZIKV E8.5 ($n = 9$ to 10 *Ifnar1*$^{-/-}$ and $n = 11$ *Ifnar1*$^{+/-}$ from five litters); and uninfected ($n = 11$ from three litters with both genotypes pooled). Data are pooled from at least two independent experiments from each infection time point. Scale bars, 1 cm. *$P < 0.05$ and ** $P < 0.01$ by Tukey's multiple comparison test.

indistinguishable from those of the uninfected controls with abundant adjacent fetal and maternal blood spaces (fig. S5). These results suggested that type I IFN induced in response to ZIKV interferes with development of fetal vasculature in the placenta labyrinth.

To examine this possibility, we stained tissue sections of E10.5 placentas from dams infected on E5.5 with cytokeratin (CK) to label trophoblasts and CD31 to label blood vessels. We observed a network of closely associated CD31$^+$ (endothelial cell demarcating fetal blood space) and CK-positive (trophoblast demarcating maternal blood space) structures in both uninfected and ZIKV-infected *Ifnar1*$^{-/-}$ placentas (Fig. 3C). In contrast, CD31 staining in the ZIKV-infected *Ifnar1*$^{+/-}$ placentas was markedly reduced, wherein the limited CD31$^+$ cells were found on the edge of the placental structure devoid of luminal spaces (Fig. 3C). Immunohistochemistry staining of the placentas with anti-CD31 antibody confirmed the collapsed vasculature and reduced number of the fetal endothelial cells (fig. S6A). Anti–E-cadherin antibody, which stains the trophoblasts, revealed that many of the densely packed cells in the E10.5 placenta were Ecad$^+$ trophoblasts (fig. S6B). These results indicate that defective development of fetal vasculature and abnormal trophoblasts in the labyrinth immediately precede the death of the IFNAR-intact fetus after ZIKV infection of pregnant dams.

### IFNAR signaling leads to increased apoptosis in the placental labyrinth, an abnormal maternal-fetal barrier, and fetal hypoxia

On the basis of the known functions of type I IFNs, we hypothesized that IFNAR signaling in the fetus inhibits placental development through three possible mechanisms: inducing immune cell recruitment and invasion of the labyrinth, blocking cellular proliferation, or inducing cell death (*10*, *11*). At E10.5, CD45$^+$ leukocytes were restricted to the decidua in all groups and did not infiltrate the CK-positive junctional zone or the labyrinth (fig. S6C), ruling out inflammatory leukocyte infiltration as the mechanism of fetal demise. Next, we examined cell proliferation in the labyrinth by Ki67 staining. All placentas showed abundant Ki67$^+$ cells at E10.5 (Fig. 4A), excluding the role of IFNAR signaling in blocking cell proliferation as the mechanism of fetal demise. To examine whether IFNAR signaling is inducing cell death, we stained for activated (cleaved) caspase-3 (Casp3) as a marker of apoptotic cells. There was no Casp3-positive staining in the labyrinth of the uninfected placentas or infected *Ifnar1*$^{-/-}$ placentas at E10.5 (Fig. 4B). In contrast, in the infected *Ifnar1*$^{+/-}$ placenta, we detected Casp3 staining in the labyrinth in a pattern consistent with the endothelial cells, fetal blood cells, or adjacent trophoblasts surrounding the spheroid structure (Fig. 4B). These results are consistent with a previous report (*13*) and suggest a role for IFNAR in mediating apoptosis of fetal

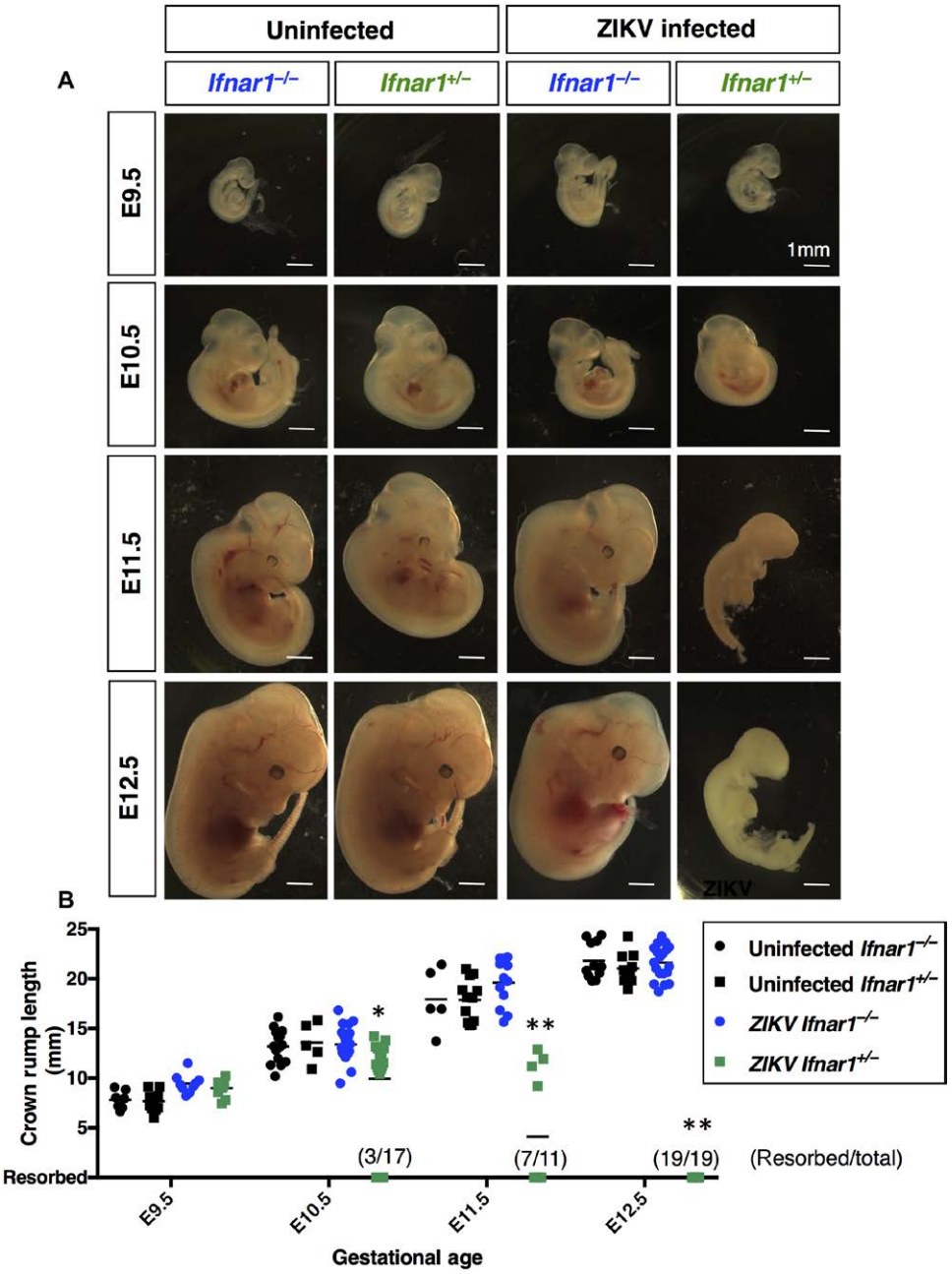


**Fig. 2. ZIKV-infected fetuses with intact IFN signaling are resorbed between E10.5 and E12.5.** *Ifnar1*$^{-/-}$ females mated to *Ifnar1*$^{+/-}$ males were infected intravaginally with $1.5 \times 10^5$ PFU Cambodian ZIKV at E5.5 and harvested at indicated time points. (**A**) Representative images of three to five litters for infected and two to three litters for uninfected are shown per time point. Scale bars, 1 mm. (**B**) Crown-rump length was measured by tracing distance from crown of head to end of tail using ImageJ. Means with individual points are graphed. Data points shown represent the following: E9.5 uninfected *Ifnar1*$^{-/-}$ ($n = 7$) and *Ifnar1*$^{+/-}$ ($n = 12$ from two litters) and infected *Ifnar1*$^{-/-}$ ($n = 9$) and *Ifnar1*$^{+/-}$ ($n = 10$ from three litters); E10.5 uninfected *Ifnar1*$^{-/-}$ ($n = 15$) and *Ifnar1*$^{+/-}$ ($n = 5$ from three litters) and infected *Ifnar1*$^{-/-}$ ($n = 24$) and *Ifnar1*$^{+/-}$ ($n = 17$ from six litters); E11.5 uninfected *Ifnar1*$^{-/-}$ ($n = 5$) and *Ifnar1*$^{+/-}$ ($n = 12$ from three litters) and infected *Ifnar1*$^{-/-}$ ($n = 12$) and *Ifnar1*$^{+/-}$ ($n = 11$ from three litters); E12.5 uninfected *Ifnar1*$^{-/-}$ ($n = 11$) and *Ifnar1*$^{+/-}$ ($n = 11$ from three litters) and infected *Ifnar1*$^{-/-}$ ($n = 19$) and *Ifnar1*$^{+/-}$ ($n = 19$ from five litters). Data are pooled from at least two independent experiments from each infection time point. *$P < 0.05$ and **$P < 0.0001$ compared with all other groups by Tukey's multiple comparison test. No significant differences were found between other groups.

endothelial cells and trophoblasts as an underlying mechanism of placental dysfunction.

To examine the abnormal placenta architecture at a cellular level, we performed electron microscopy to analyze the maternal-fetal interface on E10.5. In the uninfected placentas and infected *Ifnar1*$^{-/-}$ placentas, the expected trilaminar interhemal barrier was seen, with anucleated maternal blood (mrbc) and nucleated fetal blood (frbc) being separated by four layers of cells: the sinusoidal trophoblast giant cell (stgc) that directly contacts the maternal blood, two continuous syncytial layers of trophoblast that are closely connected (ST-I and ST-II), and a layer of endothelial cells (ec) that directly contact the fetal blood (Fig. 4C) (*32*, *36*). ST-I and ST-II were tightly adhered to one another (Fig. 4C, arrows). There was no mixing between maternal and fetal blood in the uninfected placenta. In the infected *Ifnar1*$^{+/-}$ placentas, there were multiple instances of mixing between the maternal and fetal blood in the labyrinth (Fig. 4C). When separated maternal and fetal circulations were found, the barrier between the two was highly abnormal, with no evidence of the normal four-cell layer barrier and breakdown between cells making the maternal-fetal barrier (Fig. 4C). Thus, IFNAR signaling in the placenta leads to an abnormal maternal-fetal blood barrier with local breakdown.

On the basis of the findings of an abnormal vasculature in the placental labyrinth and abnormal maternal-fetal barrier, we examined the transcriptional changes in the fetus to examine whether lack of adequate gas exchange between mother and fetus may be contributing to fetal demise. We found that hypoxia response genes, including *Vegfa*, *Adm*, *Bnip3*, *Glut1*, and *Pfkfb3*, were all significantly upregulated in the ZIKV-infected *Ifnar1*$^{+/-}$ fetuses relative to uninfected controls and to their infected *Ifnar1*$^{-/-}$ littermates (Fig. 5, A to E) (*37*, *38*). Thus, the death of the *Ifnar1*$^{+/-}$ fetuses after ZIKV infection is preceded by hypoxia.

## IFNAR signaling mediates fetal death after subcutaneous ZIKV infection and poly(I:C) treatment

To determine whether IFNAR signaling mediates fetal resorption after other routes of ZIKV infection and with other strains

www.SCIENCEIMMUNOLOGY.org 5 January 2018 Vol 3 Issue 19 aao1680

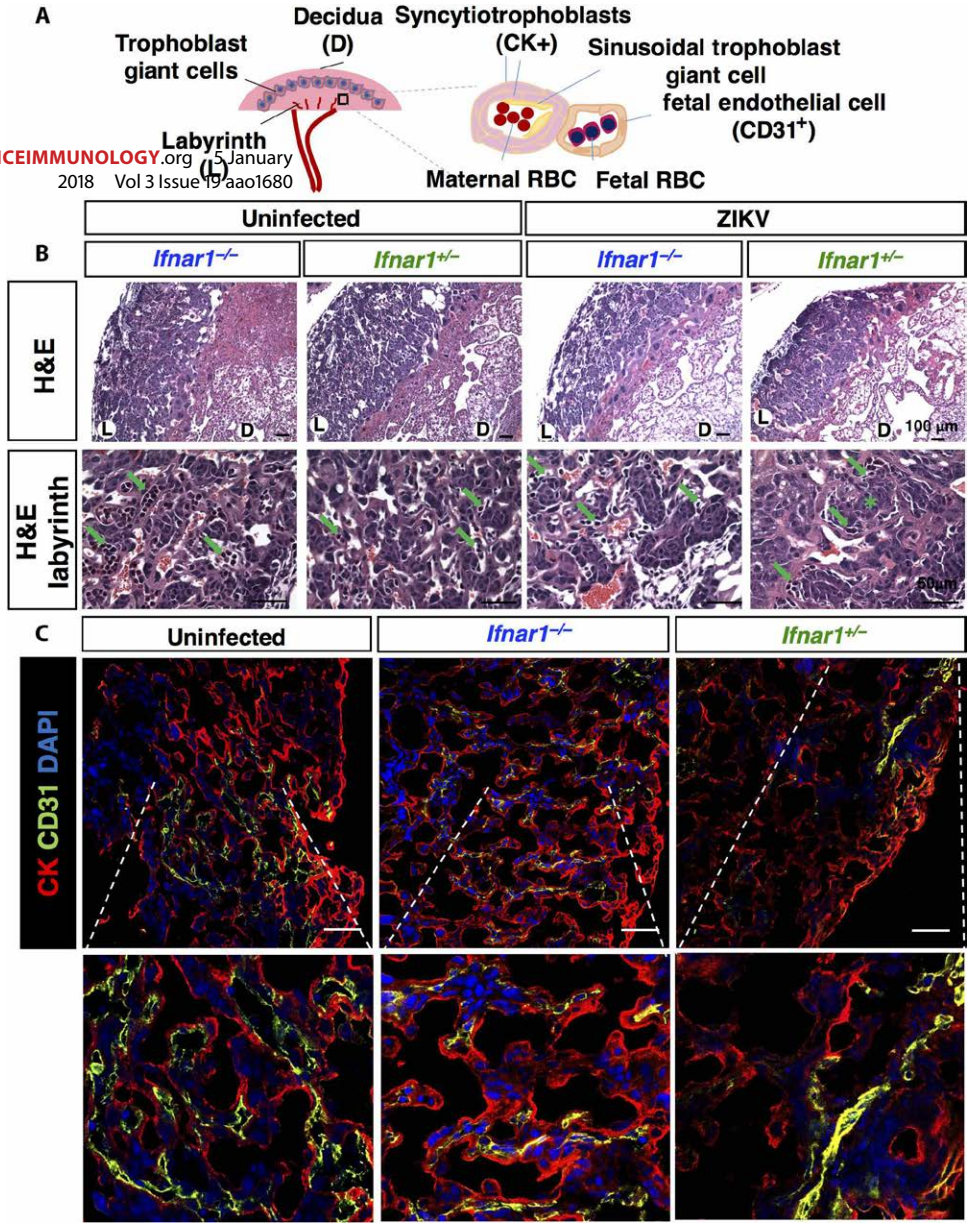


**Fig. 3. Placenta architecture of *Ifnar1*$^{+/-}$ fetuses is disrupted at E10.5.** *Ifnar1*$^{-/-}$ females mated to *Ifnar1*$^{+/-}$ males were infected intravaginally with $1.5 \times 10^5$ PFU Cambodian ZIKV at E5.5 and harvested at E10.5. (**A**) Schematic of decidua and placenta architecture and cell types. (**B**) Placentas were fixed in PFA, and paraffin-embedded sections were stained by H&E. Whole placenta and decidua (top) or magnified labyrinth (bottom) are shown. Representative images of 10 placentas/deciduas per genotype from five litters were analyzed for infected, and four placentas/deciduas per genotype per time point from two litters were analyzed for uninfected. Labyrinth, L, and decidua, D, are labeled with respective letters. The asterisk indicates abnormal spheroid structure. Arrows indicate fetal RBCs. Scale bars, 100 μm (top) and 50 μm (bottom). (**C**) PFA-fixed frozen sections from infected littermates were costained for CK (red, trophoblasts), CD31 (green, blood vessels), and DAPI (blue). Representative images from at least three placentas per genotype from at least two litters are shown. Scale bars, 75 μm.

of ZIKV, we challenged *Ifnar1*$^{-/-}$ females crossed with *Ifnar1*$^{+/-}$ males subcutaneously with the Brazilian strain of ZIKV on E6.5 (*13*). After challenging with a high dose ($3.4 \times 10^5$ PFU) of ZIKV, most *Ifnar1*$^{+/-}$ fetuses were resorbed by E12.5, but *Ifnar1*$^{-/-}$ fetuses continued to develop (fig. S7, A and B). To analyze fetal development at later time points without maternal lethality, we challenged *Ifnar1*$^{-/-}$ females mated with *Ifnar1*$^{+/-}$ males with a sublethal dose of ZIKV ($1 \times 10^3$ PFU) subcutaneously at E6.5 and harvested the fetuses at E17.5. Again, similar to the vaginal ZIKV infection, all *Ifnar1*$^{+/-}$ fetuses were resorbed, but *Ifnar1*$^{-/-}$ fetuses were grossly normal (fig. S7, C and D). Thus, IFNAR-dependent fetal resorption occurs after subcutaneous and intravaginal ZIKV challenge, with both Brazilian and Cambodian ZIKV strains.

To examine whether IFNAR signaling is sufficient to induce fetal resorption independent of ZIKV infection, we challenged mice with polyinosinic/polycytidylic acid [poly(I:C)], a double-stranded RNA viral mimic capable of eliciting robust type I IFN responses (*39*). After intraperitoneal injection of 200 μg of poly(I:C) at E7.5, all fetuses of WT females mated with WT males were resorbed by E9.5, and we could not recover any fetal material in five of six injected females by E10.5, consistent with previous reports (Fig. 6, A and C) (*40*). When we challenged *Ifnar1*$^{-/-}$ females crossed with *Ifnar1*$^{+/-}$ males with poly(I:C) on E7.5, the majority of both *Ifnar1*$^{-/-}$ and *Ifnar1*$^{+/-}$ fetuses continued to develop as examined on E10.5 and E12.5 (Fig. 6, B and C). Thus, maternal IFNAR signaling was necessary for mediating poly(I:C)-induced fetal resorption.

### Type I IFN (but not type III IFN) treatment of human midgestation villous explants leads to deformation

To determine the impact of type I IFNs on the human placenta, we treated midgestation (19 to 23 weeks) human chorionic villous explants with a type I IFN, recombinant IFN-β, or a type III IFN, recombinant IFN-λ3. Isolated villi were treated with recombinant IFN within hours after their isolation, when their structure and morphology remained completely intact, as characterized by a continuous layer of CK-positive trophoblasts covering the surfaces of the isolated villi [Fig 7, A (left) and B (top)]. After ~16 to 20 hours of treatment, the architecture of IFN-β–treated villi became markedly abnormal, with areas of aggregated nuclei formed at the distal end of villi treated with IFN-β (either 100 or 1000 U) [Fig. 7, A (arrows) to C]. In contrast, treatment of the villous explants with IFN-λ3 showed no gross impact (Fig. 7, A and C). The abnormal villous structures resembled syncytial knots, which are associated with pathological states of pregnancy; sprouts, which represent overproliferation of the syncytiotrophoblast layer; or apoptotic shedding

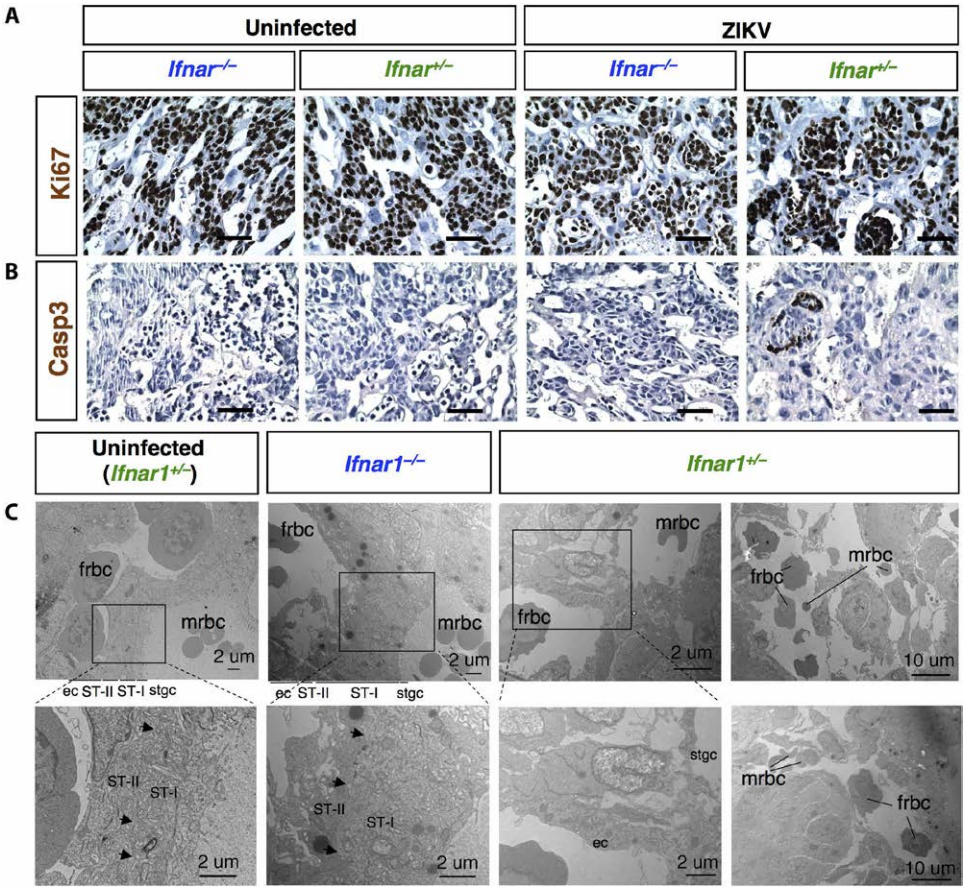


**Fig. 4. *Ifnar1*$^{+/-}$ placentas show increased apoptosis and abnormal maternal-fetal blood barrier.** *Ifnar1*$^{-/-}$ females mated to *Ifnar1*$^{+/-}$ males were infected intravaginally with $1.5 \times 10^5$ PFU Cambodian ZIKV at E5.5 and harvested at E10.5. Paraffin-embedded sections were stained for Ki67 (**A**, dividing cells) or cleaved Casp3 (**B**, apoptotic cells) with DAB. From (A) and (B), images from labyrinth are shown. Scale bars, 50 μm. Representative images from at least three placentas/deciduas per condition from at least two litters are shown. (**C**) Placentas were fixed at least 24 hours in formaldehyde with 2.5% glutaraldehyde at 4°C. The labyrinth was dissected and processed for electron microscopy. Uninfected *Ifnar1*$^{+/-}$ labyrinth shows four layers of cells between frbc and mrbc: fetal endothelial cell (ec), two syncytiotrophoblast layers (ST-II, ST-I), and the sinusoidal trophoblast giant cell (stgc). Infected *Ifnar1*$^{-/-}$ placenta is similar to the uninfected control. The barrier between maternal and fetal blood of ZIKV-infected *Ifnar1*$^{+/-}$ placentas is highly abnormal with unfused cells (left). ZIKV-infected *Ifnar1*$^{+/-}$ shows multiple examples of mixing between maternal and fetal blood (right). Scale bars, 2 or 10 μm as labeled on the image. Multiple sections and planes from one placenta per condition were analyzed.

(*41*, *42*). In addition to the formation of syncytial knot– or sprout-like structures, we noted that IFN-β–treated villi also exhibited alterations in the actin cytoskeleton within the core of the villi as characterized by actin filament disassembly, suggesting widespread damage to the villi (Fig. 7D, bottom). To examine the global transcriptional changes in response to IFN-β and IFN-λ3 treatment, we performed whole-genome RNA-seq on villi treated with IFN-β or IFN-λ isolated from three different placental preparations. We found that both IFN-β and IFN-λ treatment induced significant transcriptional changes (273 and 101 total genes, respectively; $P < 0.05$) as illustrated by MA plots (Fig. 8A). However, we found that there was little overlap between the genes induced by IFN-β and IFN-λ exposure—whereas IFN-β treatment induced the up-regulation of the majority of transcripts (260 of 273), IFN-λ treatment correlated with the down-regulation of the majority of transcripts (89 of 101) (Fig. 8B). Consistent with this differential expression pattern, only 12 transcripts were differentially expressed by both IFN-β and IFN-λ treatment (Fig. 8C). We found that whereas IFN-β treatment induced many known ISGs, IFN-λ treatment had little impact on ISG expression (Fig. 8, D to F). In addition, consistent with the significant morphologic alterations of villous architecture induced by IFN-β treatment, IFN-β–treated villi exhibited suppression (by ~4-fold, $P = 0.04$) in the expression of the β chain of human chorionic gonadotropin, which is exclusively produced by syncytiotrophoblasts and is associated with placental function. Collectively, these data suggest that type I IFN is sufficient to induce morphological alterations and also possibly adversely affect placental function in the human developing placental villi.

## DISCUSSION

Our findings highlight the detrimental impact of type I IFNs on the developing placenta and fetus by demonstrating that only the fetuses with a functional copy of IFNAR are resorbed after ZIKV infection. IFNAR signaling in the conceptus leads to abnormal placenta labyrinth development with apoptosis in the labyrinth, impaired fetal endothelial development, and disrupted maternal-fetal blood barrier. IFNAR signaling was important in controlling viral replication in the placenta. Despite this, IFNAR-mediated pathology outweighed the benefit of IFNAR-dependent control of viral replication. How exactly IFNAR signaling leads to the observed labyrinth pathology is unknown. The hypoxic state of the IFNAR-sufficient fetus, likely resulting from the fetal endothelial disruption, suggests an impaired delivery of oxygen and possibly nutrients being the underlying cause of fetal demise. Our results do not rule out a role for the direct action of ZIKV in mediating certain aspects of pathology, such as microcephaly, ocular defects, or other neurological abnormalities, which we do not address in this study. Despite having a less severe phenotype than their *Ifnar*$^{+/-}$ littermates, *Ifnar*$^{-/-}$ mice did exhibit growth restriction compared with their uninfected counterparts, consistent with previous reports (*43*). This growth restriction may be due to poor maternal health, but it could also be indicative of IFNAR-independent causes of birth defects, including direct pathogenic effects of the virus infection or immune response unrelated to type I IFNs. One limitation to our study is that the host-pathogen interactions, including the suppression of host IFNAR signaling by ZIKV NS5 protein, are not preserved in mice. Thus, to what extent the mouse model recapitulates ZIKV infection and disease in humans is unknown. An additional limitation is that the structure and development of the

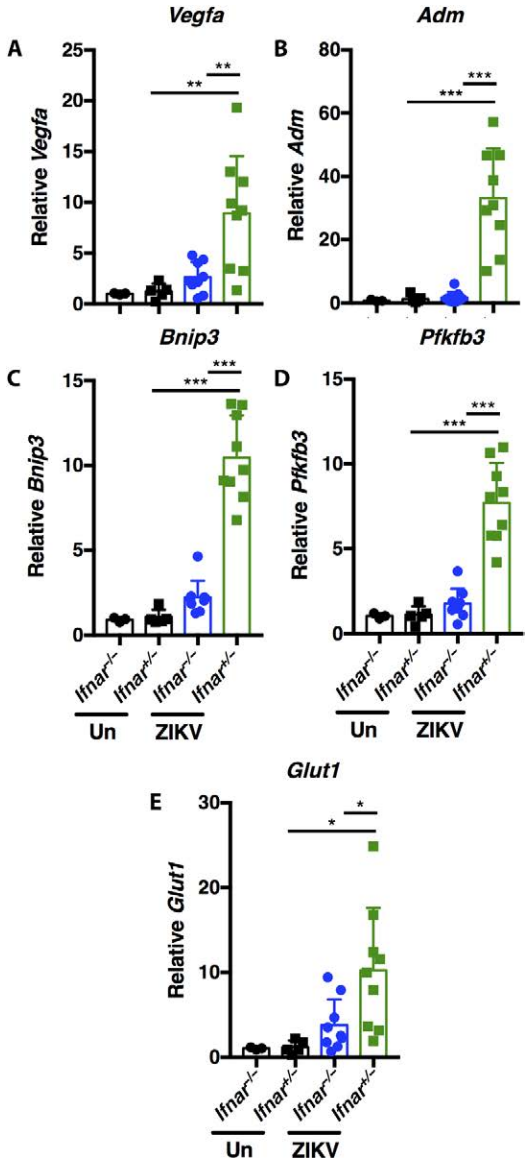


**Fig. 5. ZIKV-infected *Ifnar1*$^{+/-}$ fetuses show up-regulated hypoxia response genes just before demise.** *Ifnar1*$^{-/-}$ females mated to *Ifnar1*$^{+/-}$ males were infected intravaginally with $1.5 \times 10^5$ PFU Cambodian ZIKV at E5.5 and harvested at E10.5. RNA was extracted from fetuses, and expression of previously reported hypoxia-response genes *Vegfa* (**A**), *Adm* (**B**), *Bnip3* (**C**), *Pfkfb3* (**D**), and *Glut1* (**E**) analyzed by reverse transcription qPCR. Data represent $n = 9$ fetuses per genotype from three litters from ZIKV-infected litters and $n = 3$ *Ifnar1*$^{-/-}$ and $n = 5$ *Ifnar1*$^{+/-}$ fetuses from two uninfected litters. Data are pooled from at least two independent experiments per group. *$P < 0.05$, **$P < 0.01$, and ***$P < 0.0001$ by Tukey's multiple comparison test. Data were normalized to *Hprt* and represented as fold change over *Ifnar*$^{-/-}$ uninfected placentas.

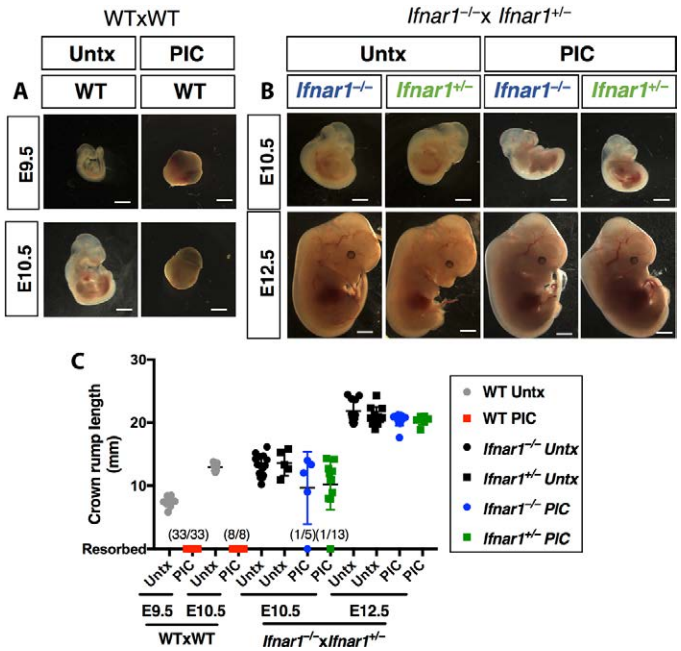


**Fig. 6. Poly(I:C) injection of pregnant dams leads to fetal resorption in a maternal-IFNAR–dependent fashion.** WT females mated to WT males (**A**) or *Ifnar1*$^{-/-}$ females mated to *Ifnar1*$^{+/-}$ males (**B**) were injected with 200-μg HMW poly(I:C) (PIC) at E7.5. Representative images from mice harvested between E9.5 and E12.5 are shown. Scale bars, 1 mm. (**C**) Crown-rump length was measured using ImageJ. Mean with SD and individual data points are shown. Data points represent the following: WTxWT litters untreated E9.5 ($n = 17$ from two litters), PIC E9.5 ($n = 33$ from four litters), untreated E10.5 ($n = 13$ from two litters), and PIC E10.5 ($n = 8$ from one litter); additional five injected litters showed no fetal remnants at time of harvest at E10.5. For *Ifnar1*$^{-/-}$x*Ifnar1*$^{+/-}$ litters, untreated E10.5 ($n = 15$ *Ifnar1*$^{-/-}$ and $n = 5$ *Ifnar1*$^{+/-}$ from three litters), PIC E10.5 ($n = 5$ *Ifnar1*$^{-/-}$ and $n = 11$ *Ifnar1*$^{+/-}$ from two litters), untreated E12.5 ($n = 11$ *Ifnar1*$^{-/-}$ and $n = 11$ *Ifnar1*$^{+/-}$ from three litters), and PIC E12.5 ($n = 13$ *Ifnar1*$^{-/-}$ and $n = 7$ *Ifnar1*$^{+/-}$ from two litters). Uninfected measurements for *Ifnar1*$^{-/-}$x*Ifnar1*$^{+/-}$ litters are the same as those shown in Fig.2B.

mouse placenta are significantly different from those of the human placenta, making it difficult to directly compare the pathological changes seen in the mouse placenta with those of humans.

To extend our findings to humans, we examined the impact of recombinant IFN-β on second-trimester villous explants. This experimental system allowed us to examine the impact of type I IFNs in the pre-existing syncytium and in a model that fully retains the architecture and multicellular composition of the human placenta. IFN-β exposure induced morphological changes in the human placenta, which correlated with alterations in syncytial and actin cytoskeletal architecture. Altered syncytial morphology resembled syncytial knots, a feature commonly associated with placentas of adverse pregnancy outcomes, including preeclampsia (*42*). Although common in full-term placentas, syncytial knots are rare in normal midgestation pregnancies (*44*). Given the short time scale over which they developed, they could also be apoptotic shedding of damaged cells. Our study required high levels (1000 U) of IFN-β to produce these effects, although we did note the appearance of syncytial knot–like structures at lower levels (100 U). It is difficult to assess whether this level of IFN may be present locally in congenital infections and what effects IFN-β may have over a longer period and during earlier stages of development, which were not possible to assess in this model. We found that treatment of villi with recombinant type III IFN, IFN-λ3, was not associated with the altered villous morphology or a strong ISG induction. These are consistent with previous reports that the syncytium constitutively produces IFN-λs (*28*) and may suggest that type III IFNs primarily function in an autocrine and paracrine manner to defend the developing fetus against viruses, as has been shown to occur in mice (*20*). Our data also showed that type I IFN, but not type III

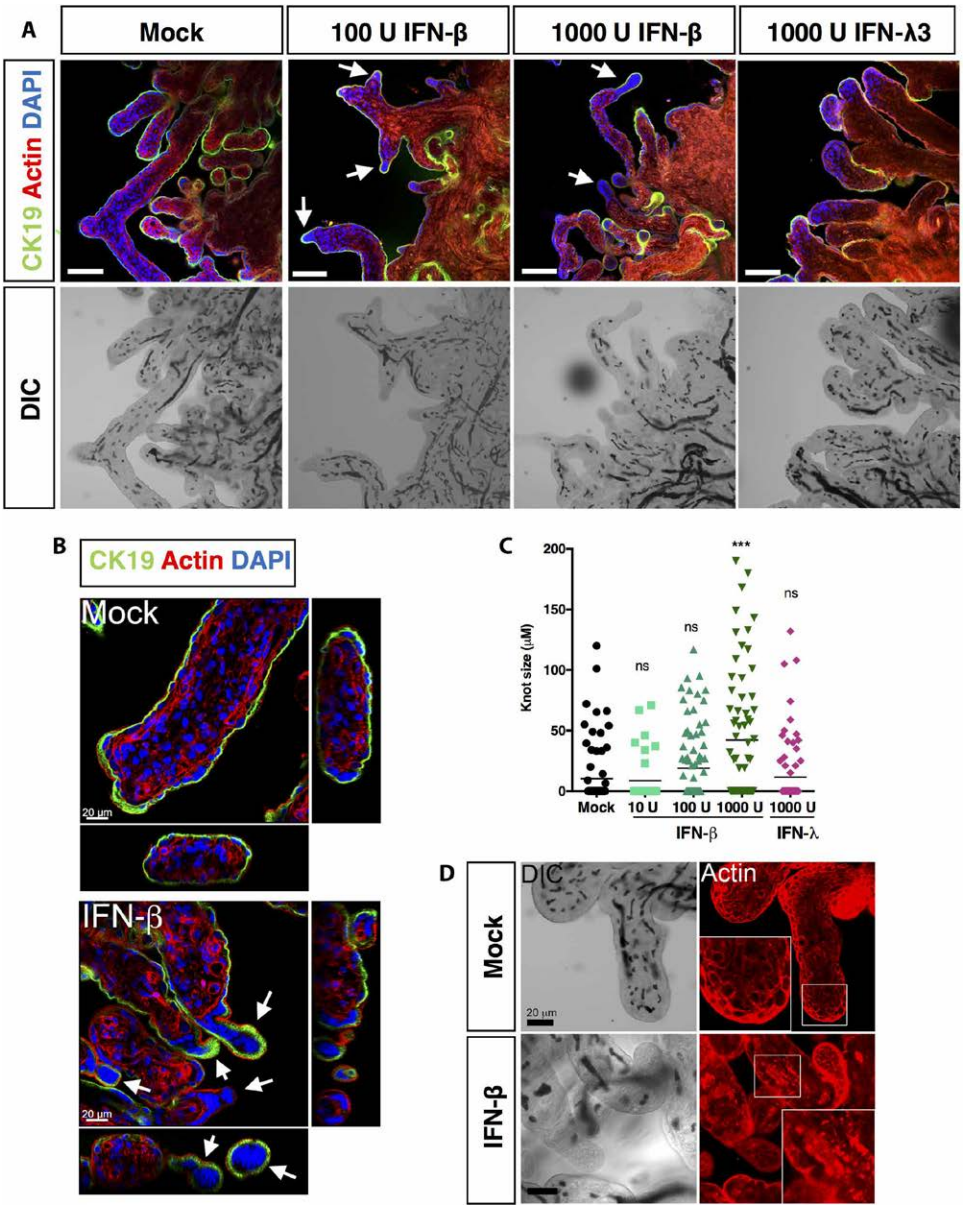


**Fig. 7. IFN treatment of human midgestation villous explants induces syncytial knot formation.** (**A**) Human midgestation (19 to 23 weeks) chorionic villi were isolated, placed in culture, and treated with 100 or 1000 U of recombinant human IFN-β or 1000 U of IFN-λ3 for ~16 to 20 hours. Villous explants were harvested, fixed in PFA, and stained for CK19 (green, trophoblasts) and actin (red). DAPI-stained nuclei are shown in blue and differential interference contrast (DIC) (bottom). Scale bars, 100 μm. Images are representative of villi isolated from four donors. Arrow indicates syncytial knot. (**B**) Three-dimensional image reconstruction of mock- or IFN-β (1000 U)–treated explants stained for CK19 (green) and actin (red). DAPI-stained nuclei are shown in blue. Scale bars, 20 μm. (**C**) Quantification of syncytial knot size using Imaris in villi treated with 10, 100, or 1000 U of IFN-β or 1000 U of IFN-λ3 for ~24 hours. Each symbol represents an individual villous from a total of three donors, and the black line represents the mean. ***$P <$ 0.001 by Dunnett's multiple comparison test to mock. ns, not significant. (**D**) Confocal micrographs of mock- or IFN-β (1000 U)–treated villi stained for actin (red, right). DIC is shown on the left. White box denotes zoomed area shown at the bottom left (mock) or right (IFN-β). Scale bars, 20 μm.

IFN, treatment led to robust ISG induction in the villous explants. The mechanistic basis for this differential signaling remains unknown but may reflect the constitutive expression of type III IFN already secreted by the syncytium during midgestation, which may affect receptor binding by the recombinant protein or perhaps reflect some level of receptor desensitization (*29*). Alternatively, it could also reflect the more restricted tissue expression of IFN-λ receptor, which is limited to the epithelium (*45*). However, midgestation explants express high basal levels of many ISGs, suggesting that the tissue is likely responsive to type III IFNs (*29*). Consistent with this, even in the placentas of mice that lack IFNAR and harbor high levels of virus in the placenta, the virus was mostly restricted from the fetus, indicating that other structures and pathways are capable of restricting ZIKV from the fetus.

How might type I IFNs trigger fetal death? We did not observe any differences in leukocyte infiltration into the placenta or block in proliferation of cells in the placenta. However, we did observe apoptosis of cells in the labyrinth, which likely represented endothelial cells or adjacent trophoblasts. Consistent with this, human explants treated with IFN-β exhibited significant alterations in actin cytoskeletal structure, consistent with cellular damage. These results are consistent with a previous report showing similar placenta damage after ZIKV infection (*13*). In addition to these possibilities, type I IFN is also known to inhibit angiogenesis and blood vessel development (*46*) and is consistent with the abnormal and reduced fetal blood vessels we observed in the labyrinth. Another possibility is that IFN may impair trophoblast fusion or differentiation. A previous report showed that IFN-β suppresses syncitin-1 expression (*47*). Consistent with this hypothesis, the placental histology and timing of death of the *Ifnar1*$^{+/-}$ fetuses resemble those of mice lacking syncitin-A, which have a defect in trophoblast fusion (*36*). We speculate that type I IFNs may serve as a quality control system to eliminate the developing embryo if coincident viral infection is detected and the levels of circulating IFNs reach a certain threshold. Many mammals carry their fetus for a prolonged period, to upward of ~650 days in elephants. This costly investment by the mothers may justify high levels of scrutiny of the health of the fetus at every level but particularly early in pregnancy when the embryo is vulnerable to various stressors (*48*, *49*). Type I IFNs may report on the viral infection status of the mother or the fetus within the local milieu, sending abortive signals to terminate pregnancy.

The effects of IFN on the developing placenta likely have implications for pregnancy complications beyond ZIKV, and it could be a

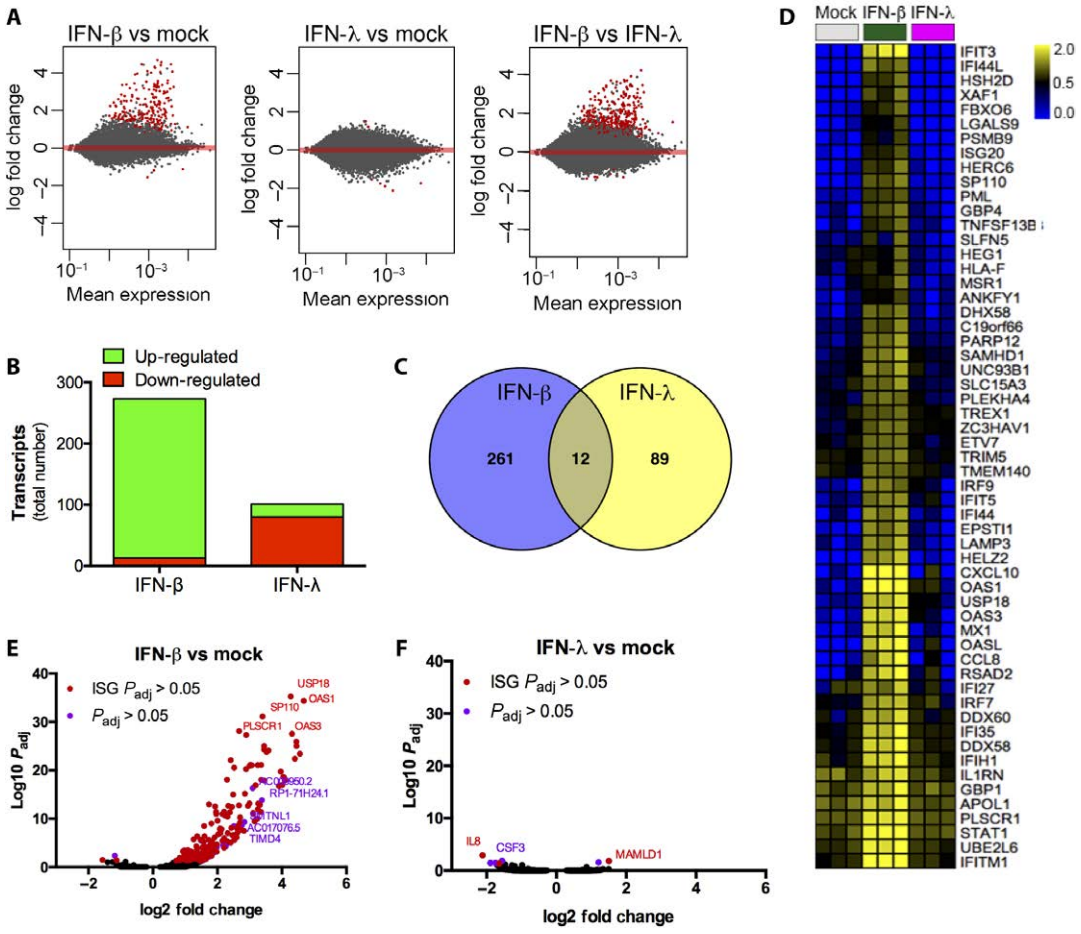


**Fig. 8. ISGs are induced in IFN-β–treated villous explants.** Human midgestation (19 to 23 weeks) chorionic villi were isolated, placed in culture, and treated with 1000 U of recombinant human IFN-β or 1000 U of IFN-λ3 for ~24 hours, and RNA was extracted. (**A**) MA plots generated in R after DeSeq2 analysis demonstrating the differential expression between IFN-β–treated (left) or IFN-λ–treated (middle) villi relative to mock-treated controls and between IFN-β– and IFN-λ–treated villi (right). Data are plotted as $\log_2$ fold changes (*y* axis) and mean expression (*x* axis). Red symbols denote transcripts whose expression was differentially expressed at $P < 0.05$. (**B**) Graph demonstrating the number of transcripts up-regulated (in green) or down-regulated (in red) after IFN-β or IFN-λ treatment of villi. (**C**) Venn diagram denoting the overlap of transcripts (12 in total) between villi treated with IFN-β and those treated with IFN-λ. (**D**) Heat map (based on log reads per kilobase of transcript per million mapped reads values) of known ISGs from mock-, IFN-β–, or IFN-λ–treated villi. (**E** and **F**) Volcano plots of villi treated with IFN-β (E) or IFN-λ (F) denoting specific ISGs differentially expressed by treatment. Red circles denote ISGs and purple circles denote non-ISG transcripts. For RNA-seq experiments, data represent villi isolated from three independent placental preparations.

mechanism for adverse pregnancy outcomes, such as IUGR or early spontaneous abortions, which often occur without a known underlying etiology. Consistent with type I IFN being an underlying cause of pregnancy complications, many congenital or "TORCH" (Toxoplasmosis, Other, Rubella, Cytomegalovirus, and Herpes) infections have a common presentation of microcephaly, cerebral calcifications, and IUGR (*3*). Beyond viral infections, our study may be relevant to diseases in which type I IFNs are overproduced, collectively known as interferonopathies (*50*). Interferonopathies may be induced by monogenic mutations, such as those found in Aicardi-Goutières syndrome, or polygenic diseases, including systemic lupus erythematosus (SLE). Fetuses with Aicardi-Goutières syndrome can present with developmental defects similar to classic TORCH infection with fetal growth restriction, microcephaly, and intracerebral calcifications (*50*). SLE is associated with pregnancy complications, including fetal death in utero, preeclampsia, and preterm birth; and elevated serum IFN is one of the key factors that closely correlate with poor pregnancy outcomes (*51*). Our study implicates type I IFNs as a possible common culprit for virus-associated pregnancy complications and suggests blockade of type I IFNs as a possible intervention to prevent pregnancy complications in the settings of nonviral interferonopathies.

## MATERIALS AND METHODS

### Study design

To test the effect that fetal IFNAR signaling has on development after ZIKV infection, *Ifnar1*$^{-/-}$ females were crossed to *Ifnar1*$^{+/-}$ males to allow for direct comparison between littermates of different genotypes. Fetuses and placentas were harvested at various time points after infection and appearance, histology, and transcriptional changes were analyzed. To test how human placentas were affected by IFN signaling, midgestation chorionic villous explants were treated with IFN-β or IFN-λ, and villi were analyzed by immunofluorescent imaging or transcriptional changes were analyzed. For mouse studies, analysis was performed on litters containing both genotypes, and genotyping of litters was performed after initial analysis of fetal weight and appearance. No other formal randomization or blinding method was used. Subjects were assigned a litter and fetus number to allow unbiased selection for sample processing (RNA and imaging). A minimum of three infected litters were analyzed per time point. Exact *n* is indicated in figure legends. No formal statistical tool was used to determine power.

### Mice

*Ifnar1*$^{-/-}$, *Ifnar1*$^{+/-}$, C57BL/6, and *Irf3*$^{-/-}$*Irf7*$^{-/-}$ mice were bred and maintained at Yale University. All pregnant dams were between 9 and

20 weeks of age. Littermates were randomly assigned to infected or uninfected groups. *Ifnar1*$^{+/-}$ male breeders are the F1 generation from cross between C57BL/6 (B6) and *Ifnar1*$^{-/-}$ parents. Matings were timed by checking for the presence of a vaginal plug, indicating gestational age E0.5. About 11% of infected concepti were analyzed between E9.5 and E12.5 and 17% of uninfected concepti developed into abnormal spheroid shapes (distinct from infection-induced resorbed fetuses), without the presence of a fetus or yolk sac. These were excluded from analysis because of inability to obtain adequate fetus-derived tissue for genotyping analysis and because it was present in equal frequencies for infected and uninfected groups. All animal procedures were performed in compliance with Yale Institutional Animal Care and Use Committee protocols.

### Midgestation chorionic villous explants

Human fetal placental tissue from 19 to 23 weeks' gestation that resulted from elective terminations was obtained from the University of Pittsburgh Health Sciences Tissue Bank through an honest broker system after approval from the University of Pittsburgh Institutional Review Board and in accordance with the University of Pittsburgh anatomical tissue procurement guidelines. Chorionic villi (about 1 cm × 1 cm in size) were dissected and cultured in Dulbecco's modified Eagle's medium (DMEM)/F12 (1:1) supplemented with 10% fetal bovine serum (FBS), penicillin/streptomycin, and amphotericin B. Immediately after isolation, isolated villi were treated with the indicated dose of recombinant IFN-β or IFN-λ for 24 hours, and then tissue was fixed and processed for imaging. For imaging studies, villi were fixed in 4% paraformaldehyde (PFA) followed by permeabilization in 0.25% Triton X-100 for 30 min at room temperature with gentle agitation, washed in phosphate-buffered saline (PBS), incubated with primary antibody, washed again in PBS, and then incubated with Alexa Fluor–conjugated secondary antibodies. Alexa Fluor–conjugated phalloidin was purchased from Invitrogen (A12379 or A12381). Rabbit anti-CK19 (ab52625) was purchased from Abcam. After staining, villi were mounted with VECTASHIELD (Vector Laboratories) containing 4′,6-diamidino-2-phenylindole (DAPI), and images were captured using an Olympus FV1000 confocal or Zeiss LSM 710 confocal microscope. Images were adjusted for brightness/contrast using Adobe Photoshop (Adobe), and syncytial knot size was calculated using Imaris.

### Viruses and in vivo infections

ZIKV Cambodian FSS13025 stain, obtained from the World Reference Center for Emerging Viruses and Arboviruses at University of Texas Medical Branch, Galveston, was used for intravaginal infection studies. Stocks were propagated in Vero cells and titrated by plaque assay as previously described (*14*). ZIKV Brazilian PE243, used for subcutaneous infections, was recovered from a 19-year-old female in Brazil from 2015 (*52*). Vero cells were obtained from the American Type Culture Collection. Cell lines were verified by morphology and were tested for mycoplasma contamination every 1 to 2 years.

Intravaginal infection was performed as previously described: At E5.5 or E8.5, a calginate swab (Fischer Scientific) was used to remove mucus from the vaginal lumen, and $1.5 \times 10^5$ PFU of ZIKV was inoculated into the vagina using a pipette (*14*). Subcutaneous infection was performed by injecting 100 μl of virus stock diluted in PBS ($3.4 \times 10^5$ or $1 \times 10^3$ PFU) into the footpad. Pregnant mice were euthanized, tissues were harvested at indicated time points, and fetuses and placentas were either collected in TRIzol (for RNA extraction), fixed in 4% PFA (for imaging), or collected in DMEM with 10% FBS and penicillin/streptomycin (for plaque assay). Fixed fetuses were imaged using a Zeiss Discovery V8 stereomicroscope (Zeiss). Yolk sac for E9.5 to E12.5 or tail for E17.5 fetuses was collected for each fetus and genotyped using the following primers: ATTATTAAAAGAAAAGACGAGGCGAAGTGG (forward) and AAGATGTGCTGTTCCCTTCCTCTGCTCTGA (reverse), with a 150–base pair product, indicating the presence of a WT copy of IFNAR.

### Poly(I:C) challenge

Two hundred micrograms of HMW VacciGrade Poly(I:C) (InvivoGen) was injected intraperitoneally into pregnant mice at E7.5. Mice were then harvested between E9.5 and E12.5 to examine fetuses.

### Quantification of ZIKV genome, ISGs, and hypoxia response genes by qRT-PCR

Tissues were extracted using TRIzol (Thermo Fischer Scientific) and purified using an RNeasy Mini Kit (Qiagen). iScript cDNA synthesis kit (Bio-Rad) was used to synthesize cDNA. Quantitative polymerase chain reaction (qPCR), which was performed using SYBR green (Bio-Rad), was used to quantify ZIKV levels, ISGs, and hypoxia response genes and ran on a CFX Connect instrument (Bio-Rad). Primer sequences are provided in table S1. Virus and ISGs were normalized to *Hprt* (*14*).

### Histology, immunofluorescence, and immunohistochemistry staining of mouse placentas

Placentas were fixed in 4% PFA overnight at 4°C. For immunohistochemical (IHC) and hematoxylin and eosin (H&E) staining, tissues were embedded in paraffin blocks and sectioned by the Yale Pathology Tissue Services. H&E was performed by the Yale Pathology Tissue Services. For IHC, paraffin sections were heated for 30 min at 55° to 60°C. Antigen retrieval was performed by boiling in sodium citrate (J.T. Baker) (pH 6.0) for 60 min. Blocking was performed using PBS (AmericanBio), 1% bovine serum albumin (BSA) (Sigma-Aldrich), and 0.5% Tween 20 (Sigma-Aldrich) adjusted to pH 7.4. Slides were stained for CD31 (goat, 1:1000, R&D AF3628), Casp3 (rabbit, 1:1000, Cell Signaling Tech 9664T), Ecad (1:500, Thermo Fischer Scientific 13-1900), and Ki67 (rabbit 1:1000, Cell Signaling Tech 12202T) at 4°C overnight. Slides were blocked with Bloxall (Vector Laboratories) and stained with rat (for Ecad), rabbit (for Casp3, Ki67), or goat (for CD31) ImmPRESS antibodies (Vector Laboratories) and 3,3′-diaminobenzidine (DAB) (Vector Laboratories) per the manufacturer's instructions. For immunofluorescence staining, slides were embedded in optimal cutting temperature media (Tissue Tek). Five- to seven-micrometer frozen sections were cut using a cryostat, and sections were allowed to dry at room temperature. Sections were blocked with 2% normal Donkey serum (Jackson ImmunoResearch) in PBS with Tween 20 and 1% BSA (Sigma-Aldrich) and stained with ZIKV-immune rat serum (*53*), CD45 (R&D Systems AF114), CK (Dako Z0622), or CD31 (R&D Systems AF3628) overnight at room temperature. Sections were then stained with A488 anti-rat secondary (Thermo Fischer), A647 anti-rabbit (Thermo Fischer), Cy3 anti-rabbit (Jackson ImmunoResearch), A488 anti-goat (Thermo Fischer), or NL557 anti-goat (R&D Systems). Samples were stained with DAPI and mounted with ProLong Diamond Antifade Mountant (Molecular Probes). H&E and IHC images were captured using light microscopy (BX51; Olympus), and immunofluorescence images were captured using fluorescence microscopy (BX51; Olympus) or confocal microscopy (TCS SP2; Leica). Images were merged and brightness and contrast were adjusted using ImageJ.

### Transmission electron microscopy of mouse placentas

Placentas were fixed in formaldehyde/glutaraldehyde 2.5% in phosphate buffer for at least 24 hours. Samples were washed and secondarily fixed in osmium tetroxide; negative staining was performed with uranyl acetate, treated in ascending alcohols, and finally embedded in Durcupan ACM (EMS 14040). Ultrathin sections (70 nM) were cut on a Leica ultramicrotome, collected on Formvar-coated grids, and analyzed on a Tecnai 12 FEI electron microscope.

### RNA-seq and qRT-PCR analysis of midgestation chorionic villous explants

RNA was isolated from the villous explants using GenElute RNA total RNA miniprep kit (Sigma-Aldrich) and treated with deoxyribonuclease (Sigma-Aldrich). For RNA-seq, as previously described (*28*, *54*), libraries were prepared using New England Biolabs Ultra Library Preparation kit. An Illumina HiSeq2500 was used for sequencing, and CLC Genomics Workbench 9.0 (Qiagen) was used to process, normalize, and map sequence data to the human reference genome (hg19). DESeq2 in R (*55*) or CLC Genomics Workbench 9 was used to identify differentially expressed genes and to generate MA plots.

### Statistical analysis

In all analyses except for RNA-seq, data analysis was performed using Microsoft Excel and GraphPad Prism. Exact statistical test and value of $n$ are detailed in the figure legends. A Tukey's multiple comparison test or Dunnett's multiple comparison test was used to determine significance when determining significance between multiple groups (>3). A paired Student's $t$ test was used when comparing only two groups. $t$ tests assumed a normal distribution for all samples and $t$ tests assume an unequal standard deviation and variance between groups.

## SUPPLEMENTARY MATERIALS

immunology.sciencemag.org/cgi/content/full/3/19/eaao1680/DC1

Methods

Fig. S1. ISG expression is elevated in *Ifnar1*$^{+/-}$ placentas and fetuses but not in *Irf3*$^{-/-}$*Irf7*$^{-/-}$ after ZIKV infection.

Fig. S2. *Ifnar1*$^{-/-}$ placentas harbor more infectious ZIKV compared with *Ifnar1*$^{+/-}$ littermates.

Fig. S3. Global gene expression analysis reveals elevated ISG levels in infected *Ifnar1*$^{+/-}$ placentas.

Fig. S4. ZIKV infection of the maternal-fetal interface is restricted to the decidua.

Fig. S5. Placental architecture of *Ifnar1*$^{+/-}$ fetuses is normal at E9.5 but disrupted at E11.5 and E12.5.

Fig. S6. Labyrinth of *Ifnar1*$^{+/-}$ placenta exhibits decreased fetal endothelial cells.

Fig. S7. *Ifnar1*$^{+/-}$ but not *Ifnar1*$^{-/-}$ fetuses are resorbed after subcutaneous infection with Brazilian ZIKV.

Table S1. Primers for mouse qPCR

Table S2. Top differentially regulated genes and pathways in ZIKV-infected *Ifnar1*$^{+/-}$ versus *Ifnar1*$^{-/-}$ placentas.

Table S3. Individual values included in all graphs

References (*56*–*61*)

## REFERENCES AND NOTES


1. Pan American Health Organization/World Health Organization, Zika suspected and confirmed cases reported by countries and territories in the Americas Cumulative cases, 2015-2016 (Washington, D.C., 2016).
2. D. Baud, D. J. Gubler, B. Schaub, M. C. Lanteri, D. Musso, An update on Zika virus infection. *Lancet* **390**, 2099–2109 (2017).
3. C. B. Coyne, H. M. Lazear, Zika virus—Reigniting the TORCH. *Nat. Rev. Microbiol.* **14**, 707–715 (2016).
4. L. Barzon, M. Pacenti, E. Franchin, E. Lavezzo, M. Trevisan, D. Sgarabotto, G. Palù, Infection dynamics in a traveller with persistent shedding of Zika virus RNA in semen for six months after returning from Haiti to Italy, January 2016. *Euro Surveill.* **21**, 30316 (2016).
5. E. D'Ortenzio, S. Matheron, Y. Yazdanpanah, X. de Lamballerie, B. Hubert, G. Piorkowski, M. Maquart, D. Descamps, F. Damond, I. Leparc-Goffart, Evidence of sexual transmission of Zika virus. *N. Engl. J. Med.* 2195–2198 (2016).
6. A. J. Sadler, B. R. G. Williams, Interferon-inducible antiviral effectors. *Nat. Rev. Immunol.* **8**, 559–568 (2008).
7. O. Takeuchi, S. Akira, Recognition of viruses by innate immunity. *Immunol. Rev.* **220**, 214–224 (2007).
8. K. Honda, T. Taniguchi, IRFs : Master regulators of signalling by Toll-like receptors and cytosolic pattern-recognition receptors. *Nat. Rev. Immunol.* **6**, 644–658 (2006).
9. J. W. Schoggins, C. M. Rice, Interferon-stimulated genes and their antiviral effector functions. *Curr. Opin. Virol.* **1**, 519–525 (2011).
10. J. Crouse, U. Kalinke, A. Oxenius, Regulation of antiviral T cell responses by type I interferons. *Nat. Rev. Immunol.* **15**, 231–242 (2015).
11. M. Chawla-Sarkar, D. J. Lindner, Y.-F. Liu, B. R. Williams, G. C. Sen, R. H. Silverman, E. C. Borden, Apoptosis and interferons: Role of interferon-stimulated genes as mediators of apoptosis. *Apoptosis* **8**, 237–249 (2003).
12. F. R. Cugola, I. R. Fernandes, F. B. Russo, B. C. Freitas, J. L. M. Dias, K. P. Guimarães, C. Benazzato, N. Almeida, G. C. Pignatari, S. Romero, C. M. Polonio, I. Cunha, C. L. Freitas, W. N. Brandão, C. Rossato, D. G. Andrade, D. de P. Faria, A. T. Garcez, C. A. Buchpigel, C. T. Braconi, E. Mendes, A. A. Sall, P. M. de A. Zanotto, J. P. S. Peron, A. R. Muotri, P. C. B. Beltrão, The Brazilian Zika virus strain causes birth defects in experimental models. *Nature* **534**, 267–271 (2016).
13. J. J. Miner, B. Cao, J. Govero, A. M. Smith, E. Fernandez, O. H. Cabrera, C. Garber, M. Noll, R. S. Klein, K. K. Noguchi, I. U. Mysorekar, M. S. Diamond, Zika virus infection during pregnancy in mice causes placental damage and fetal demise. *Cell* **165**, 1081–1091 (2016).
14. L. J. Yockey, L. Varela, T. Rakib, W. Khoury-Hanold, S. L. Fink, B. Stutz, K. Szigeti-Buck, A. Van den Pol, B. D. Lindenbach, T. L. Horvath, A. Iwasaki, Vaginal exposure to Zika virus during pregnancy leads to fetal brain infection. *Cell* **166**, 1247–1256.e4 (2016).
15. J. Xavier-Neto, M. Carvalho, B. dos Santos Pascoalino, A. C. Cardoso, Â. M. S. Costa, A. H. M. Pereira, L. N. Santos, Â. Saito, R. E. Marques, J. H. C. Smetana, S. R. Consonni, C. Bandeira, V. V. Costa, M. C. Bajgelman, P. S. Lopes de Oliveira, M. T. Cordeiro, L. H. V. G. Gil, B. A. Pauletti, D. C. Granato, A. F. P. Leme, L. Freitas-Junior, C. B. M. Holanda de Freitas, M. M. Teixeira, E. Bevilacqua, K. Franchini, Hydrocephalus and arthrogryposis in an immunocompetent mouse model of ZIKA teratogeny: A developmental study. *PLOS Neglected Trop. Dis.* **11**, e0005363 (2017).
16. C. W. Winkler, T. A. Woods, R. Rosenke, D. P. Scott, S. M. Best, K. E. Peterson, Sexual and vertical transmission of Zika virus in anti-interferon receptor-treated Rag-1deficient mice. *Sci. Rep.* **7**, 7176 (2017).
17. A. Grant, S. S. Ponia, S. Tripathi, V. Balasubramaniam, L. Miorin, M. Sourisseau, M. C. Schwarz, M. P. Sánchez-Seco, M. J. Evans, S. M. Best, A. García-Sastre, Zika virus targets human STAT2 to inhibit type I interferon signaling. *Cell Host Microbe* **19**, 882–890 (2016).
18. Y. Wu, Q. Liu, J. Zhou, W. Xie, C. Chen, Z. Wang, H. Yang, J. Cui, Zika virus evades interferon-mediated antiviral response through the co-operation of multiple nonstructural proteins in vitro. *Cell Discov.* **3**, 17006 (2017).
19. H. M. Lazear, J. Govero, A. M. Smith, D. J. Platt, E. Fernandez, J. J. Miner, M. S. Diamond, A mouse model of Zika virus pathogenesis. *Cell Host Microbe* **19**, 720–730 (2016).
20. B. W. Jagger, J. J. Miner, B. Cao, N. Arora, A. M. Smith, A. Kovacs, I. U. Mysorekar, C. B. Coyne, M. S. Diamond, Gestational stage and IFN- λ signaling regulate ZIKV infection in utero. *Cell Host Microbe* **22**, 366–376.e3 (2017).
21. J. R. Robbins, A. I. Bakardjiev, Pathogens and the placental fortress. *Curr. Opin. Microbiol.* **15**, 36–43 (2012).
22. T. Cotechini, C. H. Graham, Aberrant maternal inflammation as a cause of pregnancy complications: A potential therapeutic target? *Placenta* **36**, 960–966 (2015).
23. M. Prabhudas, E. Bonney, K. Caron, S. Dey, A. Erlebacher, A. Fazleabas, S. Fisher, T. Golos, M. Matzuk, J. M McCune, G. Mor, L. Schulz, M. Soares, T. Spencer, J. Strominger, S. S. Way, K. Yoshinaga, Immune mechanisms at the maternal-fetal interface : Perspectives and challenges. *Nat. Immunol.* **16**, 328–334 (2015).
24. G. Mor, Placental inflammatory response to Zika virus may affect fetal brain development. *Am. J. Reprod. Immunol.* **75**, 421–422 (2016).
25. M. Cappelletti, P. Presicce, M. J. Lawson, V. Chaturvedi, T. E. Stankiewicz, S. Vanoni, I. T. W. Harley, J. W. McAlees, D. A. Giles, M. E. Moreno-Fernandez, C. M. Rueda, P. Senthamaraikannan, X. Sun, R. Karns, K. Hoebe, E. M. Janssen, C. L. Karp, D. A. Hildeman, S. P. Hogan, S. G. Kallapur, C. A. Chougnet, S. S. Way, S. Divanovic, Type I interferons regulate susceptibility to inflammation-induced preterm birth. *JCI Insight* **2**, e91288 (2017).
26. K. Racicot, P. Aldo, A. El-guindy, J.-Y. Kwon, R. Romero, G. Mor, Cutting edge: Fetal/placental type I IFN can affect maternal survival and fetal viral load during viral infection. *J. Immunol.* **198**, 3029–3032 (2017).
27. R. M. Roberts, Interferon-tau, a type 1 interferon involved in maternal recognition of pregnancy. *Cytokine Growth Factor Rev.* **18**, 403–408 (2007).

28. A. Bayer, N. J. Lennemann, Y. Ouyang, J. C. Bramley, S. Morosky, E. Torres De Azeved Marques Jr., S. Cherry, Y. Sadovsky, C. B. Coyne, Type III interferons produced by human placental trophoblasts confer protection against Zika virus infection. *Cell Host Microbe* **19**, 705–712 (2016).
29. J. Corry, N. Arora, C. A. Good, Y. Sadovsky, C. B. Coyne, Organotypic models of type III interferon-mediated protection from Zika virus infections at the maternal–fetal interface. *Proc. Natl. Acad. Sci. U.S.A.* **114**, 9433–9438 (2017).
30. J. L. Sones, R. L. Davisson, Preeclampsia, of mice and women. *Physiol. Genomics* **48**, 565–572 (2016).
31. V. E. Papaioannou, R. R. Behringer, Early embryonic lethality in genetically engineered mice: Diagnosis and phenotypic analysis. *Vet. Pathol.* **49**, 64–70 (2012).
32. P. M. Coan, A. C. Ferguson-Smith, G. J. Burton, Ultrastructural changes in the interhaemal membrane and junctional zone of the murine chorioallantoic placenta across gestation. *J. Anat.* **207**, 783–796 (2005).
33. J. Rossant, J. C. Cross, Placental development: Lessons from mouse mutants. *Nat. Rev. Genet.* **2**, 538–548 (2001).
34. M. Mori, A. Bogdan, T. Balassa, T. Csabai, J. Szekeres-Bartho, The decidua—the maternal bed embracing the embryo—maintains the pregnancy. *Semin. Immunopathol.* **38**, 635–649 (2016).
35. J. Bhatnagar, D. B. Rabeneck, R. B. Martines, S. Reagan-Steiner, Y. Ermias, L. B. C. Estetter, T. Suzuki, J. M. Ritter, M. K. Keating, G. Hale, J. Gary, A. Muehlenbachs, A. J. Lambert, R. Lanciotti, T. Oduyebo, D. Meaney-Delman, F. Bolaños, E. A. Parra Saad, W.-J. Shieh, S. R. Zaki, Zika virus RNA replication and persistence in brain and placenta tissue. *Emerg. Infect. Dis.* **23**, 405–414 (2017).
36. A. Dupressoir, C. Vernochet, O. Bawa, F. Harper, G. Pierron, P. Opolon, T. Heidmann, Syncytin-A knockout mice demonstrate the critical role in placentation of a fusogenic, endogenous retrovirus-derived, envelope gene. *Proc. Natl. Acad. Sci. U.S.A.* **106**, 12127–12132 (2009).
37. M. Ream, A. M. Ray, R. Chandra, D. M. Chikaraishi, Early fetal hypoxia leads to growth restriction and myocardial thinning. *Am. J. Physiol. Regul. Integr. Comp. Physiol.* **295**, R583–R595 (2008).
38. R. Trollmann, H. Rehrauer, C. Schneider, G. Krischke, N. Huemmler, S. Keller, W. Rascher, M. Gassmann, Late-gestational systemic hypoxia leads to a similar early gene response in mouse placenta and developing brain. *Am. J. Physiol.* **299**, R1489–R1499 (2010).
39. M. Matsumoto, T. Seya, TLR3: Interferon induction by double-stranded RNA including poly(I:C). *Adv. Drug Deliv. Rev.* **60**, 805–812 (2008).
40. J. E. Thaxton, T. Nevers, E. O. Lippe, S. M. Blois, S. Saito, S. Sharma, NKG2D blockade inhibits poly(I:C)-triggered fetal loss in wild type but not IL-10$^{-/-}$ mice. *J. Immunol.* **190**, 3639–3647 (2013).
41. G. J. Burton, C. J. P. Jones, Syncytial knots, sprouts, apoptosis, and trophoblast deportation from the human placenta. *Taiwan. J. Obstet. Gynecol.* **48**, 28–37 (2009).
42. N. M. E. Fogarty, A. C. Ferguson-Smith, G. J. Burton, Syncytial knots (Tenney-Parker changes) in the human placenta: Evidence of loss of transcriptional activity and oxidative damage. *Am. J. Pathol.* **183**, 144–152 (2013).
43. R. Uraki, K. A. Jurado, J. Hwang, K. Szigeti-Buck, T. L. Hovarth, A. Iwasaki, E. Fikrig, Fetal growth restriction caused by sexual transmission of Zika virus in mice. *J. Infect. Dis.* **215**, 1720–1724 (2017).
44. K. Loukeris, R. Sela, R. N. Baergen, Syncytial knots as a reflection of placental maturity: Reference values for 20 to 40 weeks' gestational age. *Pediatr. Dev. Pathol.* **13**, 305–309 (2010).
45. C. Odendall, J. C. Kagan, The unique regulation and functions of type III interferons in antiviral immunity. *Curr. Opin. Virol.* **12**, 47–52 (2015).
46. R. A. B. Ezekowitc, J. B. Mulliken, J. Folkman, Interferon Alfa-2a therapy for life-threatening hemangiomas of infancy. *N. Engl. J. Med.* **326**, 1456–1463 (1992).
47. G. Mameli, A. Dolei, V. Astone, K. Khalili, C. Serra, B. E. Sawaya, Regulation of the syncytin-1 promoter in human astrocytes by multiple sclerosis-related cytokines. *Virology* **362**, 120–130 (2007).
48. G. Teklenburg, M. Salker, M. Molokhia, S. Lavery, G. Trew, T. Aojanepong, H. J. Mardon, A. U. Lokugamage, R. Rai, C. Landles, B. A. J. Roelen, S. Quenby, E. W. Kuijk, A. Kavelaars, C. J. Heijnen, L. Regan, J. J. Brosens, N. S. Macklon, Natural selection of human embryos: Decidualizing endometrial stromal cells serve as sensors of embryo quality upon implantation. *PLOS ONE* **5**, e10258 (2010).
49. E. C. Larsen, O. B. Christiansen, A. M. Kolte, N. Macklon, New insights into mechanisms behind miscarriage. *BMC Med.* **11**, 154 (2013).
50. Y. J. Crow, Type I interferonopathies : A novel set of inborn errors of immunity. *Ann. N.Y. Acad. Sci.* **1238**, 91–98 (2011).
51. D. Andrade, M. Kim, L. P. Blanco, S. A. Karumanchi, G. C. Koo, P. Redecha, K. Kirou, A. M. Alvarez, M. J. Mulla, M. K. Crow, V. M. Abrahams, M. J. Kaplan, J. E. Salmon, Interferon-α and angiogenic dysregulation in pregnant lupus patients who develop preeclampsia. *Arthritis Rheumatol.* **67**, 977–987 (2015).
52. M. Onorati, Z. Li, F. Liu, A. M. M. Sousa, N. Nakagawa, M. Li, M. T. Dell'Anno, F. O. Gulden, S. Pochareddy, A. T. N. Tebbenkamp, W. Han, M. Pletikos, T. Gao, Y. Zhu, C. Bichsel, L. Varela, K. Szigeti-Buck, S. Lisgo, Y. Zhang, A. Testen, X.-B. Gao, J. Mlakar, M. Popovic, M. Flamand, S. M. Strittmatter, L. K. Kaczmarek, E. S. Anton, T. L. Horvath, B. D. Lindenbach, N. Sestan, Zika virus disrupts phospho-TBK1 localization and mitosis in human neuroepithelial stem cells and radial glia. *Cell Rep.* **16**, 2576–2592 (2016).
53. A. N. van den Pol, G. Mao, Y. Yang, S. Ornaghi, J. N. Davis, Zika virus targeting in the developing brain. *J. Neurosci.* **37**, 2161–2175 (2017).
54. C. A. Mcconkey, E. Delorme-Axford, C. A. Nickerson, K. S. Kim, Y. Sadovsky, J. P. Boyle, C. B. Coyne, A three-dimensional culture system recapitulates placental syncytiotrophoblast development and microbial resistance. *Sci. Adv.* **2**, e1501462 (2016).
55. M. I. Love, W. Huber, S. Anders, Moderated estimation of fold change and dispersion for RNA-seq data with DESeq2. *Genome Biol.* **15**, 550 (2014).
56. Y. Kong, Btrim: A fast, lightweight adapter and quality trimming program for next-generation sequencing technologies. *Genomics* **98**, 152–153 (2011).
57. D. Kim, G. Pertea, C. Trapnell, H. Pimentel, R. Kelley, S. L. Salzberg, TopHat2: Accurate alignment of transcriptomes in the presence of insertions, deletions and gene fusions. *Genome Biol.* **14**, R36 (2013).
58. A. Subramanian, P. Tamayo, V. K. Mootha, S. Mukherjee, B. L. Ebert, M. A. Gillette, A. Paulovich, S. L. Pomeroy, T. R. Golub, E. S. Lander, J. P. Mesirov, Gene set enrichment analysis: A knowledge-based approach for interpreting genome-wide expression profiles. *Proc. Natl. Acad. Sci. U.S.A.* **102**, 15545–15550 (2005).
59. V. K. Mootha, C. M. Lindgren, K.-F. Eriksson, A. Subramanian, S. Sihag, J. Lehar, P. Puigserver, E. Carlsson, M. Ridderstråle, E. Laurila, N. Houstis, M. J. Daly, N. Patterson, J. P. Mesirov, T. R. Golub, P. Tamayo, B. Spiegelman, E. S. Lander, J. N. Hirschhorn, D. Altshuler, L. C. Groop, PGC-1α-responsive genes involved in oxidative phosphorylation are coordinately downregulated in human diabetes. *Nat. Genet.* **34**, 267–273 (2003).
60. E. F. Foxman, J. A. Storer, M. E. Fitzgerald, B. R. Wasike, L. Houf, H. Zhaof, P. E. Turnere, A. Marie Pyle, A. Iwasaki, Temperature-dependent innate defense against the common cold virus limits viral replication at warm temperature in mouse airway cells. *Proc. Natl. Acad. Sci. U.S.A.* **112**, 827–832 (2014).
61. V. C. Thompson, T. K. Day, T. Bianco-Miotto, L. A. Selth, G. Han, M. Thomas, G. Buchanan, H. I. Scher, C. C. Nelson; Australian Prostate Cancer BioResource, N. M. Greenberg, L. M. Butler, W. D. Tilley, A gene signature identified using a mouse model of androgen receptor-dependent prostate cancer predicts biochemical relapse in human disease. *Int. J. Cancer* **131**, 662–672 (2012).

**Acknowledgments:** We thank B. Lindenbach for providing ZIKV stocks, A. Van den Pol for providing the ZIKV antibody, R. Medzhitov for mice, H. Dong and M. Linehan for technical assistance, and the University of Pittsburgh Medical Center Tissue and Research Pathology Services/Health Sciences Tissue Bank, which receives funding from P30CA047904. **Funding:** This study was supported in part by the NIH (1R21AI131284 to A.I., T32GM007205 and F30 HD094717-01 to L.J.Y., 4T32AI007019-41 to K.A.J, and R01HD075665 to C.B.C) and a Burroughs Wellcome Investigators in the Pathogenesis of Infectious Disease Award to C.B.C. K.A.J. is a recipient of the Burroughs Wellcome Fund Postdoctoral Enrichment Program. A.I. and E.F. are investigators of the Howard Hughes Medical Institute. **Author contributions:** Conceptualization and methodology: L.J.Y., K.A.J., N.A., K.M.M., Y.K., S.W., H.J.K., C.B.C., and A.I. Investigation: L.J.Y., K.A.J., N.A., T.R., and A.K.H. Formal analysis: L.J.Y., K.A.J., N.A., A.M., Y.K., S.W., H.J.K., C.B.C., and A.I. Resources: E.F., T.L.H. Writing: L.J.Y., N.A., C.B.C., and A.I. (original draft), and L.J.Y., K.A.J., N.A., A.M., A.J.K., E.F., S.W., H.J.K., C.B.C., and A.I. (review and editing). Funding acquisition: C.B.C. and A.I. Supervision: S.W., H.K.J., C.B.C., and A.I. **Competing interests:** The authors declare that they have no competing interests. **Data and materials availability:** Data from RNA-seq analysis are available through the GEO database [accession numbers GSE98423 (mouse placentas; fig S3 and table S2) and GSE104349 (human chorionic villi; Fig.7)].

Submitted 21 June 2017
Accepted 2 November 2017
Published 5 January 2018
10.1126/sciimmunol.aao1680

**Citation:** L. J. Yockey, K. A. Jurado, N. Arora, A. Millet, T. Rakib, K. M. Milano, A. K. Hastings, E. Fikrig, Y. Kong, T. L. Horvath, S. Weatherbee, H. J. Kliman, C. B. Coyne, A. Iwasaki, Type I interferons instigate fetal demise after Zika virus infection. *Sci. Immunol.* **3**, eaao1680 (2018).

CALL FOR PAPERS

SPJ
SCIENCE PARTNER JOURNALS

spj.ScienceMag.org/research

# Research

OFFICIAL JOURNAL OF CAST

## An Open Access Journal

*Research* is a comprehensive, interdisciplinary, and selective **Open Access journal from the China Association of Science and Technology (CAST)**, published quarterly and distributed by the **American Association for the Advancement of Science (AAAS)**. *Research* provides an international platform for academic exchange, research collaboration, and technological advancements. The journal will publish fundamental research in the life and physical sciences as well as important findings or issues in engineering and applied science.

The Science Partner Journals (SPJ) program was established by AAAS, the nonprofit publisher of the *Science* family of journals. The SPJ program features high-quality, online-only open access publications produced in collaboration with international research institutions, foundations, funders and societies. Through these collaborations, AAAS expands its efforts to communicate science broadly and for the benefit of all people by providing top-tier international research organizations with the technology, visibility and publishing expertise that AAAS is uniquely positioned **to offer as the world's largest general science membership society**.

IMMUNOLOGY

# Resveratrol stimulates the metabolic reprogramming of human CD4$^+$ T cells to enhance effector function

Marco Craveiro,[1,2]* Gaspard Cretenet,[1]* Cédric Mongellaz,[1] Maria I. Matias,[1] Olivier Caron,[3,4] Maria C. Pedroso de Lima,[2] Valérie S. Zimmermann,[1] Eric Solary,[3,4] Valérie Dardalhon,[1] Vjekoslav Dulić,[1†] Naomi Taylor[1†]



**The polyphenol resveratrol activates the deacetylase Sirt1, resulting in various antioxidant, chemoprotectant, neuroprotective, cardioprotective, and anti-inflammatory properties. We found that at high concentrations of resveratrol, human CD4$^+$ T cells showed defective antigen receptor signaling and arrest at the $G_1$ stage of the cell cycle, whereas at low concentrations, cells were readily activated and exhibited enhanced Sirt1 deacetylase activity. Nevertheless, low-dose resveratrol rapidly stimulated genotoxic stress in the T cells, which resulted in engagement of a DNA damage response pathway that depended on the kinase ATR [ataxia telangiectasia–mutated (ATM) and Rad3-related], but not ATM, and subsequently in premitotic cell cycle arrest. The concomitant activation of p53 was coupled to the expression of gene products that regulate cell metabolism, leading to a metabolic reprogramming that was characterized by decreased glycolysis, increased glutamine consumption, and a shift to oxidative phosphorylation. These alterations in the bioenergetic homeostasis of CD4$^+$ T cells resulted in enhanced effector function, with both naïve and memory CD4$^+$ T cells secreting increased amounts of the inflammatory cytokine interferon-γ. Thus, our data highlight the wide range of metabolic adaptations that CD4$^+$ T lymphocytes undergo in response to genomic stress.**

## INTRODUCTION

Resveratrol (3,5,4′-trihydroxy-*trans*-stilbene) is a natural polyphenolic compound that is produced by plants in response to environmental stress, providing them with protection from microbial infections (*1*–*4*). Resveratrol appears to mimic the effects of caloric restriction, increasing life span in lower organisms (*5*). Furthermore, this pharmacological agent has elicited much interest because of its potential to modulate a diverse array of pathological conditions, and it is associated with anticancer, antiaging, and anti-inflammatory properties (*6*–*10*). On the basis of the promising data emerging from ex vivo studies and preclinical animal models, resveratrol has been tested in more than 30 clinical trials involving more than 1000 individuals. Nevertheless, the specific pathologies in which resveratrol has substantial clinical benefits are not yet clear (*11*–*16*).

The pharmacological properties of resveratrol have been attributed, at least in part, to its activation of the nicotinamide adenine dinucleotide ($NAD^+$)–dependent silent information regulator 2 (Sir2) deacetylase (*17*) both in vitro (*18*, *19*) and in vivo (*20*). Overexpression of the mammalian Sir2 homolog sirtuin-1 (Sirt1) in mice extends their life span (*21*, *22*) and protects them from a diverse array of diseases (*23*–*28*). Conversely, knocking out Sirt1 is associated with autoimmunity (*29*–*32*). However, the effects of Sirt1 are likely to be complex. Although Sirt1 attenuates murine T cell signaling and effector function (*29*, *30*, *33*–*35*), it also promotes the differentiation of naïve CD4$^+$ T cells into T helper 17 ($T_H17$) effector cells in mice (*36*). Furthermore, physiological modifications of Sirt1 function in human T cell subsets have thus far not been evaluated.

T cell activity is of great importance in a wide range of pathophysiological conditions for which resveratrol activity is being clinically evaluated. Hence, elucidating the potential on-target and off-target effects of resveratrol on T lymphocytes is critical. T cells present a complex target because their cellular metabolism is altered after activation by a cognate antigen. The capacity of T lymphocytes to respond to stimulation by antigen depends on an extensive proliferative response, a process that requires new energetic and biosynthetic components that are supplied, at least in part, through a metabolic shift from oxidative phosphorylation (OXPHOS) toward glycolytic and glutaminolytic pathways (*37*–*39*). This shift from OXPHOS contrasts with the activity of resveratrol, a compound that generally increases mitochondrial activity and associated OXPHOS (*40*–*42*). However, note that resveratrol leads to a wide range of effects, including decreased, stabilized, and enhanced T cell effector functions (*43*–*46*).

Disparate effects of resveratrol on genomic stability have also been reported. In some studies, resveratrol contributes to genomic stability and reduces tumorigenesis by reducing the amount of reactive oxygen species (ROS), which leads to oxidative damage (*47*–*51*). However, in other studies, resveratrol mediates DNA damage, facilitating antitumor treatments (*47*, *52*–*59*). One possible reason for these discrepancies could be that resveratrol has distinct effects on quiescent cells versus proliferating cells. In this regard, T lymphocytes present a challenging target. Although they are generally quiescent, exposure to foreign antigen rapidly stimulates cell cycle entry and cellular proliferation. A coordinated response to genotoxic stress is regulated by the kinases ATM (ataxia telangiectasia–mutated) and ATR (ATM and Rad3-related) (*60*, *61*). Of interest are reports that resveratrol activates one or both of these kinases in different cellular contexts (*53*–*55*). Here, we report that resveratrol rapidly stimulates the ATR-dependent damage pathway in antigen-stimulated human CD4$^+$ T cells, with activation of the tumor suppressor p53. This genotoxic stress response links a metabolic reprogramming to an enhanced CD4 T cell effector function characterized by increased production of the cytokine interferon-γ (IFN-γ).

[1]IGMM, CNRS, Université de Montpellier, Montpellier, France. [2]CNC–Centre for Neuroscience and Cell Biology, University of Coimbra, Coimbra, Portugal. [3]INSERM U1170, Gustave Roussy Cancer Center, Villejuif, France. [4]Faculty of Medicine, Université Paris-Sud, Le Kremlin-Bicêtre, France.
*These authors contributed equally to this work.
†Corresponding author. Email: vjekoslav.dulic@igmm.cnrs.fr (V.D.); taylor@igmm.cnrs.fr (N.T.)

## RESULTS

### Low-dose resveratrol increases the activity of the NAD$^+$-dependent deacetylase Sirt1 in primary human CD4$^+$ T cells

To gain insight into the role of resveratrol in modulating Sirt1 function in human CD4$^+$ T lymphocytes, we first examined its expression profile in response to T cell receptor (TCR) stimulation. We found that TCR engagement resulted in a substantial increase in Sirt1 abundance, with augmented nuclear localization and aggregation (Fig. 1A). Low-dose resveratrol (20 μM) further increased the mean fluorescence intensity (MFI) of Sirt1 staining by about twofold (Fig. 1A and fig. S1A). However, high-dose resveratrol (100 μM) attenuated the TCR-mediated increase in Sirt1 abundance, and these CD4$^+$ lymphocytes did not undergo blast formation (Fig. 1A and fig. S2A). This differed markedly from treatment with low-dose resveratrol, which augmented blast size (fig. S2A). Separating subsets of TCR-stimulated CD4$^+$ T cells based on their forward scatter (FSC) and side scatter (SSC) profiles demonstrated that Sirt1 abundance paralleled increases in cell size and granularity (Fig. 1B). As expected from these data, low-dose resveratrol substantially increased Sirt1 activity in TCR-stimulated lymphocytes, as monitored by the generation of *O*-acetyl–adenosine diphosphate–ribose (OAADPr), a reaction product of the Sirt-catalyzed, NAD$^+$-dependent deacetylation of target proteins (Fig. 1C). Thus, TCR stimulation combined with low-dose, but not high-dose, resveratrol augments Sirt1 activity in human T lymphocytes.

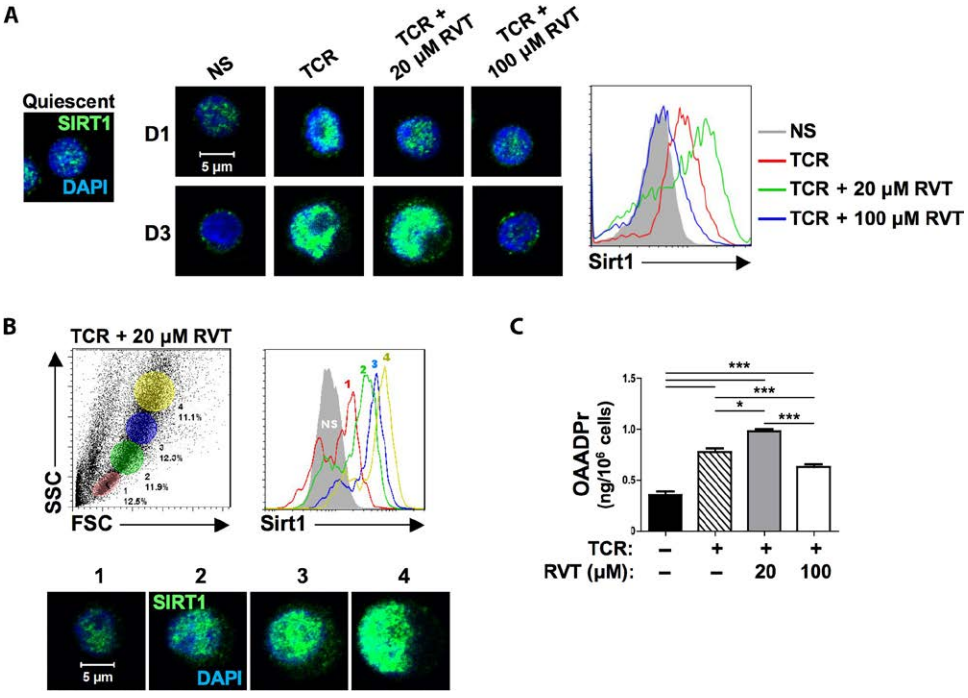


**Fig. 1. Resveratrol modulates the TCR-stimulated activity of the NAD$^+$-dependent deacetylase Sirt1 and blast formation in human CD4$^+$ T cells.** (**A**) Left: The presence of Sirt1 in freshly isolated quiescent human CD4$^+$ T cells was assessed by staining with a Sirt1 polyclonal antibody (green) and the nuclear stain 4′,6-diamidino-2-phenylindole (DAPI) (blue). The presence and localization of Sirt1 were also assessed after 1 (D1) or 3 (D3) days under nonstimulating conditions (NS) or after TCR stimulation (TCR) in the absence or presence of 20 or 100 μM resveratrol (RVT). Images are representative of 50 cells in three independent experiments. Right: Sirt1 was also monitored by flow cytometric analysis of quiescent human CD4$^+$ T cells and cells that were stimulated for 3 days through the TCR in the absence or presence of 20 or 100 μM resveratrol. Data are representative of four independent experiments. (**B**) Left: Sirt1 abundance in CD4$^+$ T cells treated with 20 μM resveratrol was monitored by flow cytometry as a function of both FSC and SSC. The four numbered populations of cells were distinguished on the basis of their FSC-SSC characteristics (dot plot), and Sirt1 abundance in the indicated populations was further analyzed. Right: Histograms are representative of 10 independent experiments. Bottom: Sirt1 abundance and localization in cells from the indicated populations were also analyzed by immunofluorescence staining. Images are representative of three experiments. (**C**) Sirt1 deacetylase activity was monitored as a function of the generation of OAADPr generation, a reaction product of Sirt1-catalyzed NAD$^+$-dependent protein deacetylation. CD4$^+$ T cells were untreated or were stimulated through the TCR in the absence or presence of 20 or 100 μM resveratrol for 3 days before the amount of OAADPr in each sample was determined. Data are means ± SEM of six independent experiments. *$P$ < 0.05, **$P$ < 0.01, and ***$P$ < 0.0001 by one-way analysis of variance (ANOVA) and Tukey's post hoc test.

### Low- and high-dose resveratrol stimulate distinct types of $G_1$ and premitotic cell cycle arrest in TCR-stimulated CD4$^+$ T cells

In light of our findings that high-dose resveratrol inhibited TCR-mediated increases in T cell size and granularity, it was of interest to determine how different doses of resveratrol affected T cell proliferation and cell cycle progression. Although cell viability was not affected by resveratrol (fig. S2A), high-dose resveratrol inhibited the entry of T lymphocytes into the $G_1$ phase of the cell cycle, as assessed by the detection of reduced amounts of total RNA (Fig. 2A and fig. S1B). On the other hand, T cells exposed to low-dose resveratrol exhibited a cell cycle entry and progression that was equivalent to that observed in control TCR-stimulated cells, with about 40% of cells having entered into S phase by day 3 of stimulation (Fig. 2A and fig. S1B). However, note that low-dose resveratrol almost completely abrogated TCR-mediated cellular proliferation (Fig. 2B and fig. S1C), an effect that was not ameliorated by the addition of exogenous interleukin-2 (IL-2) nor by extended time in culture (fig. S2, B and C).

Cell cycle entry and progression are tightly controlled processes involving the action of cyclin-dependent kinases (Cdks) and cyclins (Fig. 2C). To understand the molecular bases underlying the cell cycle arrest caused by different doses of resveratrol, we investigated the regulation of components of the cell cycle machinery. Cyclins D2, E1 and A2, and B1, as well as their cognate kinases, Cdk4/Cdk6, Cdk2, and Cdk1, respectively, were increased in abundance upon T cell activation. Although this increased abundance was not altered by low-dose resveratrol, it was significantly attenuated by high-dose resveratrol under conditions in which high amounts of the Cdk inhibitor p27$^{Kip1}$ were maintained ($P$ < 0.05 at day 1 and $P$ < 0.005 at day 3; Fig. 2, D and E, and fig. S1D). However, by day 3 of activation, high-dose resveratrol-treated cells showed increased cyclin D2 and cyclin E1, but these cells did not progress into S phase (Fig. 2A). Cdk2, cyclin A2, and Cdk1 were not detectable, and phosphorylation of the

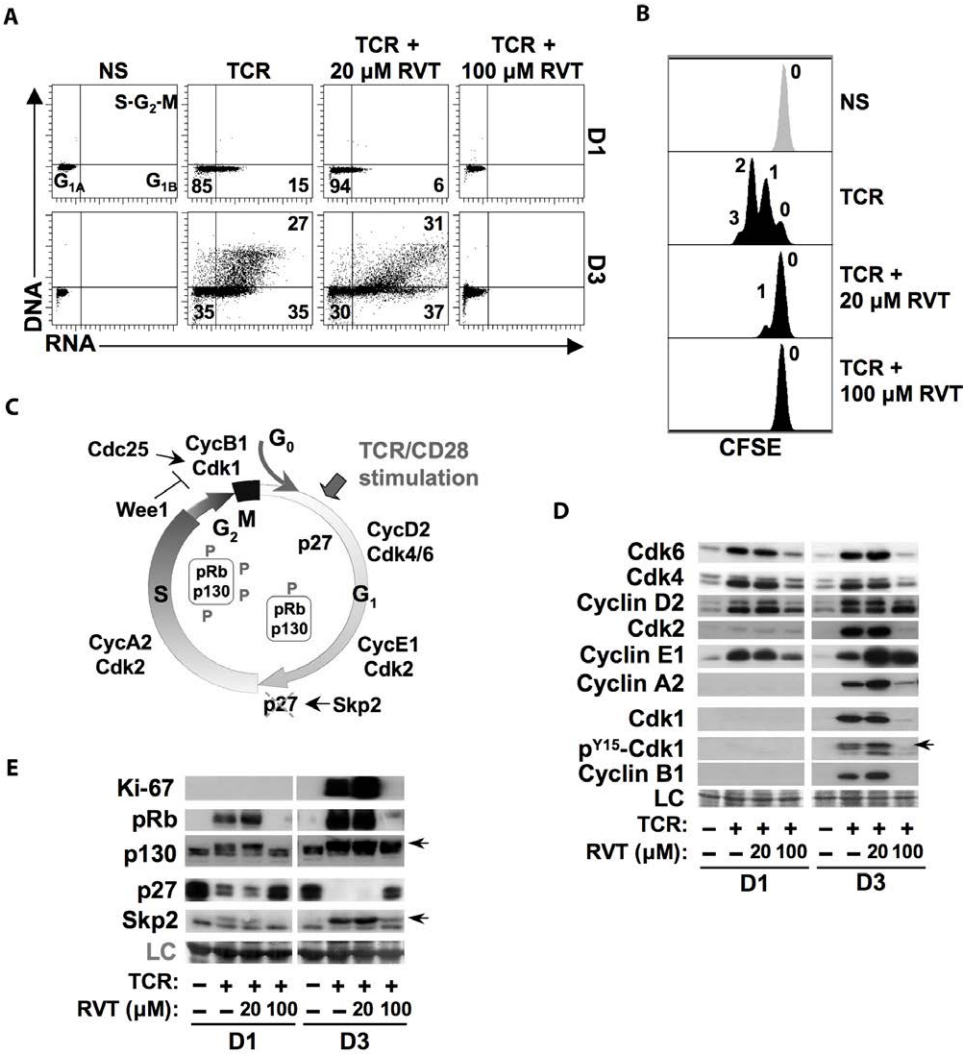


**Fig. 2. Low- and high-dose resveratrol block TCR-mediated cell cycle progression at distinct stages of the cell cycle.** (**A**) Cell cycle entry after TCR stimulation at day 1 (D1; top) and day 3 (D3; bottom) in the presence or absence of resveratrol was monitored by simultaneous staining of DNA and RNA with 7-aminoactinomycin D and pyronin Y, respectively. Representative dot plots from five experiments of nonstimulated and TCR-activated CD4 T cells, in the absence or presence of resveratrol, are shown. The percentages of cells in $G_0$-$G_{1A}$ phase (lower left quadrant), $G_{1B}$ phase (lower right quadrant), and S, $G_2$, and M phases (upper right quadrant) are indicated. (**B**) T cell proliferation under the indicated conditions was monitored by carboxyfluorescein diacetate succinimidyl ester (CFSE) labeling, and dilution of the fluorescent dye was assessed at 72 hours. The number of division peaks is indicated in each histogram. Data are representative of six experiments. (**C**) Schematic representation of cell cycle regulators that are altered upon TCR-mediated cell cycle entry. Cell cycle progression requires the expression of cyclins and Cdks, the F-box protein Skp2-dependent and ubiquitin-mediated degradation of the $p27^{Kip1}$ Cdk inhibitor, and Cdk-mediated hyperphosphorylation of the pRb tumor suppressor and the related p130 pocket protein. Cdk1 activity and mitotic entry are regulated by the kinase Wee1 and the phosphatase of Cdc25. (**D**) The abundances of the cyclins-Cdks that regulate cell cycle entry, including cyclins D2, E1, A2, and B1, and Cdk4, Cdk6, Cdk2, and Cdk1 were monitored by Western blotting analysis on days 1 and 3 of activation. Data are representative of three independent experiments. The arrow indicates the hyperphosphorylated Cdk1 isoform. (**E**) The abundances of the Ki-67 proliferation marker, cell division inhibitors (pRb, p130, and p27), and the p27 regulator Skp2 under the indicated conditions were monitored by Western blotting analysis. Data are representative of three independent experiments. Arrows indicated hyperphosphorylated p130 and phosphorylated Skp2. Quantification of all panels is shown in fig. S1.

pocket proteins pRb (retinoblastoma protein) and p130, hallmarks of S-phase progression, was also not observed (Fig. 2, D and E, and fig. S1E). Furthermore, the Cdks regulating the $G_1$-S phase progression (Cdk4, Cdk6, Cdk2, and Cdk1) were not increased in abundance (Fig. 2D). We found that this was likely because of the reduced abundance and phosphorylation of the F-box protein Skp2 (Fig. 2E, upper band, and fig. S1E), the rate-limiting component responsible for $p27^{Kip1}$ ubiquitination and degradation (*62*, *63*). The premitotic cell cycle arrest that was triggered by low-dose resveratrol did not result in senescence, as shown by the enhanced phosphorylation of pocket proteins, increased amounts of cyclins A2 and B1 and the proliferation marker Ki-67, as well as decreased $p27^{Kip1}$ abundance (Fig. 2, D and E, and fig. S1, D and E). Furthermore, accumulation of hyperphosphorylated Cdk1 (Fig. 2D, arrow) suggests that resveratrol blocks the $G_2$-M transition of the cell cycle by abrogating the Cdc25-mediated activation of Cdk1 (Fig. 2C).

### Low-dose resveratrol does not alter TCR-stimulated proximal and distal signaling cascades

To determine whether the cell cycle blockade mediated by low-dose resveratrol was due to defective initiation of the TCR signaling cascade, we first assessed proximal signaling intermediates. The kinase ZAP-70, which is associated with the TCRζ chain in activated lymphocytes, was phosphorylated by 1 min after TCR engagement and was not affected by either low- or high-dose resveratrol (Fig. 3A). Further downstream signaling was monitored as a function of extracellular signal–regulated kinase 1/2 (ERK1/2) and AKT phosphorylation. Neither ERK1/2 nor AKT phosphorylation was altered by low-dose resveratrol, and phosphorylation was only marginally decreased in the presence of high-dose resveratrol (Fig. 3, A and B, and fig. S1F).

TCR signaling also activates mammalian target of rapamycin (mTOR) (*64*–*66*), a serine/threonine protein kinase that integrates environmental cues such as nutrients, growth factors, and stress signals into an "optimal" cellular response (*67*, *68*). Sirt1 activity generally inhibits mTOR signaling (*69*–*71*), but in murine T cells, ectopic Sirt1 has not been shown to alter this cascade (*35*). mTOR complex 1 (mTORC1) activity is negatively regulated by tuberous sclerosis complex 1/2 (TSC1/2), which serves as a hub for both positive and negative cues for signaling kinases. Phosphorylation of TSC2 at T1462 by Akt leads to the activation of mTORC1, and in human $CD4^+$ T cells, low-dose resveratrol did not affect the TCR-mediated phosphorylation of this signaling molecule.

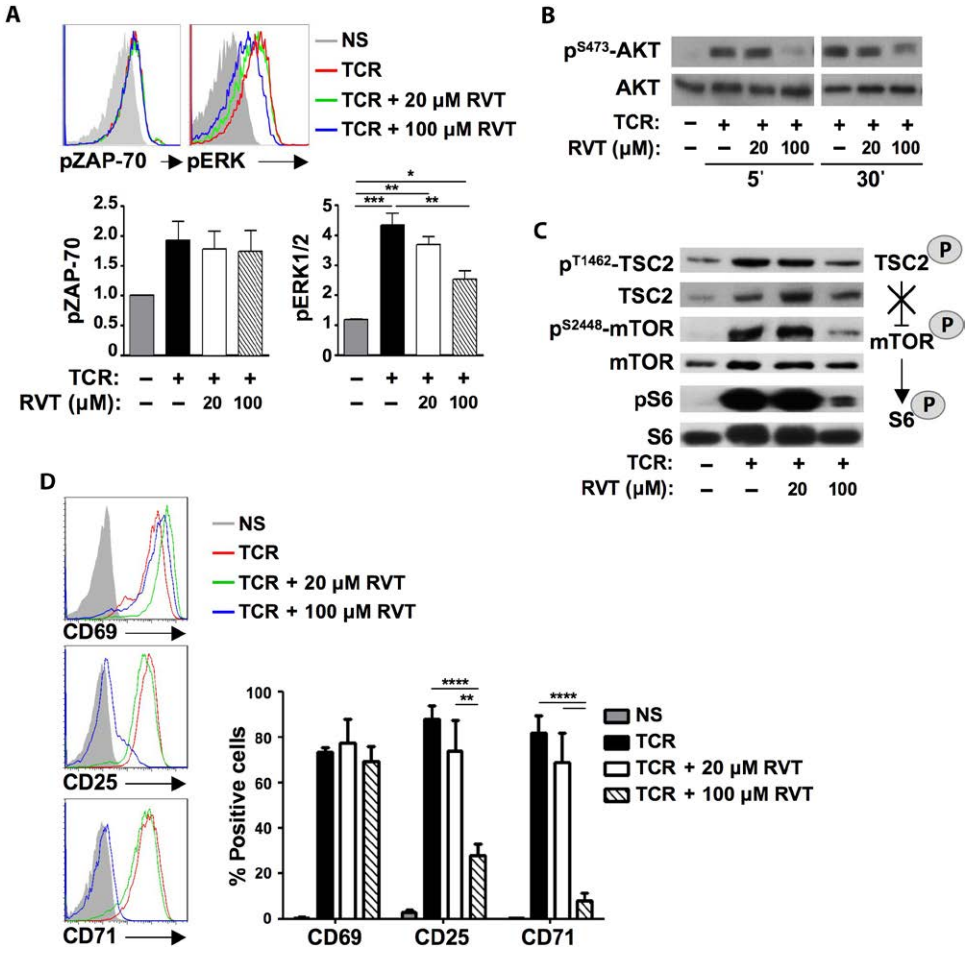


**Fig. 3. TCR signaling is attenuated by high-dose, but not low-dose, resveratrol.** (**A**) Top: Phosphorylation of ZAP-70 and ERK after TCR stimulation of human CD4$^+$ T cells in the presence of 20 or 100 μM resveratrol was monitored by flow cytometry. Representative histograms at 1 min after stimulation are presented. Bottom: Quantification of the fold increase in MFIs of the indicated proteins in stimulated relative to nonstimulated CD4$^+$ T cells. Data are means ± SEM of three independent experiments. *$P$ < 0.05, **$P$ < 0.01, and ***$P$ < 0.005 by one-way ANOVA and Tukey's post hoc test. (**B**) The relative amounts of total and phosphorylated Akt in T cells 5 and 30 min after activation under the indicated conditions were determined by Western blotting analysis. Data are representative of three experiments. (**C**) The extent of phosphorylation of TSC2, mTOR, and S6 in CD4$^+$ T cells 24 hours after stimulation under the indicated conditions was monitored by Western blotting analysis. Data are representative of three experiments. (**D**) Left: The cell surface expression of the CD69, IL-2Rα (CD25), and transferrin receptor (CD71) activation markers on CD4$^+$ T cells stimulated under the indicated conditions were assessed by flow cytometry. Histograms are representative of three independent experiments. Right: Quantification of the percentages of positive cells under each condition. **$P$ < 0.01 and ****$P$ < 0.0001 by two-way ANOVA with Bonferroni's post hoc test. Quantification data are shown in fig. S1.

Furthermore, neither phosphorylation of mTOR itself nor S6 ribosomal protein, a downstream mTOR substrate, was altered by low-dose resveratrol. Note that phosphorylation was significantly decreased in the presence of 100 μM resveratrol ($P$ < 0.01; Fig. 3C and fig. S1G). Thus, mTOR signaling in TCR-stimulated T cells is attenuated by high-dose resveratrol, whereas at low doses, the activity resulting from TCR engagement is maintained.

We next assessed whether distal TCR signaling was altered by resveratrol, monitored as a function of the cell surface abundance of the CD69, CD25 (IL-2Rα subunit), and CD71 (transferrin receptor) activation markers. Surface abundance of CD69, due to the translocation of intracellular stores to the cell membrane without a requirement for protein synthesis (*72*, *73*), was increased in most of the activated cells, irrespective of the presence of resveratrol (Fig. 3D). In marked contrast, induction of CD25 and CD71, both of which are dependent on de novo protein synthesis, was significantly attenuated by high-dose resveratrol but was unaffected by low doses of the polyphenol ($P$ < 0.001; Fig. 3D). Thus, only high-dose resveratrol impedes mTOR and distal TCR signaling cascades.

## Low-dose resveratrol stimulates a replication stress response in TCR-stimulated CD4$^+$ T cells

The experiments performed thus far demonstrated that low-dose resveratrol inhibits CD4$^+$ T cell division under conditions in which TCR and mTOR signaling responses are maintained. To further explore this phenomenon and to determine the origin of the cell cycle arrest, we focused on the effects of low-dose resveratrol on genomic integrity. Resveratrol has been found to both positively and negatively affect genome integrity in cancer cells (*57*, *74*–*78*), but its function in primary human T cells has not been elucidated. To specifically address this point in T lymphocytes, we monitored histone H2AX phosphorylation (γH2AX). This modification identifies DNA damage foci as well as stalled replication forks that promote the concentration of repair proteins (*79*, *80*).

TCR engagement of CD4$^+$ T cells did not result in the augmentation of γH2AX (Fig. 2, A and D), at least at time points before entry into S phase (2 to 24 hours; Fig. 4A). However, in low-dose resveratrol, γH2AX$^+$ cells reached significantly higher percentages by 24 hours (45%, $P$ < 0.005; Fig. 4A); these percentages were similar to those detected in the presence of aphidicolin, an inhibitor of replication polymerases that stalls replication forks and results in a late $G_1$-phase arrest (*81*). High-dose resveratrol had a distinct effect, increasing the abundance of H2AX foci in 7 to 10% of cells, irrespective of the kinetics or TCR stimulation. The lower amount of H2AX phosphorylation in cells treated with high-dose resveratrol may be due to their attenuated response to TCR stimulation (Fig. 3). Notably, stimulation with the homeostatic cytokine IL-7 significantly increased γH2AX in cells treated with high, but not low, doses of resveratrol ($P$ < 0.005; Fig. 4B), suggesting that resveratrol effects on genomic integrity are likely to be dependent on the nature of the activation signal. Whereas it is not known how IL-7 signaling affects the potential of resveratrol to alter genomic integrity or its response to this stress, note that the addition of IL-2 did not alter resveratrol-driven H2AX phosphorylation in TCR-stimulated T cells (Fig. 4C).

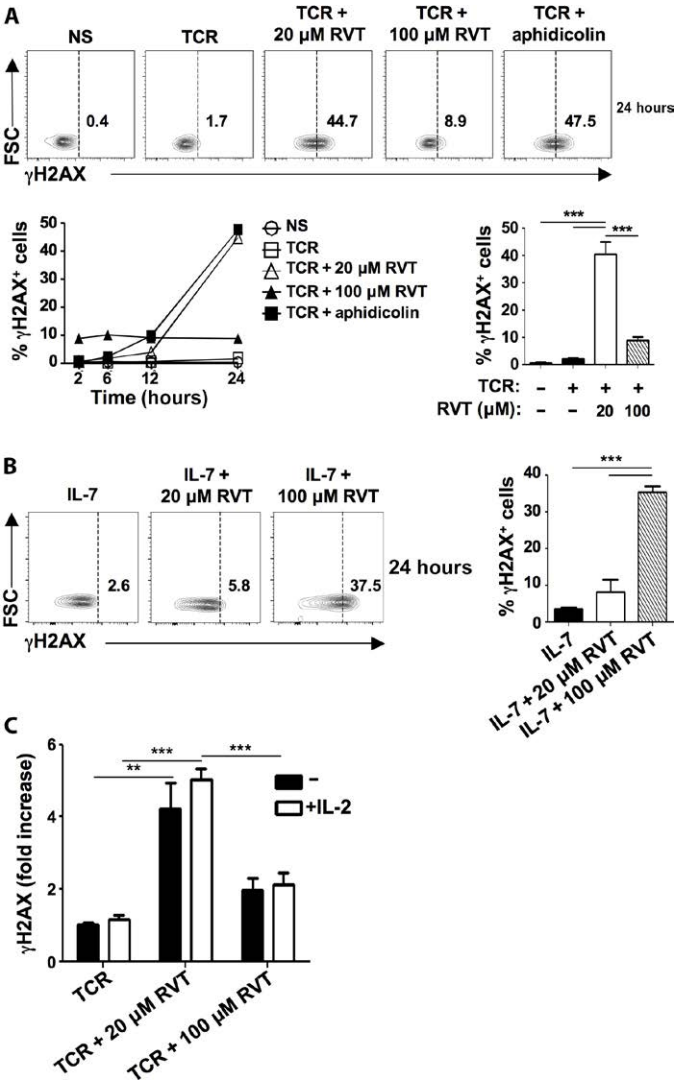


**Fig. 4. Low-dose resveratrol stimulates H2AX phosphorylation in TCR-stimulated CD4$^+$ T lymphocytes.** (**A**) Top: Freshly isolated quiescent CD4$^+$ T cells were either left nonstimulated or were TCR-stimulated in the presence of resveratrol (20 and 100 μM) or aphidicolin. The amount of H2AX phosphorylation (γH2AX) was assessed at 24 hours by flow cytometry. Data are representative of four independent experiments. Bottom left: The percentages of γH2AX-positive cells were quantified after 2, 6, 12, and 24 hours of stimulation. Data are representative of four independent experiments. Bottom right: Means ± SEM of γH2AX-positive cells from three independent experiments. Statistical significance was determined by one-way ANOVA with Tukey's post hoc test. ***$P$ < 0.005. (**B**) Left: CD4$^+$ T cells were cultured with the homeostatic cytokine IL-7 (10 ng/ml) in the absence or presence of resveratrol (20 and 100 μM). H2AX phosphorylation (γH2AX) was assessed at 24 hours by flow cytometry. Dot plots are representative of three experiments. Right: Means ± SEM of three independent experiments. Data were analyzed by one-way ANOVA with Tukey's post hoc test. (**C**) CD4$^+$ T cells were TCR-stimulated in the presence or absence of resveratrol (20 and 100 μM) and in the presence or absence of IL-2 (50 U/ml). H2AX phosphorylation was assessed by flow cytometry as described earlier, and the increase in phosphorylation relative to that in cells stimulated by TCR engagement alone is shown. Data are means ± SEM of three experiments with statistical significance determined by one-way ANOVA with Tukey's post hoc test. **$P$ < 0.01 and ***$P$ < 0.005.

## Resveratrol stimulates p53 phosphorylation and ATR-mediated cell cycle arrest

In light of the data shown earlier, it was critical to monitor activation of the p53 tumor suppressor, a protein that is phosphorylated in response to a wide range of genotoxic insults (*60*). At day 1 of TCR stimulation, low-dose resveratrol resulted in the accumulation and phosphorylation of p53, similar to that detected under conditions of aphidicolin-mediated stalled replication. Furthermore, by day 3, p53 phosphorylation was also increased under high-dose resveratrol conditions ($P$ < 0.005; Fig. 5A and fig. S1H). Several hypotheses could account for the phosphorylation of p53: first, activation of the adenosine monophosphate–activated protein kinase (AMPK) pathway (*82*–*84*); second, activation of the ATM pathway in response to double-stranded DNA breaks (*60*, *85*); and third, activation of the ATR pathway in response to single-stranded breaks and replication stress due to stalled fork progression or DNA synthesis (*61*). Regarding the first hypothesis, glucose deprivation and AMPK activation have been specifically shown to stimulate p53 phosphorylation (*82*, *83*). However, an AMPK inhibitor (compound C) did not significantly alter resveratrol-stimulated p53 phosphorylation, although it decreased AMPK phosphorylation by a mean of 75% (Fig. 5B and fig. S1I). These data suggest that AMPK signaling does not drive p53 phosphorylation in resveratrol-treated CD4$^+$ T lymphocytes.

To address the second and third hypotheses, we assessed the implication of the ATM and ATR pathways in the response of CD4$^+$ T cells to resveratrol. Classically, ATR is stimulated by replication stress or single-stranded DNA breaks, resulting in the activation of checkpoint kinase 1 (Chk1) (*86*) and its downstream target, the kinase Wee1, a negative mitotic regulator (Fig. 5C) (*85*). Although Chk1 activation is often underestimated because of its transient phosphorylation (*87*), resveratrol stimulated both Chk1 and Wee1 phosphorylation (Fig. 5D and fig. S1J). Chk1 and Wee1 block Cdk1 activation by inhibiting Cdc25 phosphatase and hyperphosphorylating Cdk1, respectively (Fig. 5C). Accordingly, ATR signaling in response to low-dose resveratrol was associated with a defective dephosphorylation of Cdk1 that is required for Cdk1 activation and mitotic entry (Fig. 5D, arrow). In contrast, the ATM pathway was not activated by low-dose resveratrol because neither phosphorylation of Chk2 nor the downstream Cdk inhibitor p21$^{Waf1/Cip1}$ (p21) was detected (Fig. 5D and fig. S1J). As positive controls, we assessed the capacity of bleomycin and aphidicolin to efficiently activate ATM/ATR and ATR pathway intermediates, respectively (Fig. 5, C and D).

These data suggested that the early H2AX phosphorylation in resveratrol-treated CD4$^+$ T cells was due to a replication stress–like insult rather than an ATM signaling cascade stimulated by double-stranded DNA breaks. To test this possibility, we assessed the phosphorylation of the minichromosome maintenance (MCM) helicase complex, a key component of the prereplication complex that is specifically phosphorylated by ATR at Ser$^{108}$ in response to multiple forms of DNA damage (*88*–*90*). Before the onset of S phase (24 hours), Mcm2 phosphorylation at S108 was augmented by low-dose resveratrol to a similar extent to that detected in response to aphidicolin and bleomycin (Fig. 5D and fig. S1J). Furthermore, although T cells exposed to high-dose resveratrol never progressed to S phase (Fig. 2, A and D), p53, Chk1, Wee1, and Mcm2 phosphorylation were also detected in these cells by 72 hours after stimulation (Fig. 5D). Together, these data suggest that resveratrol activates the ATR, but not ATM, signaling cascade in stimulated CD4$^+$ T cells.

We therefore assessed whether the resveratrol-stimulated phosphorylation of p53 was directly regulated by ATR signaling in resveratrol-treated

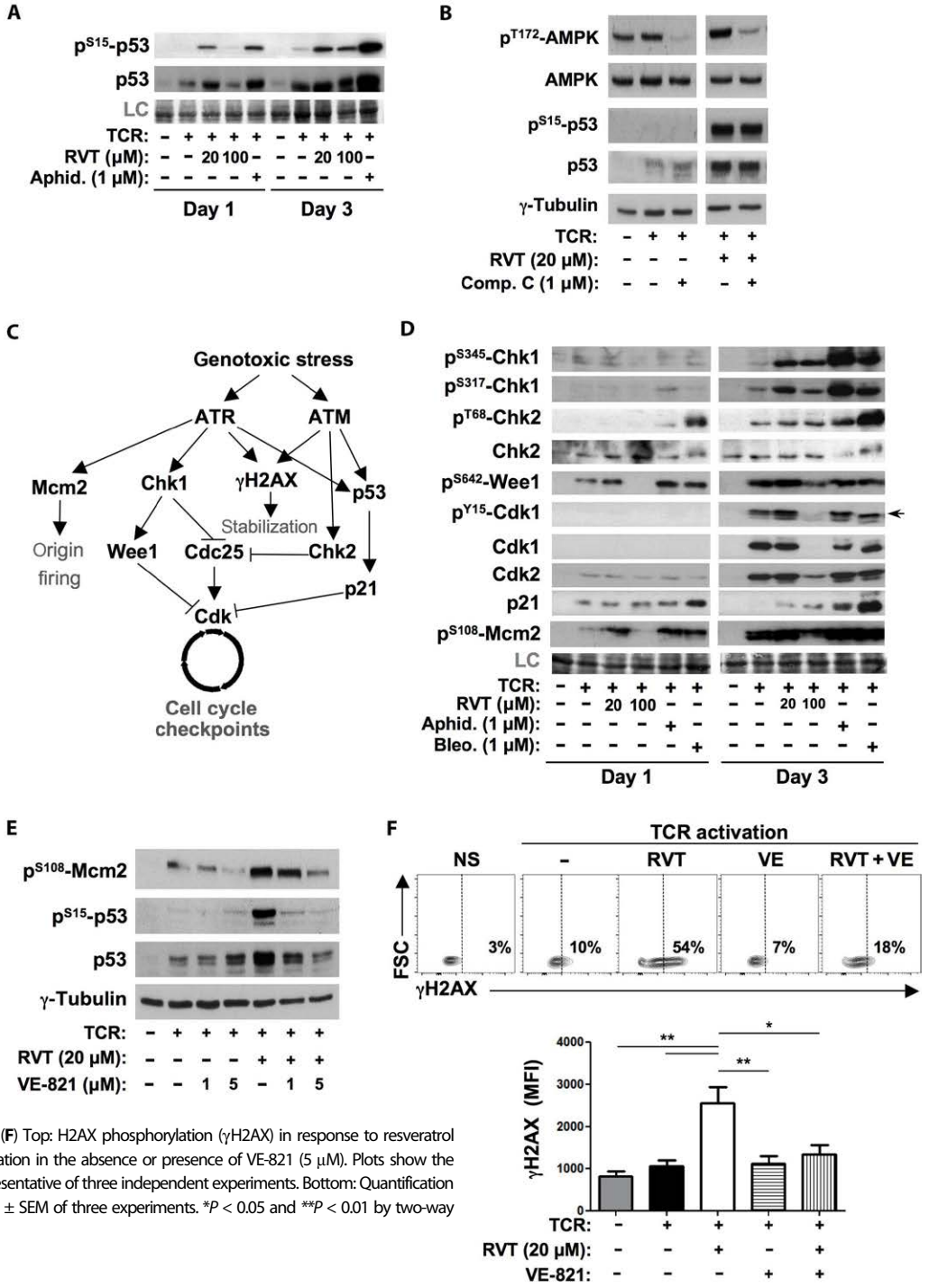


**Fig. 5. Resveratrol stimulates p53 phosphorylation and the ATR-mediated arrest of the cell cycle.** (**A**) Phosphorylation of p53 at Ser[15] and total p53 were monitored by Western blotting analysis of CD4$^+$ T cells activated in the absence or presence of resveratrol (20 and 100 μM) or aphidicolin (1 μM). Representative blots at days 1 and 3 of activation and loading controls (LC) are shown. Data are representative of three experiments; quantification data are shown in fig. S1. (**B**) Phosphorylation of AMPK and p53 was assessed by Western blotting analysis of CD4$^+$ T cells at day 1 after treatment as indicated with resveratrol and the AMPK inhibitor (compound C; 1 μM). Representative blots showing phosphorylated and total proteins under the indicated conditions are shown. Data are representative of three experiments; quantification data are shown in fig. S1. (**C**) Schematic model of the ATR and ATM signaling cascades culminating in cell cycle arrest. The former results in Chk1 activation, whereas the latter proceeds through Chk2 activation and the p53-mediated expression of p21. p21 directly inhibits Cdks, whereas Chk1 blocks cell cycle progression by activating Wee1 and preventing the Cdc25-mediated dephosphorylation of Cdk1. (**D**) The abundance and phosphorylation of Chk1 and Chk2 and the cell cycle regulators Wee1, Cdk1, Cdk2, p21, and Mcm2 were monitored by Western blotting analysis of cells treated under the indicated conditions. Blots of samples at days 1 and 3 are representative of three experiments. The arrow indicates hyperphosphorylated Cdk1. Quantification data are shown in fig. S1. (**E**) Phosphorylation of Mcm2 and p53 in cells was assessed by Western blotting analysis with the appropriate phosphospecific antibodies at day 1 after treatment with resveratrol and the ATR inhibitor (VE-821; 1 and 5 μM). The amounts of total p53 and γ-tubulin were assessed. Data are representative of three independent experiments. Quantification data are shown in fig. S1. (**F**) Top: H2AX phosphorylation (γH2AX) in response to resveratrol treatment was assessed at 24 hours after stimulation in the absence or presence of VE-821 (5 μM). Plots show the percentages of γH2AX-positive cells and are representative of three independent experiments. Bottom: Quantification of the MFI of γH2AX staining is shown as means ± SEM of three experiments. *$P$ < 0.05 and **$P$ < 0.01 by two-way ANOVA with Bonferroni's post hoc test.

T cells. To this end, we tested the effects of VE-821, a potent ATR inhibitor (*91*, *92*). As expected, VE-821 decreased Mcm2 phosphorylation (Fig. 5E and fig. S1K). Moreover, p53 phosphorylation was attenuated by a mean of 90% in the presence of VE-821, and the global amount of p53 decreased ($P$ < 0.001; Fig. 5E and fig. S1K), demonstrating that the ATR stress response pathway regulates the resveratrol activation of p53 in TCR-stimulated CD4$^+$ T cells. We also found that the ATR pathway is directly implicated in the formation of γH2AX foci (*61*) as VE-821 inhibited resveratrol activation of H2AX phosphorylation ($P$ < 0.05; Fig. 5F). Together, these data reveal a critical role for the ATR cascade in mediating a p53-associated stress response in response to resveratrol.

## CD4$^+$ T cells exhibit increased expression of p53-dependent target genes and undergo a metabolic switch in response to low-dose resveratrol

To elucidate potential molecular mechanisms associated with resveratrol treatment of CD4$^+$ T cells, we performed an array analysis of genes involved in DNA damage signaling responses. Whereas the expression

of multiple genes was altered after treatment with high-dose resveratrol or aphidicolin, only 1 of 84 assessed genes, *Bbc3* [*PUMA* (p53 upregulated modulator of apoptosis)], was consistently increased in expression in low-dose resveratrol–treated CD4 T cells (4.1- to 6.4-fold, $n = 3$; Fig. 6A and fig. S3). Furthermore, it was even more highly expressed at high-dose resveratrol (8- to 22-fold, $n = 3$; fig. S3). Notably, *PUMA* is a proapoptotic gene whose transcription is directly regulated by p53 (*93*). Because the p53 pathway has also been linked to a metabolic reprogramming (*94*–*96*), at least in part through the regulation of metabolic genes, we assessed whether expression of these genes is altered by resveratrol. Notably, expression of *TIGAR* (TP53-induced glycolysis and apoptosis regulator), *PGM* (phosphoglycerate mutase), *GLS2* (glutaminase 2), and *SCO2* (synthesis of cytochrome c oxidase 2) was significantly altered by resveratrol (Fig. 6B). p53-mediated induction of TIGAR, a fructose-2,6-bisphosphatase, and attenuated amounts of *PGM*, would both be expected to decrease glycolysis (*97*–*99*). Moreover, we found that whereas TCR engagement significantly increased the cell surface abundance of the glucose transporter Glut1, the amount was significantly lower in the presence of low-dose resveratrol and was abrogated by high-dose resveratrol ($P < 0.05$ and $P < 0.001$; Fig. 6C and fig. S1L). The changes correlated directly with glucose uptake and glycolysis, as monitored by the production of lactate and extracellular acidification ($P < 0.001$; Fig. 6D).

Glucose metabolism was decreased in the presence of resveratrol, but lymphocyte metabolism can also be fueled by other nutrients such as glutamine. Notably, the ASCT2 glutamine transporter, recently shown to be critical for T cell activation (*100*), was augmented in the presence of low-dose, but not high-dose, resveratrol. Moreover, the ratio of surface ASCT2/Glut1 was significantly increased by low-dose resveratrol as compared to TCR activation alone ($P < 0.01$; Fig. 6D). The potential importance of resveratrol-linked glutaminolysis in $CD4^+$ T cells was also suggested by the induction of the p53-dependent *GLS2* gene (Fig. 6B), catalyzing the hydrolysis of glutamine to glutamate (*101*–*103*). This link was corroborated by an increased glutamine uptake in activated T cells treated with low-dose resveratrol (Fig. 6E).

The increase in glutamine entry and the enzymes involved in the first steps of glutaminolysis suggested that p53 activation might augment OXPHOS in these T lymphocytes. In tumor cells, p53 decreases glycolysis while enhancing OXPHOS (*104*, *105*). One of the mechanisms through which p53 augments tricarboxylic acid (TCA) cycling from glutamine intermediates (anaplerosis) is through the expression of *SCO2*, a protein that catalyzes the transfer of reducing equivalents from cytochrome c to molecular oxygen in mitochondria (*103*). To assess the extent of OXPHOS in human $CD4^+$ T cells, we directly monitored the oxygen consumption rate (OCR) and found that TCR stimulation significantly increased the basal cellular respiration of $CD4^+$ T cells ($P < 0.005$; Fig. 6F). Low-dose resveratrol further enhanced respiration, but TCR-stimulated respiration was almost completely abrogated by high-dose resveratrol ($P < 0.05$; Fig. 6F). Increased oxygen consumption would also be expected to result in increased ROS, with mitochondria serving as the major intracellular source of ROS. Superoxide anion—the predominant ROS in mitochondria—was significantly augmented by resveratrol, as monitored by MitoSOX staining ($P < 0.05$; Fig. 6F). These metabolic parameters correlated directly with the bioenergetic profile of the $CD4^+$ T cells; intracellular adenosine triphosphate (ATP) was significantly increased in low-dose resveratrol–treated cells but was attenuated in lymphocytes treated with high-dose resveratrol ($P < 0.005$; Fig. 6F). Thus, resveratrol significantly modulated the expression of p53 target genes, concordant with changes in the metabolic state of these lymphocytes.

### Altered metabolism in resveratrol-treated naïve and memory $CD4^+$ T cells enhances their effector function

In recent years, the critical importance of metabolism (and most specifically glucose metabolism) in T cell effector function has been established (*37*, *106*–*108*). However, entry of glutamine via the ASCT2 amino acid transporter (*SLC1A5*) has been shown to be a sine qua non for the effector function of murine $CD4^+$ T cells (*100*, *109*). Furthermore, although it has not been specifically shown for T cells, a heightened need for biosynthetic intermediates is often associated with a metabolic switch resulting in a disproportionate dependency on glutamine, undergoing anaplerotic reactions to form α-ketoglutarate for use in the TCA cycle (*110*–*112*). It was therefore of interest to assess whether $CD4^+$ T cell effector function is altered in the presence of resveratrol wherein biosynthetic intermediates were not required for proliferation, due to the block in cell cycle, and a switch to an oxidative metabolism was associated with increased intracellular ATP stores (Fig. 6).

T cell effector function is tightly linked to the differentiation state of the lymphocyte, and different subsets of memory T helper cells can be distinguished on the basis of chemokine receptor markers [reviewed in (*113*)]. It was therefore important to determine whether resveratrol potentially changed the survival of sorted naïve and memory T cell subsets (fig. S4A) or, rather, whether it altered the effector profile of memory T helper cells. We therefore monitored the surface abundance of CXCR3, CCR4, and CCR6 on memory $CD4^+$ T cells (fig. S4B). Although $CXCR3^+$ and $CCR4^+CCR6^+$ profiles are associated with $T_H1$ and $T_H17$ subsets, respectively, we found that CXCR3 and CCR4 were increased in most of the $CD4^+$ T cells after TCR stimulation (fig. S4B). Notably, the relative percentage of $CXCR3^+CCR6^+$ cells within the $CD4^+$ T cell subset was 1.7 ± 0.2–fold higher in the presence of low-dose resveratrol ($P < 0.01$; fig. S4B), suggesting a higher cytokine secretion potential. The percentages of naïve and memory $CD4^+$ T cells secreting IFN-γ after TCR stimulation (day 6) was greater than four- and twofold higher in the presence of low-dose resveratrol, respectively ($P < 0.005$; Fig. 7A). Furthermore, most of the T cells that secreted IFN-γ also produced IL-2 ($P < 0.005$; Fig. 7A). The increased capacity of resveratrol-treated T cells to secrete cytokines was also detected in the total $CD4^+$ population (fig. S4C). Thus, low-dose resveratrol stimulates an ATR-mediated cell cycle arrest in antigen receptor–stimulated $CD4^+$ T lymphocytes that is coupled to a metabolic reprogramming and augmented effector function.

## DISCUSSION

Our study demonstrates that resveratrol modulates the potential of human $CD4^+$ T lymphocytes to respond to antigen receptor stimulation. Although resveratrol exerts effects in both Sirt1-dependent and Sirt1-independent manners (*20*, *114*), we found that high-dose resveratrol (100 μM) inhibited the TCR-induced expression of Sirt1 in T lymphocytes. In this condition, this was likely caused by an attenuation of mTOR and distal TCR signaling. In contrast, low-dose resveratrol (20 μM) markedly increased TCR-stimulated Sirt1 activity. Furthermore, p53—a tumor suppressor whose activity is coordinated by and coordinates that of Sirt1 (*115*)—was highly phosphorylated in response to low-dose resveratrol. We determined that this p53 phosphorylation was mediated by the kinase ATR, a key regulator of the genotoxic stress response pathway. Concordant with ATR and p53 signaling, T cells exposed to low-dose resveratrol underwent Chk1- and Wee1-mediated premitotic cell cycle arrest and induced expression of p53-dependent metabolic target genes, resulting in a metabolic shift with increased OXPHOS. Note that these conditions,

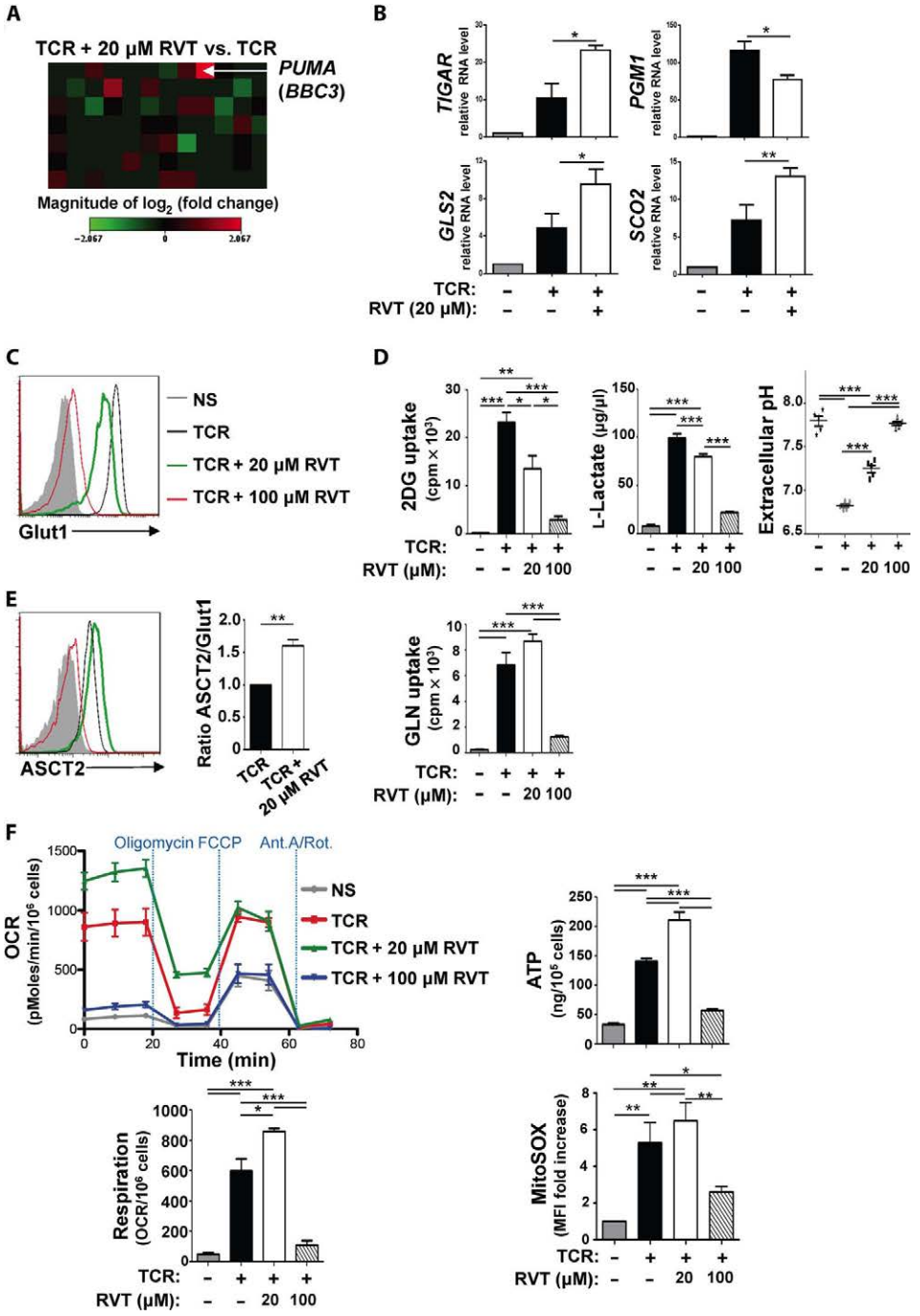


**Fig. 6. TCR-stimulated CD4$^+$ T cells exhibit increased transcription of p53-dependent metabolic target genes and an altered T cell metabolism after exposure to resveratrol.** (**A**) The expression of 84 genes involved in DNA damage signaling pathways was evaluated in CD4$^+$ T cells activated by TCR engagement alone as compared to TCR engagement in the presence of resveratrol (20 μM) using a polymerase chain reaction (PCR) array profile (Qiagen; fig. S3). Representative data in one of three samples at day 1 of stimulation are shown with only *Bbc3* (PUMA) significantly induced in the latter conditions (4.2- to 6.4-fold induction, $n = 3$). (**B**) Transcripts of p53 metabolic target genes including *TIGAR*, *PGM*, *GLS2*, and *SCO2* were monitored by quantitative reverse transcription PCR analysis of cells under the indicated conditions (day 3) and were normalized against the abundance of 18*S* ribosomal RNA. Data are means ± SEM of four independent experiments. *$P < 0.05$ and **$P < 0.01$ by paired *t* test. (**C**) Glut1 surface expression was monitored by flow cytometry, and representative histograms from three experiments under the indicated conditions (day 3) are shown, with quantifications shown in fig. S1. (**D**) 2-Deoxy-D[1-$^3$H] glucose (2DG) uptake ($n = 3$), lactate production ($n = 5$), and extracellular acidification ($n = 5$) were monitored in cells under the indicated conditions at day 3. Data are means ± SEM of the indicated number of experiments. *$P < 0.05$, **$P < 0.01$, and ***$P < 0.005$ by one-way ANOVA with Tukey's post hoc test. (**E**) Left: ASCT2 surface expression was monitored by flow cytometry, and representative histograms are shown. Middle: The ratio ± SEM of ASCT2 to Glut1 abundance in cells stimulated through the TCR in the presence or absence of resveratrol are presented as a function of the MFI of both transporters ($n = 3$; paired *t* test). Right: Uptake of L-2,3,4-[$^3$H]glutamine was performed for 10 min, and mean counts per minute ± SEM for triplicate samples from three independent experiments at day 3 are presented. Data were analyzed by one-way ANOVA with Tukey's post hoc test. **$P < 0.01$. (**F**) Left: Cellular respiration was monitored on a Seahorse XF-24 analyzer, and OCRs of triplicate samples under basal conditions and in response to the indicated mitochondrial inhibitors are presented for cells on day 3 of activation. Mean basal consumption rates (OCR; picomoles/min per $10^6$ cells) ± SEM of triplicate samples from three independent experiments are shown (upper right). Right: ATP was measured in cells under the same conditions by luminescent detection, and mean intracellular amounts ± SEM from data obtained in 10 independent experiments are presented. Data were analyzed by one-way ANOVA with Tukey's post hoc test. Mitochondrial superoxide anion was monitored using MitoSOX Red reagent, and the MFI ± SEM of triplicate samples are presented. Data were analyzed by paired *t* test. FCCP, carbonyl cyanide *p*-trifluoromethoxyphenylhydrazone; Ant.A, antimycin A; Rot., rotenone. *$P < 0.05$, **$P < 0.01$, and ***$P < 0.005$.

which promoted an enhanced bioenergetic profile, endowed CD4$^+$ T cells with a substantially enhanced cytokine secretion potential (Fig. 7B).

The role of resveratrol in protecting against carcinogenesis has been the subject of intense study, and multiple reports showed that resveratrol functions by preventing DNA damage formation as well as by improving DNA damage repair (*47*, *50*, *116*). Resveratrol affects multiple aspects of DNA metabolism, including DNA replication, recombination, repair, and telomere maintenance, as well as the redox state, thereby promoting the integrity of genomic DNA. However, in vitro, resveratrol mediates DNA cleavage in a process requiring DNA-bound copper [Cu(II)] ions (*49*, *57*, *59*, *117*–*119*). On the basis of diverse studies, it is nearly impossible to draw clear-cut conclusions about the effects of sirtuins or resveratrol on genomic stability. Both reduction of DNA breaks and an inhibition of replicative senescence (*57*, *74*–*78*), as well as the generation

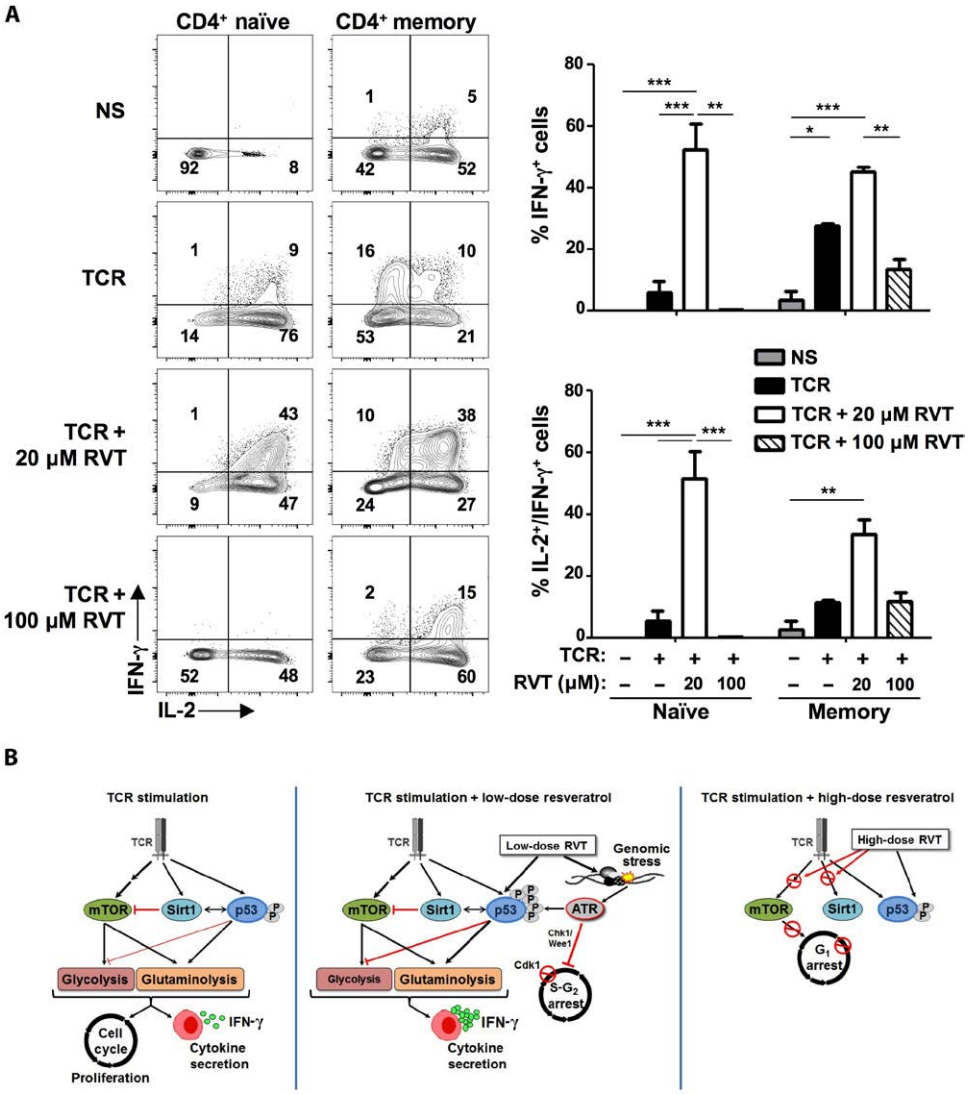


**Fig. 7. IFN-γ secretion by TCR-stimulated naïve and memory CD4$^+$ T cells is markedly enhanced by low-dose resveratrol.** (**A**) Left: Naïve and memory CD4$^+$ T cells were isolated, as described in fig. S4A, and were stimulated through the TCR in the presence or absence of resveratrol (20 and 100 μM). Secretion of IL-2 and IFN-γ was monitored by intracellular staining at day 6, and representative dot plots of three representative experiments are shown. Right: Quantification of the mean percentages ± SEM of IFN-γ–secreting and double IL-2/IFN-γ–secreting cells are shown. Data were analyzed by two-way ANOVA with Bonferroni's post hoc test. (**B**) Proposed model showing the effects of resveratrol on TCR-stimulated CD4$^+$ T cells. Left: Sirt1 and p53 are interrelated, regulating mTOR signals and metabolic networks (*115*), and both are activated in response to TCR stimulation of human CD4$^+$ T cells. The integration of TCR signals stimulates intracellular glycolysis and glutaminolysis, resulting in proliferation and effector function. Middle: In response to low-dose resveratrol, TCR-engaged CD4$^+$ T cells undergo a genomic stress response, which results in an ATR- and Chk1-mediated S-$G_2$ cell cycle arrest. Moreover, ATR-mediated p53 signaling decreases glycolysis and increases glutaminolysis. Under these conditions, wherein cell cycle progression is blocked and OXPHOS is augmented, there is a substantial increase in IFN-γ secretion. Right: In response to high-dose resveratrol, TCR-mediated mTOR and Sirt1 signaling pathways are markedly attenuated, leading to p27-mediated $G_1$ cell cycle arrest.

of DNA breaks with associated senescence (*57*, *76*, *77*), have been reported (*120*). Here, we found that low-dose resveratrol triggered a marked DNA damage response in TCR-stimulated T cells, as shown by the presence of γH2AX in 20 to 50% of cells. Furthermore, DNA damage, or more precisely the response to genotoxic stress, was linked to the activation state of the T cell. Low-dose resveratrol was associated with H2AX phosphorylation in TCR-stimulated cells, whereas high-dose resveratrol resulted in H2AX phosphorylation in T cells exposed to the homeostatic cytokine IL-7.

The ATR pathway is activated under conditions of single-stranded DNA breaks or instability of replication forks (*85*). We find that low-dose resveratrol activated the ATR pathway within 24 hours of the treatment of stimulated CD4$^+$ T cells, well before S-phase entry. Under these conditions, ATR rapidly phosphorylated histone H2AX and Mcm2 at Ser$^{108}$, with the latter potentially stabilizing prereplication complexes in response to DNA damage (*121*). In addition, at later time points, we found that resveratrol stimulated the ATR-mediated phosphorylation of Chk1 and Wee1, blocking Cdc25-mediated Cdk1 activation and mitotic entry (Fig. 7B). Although both ATR and ATM phosphorylate Ser$^{15}$ of p53 (*60*), we found no evidence that resveratrol activated an ATM-Chk2-p53-p21 pathway, a pathway that is generally activated in response to double-stranded DNA breaks. Thus, our data suggest that resveratrol triggers a replication stress–like response rather than classical DNA damage. In this state, p53 appears to serve as a node between upstream stress signaling cascades and downstream DNA repair pathways (Fig. 7B) (*122*).

In CD4$^+$ T cells, both low- and high-dose resveratrol induced transcription of the p53 proapoptotic target, *PUMA*. This was the only gene in an 84-gene DNA damage signaling pathway array to exhibit increased expression in response to low-dose resveratrol (fig. S3), suggesting that many of the effects of low-dose resveratrol occur at a posttranscriptional level. However, low-dose resveratrol altered the expression of all p53-directed metabolic gene targets that we assessed. Although other transcription factors, such as c-Myc and HIF-1α, also regulate cell metabolism and are produced in TCR-stimulated human CD4$^+$ T cells, their abundance was not substantially modulated by resveratrol (fig. S5). Thus, we focused on p53, a tumor suppressor whose function has paradoxically been found to protect tumor cells from modest amounts of stress through metabolic reprogramming (*95*, *123*). The p53-mediated decreases in Glut1 and PGM abundance, together with increased TIGAR, attenuate aerobic glycolysis, whereas increased SCO2 and GLS2 abundance drives glutamine-driven OXPHOS (*97*, *101*–*103*, *124*), which was the case that we observed in resveratrol-treated CD4$^+$ T cells. Note that cell cycle arrest and senescence act as signals for a cell to undergo metabolic reprogramming, decreasing glycolysis and increasing TCA cycle usage (*96*, *125*–*127*). Thus, our data suggest that the ATR-mediated cell cycle arrest initiated by low-dose resveratrol in CD4$^+$ T cells was coupled to a

metabolic shift, adjusting the balance between glycolysis and OXPHOS (Fig. 7B).

The bioenergetic profile of resveratrol-treated T cells was altered by this skewing of metabolism away from glycolysis and toward a setting characterized by an increased ASCT2-to-Glut1 ratio, with an augmented glutamine transport, substantially increased mitochondrial ROS production, and increased OXPHOS. How this would affect T cell effector function is unclear because glycolysis can increase and decrease the potential of T cells to secrete effector cytokines, such as IFN-γ and IL-17 (*128*–*133*). Note that amino acid metabolism is essential for effector T cell differentiation (*100*, *109*, *134*, *135*), and memory cells rely more on OXPHOS than on glycolysis (*38*, *130*). In both naïve and memory $CD4^+$ T cells, low-dose resveratrol markedly augmented the amount of IFN-γ secreted, but this increase was even higher for naïve cells than for memory cells (means of 10- and 2-fold, respectively). Furthermore, in both cell types, resveratrol substantially increased the number of cells that produced both IL-2 and IFN-γ. Thus, our data suggest that resveratrol is an agent that, by altering the metabolic fitness of T lymphocytes, enhances their cytokine effector potential.

Adjusting the balance between glycolysis and OXPHOS can also have substantial effects in other cell types. Decreasing OXPHOS in mice expressing a mutant p53 markedly attenuates tumorigenesis (*136*). Thus, generating a context that is the converse of that shaped by resveratrol, that is, inhibiting a p53-mediated shift to mitochondrial metabolism, may be beneficial for individuals with an increased risk of developing cancers, such as Li-Fraumeni syndrome patients with germline mutations in the *TP53* gene. The potential use of resveratrol as a therapy for the treatment of neurological, cardiovascular, hepatic, and metabolic pathologies therefore necessitates a critical evaluation of its effect on T lymphocytes in vivo, especially in an autoimmune setting. The data shown here reveal a complex network of resveratrol-stimulated changes in cell cycle progression and metabolism, altering the potential of T lymphocytes to respond to foreign antigens.

## MATERIALS AND METHODS

### T cell isolation and culture

$CD4^+$ T cells were isolated from adult peripheral blood, obtained from healthy donors after informed consent. Cells were purified using negative-selection Rosette tetramers (STEMCELL Technologies), and the purity of the cell population was monitored on a FACSCanto II (BD Biosciences). Purities were always greater than 94%. Naïve and memory $CD4^+$ T cells were sorted on a FACSAria after staining with anti-CD4, anti-CD45RA, anti-CD45RO, CD62L, CD127, and CD25 antibodies (fig. S4A). Lymphocytes ($1 \times 10^6$ per well in a 24-well plate) were cultured in RPMI 1640 + GlutaMAX (Gibco, Life Technologies) supplemented with 10% fetal calf serum (FCS) and 2% penicillin/streptomycin (Gibco, Life Technologies). For TCR stimulation, 24-well plates were coated with anti-CD3 (clone OKT3, BioLegend) and anti-CD28 (clone 9.3, provided by C. June) monoclonal antibodies (mAbs) at a concentration of 1 μg/ml, and recombinant IL-2 (rIL-2) (50 U/ml) was added as indicated. T cells were also cultured in the presence of rIL-7 (10 ng/ml). As indicated, resveratrol (20 or 100 μM; Sigma-Aldrich), compound C1 (1 μM; Sigma-Aldrich), VE-821 (1 and 5 μM; Euromedex), aphidicolin (1 μM), and bleomycin (1 μM) were added to T cell cultures 1 hour before TCR stimulation.

### Immunofluorescence

Cells were collected and coated on poly-L-lysine–treated slides. Cells were fixed in a 4% paraformaldehyde (PFA) solution [phosphate-buffered saline (PBS), 4% PFA] at 37°C for 15 min, permeabilized in PBS containing 3% bovine serum albumin (BSA)/0.1% saponin for 10 min, and blocked for nonspecific protein binding with 10% FCS. Staining with primary anti-Sirt1 antibody (Ab) (Santa Cruz Biotechnology) and a secondary Alexa Fluor 488–coupled anti-rabbit immunoglobulin G (Invitrogen) was performed in PBS containing 3% BSA for 1 hour at room temperature. Nuclei were then labeled by DAPI staining for 10 min at room temperature.

### Flow cytometric analyses

To detect cell surface markers, cells were incubated with the appropriate fluorochrome-conjugated mAbs, and expression was monitored in comparison with isotype controls. Antibodies against CD4, CD25, CD69, and CD71 were from Beckman Coulter. Y319-phosphorylated ZAP-70 (BD Biosciences), T202/Y204-phosphorylated ERK1/2 (BD Biosciences), and phosphorylated H2AX (BioLegend) were detected after cell fixation and permeabilization. Surface Glut1 and ASCT2 were detected by binding to their respective retroviral envelope ligands fused to enhanced green fluorescent protein or recombinant rabbit fragment crystallizable (rFc) (Metafora Biosystems), as previously described (*72*, *137*–*139*). The presence of mitochondrial superoxide was assessed by staining with MitoSOX Red indicator (1 μM; Invitrogen). Proliferation was monitored as a function of carboxyfluorescein diacetate succinimidyl ester (Invitrogen) or violet proliferation dye (Invitrogen) dilution. Before staining for intracellular IFN-γ and IL-2 (BD Biosciences), cells were activated with phorbol 12-myristate 13-acetate (100 ng/ml; Sigma-Aldrich) and ionomycin (1 μg/ml; Sigma-Aldrich) in the presence of brefeldin A (10 μg/ml; Sigma-Aldrich) for 3.5 to 4 hours at 37°C. Cell cycle analysis was performed by simultaneous staining for DNA and RNA using 7-aminoactinomycin D (20 μM; Sigma-Aldrich) and pyronin Y (5 μM; Sigma-Aldrich), respectively. Cells were assessed on a FACSCanto II or BD LSR II Fortessa (BD Biosciences), and data were analyzed using FACSDiva (BD Biosciences) or FlowJo (Tree Star) software.

### Metabolic assays

OCRs were measured on an XF-24 Extracellular Flux Analyzer (Seahorse Bioscience). TCR-stimulated T cells with and without low-dose resveratrol (20 μM) were seeded at a concentration of $1.5 \times 10^6$ cells, whereas nonstimulated and high-dose resveratrol-stimulated cells were seeded at a concentration of $2.0 \times 10^6$ cells in XF medium (nonbuffered Dulbecco's modified Eagle's medium containing 2.5 mM glucose, 2 mM L-glutamine, and 1 mM sodium pyruvate). Oxygen consumption was monitored under basal conditions and in response to oligomycin (1 μM), carbonyl cyanide *p*-trifluoromethoxyphenylhydrazone (1.5 μM), rotenone (100 nM), and antimycin A (1 μM; Sigma-Aldrich). The basal respiration rate was calculated as the difference between basal OCR and the OCR after inhibition of mitochondrial complexes 1 and 3 with rotenone and antimycin A, respectively. ATP and L-lactate were measured according to the standard procedures of the ATPlite kit (PerkinElmer) and L-lactate kit (Eton Bioscience), respectively. Extracellular pH was measured immediately after harvesting of medium using a standard pH meter.

### Glucose and glutamine uptake assays

Cells ($2 \times 10^6$) were starved by incubation at 37°C in serum and glucose- or glutamine-free RPMI 1640 for 30 min. Radiolabeled 2-deoxy-D-[1-$^3$H] glucose or glutamine-L-[3,4-$^3$H(N)] (PerkinElmer) was added to a final concentration of 0.1 mM (2 μCi/ml). Cells were incubated for 10 min at room temperature, washed in cold serum/glucose/glutamine-free RPMI 1640, and solubilized in 500 μl of 0.1% SDS. Radioactivity was measured by liquid scintillation.

### Total protein extraction and analyses

Cells were lysed in lysis buffer containing 20 mM Hepes (pH 7.6), 100 mM KCl, 0.1 mM EDTA, 1 mM NaF, 1 mM sodium orthovanadate, 1% Triton X-100, 0.5% NP-40, 0.15 mM spermine, 0.5 mM spermidine, 1 mM dithiothreitol, and a protease inhibitor cocktail. After a 30-min incubation on ice, extracts were centrifuged, and supernatants were harvested. Extracts (20 μg) were resolved on SDS–polyacrylamide gel electrophoresis gels (8.5 to 12%) and transferred electrophoretically onto polyvinylidene difluoride (PVDF) membranes. PVDF membranes were incubated with the indicated antibodies (table S1) for 1 hour at room temperature or overnight at 4°C and with horseradish peroxidase–conjugated anti-goat, anti-rabbit, or anti-mouse secondary Abs, and immunoreactive proteins were visualized using enhanced chemiluminescence (ECL, Amersham) according to the manufacturer's instructions. Proteins were quantified with ImageJ software and normalized to amido black–stained proteins (loading controls) or tubulin as indicated.

### Gene expression analysis by PCR array

Total RNA was isolated with the RNeasy Mini Kit (Qiagen) and was reverse-transcribed with QuantiTect Reverse Transcription Kit (Qiagen). SYBR Green–based (SYBR Green I Master, Roche) real-time quantitative PCR (qPCR) for *TIGAR*, *PGM*, *GLS2*, SCO2, *HIF1A*, and *RNA18S* was performed with the LightCycler 480 Real-Time PCR System (Roche), and all primers are shown in table S2. To determine relative expression, samples for each experimental condition were run in duplicate and were normalized to 18S. Primer sequences used for amplification were designed with Primer3 and NetPrimer (PREMIER Biosoft) software packages. The expression of 84 genes involved in DNA damage signaling pathways was analyzed with the RT$^2$ Profiler PCR Array (SABiosciences, Qiagen) according to the manufacturer's instructions. Briefly, RNA was prepared from 5 million cells after 24 hours in culture under the indicated conditions using the Qiagen RNeasy kit. First-strand complementary DNA was then prepared and used in the PCR array in combination with SYBR Green qPCR master mixes on a Roche Light Cycler 480. Data were normalized to *ACTB* (actin beta), *B2M* ($\beta_2$-microglobulin), and *RPLP0* using the SABiosciences DNA template analysis software.

### Statistical analyses

Data were analyzed with GraphPad Software (GraphPad Prism), and *P* values were calculated by one-way ANOVA (Tukey's post hoc test), two-way ANOVA (with Tukey's post hoc or Bonferroni's tests), or paired *t* tests, as indicated.

## SUPPLEMENTARY MATERIALS

www.sciencesignaling.org/cgi/content/full/10/501/eaal3024/DC1

Fig. S1. Quantification and statistical analyses of main data panels.

Fig. S2. Effects of resveratrol on the formation of CD4$^+$ T cell blasts and cell counts in response to TCR engagement.

Fig. S3. Effect of resveratrol treatment on the expression of DNA damage signaling pathway genes.

Fig. S4. Sorting of naïve and memory CD4$^+$ T cells for the assessment of phenotype and cytokine secretion profiles.

Fig. S5. TCR-mediated induction of *HIF1A* and c-Myc in human CD4$^+$ cells is not altered by low-dose resveratrol.

Table S1. Antibody list.

Table S2. Primer sequences.

## REFERENCES AND NOTES


1. B. B. Aggarwal, A. Bhardwaj, R. S. Aggarwal, N. P. Seeram, S. Shishodia, Y. Takada, Role of resveratrol in prevention and therapy of cancer: Preclinical and clinical studies. *Anticancer Res.* **24**, 2783–2840 (2004).
2. B. P. Hubbard, D. A. Sinclair, Small molecule SIRT1 activators for the treatment of aging and age-related diseases. *Trends Pharmacol. Sci.* **35**, 146–154 (2014).
3. K. S. Bhullar, B. P. Hubbard, Lifespan and healthspan extension by resveratrol. *Biochim. Biophys. Acta* **1852**, 1209–1218 (2015).
4. A. Chalkiadaki, L. Guarente, Sirtuins mediate mammalian metabolic responses to nutrient availability. *Nat. Rev. Endocrinol.* **8**, 287–296 (2012).
5. B. Agarwal, J. A. Baur, Resveratrol and life extension. *Ann. N. Y. Acad. Sci.* **1215**, 138–143 (2011).
6. B. Poussier, A. C. Cordova, J.-P. Becquemin, B. E. Sumpio, Resveratrol inhibits vascular smooth muscle cell proliferation and induces apoptosis. *J. Vasc. Surg.* **42**, 1190–1197 (2005).
7. Z. Estrov, S. Shishodia, S. Faderl, D. Harris, Q. Van, H. M. Kantarjian, M. Talpaz, B. B. Aggarwal, Resveratrol blocks interleukin-1β-induced activation of the nuclear transcription factor NF-κB, inhibits proliferation, causes S-phase arrest, and induces apoptosis of acute myeloid leukemia cells. *Blood* **102**, 987–995 (2003).
8. P. Signorelli, R. Ghidoni, Resveratrol as an anticancer nutrient: Molecular basis, open questions and promises. *J. Nutr. Biochem.* **16**, 449–466 (2005).
9. S. Das, D. K. Das, Resveratrol: A therapeutic promise for cardiovascular diseases. *Recent Pat. Cardiovasc. Drug Discov.* **2**, 133–138 (2007).
10. S. Das, D. K. Das, Anti-inflammatory responses of resveratrol. *Inflamm. Allergy Drug Targets* **6**, 168–173 (2007).
11. O. Vang, What is new for resveratrol? Is a new set of recommendations necessary? *Ann. N. Y. Acad. Sci.* **1290**, 1–11 (2013).
12. J. Tomé-Carneiro, M. Larrosa, A. González-Sarrías, F. A. Tomás-Barberán, M. T. García-Conesa, J. C. Espín, Resveratrol and clinical trials: The crossroad from in vitro studies to human evidence. *Curr. Pharm. Des.* **19**, 6064–6093 (2013).
13. J. M. Smoliga, E. S. Colombo, M. J. Campen, A healthier approach to clinical trials evaluating resveratrol for primary prevention of age-related diseases in healthy populations. *Aging* **5**, 495–506 (2013).
14. R. S. Turner, R. G. Thomas, S. Craft, C. H. van Dyck, J. Mintzer, B. A. Reynolds, J. B. Brewer, R. A. Rissman, R. Raman, P. S. Aisen; Alzheimer's Disease Cooperative Study, A randomized, double-blind, placebo-controlled trial of resveratrol for Alzheimer disease. *Neurology* **85**, 1383–1391 (2015).
15. O. Vang, Resveratrol: Challenges in analyzing its biological effects. *Ann. N. Y. Acad. Sci.* **1348**, 161–170 (2015).
16. R. H. X. Wong, R. S. Nealon, A. Scholey, P. R. C. Howe, Low dose resveratrol improves cerebrovascular function in type 2 diabetes mellitus. *Nutr. Metab. Cardiovasc. Dis.* **26**, 393–399 (2016).
17. S.-J. Lin, P.-A. Defossez, L. Guarente, Requirement of NAD and *SIR2* for life-span extension by calorie restriction in *Saccharomyces cerevisiae*. *Science* **289**, 2126–2128 (2000).
18. K. T. Howitz, K. J. Bitterman, H. Y. Cohen, D. W. Lamming, S. Lavu, J. G. Wood, R. E. Zipkin, P. Chung, A. Kisielewski, L.-L. Zhang, B. Scherer, D. A. Sinclair, Small molecule activators of sirtuins extend *Saccharomyces cerevisiae* lifespan. *Nature* **425**, 191–196 (2003).
19. M. Gertz, G. T. Nguyen, F. Fischer, B. Suenkel, C. Schlicker, B. Fränzel, J. Tomaschewski, F. Aladini, C. Becker, D. Wolters, C. Steegborn, A molecular mechanism for direct sirtuin activation by resveratrol. *PLOS ONE* **7**, e49761 (2012).
20. J. A. Baur, K. J. Pearson, N. L. Price, H. A. Jamieson, C. Lerin, A. Kalra, V. V. Prabhu, J. S. Allard, G. Lopez-Lluch, K. Lewis, P. J. Pistell, S. Poosala, K. G. Becker, O. Boss, D. Gwinn, M. Wang, S. Ramaswamy, K. W. Fishbein, R. G. Spencer, E. G. Lakatta, D. Le Couteur, R. J. Shaw, P. Navas, P. Puigserver, D. K. Ingram, R. de Cabo, D. A. Sinclair, Resveratrol improves health and survival of mice on a high-calorie diet. *Nature* **444**, 337–342 (2006).
21. A. Satoh, C. S. Brace, N. Rensing, P. Cliften, D. F. Wozniak, E. D. Herzog, K. A. Yamada, S.-i. Imai, Sirt1 extends life span and delays aging in mice through the regulation of Nk2 homeobox 1 in the DMH and LH. *Cell Metab.* **18**, 416–430 (2013).
22. Y. Kanfi, S. Naiman, G. Amir, V. Peshti, G. Zinman, L. Nahum, Z. Bar-Joseph, H. Y. Cohen, The sirtuin SIRT6 regulates lifespan in male mice. *Nature* **483**, 218–221 (2012).
23. A. S. Banks, N. Kon, C. Knight, M. Matsumoto, R. Gutiérrez-Juárez, L. Rossetti, W. Gu, D. Accili, SirT1 gain of function increases energy efficiency and prevents diabetes in mice. *Cell Metab.* **8**, 333–341 (2008).
24. D. Herranz, M. Serrano, SIRT1: Recent lessons from mouse models. *Nat. Rev. Cancer* **10**, 819–823 (2010).
25. D. Herranz, M. Muñoz-Martin, M. Cañamero, F. Mulero, B. Martinez-Pastor, O. Fernandez-Capetillo, M. Serrano, Sirt1 improves healthy ageing and protects from metabolic syndrome-associated cancer. *Nat. Commun.* **1**, 3 (2010).
26. G. Donmez, L. Guarente, Aging and disease: Connections to sirtuins. *Aging Cell* **9**, 285–290 (2010).
27. G. Donmez, D. Wang, D. E. Cohen, L. Guarente, SIRT1 suppresses β-amyloid production by activating the α-secretase gene ADAM10. *Cell* **142**, 320–332 (2010).

28. P. T. Pfluger, D. Herranz, S. Velasco-Miguel, M. Serrano, M. H. Tschöp, Sirt1 protects against high-fat diet-induced metabolic damage. *Proc. Natl. Acad. Sci. U.S.A.* **105**, 9793–9798 (2008).
29. J. Sequeira, G. Boily, S. Bazinet, S. Saliba, X. He, K. Jardine, C. Kennedy, W. Staines, C. Rousseaux, R. Mueller, M. W. McBurney, *sirt1*-null mice develop an autoimmune-like condition. *Exp. Cell Res.* **314**, 3069–3074 (2008).
30. J. Zhang, S.-M. Lee, S. Shannon, B. Gao, W. Chen, A. Chen, R. Divekar, M. W. McBurney, H. Braley-Mullen, H. Zaghouani, D. Fang, The type III histone deacetylase Sirt1 is essential for maintenance of T cell tolerance in mice. *J. Clin. Invest.* **119**, 3048–3058 (2009).
31. A. Purushotham, T. T. Schug, Q. Xu, S. Surapureddi, X. Guo, X. Li, Hepatocyte-specific deletion of SIRT1 alters fatty acid metabolism and results in hepatic steatosis and inflammation. *Cell Metab.* **9**, 327–338 (2009).
32. H.-L. Cheng, R. Mostoslavsky, S. Saito, J. P. Manis, Y. Gu, P. Patel, R. Bronson, E. Appella, F. W. Alt, K. F. Chua, Developmental defects and p53 hyperacetylation in Sir2 homolog (SIRT1)-deficient mice. *Proc. Natl. Acad. Sci. U.S.A.* **100**, 10794–10799 (2003).
33. S. Kong, S.-J. Kim, B. Sandal, S.-M. Lee, B. Gao, D. D. Zhang, D. Fang, The type III histone deacetylase Sirt1 protein suppresses p300-mediated histone H3 lysine 56 acetylation at Bclaf1 promoter to inhibit T cell activation. *J. Biol. Chem.* **286**, 16967–16975 (2011).
34. V. K. Nimmagadda, C. T. Bever, N. R. Vattikunta, S. Talat, V. Ahmad, N. K. Nagalla, D. Trisler, S. I. V. Judge, W. Royal III, K. Chandrasekaran, J. W. Russell, T. K. Makar, Overexpression of SIRT1 protein in neurons protects against experimental autoimmune encephalomyelitis through activation of multiple SIRT1 targets. *J. Immunol.* **190**, 4595–4607 (2013).
35. Y. Wang, Y. Bi, C. Li, Y. Li, Z. Zhang, J. Wang, Y. Lu, Q. Yu, H. Su, H. Yang, G. Liu, Histone deacetylase SIRT1 negatively regulates the differentiation of interleukin-9-producing $CD4^+$ T Cells. *Immunity* **44**, 11337–11349 (2016).
36. H. W. Lim, S. G. Kang, J. K. Ryu, B. Schilling, M. Fei, I. S. Lee, A. Kehasse, K. Shirakawa, M. Yokoyama, M. Schnölzer, H. G. Kasler, H.-S. Kwon, B. W. Gibson, H. Sato, K. Akassoglou, C. Xiao, D. R. Littman, M. Ott, E. Verdin, SIRT1 deacetylates RORγt and enhances Th17 cell generation. *J. Exp. Med.* **212**, 607–617 (2015).
37. N. J. Maciver, R. D. Michalek, J. C. Rathmell, Metabolic regulation of T lymphocytes. *Annu. Rev. Immunol.* **31**, 259–283 (2013).
38. G. J. W. van der Windt, E. L. Pearce, Metabolic switching and fuel choice during T-cell differentiation and memory development. *Immunol. Rev.* **249**, 27–42 (2012).
39. E. L. Pearce, E. J. Pearce, Metabolic pathways in immune cell activation and quiescence. *Immunity* **38**, 633–643 (2013).
40. R. H. Houtkooper, E. Pirinen, J. Auwerx, Sirtuins as regulators of metabolism and healthspan. *Nat. Rev. Mol. Cell Biol.* **13**, 225–238 (2012).
41. C. Cantó, R. H. Houtkooper, E. Pirinen, D. Y. Youn, M. H. Oosterveer, Y. Cen, P. J. Fernandez-Marcos, H. Yamamoto, P. A. Andreux, P. Cettour-Rose, K. Gademann, C. Rinsch, K. Schoonjans, A. A. Sauve, J. Auwerx, The $NAD^+$ precursor nicotinamide riboside enhances oxidative metabolism and protects against high-fat diet-induced obesity. *Cell Metab.* **15**, 838–847 (2012).
42. R. Cerutti, E. Pirinen, C. Lamperti, S. Marchet, A. A. Sauve, W. Li, V. Leoni, E. A. Schon, F. Dantzer, J. Auwerx, C. Viscomi, M. Zeviani, $NAD^+$-dependent activation of Sirt1 corrects the phenotype in a mouse model of mitochondrial disease. *Cell Metab.* **19**, 1042–1049 (2014).
43. G. Xuzhu, M. Komai-Koma, B. P. Leung, H. S. Howe, C. McSharry, I. B. McInnes, D. Xu, Resveratrol modulates murine collagen-induced arthritis by inhibiting Th17 and B-cell function. *Ann. Rheum. Dis.* **71**, 129–135 (2012).
44. R. Falchetti, M. P. Fuggetta, G. Lanzilli, M. Tricarico, G. Ravagnan, Effects of resveratrol on human immune cell function. *Life Sci.* **70**, 81–96 (2001).
45. Y. Yang, J. H. Paik, D. Cho, J.-A. Cho, C.-W. Kim, Resveratrol induces the suppression of tumor-derived $CD4^+CD25^+$ regulatory T cells. *Int. Immunopharmacol.* **8**, 542–547 (2008).
46. S.-L. Wu, L. Yu, X.-Y. Jiao, K.-W. Meng, C.-E. Pan, The suppressive effect of resveratrol on protein kinase Cθ in peripheral blood T lymphocytes in a rat liver transplantation model. *Transplant. Proc.* **38**, 3052–3054 (2006).
47. S. A. Gatz, L. Wiesmüller, Take a break—Resveratrol in action on DNA. *Carcinogenesis* **29**, 321–332 (2008).
48. N. G. Denissova, C. M. Nasello, P. L. Yeung, J. A. Tischfield, M. A. Brenneman, Resveratrol protects mouse embryonic stem cells from ionizing radiation by accelerating recovery from DNA strand breakage. *Carcinogenesis* **33**, 149–155 (2012).
49. M. J. Burkitt, J. Duncan, Effects of *trans*-resveratrol on copper-dependent hydroxyl-radical formation and DNA damage: Evidence for hydroxyl-radical scavenging and a novel, glutathione-sparing mechanism of action. *Arch. Biochem. Biophys.* **381**, 253–263 (2000).
50. R.-H. Wang, K. Sengupta, C. Li, H.-S. Kim, L. Cao, C. Xiao, S. Kim, X. Xu, Y. Zheng, B. Chilton, R. Jia, Z.-M. Zheng, E. Appella, X. W. Wang, T. Ried, C.-X. Deng, Impaired DNA damage response, genome instability, and tumorigenesis in SIRT1 mutant mice. *Cancer Cell* **14**, 312–323 (2008).
51. H. D. Halicka, H. Zhao, J. Li, Y. S. Lee, T. C. Hsieh, J. M. Wu, Z. Darzynkiewicz, Potential anti-aging agents suppress the level of constitutive mTOR- and DNA damage- signaling. *Aging* **4**, 952–965 (2012).
52. A. Tyagi, R. P. Singh, C. Agarwal, S. Siriwardana, R. A. Sclafani, R. Agarwal, Resveratrol causes Cdc2-tyr15 phosphorylation via ATM/ATR-Chk1/2-Cdc25C pathway as a central mechanism for S phase arrest in human ovarian carcinoma Ovcar-3 cells. *Carcinogenesis* **26**, 1978–1987 (2005).
53. D. J. Colin, E. Limagne, K. Ragot, G. Lizard, F. Ghiringhelli, É. Solary, B. Chauffert, N. Latruffe, D. Delmas, The role of reactive oxygen species and subsequent DNA-damage response in the emergence of resistance towards resveratrol in colon cancer models. *Cell Death Dis.* **5**, e1533 (2014).
54. A. Rashid, C. Liu, T. Sanli, E. Tsiani, G. Singh, R. G. Bristow, I. Dayes, H. Lukka, J. Wright, T. Tsakiridis, Resveratrol enhances prostate cancer cell response to ionizing radiation. Modulation of the AMPK, Akt and mTOR pathways. *Radiat. Oncol.* 6, 144 (2011).
55. E. H. Heiss, Y. D. C. Schilder, V. M. Dirsch, Chronic treatment with resveratrol induces redox stress- and ataxia telangiectasia-mutated (ATM)-dependent senescence in p53-positive cancer cells. *J. Biol. Chem.* **282**, 26759–26766 (2007).
56. A. R. Hussain, S. Uddin, R. Bu, O. S. Khan, S. O. Ahmed, M. Ahmed, K. S. Al-Kuraya, Resveratrol suppresses constitutive activation of AKT via generation of ROS and induces apoptosis in diffuse large B cell lymphoma cell lines. *PLOS ONE* **6**, e24703 (2011).
57. H. Luo, A. Yang, B. A. Schulte, M. J. Wargovich, G. Y. Wang, Resveratrol induces premature senescence in lung cancer cells via ROS-mediated DNA damage. *PLOS ONE* **8**, e60065 (2013).
58. K. Fukuhara, M. Nagakawa, I. Nakanishi, K. Ohkubo, K. Imai, S. Urano, S. Fukuzumi, T. Ozawa, N. Ikota, M. Mochizuki, N. Miyata, H. Okuda, Structural basis for DNA-cleaving activity of resveratrol in the presence of Cu(II). *Bioorg. Med. Chem.* **14**, 1437–1443 (2006).
59. N. Ahmad, V. M. Adhami, F. Afaq, D. K. Feyes, H. Mukhtar, Resveratrol causes WAF-1/p21-mediated $G_1$-phase arrest of cell cycle and induction of apoptosis in human epidermoid carcinoma A431 cells. *Clin. Cancer Res.* **7**, 1466–1473 (2001).
60. T. Sperka, J. Wang, K. L. Rudolph, DNA damage checkpoints in stem cells, ageing and cancer. *Nat. Rev. Mol. Cell Biol.* **13**, 579–590 (2012).
61. M. K. Zeman, K. A. Cimprich, Causes and consequences of replication stress. *Nat. Cell Biol.* **16**, 2–9 (2014).
62. A. C. Carrano, E. Eytan, A. Hershko, M. Pagano, SKP2 is required for ubiquitin-mediated degradation of the CDK inhibitor p27. *Nat. Cell Biol.* **1**, 193–199 (1999).
63. H. Sutterlüty, E. Chatelain, A. Marti, C. Wirbelauer, M. Senften, U. Muller, W. Krek, $p45^{SKP2}$ promotes $p27^{Kip1}$ degradation and induces S phase in quiescent cells. *Nat. Cell Biol.* **1**, 207–214 (1999).
64. S. Colombetti, V. Basso, D. L. Mueller, A. Mondino, Prolonged TCR/CD28 engagement drives IL-2-independent T cell clonal expansion through signaling mediated by the mammalian target of rapamycin. *J. Immunol.* **176**, 2730–2738 (2006).
65. S. Sauer, L. Bruno, A. Hertweck, D. Finlay, M. Leleu, M. Spivakov, Z. A. Knight, B. S. Cobb, D. Cantrell, E. O'Connor, K. M. Shokat, A. G. Fisher, M. Merkenschlager, T cell receptor signaling controls Foxp3 expression via PI3K, Akt, and mTOR. *Proc. Natl. Acad. Sci. U.S.A.* **105**, 7797–7802 (2008).
66. G. M. Delgoffe, T. P. Kole, Y. Zheng, P. E. Zarek, K. L. Matthews, B. Xiao, P. F. Worley, S. C. Kozma, J. D. Powell, The mTOR kinase differentially regulates effector and regulatory T cell lineage commitment. *Immunity* **30**, 832–844 (2009).
67. M. Laplante, D. M. Sabatini, mTOR signaling at a glance. *J. Cell Sci.* **122**, 3589–3594 (2009).
68. S. Sengupta, T. R. Peterson, D. M. Sabatini, Regulation of the mTOR complex 1 pathway by nutrients, growth factors, and stress. *Mol. Cell* **40**, 310–322 (2010).
69. H. S. Ghosh, M. McBurney, P. D. Robbins, SIRT1 negatively regulates the mammalian target of rapamycin. *PLOS ONE* **5**, e9199 (2010).
70. S. Hong, B. Zhao, D. B. Lombard, D. C. Fingar, K. Inoki, Cross-talk between sirtuin and mammalian target of rapamycin complex 1 (mTORC1) signaling in the regulation of S6 kinase 1 (S6K1) phosphorylation. *J. Biol. Chem.* **289**, 13132–13141 (2014).
71. Y. Wang, Y. Bi, X. Chen, C. Li, Y. Li, Z. Zhang, J. Wang, Y. Lu, Q. Yu, H. Su, H. Yang, G. Liu, Histone deacetylase SIRT1 negatively regulates the differentiation of interleukin-9-producing $CD4^+$ T cells. *Immunity* **44**, 1337–1349 (2016).
72. N. Manel, S. Kinet, J.-L. Battini, F. J. Kim, N. Taylor, M. Sitbon, The HTLV receptor is an early T-cell activation marker whose expression requires de novo protein synthesis. *Blood* **101**, 1913–1918 (2003).
73. M. Lavanya, S. Kinet, A. Montel-Hagen, C. Mongellaz, J.-L. Battini, M. Sitbon, N. Taylor, Cell surface expression of the bovine leukemia virus-binding receptor on B and T lymphocytes is induced by receptor engagement. *J. Immunol.* **181**, 891–898 (2008).
74. Y. Tang, J. Xu, W. Qu, X. Peng, P. Xin, X. Yang, C. Ying, X. Sun, L. Hao, Resveratrol reduces vascular cell senescence through attenuation of oxidative stress by SIRT1/NADPH oxidase-dependent mechanisms. *J. Nutr. Biochem.* **23**, 1410–1416 (2012).
75. X. B. Wang, L. Zhu, J. Huang, Y. G. Yin, X. Q. Kong, Q. F. Rong, A. W. Shi, K. J. Cao, Resveratrol-induced augmentation of telomerase activity delays senescence of endothelial progenitor cells. *Chin Med J (Engl)* **124**, 4310–4315 (2011).

76. Z. Gao, M. S. Xu, T. L. Barnett, C. W. Xu, Resveratrol induces cellular senescence with attenuated mono-ubiquitination of histone H2B in glioma cells. *Biochem. Biophys. Res. Commun.* **407**, 271–276 (2011).
77. L. Peltz, J. Gomez, M. Marquez, F. Alencastro, N. Atashpanjeh, T. Quang, T. Bach, Y. Zhao, Resveratrol exerts dosage and duration dependent effect on human mesenchymal stem cell development. *PLOS ONE* **7**, e37162 (2012).
78. S. Yamashita, K. Ogawa, T. Ikei, M. Udono, T. Fujiki, Y. Katakura, SIRT1 prevents replicative senescence of normal human umbilical cord fibroblast through potentiating the transcription of human telomerase reverse transcriptase gene. *Biochem. Biophys. Res. Commun.* **417**, 630–634 (2012).
79. O. Fernandez-Capetillo, A. Celeste, A. Nussenzweig, Focusing on foci: H2AX and the recruitment of DNA-damage response factors. *Cell Cycle* **2**, 426–427 (2003).
80. M. Fragkos, J. Jurvansuu, P. Beard, H2AX is required for cell cycle arrest via the p53/p21 pathway. *Mol. Cell. Biol.* **29**, 2828–2840 (2009).
81. I. M. Ward, J. Chen, Histone H2AX is phosphorylated in an ATR-dependent manner in response to replicational stress. *J. Biol. Chem.* **276**, 47759–47762 (2001).
82. Z. Feng, H. Zhang, A. J. Levine, S. Jin, The coordinate regulation of the p53 and mTOR pathways in cells. *Proc. Natl. Acad. Sci. U.S.A.* **102**, 8204–8209 (2005).
83. R. G. Jones, D. R. Plas, S. Kubek, M. Buzzai, J. Mu, Y. Xu, M. J. Birnbaum, C. B. Thompson, AMP-activated protein kinase induces a p53-dependent metabolic checkpoint. *Mol. Cell* **18**, 283–293 (2005).
84. K. H. Vousden, K. M. Ryan, p53 and metabolism. *Nat. Rev. Cancer* **9**, 691–700 (2009).
85. J. Smith, L. M. Tho, N. Xu, D. A. Gillespie, The ATM–Chk2 and ATR–Chk1 pathways in DNA damage signaling and cancer. *Adv. Cancer Res.* **108**, 73–112 (2010).
86. L. I. Toledo, M. Murga, P. Gutierrez-Martinez, R. Soria, O. Fernandez-Capetillo, ATR signaling can drive cells into senescence in the absence of DNA breaks. *Genes Dev.* **22**, 297–302 (2008).
87. G. Lossaint, E. Besnard, D. Fisher, J. Piette, V. Dulic, Chk1 is dispensable for G2 arrest in response to sustained DNA damage when the ATM/p53/p21 pathway is functional. *Oncogene* **30**, 4261–4274 (2011).
88. C. Evrin, P. Clarke, J. Zech, R. Lurz, J. Sun, S. Uhle, H. Li, B. Stillman, C. Speck, A double-hexameric MCM2-7 complex is loaded onto origin DNA during licensing of eukaryotic DNA replication. *Proc. Natl. Acad. Sci. U.S.A.* **106**, 20240–20245 (2009).
89. D. Cortez, G. Glick, S. J. Elledge, Minichromosome maintenance proteins are direct targets of the ATM and ATR checkpoint kinases. *Proc. Natl. Acad. Sci. U.S.A.* **101**, 10078–10083 (2004).
90. K. A. Cimprich, D. Cortez, ATR: An essential regulator of genome integrity. *Nat. Rev. Mol. Cell Biol.* **9**, 616–627 (2008).
91. R. Prevo, E. Fokas, P. M. Reaper, P. A. Charlton, J. R. Pollard, W. G. McKenna, R. J. Muschel, T. B. Brunner, The novel ATR inhibitor VE-821 increases sensitivity of pancreatic cancer cells to radiation and chemotherapy. *Cancer Biol. Ther.* **13**, 1072–1081 (2012).
92. J. Vávrová, L. Zárybnická, E. Lukášová, M. Řezáčová, E. Novotná, Z. Šinkorová, A. Tichý, J. Pejchal, K. Ďurišová, Inhibition of ATR kinase with the selective inhibitor VE-821 results in radiosensitization of cells of promyelocytic leukaemia (HL-60). *Radiat. Environ. Biophys.* **52**, 471–479 (2013).
93. K. Nakano, K. H. Vousden, *PUMA*, a novel proapoptotic gene, is induced by p53. *Mol. Cell* **7**, 683–694 (2001).
94. C. R. B. Berkers, O. D. K. Maddocks, E. C. Cheung, I. Mor, K. H. Vousden, Metabolic regulation by p53 family members. *Cell Metab.* **18**, 617–633 (2013).
95. E. Gottlieb, K. H. Vousden, p53 regulation of metabolic pathways. *Cold Spring Harb. Perspect. Biol.* **2**, a001040 (2010).
96. K. M. Aird, R. Zhang, Nucleotide metabolism, oncogene-induced senescence and cancer. *Cancer Lett.* **356**, 204–210 (2015).
97. K. Bensaad, A. Tsuruta, M. A. Selak, M. N. C. Vidal, K. Nakano, R. Bartrons, E. Gottlieb, K. H. Vousden, TIGAR, a p53-inducible regulator of glycolysis and apoptosis. *Cell* **126**, 107–120 (2006).
98. H. Kondoh, M. E. Lleonart, J. Gil, J. Wang, P. Degan, G. Peters, D. Martinez, A. Carnero, D. Beach, Glycolytic enzymes can modulate cellular life span. *Cancer Res.* **65**, 177–185 (2005).
99. A. M. Puzio-Kuter, The role of p53 in metabolic regulation. *Genes Cancer* **2**, 385–391 (2011).
100. M. Nakaya, Y. Xiao, X. Zhou, J.-H. Chang, M. Chang, X. Cheng, M. Blonska, X. Lin, S.-C. Sun, Inflammatory T cell responses rely on amino acid transporter ASCT2 facilitation of glutamine uptake and mTORC1 kinase activation. *Immunity* **40**, 692–705 (2014).
101. W. Hu, C. Zhang, R. Wu, Y. Sun, A. Levine, Z. Feng, Glutaminase 2, a novel p53 target gene regulating energy metabolism and antioxidant function. *Proc. Natl. Acad. Sci. U.S.A.* **107**, 7455–7460 (2010).
102. S. Suzuki, T. Tanaka, M. V. Poyurovsky, H. Nagano, T. Mayama, S. Ohkubo, M. Lokshin, H. Hosokawa, T. Nakayama, Y. Suzuki, S. Sugano, E. Sato, T. Nagao, K. Yokote, I. Tatsuno, C. Prives, Phosphate-activated glutaminase (GLS2), a p53-inducible regulator of glutamine metabolism and reactive oxygen species. *Proc. Natl. Acad. Sci. U.S.A.* **107**, 7461–7466 (2010).
103. S. Matoba, J.-G. Kang, W. D. Patino, A. Wragg, M. Boehm, O. Gavrilova, P. J. Hurley, F. Bunz, P. M. Hwang, p53 regulates mitochondrial respiration. *Science* **312**, 1650–1653 (2006).
104. W. Ma, H. Sung, J. Park, S. Matoba, P. Hwang, A pivotal role for p53: Balancing aerobic respiration and glycolysis. *J. Bioenerg. Biomembr.* **39**, 243–246 (2007).
105. X.-d. Zhang, Z.-h. Qin, J. Wang, The role of p53 in cell metabolism. *Acta Pharmacol. Sin.* **31**, 1208–1212 (2010).
106. E. L. Pearce, M. C. Poffenberger, C.-H. Chang, R. G. Jones, Fueling immunity: Insights into metabolism and lymphocyte function. *Science* **342**, 1242454 (2013).
107. G. M. Delgoffe, K. N. Pollizzi, A. T. Waickman, E. Heikamp, D. J. Meyers, M. R. Horton, B. Xiao, P. F. Worley, J. D. Powell, The kinase mTOR regulates the differentiation of helper T cells through the selective activation of signaling by mTORC1 and mTORC2. *Nat. Immunol.* **12**, 295–303 (2011).
108. M. D. Buck, D. O'Sullivan, E. L. Pearce, T cell metabolism drives immunity. *J. Exp. Med.* **212**, 1345–1360 (2015).
109. D. Klysz, X. Tai, P. A. Robert, M. Craveiro, G. Cretenet, L. Oburoglu, C. Mongellaz, S. Floess, V. Fritz, M. I. Matias, C. Yong, N. Surh, J. C. Marie, J. Huehn, V. Zimmermann, S. Kinet, V. Dardalhon, N. Taylor, Glutamine-dependent α-ketoglutarate production regulates the balance between T helper 1 cell and regulatory T cell generation. *Sci. Signal.* **8**, ra97 (2015).
110. R. J. DeBerardinis, A. Mancuso, E. Daikhin, I. Nissim, M. Yudkoff, S. Wehrli, C. B. Thompson, Beyond aerobic glycolysis: Transformed cells can engage in glutamine metabolism that exceeds the requirement for protein and nucleotide synthesis. *Proc. Natl. Acad. Sci. U.S.A.* **104**, 19345–19350 (2007).
111. C. A. Lyssiotis, J. Son, L. C. Cantley, A. C. Kimmelman, Pancreatic cancers rely on a novel glutamine metabolism pathway to maintain redox balance. *Cell Cycle* **12**, 1987–1988 (2013).
112. J. Son, C. A. Lyssiotis, H. Ying, X. Wang, S. Hua, M. Ligorio, R. M. Perera, C. R. Ferrone, E. Mullarky, N. Shyh-Chang, Y. Kang, J. B. Fleming, N. Bardeesy, J. M. Asara, M. C. Haigis, R. A. DePinho, L. C. Cantley, A. C. Kimmelman, Glutamine supports pancreatic cancer growth through a KRAS-regulated metabolic pathway. *Nature* **496**, 101–105 (2013).
113. E. Lubberts, The IL-23-IL-17 axis in inflammatory arthritis. *Nat. Rev. Rheumatol.* **11**, 415–429 (2015).
114. N. L. Price, A. P. Gomes, A. J. Y. Ling, F. V. Duarte, A. Martin-Montalvo, B. J. North, B. Agarwal, L. Ye, G. Ramadori, J. S. Teodoro, B. P. Hubbard, A. T. Varela, J. G. Davis, B. Varamini, A. Hafner, R. Moaddel, A. P. Rolo, R. Coppari, C. M. Palmeira, R. de Cabo, J. A. Baur, D. A. Sinclair, SIRT1 is required for AMPK activation and the beneficial effects of resveratrol on mitochondrial function. *Cell Metab.* **15**, 675–690 (2012).
115. T. F. Liu, C. E. McCall, Deacetylation by SIRT1 reprograms inflammation and cancer. *Genes Cancer* **4**, 135–147 (2013).
116. M. Jang, L. Cai, G. O. Udeani, K. V. Slowing, C. F. Thomas, C. W. Beecher, H. H. Fong, N. R. Farnsworth, A. D. Kinghorn, R. G. Mehta, R. C. Moon, J. M. Pezzuto, Cancer chemopreventive activity of resveratrol, a natural product derived from grapes. *Science* **275**, 218–220 (1997).
117. K. Fukuhara, N. Miyata, Resveratrol as a new type of DNA-cleaving agent. *Bioorg. Med. Chem. Lett.* **8**, 3187–3192 (1998).
118. M. Subramanian, U. Shadakshari, S. Chattopadhyay, A mechanistic study on the nuclease activities of some hydroxystilbenes. *Bioorg. Med. Chem.* **12**, 1231–1237 (2004).
119. S. A. Gatz, M. Keimling, C. Baumann, T. Dörk, K.-M. Debatin, S. Fulda, L. Wiesmuller, Resveratrol modulates DNA double-strand break repair pathways in an ATM/ATR–p53- and –Nbs1-dependent manner. *Carcinogenesis* **29**, 519–527 (2008).
120. L. Bosch-Presegue, A. Vaquero, The dual role of sirtuins in cancer. *Genes Cancer* **2**, 648–662 (2011).
121. B. E. Stead, C. J. Brandl, M. K. Sandre, M. J. Davey, Mcm2 phosphorylation and the response to replicative stress. *BMC Genet.* **13**, 36 (2012).
122. S. Sengupta, C. C. Harris, p53: Traffic cop at the crossroads of DNA repair and recombination. *Nat. Rev. Mol. Cell Biol.* **6**, 44–55 (2005).
123. E. Kim, A. Giese, W. Deppert, Wild-type p53 in cancer cells: When a guardian turns into a blackguard. *Biochem. Pharmacol.* **77**, 11–20 (2009).
124. O. D. K. Maddocks, K. H. Vousden, Metabolic regulation by p53. *J. Mol. Med.* **89**, 237–245 (2011).
125. S. Mazurek, W. Zwerschke, P. Jansen-Dürr, E. Eigenbrodt, Metabolic cooperation between different oncogenes during cell transformation: Interaction between activated ras and HPV-16 E7. *Oncogene* **20**, 6891–6898 (2001).
126. J. Kaplon, L. Zheng, K. Meissl, B. Chaneton, V. A. Selivanov, G. Mackay, S. H. van der Burg, E. M. E. Verdegaal, M. Cascante, T. Shlomi, E. Gottlieb, D. S. Peeper, A key role for mitochondrial gatekeeper pyruvate dehydrogenase in oncogene-induced senescence. *Nature* **498**, 109–112 (2013).
127. M. Li, K. R. Durbin, S. M. Sweet, J. D. Tipton, Y. Zheng, N. L. Kelleher, Oncogene-induced cellular senescence elicits an anti-Warburg effect. *Proteomics* **13**, 2585–2596 (2013).
128. R. D. Michalek, V. A. Gerriets, S. R. Jacobs, A. N. Macintyre, N. J. MacIver, E. F. Mason, S. A. Sullivan, A. G. Nichols, J. C. Rathmell, Cutting edge: Distinct glycolytic and lipid

oxidative metabolic programs are essential for effector and regulatory CD4+ T cell subsets. *J. Immunol.* **186**, 3299–3303 (2011).
129. C.-H. Chang, J. D. Curtis, L. B. Maggi Jr., B. Faubert, A. V. Villarino, D. O'Sullivan, S. C.-C. Huang, G. J. W. van der Windt, J. Blagih, J. Qiu, J. D. Weber, E. J. Pearce, R. G. Jones, E. L. Pearce, Posttranscriptional control of T cell effector function by aerobic glycolysis. *Cell* **153**, 1239–1251 (2013).
130. M. Sukumar, J. Liu, Y. Ji, M. Subramanian, J. G. Crompton, Z. Yu, R. Roychoudhuri, D. C. Palmer, P. Muranski, E. D. Karoly, R. P. Mohney, C. A. Klebanoff, A. Lal, T. Finkel, N. P. Restifo, L. Gattinoni, Inhibiting glycolytic metabolism enhances CD8+ T cell memory and antitumor function. *J. Clin. Invest.* **123**, 4479–4488 (2013).
131. C.-H. Chang, J. Qiu, D. O'Sullivan, M. D. Buck, T. Noguchi, J. D. Curtis, Q. Chen, M. Gindin, M. M. Gubin, G. J. W. van der Windt, E. Tonc, R. D. Schreiber, E. J. Pearce, E. L. Pearce, Metabolic competition in the tumor microenvironment is a driver of cancer progression. *Cell* **162**, 1229–1241 (2015).
132. P.-C. Ho, J. D. Bihuniak, A. N. Macintyre, M. Staron, X. Liu, R. Amezquita, Y.-C. Tsui, G. Cui, G. Micevic, J. C. Perales, S. H. Kleinstein, E. D. Abel, K. L. Insogna, S. Feske, J. W. Locasale, M. W. Bosenberg, J. C. Rathmell, S. M. Kaech, Phosphoenolpyruvate is a metabolic checkpoint of anti-tumor T cell responses. *Cell* **162**, 1217–1228 (2015).
133. G. Cretenet, I. Clerc, M. Matias, S. Loisel, M. Craveiro, L. Oburoglu, S. Kinet, C. Mongellaz, V. Dardalhon, N. Taylor, Cell surface Glut1 levels distinguish human CD4 and CD8 T lymphocyte subsets with distinct effector functions. *Sci. Rep.* **6**, 24129 (2016).
134. L. V. Sinclair, J. Rolf, E. Emslie, Y.-B. Shi, P. M. Taylor, D. A. Cantrell, Control of amino-acid transport by antigen receptors coordinates the metabolic reprogramming essential for T cell differentiation. *Nat. Immunol.* **14**, 500–508 (2013).
135. A. N. Macintyre, V. A. Gerriets, A. G. Nichols, R. D. Michalek, M. C. Rudolph, D. Deoliveira, S. M. Anderson, E. D. Abel, B. J. Chen, L. P. Hale, J. C. Rathmell, The glucose transporter Glut1 is selectively essential for CD4 T cell activation and effector function. *Cell Metab.* **20**, 61–72 (2014).
136. P.-y. Wang, J. Li, F. L. Walcott, J.-G. Kang, M. F. Starost, S. L. Talagala, J. Zhuang, J.-H. Park, R. D. Huffstutler, C. M. Bryla, P. L. Mai, M. Pollak, C. M. Annunziata, S. A. Savage, A. T. Fojo, P. M. Hwang, Inhibiting mitochondrial respiration prevents cancer in a mouse model of Li-Fraumeni syndrome. *J. Clin. Invest.* **127**, 132–136 (2017).
137. F. J. Kim, N. Manel, E. N. Garrido, C. Valle, M. Sitbon, J.-L. Battini, HTLV-1 and -2 envelope SU subdomains and critical determinants in receptor binding. *Retrovirology* **1**, 41 (2004).
138. L. Swainson, S. Kinet, N. Manel, J.-L. Battini, M. Sitbon, N. Taylor, Glucose transporter 1 expression identifies a population of cycling CD4+ CD8+ human thymocytes with high CXCR4-induced chemotaxis. *Proc. Natl. Acad. Sci. U.S.A.* **102**, 12867–12872 (2005).
139. S. Kinet, L. Swainson, M. Lavanya, C. Mongellaz, A. Montel-Hagen, M. Craveiro, N. Manel, J.-L. Battini, M. Sitbon, N. Taylor, Isolated receptor binding domains of HTLV-1 and HTLV-2 envelopes bind Glut-1 on activated CD4+ and CD8+ T cells. *Retrovirology* **4**, 31 (2007).

**Acknowledgments:** We thank all members of our laboratories for discussions, scientific critique, and continual support. We are grateful to Montpellier RIO Imaging for support in cytometry experiments and the RAM (Animal House Network of Montpellier) animal facility of the Institut de Génétique Moléculaire de Montpellier. We are indebted to T. Gostan of the Service d'Analyse de Données Biologiques Complexes platform for data and biostatistical analyses and to M. Sitbon and A. Singer for critical discussions and reading of the manuscript. **Funding:** M.C. was supported by a fellowship from the Portuguese Foundation for Science and Technology. G.C. was supported by a fellowship from the Ligue Contre le Cancer. M.I.M. received funding from the French Ministry of Education. C.M., V. Dardalhon, V.S.Z. and V. Dulić are supported by CNRS. N.T. is supported by INSERM. This work was supported by funding from the Association de la Recherche contre le Cancer, French national (Agence Nationale de la Recherche) research grants (PolarATTACK and GlutStem), Institut National du Cancer, the European Community (contracts LSHC-CT-2005-018914 "ATTACK" and PIRG5-GA-2009-249227 "T cell homeostasis"), and the French laboratory consortiums (Labex) EpiGenMed and GR-Ex and support by the Labex EpiGenMed and GR-Ex programs, reference ANR-10-LABX-12-01 and ANR-11-LABX-0051. **Author contributions:** M.C., G.C., C.M., V. Dulić, and N.T. conceived the project and designed the experiments. M.C., G.C., C.M., M.I.M., V.S.Z., V. Dardalhon, and V. Dulić executed the experiments, and all authors contributed to data analyses and interpretations of the results. M.C., G.C., C.M., V. Dulić, and N.T. wrote the manuscript, and all authors added critical reviews and modifications. **Competing interests:** The authors declare that they have no competing interests.

Submitted 1 November 2016
Accepted 29 September 2017
Published 17 October 2017
10.1126/scisignal.aal3024

**Citation:** M. Craveiro, G. Cretenet, C. Mongellaz, M. I. Matias, O. Caron, M. C. P. de Lima, V. S. Zimmermann, E. Solary, V. Dardalhon, V. Dulić, N. Taylor, Resveratrol stimulates the metabolic reprogramming of human CD4+ T cells to enhance effector function. *Sci. Signal.* **10**, eaal3024 (2017).

Science Signaling

CANCER IMMUNOLOGY

# IL-33 and ST2 mediate FAK-dependent antitumor immune evasion through transcriptional networks

**Bryan Serrels,[1]*† Niamh McGivern,[1]† Marta Canel,[2] Adam Byron,[1] Sarah C. Johnson,[3] Henry J. McSorley,[2] Niall Quinn,[1] David Taggart,[2] Alex Von Kreigsheim,[1] Stephen M. Anderton,[2] Alan Serrels,[1,2]* Margaret C. Frame[1]***



**Focal adhesion kinase (FAK) mediates tumor cell–intrinsic behaviors that promote tumor growth and metastasis. We previously showed that FAK also induces the expression of inflammatory genes that inhibit antitumor immunity in the microenvironment. We identified a crucial, previously unknown role for the dual-function cytokine interleukin-33 (IL-33) in FAK-dependent immune evasion. In murine squamous cell carcinoma (SCC) cells, specifically nuclear FAK enhanced the expression of the genes encoding IL-33, the chemokine CCL5, and the soluble, secreted form of the IL-33 receptor, called soluble ST2 (sST2). The abundance of IL-33 and CCL5 was increased in FAK-positive SCC cells but not in normal keratinocytes. IL-33 associated with FAK in the nucleus, and the FAK–IL-33 complex interacted with a network of chromatin modifiers and transcriptional regulators, including TAF9, WDR82, and BRD4, which promote the activity of nuclear factor κB (NF-κB) and its induction of genes encoding chemokines, including CCL5. We did not detect secretion of IL-33 from FAK-positive SCC cells; thus, we propose that the increased production and secretion of sST2 likely sequesters IL-33 secreted by other cell types within the tumor environment, thus blocking its stimulatory effects on infiltrating host immune cells. Depleting FAK, IL-33, or sST2 from SCC cells before implantation induced tumor regression in syngeneic mice, except when $CD8^+$ T cells were co-depleted. Our data provide mechanistic insight into how FAK controls the tumor immune environment, namely, through a transcriptional regulatory network mediated by nuclear IL-33. Targeting this axis may boost antitumor immunity in patients.**

## INTRODUCTION

Reprogramming the immunosuppressive tumor environment to promote antitumor immunity is a major objective of immunomodulatory therapies currently in clinical use or development. Cancer cells contribute to orchestrating the composition of this environment through driving enrichment of immune cell populations with intrinsic immunosuppressive function, thereby evading the antitumor activity of cytotoxic CD8 T cells. Identification and characterization of key molecular pathways that regulate cancer cell expression of immune modulators, such as chemokines and cytokines, may therefore provide new therapeutic strategies for use in combination immunotherapy.

Focal adhesion kinase (FAK) is a nonreceptor tyrosine kinase that signals downstream of integrins and growth factor receptors to control the malignant phenotype in multiple ways, including by regulating adhesion, migration, proliferation, and survival (*1*). FAK is frequently increased in abundance in human cancers (*2*–*4*) and contributes to skin, mammary, intestinal, and prostate tumorigenesis in mouse models (*5*–*8*). A number of small-molecule FAK kinase inhibitors are now in early-phase clinical trials. In addition to its role at the plasma membrane, FAK can also translocate to the nucleus, where it can regulate gene expression (*9*–*11*). In a mouse model of skin squamous cell carcinoma (SCC) (*12*), we demonstrated that nuclear FAK controls expression of chemokines and cytokines, including *Ccl5* and *Tgfb2*, that drive increased numbers of regulatory T ($T_{reg}$) cells in the tumor environment, resulting in protection from an antitumor $CD8^+$ T cell response (*9*).

[1]Cancer Research UK Edinburgh Centre, Institute of Genetics and Molecular Medicine, University of Edinburgh, Edinburgh EH4 2XR, UK. [2]Medical Research Council Centre for Inflammation Research, Queen's Medical Research Institute, University of Edinburgh, Edinburgh EH16 4TJ, UK. [3]Barts Cancer Institute, Queen Mary University of London, Charterhouse Square, London EC1M 6BQ, UK.
*Corresponding author. Email: m.frame@ed.ac.uk (M.C.F.); b.serrels@ed.ac.uk (B.S.); a.serrels@ed.ac.uk (A.S.)
†These authors contributed equally to this work.

Interleukin-33 (IL-33) is a member of the IL-1 family of cytokines and is secreted by necrotic epithelial cells and activated innate immune cells or held within the cell as a nuclear factor. Secreted IL-33 binds to its cognate receptor, a heterodimeric complex composed of ST2L [interleukin 1 receptor-like 1 (IL1RL1)] and IL-1 receptor accessory protein (IL-1RAcP), to initiate activation of mitogen-activated protein kinase and nuclear factor κB (NF-κB) (*13*), wherein IL-33 has potent proinflammatory functions and is considered a "danger" signal. IL-33 released into the tumor environment has been suggested to both inhibit (*14*) and promote tumor formation (*15*), indicating that IL-33's roles in cancer development and progression are unclear. IL-33 can also localize to the nucleus, where it either activates or represses transcription through association with the transcription factor NF-κB or the NF-κB p65 promoter, respectively (*16*, *17*). The precise mechanisms that underpin IL-33's regulation of transcription are not well understood.

ST2, a component of the IL-33 receptor complex, can exist as a functional transmembrane receptor (ST2L) or as a shorter secreted decoy receptor [soluble ST2 (sST2)] (*13*). ST2L is present on the cell surface of several hematopoietic cells, including T cells, macrophages, neutrophils, and myeloid-derived suppressor cells (MDSCs), and activation of downstream signaling can alter cytokine production or immunosuppressive capacity (*14*, *18*). ST2L of host immune cells is required for tumor clearance; hence, it has been linked to the antitumor properties of IL-33 (*14*). Conversely, sST2 is proposed to function as a decoy receptor for IL-33, suppressing its potent proinflammatory functions, and high serum levels of sST2 have been correlated with poor prognosis in estrogen receptor–positive breast cancer (*19*). Like IL-33, the precise role of sST2 in cancer remains somewhat controversial.

Here, we found that nuclear FAK is critical for the expression of *IL33* and *ST2* in cancer cells. IL-33 was restricted to the nucleus in murine SCC cells, where it acts downstream of FAK to promote

*Ccl5* expression and tumor growth. Mechanistic protein network analyses suggested that IL-33 regulates gene expression by interacting with chromatin modifiers and transcriptional regulators. ST2 was secreted by SCC cells, and it suppressed $CD8^+$ T cell–mediated tumor clearance. Our findings reveal new insight into the molecular mechanisms by which nuclear FAK regulates chemokine expression, placing nuclear IL-33 at the heart of a complex transcriptional network that specifies the antitumor immune response.

## RESULTS

### Nuclear FAK regulates expression of IL-33 and its receptor ST2

We have previously reported that nuclear FAK regulates the expression of chemokines, including *Ccl5*, and this is important for driving infiltration of $T_{reg}$ cells into murine SCC tumors, enabling them to evade the antitumor immune response (*9*). To explore the mechanisms of FAK-dependent chemokine regulation, we analyzed Affymetrix microarray data comparing murine $FAK^{-/-}$ SCC cells with those re-expressing FAK-WT (wild-type) (herein referred to as FAK-WT) to identify genes that are regulated by FAK. In the set of genes that significantly down-regulated after FAK depletion, the only significantly enriched gene ontology term was "extracellular region" ($P = 0.049$). Using the genes contained within this category, we generated a protein interaction network based on direct physical interactions. The largest connected network was found to contain *Ccl5* and the gene encoding the cytokine *IL33* (Fig. 1A). Given the link between IL-33 and the regulation of gene expression (*16*, *17*), we investigated whether, and if so how, IL-33 contributed to FAK-dependent transcription of chemokines.

We first used quantitative real-time polymerase chain reaction (qRT-PCR) to compare *IL33* expression in SCC cells expressing FAK-WT, $FAK^{-/-}$, FAK-nls (a mutant that is largely excluded from the nucleus), and FAK-kd (a kinase-deficient mutant) and found that regulation of *IL33* mRNA was dependent on both FAK kinase activity and its nuclear localization (Fig. 1B). Western blotting for IL-33 abundance in whole-cell lysates revealed similar findings at the protein level (Fig. 1C and fig. S1A). We have shown previously that mutation of the nuclear localization signal in FAK does not completely abolish FAK nuclear localization. We believe that this explains why we observed slightly increased abundance of IL-33 in cells expressing this mutant when compared to $FAK^{-/-}$ or FAK-kd SCC cells. Similarly, analysis of SCC cells expressing FAK-Y397F, an autophosphorylation-defective mutant of FAK that is kinase-deficient, showed reduced *IL33* expression similar to that observed in $FAK^{-/-}$ SCC cells (fig. S1B). Treatment of FAK-WT cells with the FAK catalytic inhibitor VS4718 inhibited IL-33 abundance on both mRNA and protein levels (Fig. 1, D and E), even with a low (50 nM) concentration of VS4718 (fig. S1, C and D). IL-33 can function both as a nuclear cytokine and a secreted alarmin (*20*). Using both an anti–IL-33 enzyme-linked immunosorbent assay (ELISA; Fig. 1F) and Western blotting (fig. S1E), we could not detect IL-33 in SCC cell–conditioned media, implying that IL-33 predominantly functions as a nuclear cytokine in SCC cells.

As an extracellular cytokine, IL-33 mediates signaling by binding to the IL-33R complex, composed of ST2 (also termed IL1RL1) and IL-1RAcP (*21*). Furthermore, both IL-33 signaling and nuclear IL-33 have been shown to regulate *ST2* expression (*22*, *23*). The protein encoded by *ST2* exists in two forms: (i) as ST2L, a membrane-anchored receptor that activates downstream signaling upon IL-33 engagement, or (ii) as sST2, a secreted soluble decoy receptor that inhibits IL-33 signaling (*13*). Using qRT-PCR with a primer set that would detect cumulative amounts of mRNA encoding both ST2L and sST2, we found that *ST2* expression was greater in FAK-WT cells when compared to $FAK^{-/-}$, FAK-nls, or FAK-kd cells (Fig. 1G). Thus, FAK's regulation of *ST2* expression is also dependent on both nuclear localization and kinase activity. Using an anti-ST2 ELISA, we found abundant secreted amounts of sST2 in FAK-WT cell–conditioned medium, and this was reduced in media conditioned by $FAK^{-/-}$, FAK-nls, and FAK-kd cells (Fig. 1H). However, flow cytometry analysis did not detect the presence of ST2L on the surface of FAK-WT and $FAK^{-/-}$ SCC cells (fig. S1F), indicating that sST2 is the predominantly produced isoform upon *ST2* induction in SCC cells. Treatment with the FAK inhibitor VS4718 reduced its expression and secretion (Fig. 1, I and J). Collectively, these results indicate that the kinase activity of FAK in the nucleus is a key regulator of the abundance of both nuclear IL-33 and sST2, thereby influencing both the nuclear and extracellular/alarmin functions of IL-33 signaling.

We next investigated the mechanism by which FAK controls *IL33* expression and sST2 abundance in SCC cells. Using an experimentally derived nuclear FAK interactome from FAK-WT cells (*9*), we used Ingenuity Pathway Analysis (IPA) to identify direct experimentally observed relationships between nuclear FAK-interacting proteins and transcription factors that regulate the expression of *IL33* and *ST2* (obtained from Qiagen's DECODE database; fig. S1G). This identified associations with several *IL33*- and *ST2*-regulatory transcription factors. We noticed that four of these associations, RUNX1, SP1, NCOA2, and NR3C1, were linked to transcription factors associated with regulating the expression of both *IL33* and *ST2*. We know that FAK associates with SP1 (confirmed in fig. S1, H and I) and RUNX1 (*24*) and is involved in regulating RUNX1-containing protein complexes, posttranslational modification, and, ultimately, transcription factor function. Small interfering RNA (siRNA)–mediated depletion of both RUNX1 and SP1 suggested that these transcription factors acted together to regulate IL-33 abundance (fig. S1, J and K). The precise details of their coordinated activities require further investigation, but nonetheless, our findings identify several connections between FAK-interacting proteins and transcription factors that regulate *IL33* and *ST2*.

### IL-33 is required for FAK-dependent expression of a subset of chemokines

Nuclear IL-33 has been linked to regulation of gene expression in several model systems (*16*, *17*). To determine whether nuclear IL-33 was required for FAK-dependent chemokine expression, we depleted IL-33 in FAK-WT SCC cells using both short hairpin RNA (shRNA; Fig. 2, A and B, and fig. S2A) and clustered regularly interspaced short palindromic repeats (CRISPR)/CRISPR-associated protein 9 (Cas9) (fig. S2B). IL-33 has previously been linked to the regulation of *Ccl5* (*23*), and we have shown that FAK-dependent *Ccl5* expression regulates the antitumor immune response (*9*). We found that *IL33* and *Ccl5* expression was increased in SCC cells when compared to primary keratinocytes (Fig. 2, C and D), correlating with nuclear FAK in SCC cells, and that IL-33 was required for *Ccl5* expression in FAK-WT SCC cells (Fig. 2E and fig. S2C). A previous study in endothelial cells (*23*) demonstrated that IL-33 silencing increased *sST2* expression. Here, we found that IL-33 silencing reduced sST2 abundance (fig. S2D). Although we have used different readouts (mRNA versus protein), it is likely that the regulation of *ST2* by IL-33 may be context-dependent. To investigate further the requirement for IL-33 in FAK-dependent

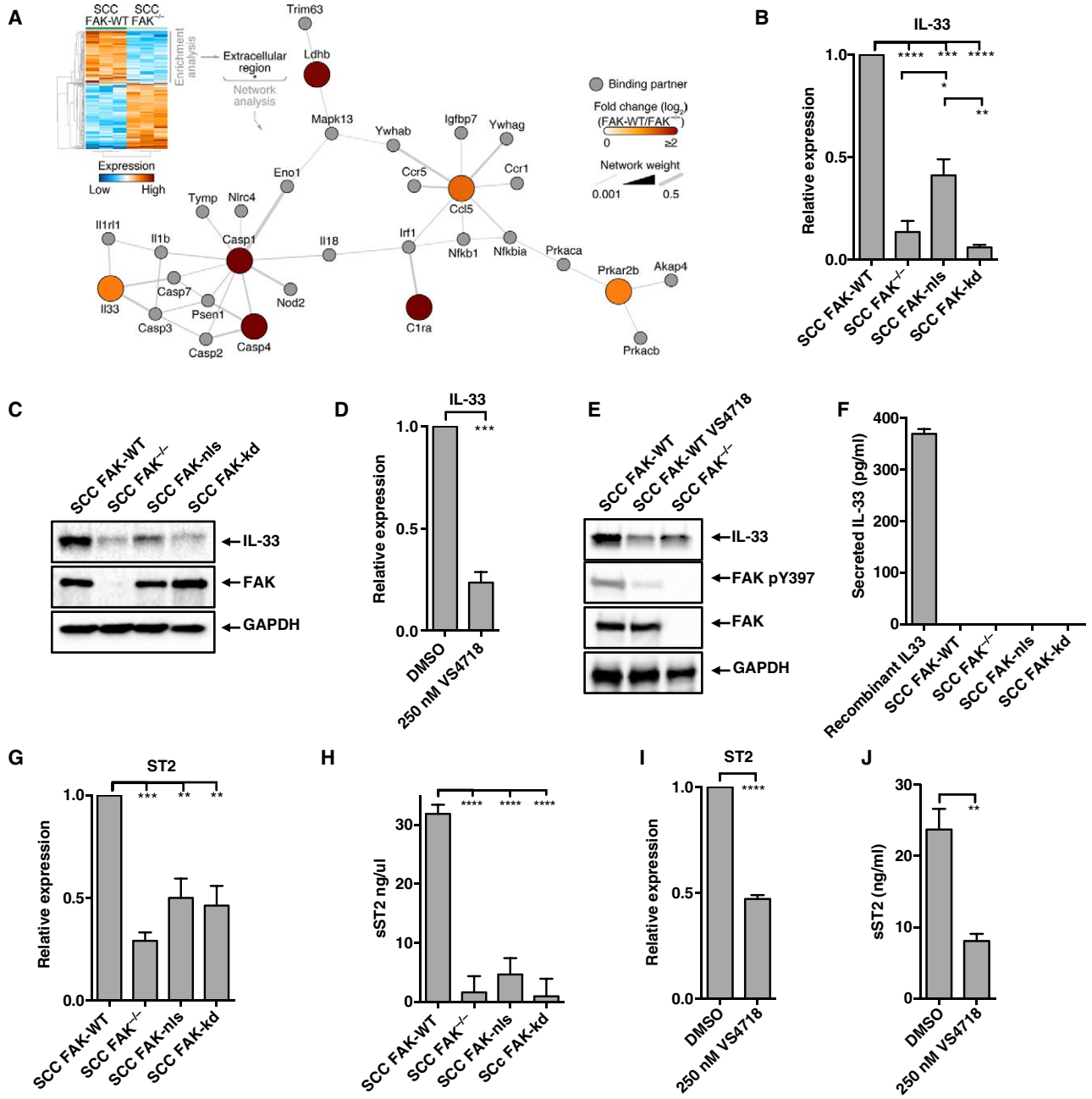


**Fig. 1. Nuclear FAK regulates expression of IL-33 and its receptor ST2.** (**A**) Gene ontology enrichment analysis (cellular component terms) on the significantly down-regulated set of genes in the *FAK*$^{-/-}$ SCC transcriptome relative to the wild-type [WT; percentage false-positives (*pfp*) < 0.05]. Genes annotated with the over-represented term (extracellular region; Benjamini-Hochberg–corrected hypergeometric test) were used to seed a protein interaction network based on direct physical interactions (gray lines). Color of each node (circle) is proportional to the log-transformed fold change in gene expression. The largest connected graph component is displayed. (**B** and **C**) Abundance of IL-33 at the mRNA level [(B); by qRT-PCR] and protein level [(C); by Western blot] in FAK-WT, *FAK*$^{-/-}$, FAK-nls (a mutant that is largely excluded from the nucleus), and FAK-kd (a kinase-deficient mutant) SCC cells. (**D** and **E**) Abundance of *Il33* mRNA [(D); by qRT-PCR] and IL-33 protein [(E); by Western blot] in FAK-WT SCC cells treated with control [dimethyl sulfoxide (DMSO)] or VS4718 (250 nM; for 24 hours). Western blot additionally assessed in *FAK*$^{-/-}$ SCC cells for reference. (**F**) Analysis of enzyme-linked immunosorbent assay (ELISA) for IL-33 in conditioned media from FAK-WT, *FAK*$^{-/-}$, FAK-nls, and FAK-kd SCC cells. (**G**) qRT-PCR analysis of *ST2* expression in FAK-WT, *FAK*$^{-/-}$, FAK-nls, and FAK-kd SCC cells. (**H**) Analysis of ELISA for sST2 in conditioned media from FAK-WT, *FAK*$^{-/-}$, FAK-nls, and FAK-kd SCC cells. (**I**) qRT-PCR analysis of *ST2* expression in FAK-WT SCC cells treated with control (DMSO) or VS4718 (250 nM; for 24 hours). (**J**) Analysis of ELISA for sST2 in conditioned media from FAK-WT SCC cells treated with control (DMSO) or VS4718 (250 nM; for 24 hours). Data are means ± SEM. $n = 3$ experiments. *$P \leq 0.05$, **$P \leq 0.01$, ***$P \leq 0.001$, ****$P \leq 0.0001$ by Tukey's corrected one-way analysis of variance (ANOVA) (B, G, and H) or two-tailed unpaired $t$ test (D, I, and J).

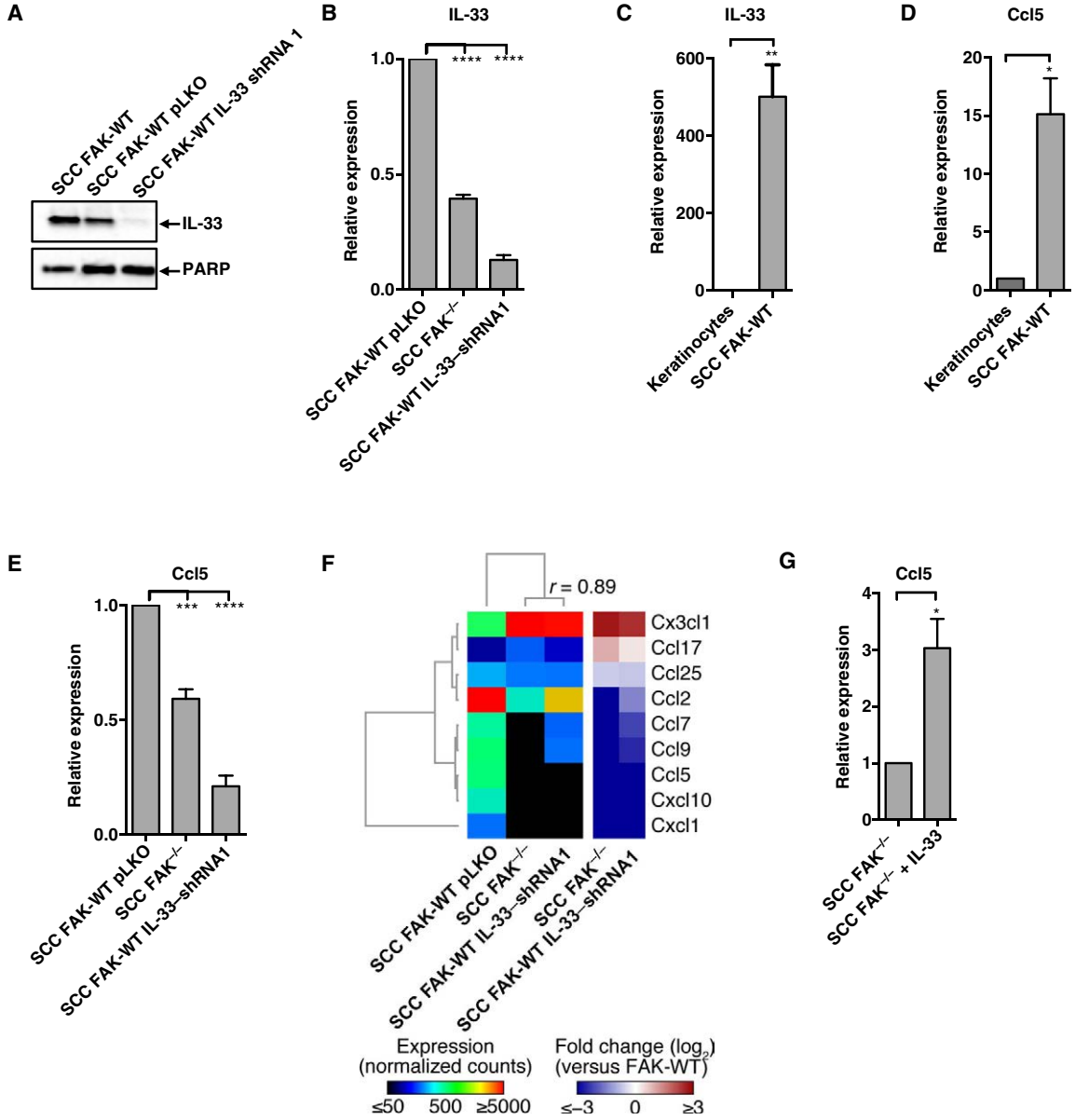


**Fig. 2. Nuclear FAK and IL-33 cooperate to regulate chemokine expression.** (**A**) Representative Western blot of IL-33 abundance in FAK-WT, FAK-WT pLKO, and FAK-WT IL-33 short hairpin RNA 1 (shRNA1) SCC cells. PARP, poly(ADP-ribose) polymerase. (**B**) qRT-PCR analysis of *IL33* expression in FAK-WT pLKO, *FAK*$^{-/-}$, and FAK-WT IL-33–shRNA1 SCC cells. (**C** and **D**) qRT-PCR analysis of *IL33* (C) and *Ccl5* (D) expression in primary keratinocytes and FAK-WT SCC cells. (**E**) qRT-PCR analysis of *Ccl5* expression in FAK-WT pLKO, *FAK*$^{-/-}$, and FAK-WT IL-33–shRNA1 cells. (**F**) NanoString analysis of chemokine expression in FAK-WT pLKO, *FAK*$^{-/-}$, and FAK-WT IL-33–shRNA1 SCC cells. $Log_{10}$-transformed expression levels for chemokines with at least 50 counts were hierarchically clustered and displayed as a heat map. Pearson correlation coefficient between expression profiles in *FAK*$^{-/-}$ and FAK-WT IL-33–shRNA1 SCC cells is shown. $Log_2$-transformed fold changes (over SCC FAK-WT pLKO) are also displayed. (**G**) qRT-PCR analysis of *Ccl5* expression in SCC *FAK*$^{-/-}$ and *FAK*$^{-/-}$ + IL-33 cells. Data are means ± SEM. $n = 3$ for all experiments. $^{*}P \le 0.05$, $^{**}P \le 0.01$, $^{***}P \le 0.001$, $^{****}P \le 0.0001$ by Tukey's corrected one-way ANOVA (B and E) or two-tailed unpaired *t* test (C, D, and G).

chemokine expression, we performed NanoString PanCancer Immune Profiling of FAK-WT/pLKO, *FAK*$^{-/-}$, and FAK-WT/IL-33–shRNA cells. Hierarchical clustering of log-transformed fold changes, relative to control cells, identified a subset of chemokines coregulated by FAK and IL-33 (Fig. 2F), including CCL5. Furthermore, overexpression of IL-33 in *FAK*$^{-/-}$ SCC cells increased *Ccl5* expression (Fig. 2G), suggesting that IL-33 is sufficient to promote *Ccl5* expression. Therefore, FAK regulates IL-33, which in turn can mediate FAK-dependent chemokine expression.

## IL-33/ST2 axis supports tumor growth by suppressing the immune response

*IL33* is expressed by several cell types within the tumor environment, and secreted IL-33 can have both pro- and antitumor effects (*14*, *15*). ST2L, the IL-33 receptor, is present on various immune cells, including $T_{reg}$ cells, macrophages, and $CD8^+$ T cells, and activation of ST2L signaling can alter their phenotype and/or function. For example, ST2L-positive $T_{reg}$ cells exhibit a more potent immunosuppressive function than ST2L-negative $T_{reg}$ cells (*25*), implying that IL-33–ST2L

signaling could enhance the suppressive activity of $T_{reg}$ cells, thereby promoting tumor growth. In contrast, activation of ST2L on cytotoxic $CD8^+$ T cells enhances the cells' cytotoxic function (*18*), resulting in an improved antitumor immune response. Therefore, it is possible that FAK-dependent regulation of the decoy receptor sST2 could have pro- or antitumor effects.

Having established that nuclear IL-33 regulates chemokine expression, including *Ccl5*, we next assessed the effects of IL-33 depletion on SCC tumor growth. Therefore, $1 \times 10^6$ FAK-WT, $FAK^{-/-}$, and FAK-WT/IL-33–shRNA1 cells were injected subcutaneously into Friend leukemia virus B strain (FVB) mice (the syngeneic host strain), and tumor growth was monitored. FAK-WT tumors exhibited exponential growth until they reached defined end points by which time the mice had to be sacrificed (see Materials and Methods). In contrast, $FAK^{-/-}$ SCC tumors grew until about day 7, after which they stalled and underwent complete regression (Fig. 3A, left graph), as we have also reported previously (*9*). IL-33 depletion from FAK-WT cells resulted in six of eight tumors exhibiting a period of growth followed by complete regression, in a similar manner to $FAK^{-/-}$ tumors, whereas two of eight tumors showed a growth delay (Fig. 3A). Similar studies using CRISPR/Cas9 to deplete IL-33 from FAK-WT cells confirmed the requirement for IL-33 in supporting SCC tumor growth (Fig. 3B). Thus, IL-33 is required to support tumor growth and permit immune evasion, likely by regulating transcription of vital chemokines, including *Ccl5*.

To next probe the role of sST2 in tumor growth, we generated sST2-depleted FAK-WT SCC cell lines using shRNA (Fig. 3C) and injected $1 \times 10^6$ FAK-WT, FAK-WT/pLKO (shRNA control), FAK-WT/ST2-shRNA1, and FAK-WT/ST2-shRNA2 SCC cells into syngeneic FVB mice. We found that most tumors (six of eight for shRNA1 and five of eight for shRNA2) exhibited a period of growth followed by complete regression (Fig. 3D) like $FAK^{-/-}$ tumors, albeit with different kinetics. To address how sST2 depletion might result in tumor regression, we profiled the immune cells in FAK-WT tumors to determine the quantity of ST2L on the cell surface. We found that after 12 days of growth, FAK-WT tumors have an extensive immune cell infiltrate accounting for about 60% of the viable cell population (Fig. 3, E and F). Using a range of surface and intracellular markers (table S1), we identified activated $CD8^+$ T cells, activated $CD4^+$ T cells, $T_{reg}$ cells, neutrophils, and macrophages as the major immune cell populations that displayed surface-bound ST2L (Fig. 3, G and H). Because IL-33 engagement with ST2L expressed on activated $CD8^+$ T cells can enhance cytotoxic function and drive increased expression of the effector cytokine interferon-γ (IFN-γ) (*14*), we hypothesized that tumor regression in response to depletion of sST2 from SCC cancer cells was likely $CD8^+$ T cell–dependent. To test this, we used CD8-depleting antibodies (Abs) and found that depletion of $CD8^+$ T cells was sufficient to completely rescue the growth of FAK-WT/ST2-shRNA SCC tumors (Fig. 3I), implying that sST2 from the tumor cells plays an important role in suppressing $CD8^+$ T cell–mediated antitumor immunity. Consistent with previous results (*9*), we also observed enhanced growth of FAK-WT tumors upon depletion of $CD8^+$ T cells, implying that even the FAK-WT cells remain under negative pressure from the $CD8^+$ T cell–mediated immune response.

### Nuclear IL-33 interacts with an extensive network of transcriptional regulators

Having established an important role for nuclear IL-33 in the regulation of chemokine expression and tumor growth, we addressed the molecular mechanisms that may underpin IL-33's regulation of chemokine transcription. Using cellular fractionation, we prepared cytoplasmic, nuclear, and chromatin extracts from FAK-WT and $FAK^{-/-}$ SCC cells as we have done before (*9*). Our results show that IL-33 is largely chromatin-associated (Fig. 4A), in agreement with previous studies that identified IL-33 as a histone 2A (H2A)/2B–binding protein (*26*). To investigate the functional significance of IL-33 association with chromatin, we made use of a proteomics technique called "BioID" (*27*). First, we generated an IL-33 protein fused to the 35-kDa *Escherichia coli* biotin protein ligase BirA (IL-33–BirA). Next, we expressed either IL-33–BirA or BirA alone in FAK-WT cells, from which endogenous IL-33 was deleted (FAK-WT/IL-33–CRISPR SCC cells; Fig. 4, B and C), and cultured these in the presence of biotin for 24 hours. This resulted in the biotinylation of proximal interacting proteins, enabling their purification and identification by mass spectrometry (MS). To ensure identification of robust interactions, we applied stringent criteria, including that (i) proteins must be present in all three biological replicates, (ii) proteins must have greater than threefold enrichment when compared to BirA-only control, and (iii) fold enrichment must be statistically significant ($P < 0.05$). With these criteria, we identified 105 proteins that associated with IL-33. Gene ontology analysis of both biological and cellular processes [Database for Annotation, Visualization and Integrated Discovery (DAVID) bioinformatics database] represented within the data set identified significantly enriched terms associated with chromatin organization and transcriptional regulation (fig. S3, A and B). Further analysis of the nuclear IL-33 interactome using IPA identified a connected network of proteins that were implicated in regulation of transcription, chromatin remodeling, and nucleosome disassembly (Fig. 4D). There were several members of the Baf-type complex (also known as SWI/SNF), the PTW/PP1 phosphatase complex, and the transcription factor transcription factor IID (TFIID) complex, establishing a link between nuclear IL-33 and the core transcriptional machinery. We extracted a complete list of genes belonging to these complexes from the gene ontology database AmiGO and used IPA to reconstruct all three complexes on the basis of known physical interactions (fig. S3, C to E). We next contextualized the BioID proteomics–informed IL-33 nuclear interactome onto these networks (highlighted in pink in fig. S3, C to E) and identified potential interactions linking IL-33 to key members of these complexes. Using streptavidin pulldown after incubation of IL-33–BirA fusion protein–expressing FAK-WT/IL-33–CRISPR SCC cells in the presence of biotin, we confirmed the interactions of IL-33 with WDR82, SMARCC1, and TAF9 (Fig. 4E). We found that IL-33 depletion in FAK-WT cells resulted in loss of WDR82 from the chromatin fraction (Fig. 4F), implying that IL-33 is required to stabilize the association of WDR82 with chromatin. We find this interesting because WDR82 is a key component of complexes associated with chromatin modification, such as the PTW/PP1 phosphatase complex (*28*) and the Set1A/Set1B histone $H3\text{-}Lys^4$ (H3K4) methyltransferase complex (*29*). Therefore, IL-33 likely plays a key role in scaffolding complexes required to modulate chromatin structure and permit transcription.

### IL-33 interacts with and enhances regulators of *Ccl5* expression

As mentioned above, we previously showed that CCL5 secreted by FAK-WT SCC cells drives the infiltration of immunosuppressive $T_{reg}$ cells into SCC tumors, shifting the $CD8^+$ T cell/$T_{reg}$ ratio in favor of tumor tolerance (*9*). Thus far, we have found that IL-33 is both necessary and sufficient to drive *Ccl5* expression downstream of FAK (Fig. 2, E and G). To define how IL-33 contributes to regulation of

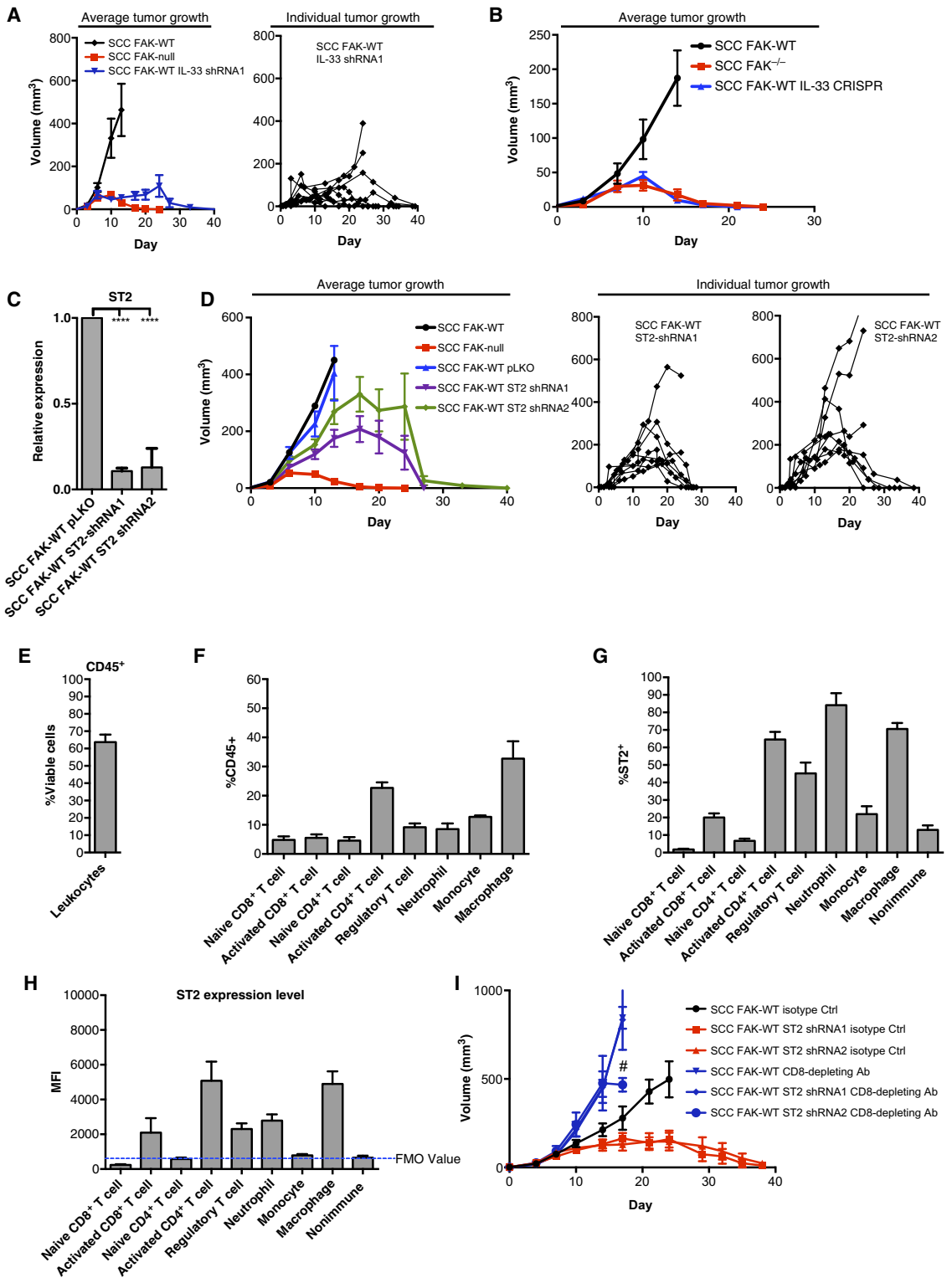


**Fig. 3. IL-33 and sST2 support SCC tumor growth through suppressing the antitumor immune response.** (**A** and **B**) Representative growth of FAK-WT, *FAK*$^{-/-}$, and FAK-WT IL-33–shRNA1 (A) or FAK-WT IL-33–CRISPR (clustered regularly interspaced short palindromic repeats) (B) SCC tumors after orthotopic subcutaneous implantation. (**C**) qRT-PCR analysis of *ST2* expression in FAK-WT pLKO, FAK-WT ST2-shRNA1, and FAK-WT ST2-shRNA2 SCC cells. (**D**) Growth of FAK-WT ST2-shRNA (pools 1 and 2) SCC tumors after orthotopic subcutaneous implantation. (**E**) CD45$^{+}$ cells as a percentage of live cells isolated from FAK-WT SCC tumors 12 days after implantation. (**F**) Abundance of different immune cell populations as a percentage of CD45$^{+}$ cells. Marker sets used to identify cell populations are listed in fig. S3. (**G**) Percentage ST2$^{+}$ cells in different immune cell populations. (**H**) Mean fluorescent intensity (MFI) of ST2 expression in different immune cell populations. MFO, fluorescence minus one. (**I**) Representative growth of FAK-WT, FAK-WT ST2-shRNA1, and FAK-WT ST2-shRNA2 SCC tumors receiving treatment with either a CD8-depleting antibody (Ab) or isotype control (Ctrl) Ab. Statistics in (C): ****$P \leq$ 0.0001 by Tukey's corrected one-way ANOVA. Data are means ± SEM. $n$ = 3 for qRT-PCR, $n$ = 6 to 8 tumors.

*Ccl5* expression, we mapped the nuclear IL-33 interactome onto a network of proteins associated with predicted *Ccl5* transcription factors (Fig. 4G). This revealed that IL-33 interacts with transcription factors and transcriptional regulators that affect expression of *Ccl5*. Notably, three factors belonging to the TFIID complex were found to interact with nuclear IL-33, including TAF9, a protein that we found previously to form complexes with FAK (*9*). To explore the connection between FAK, IL-33, and *Ccl5* transcription, we mapped the nuclear FAK interactome onto the set of *Ccl5* regulatory proteins found to interact with nuclear IL-33 (Fig. 4G). This identified proteins

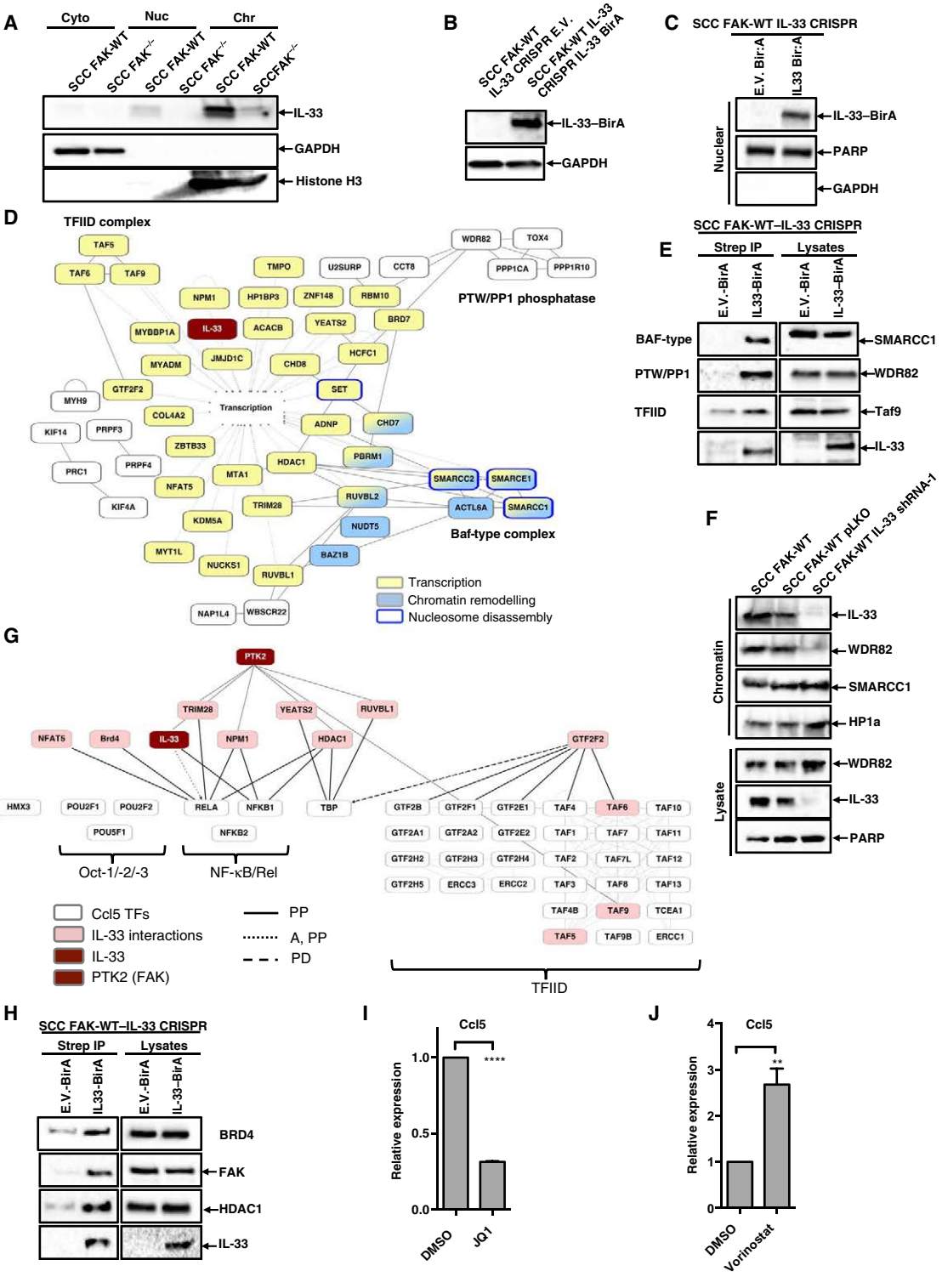


**Fig. 4. Nuclear IL-33 interacts with an extensive network of transcriptional regulators.** (**A**) Representative Western blot of IL-33 abundance in cytoplasmic (Cyto), nuclear (Nuc), and chromatin (Chr) fractions from FAK-WT and *FAK*$^{-/-}$ SCC cells. (**B**) Representative Western blot of IL-33 abundance in FAK-WT IL-33–CRISPR/BirA-E.V. and FAK-WT IL-33–CRISPR/IL-33–BirA SCC cells. (**C**) Western blot analysis of lysates from nuclear fractionations of IL-33–BirA fusion protein expression in FAK-WT IL-33–CRISPR/E.V. (empty vector) or FAK-WT IL-33–CRISPR/IL-33–BirA SCC cells. (**D**) Functional interaction network analysis of the IL-33 interactome. Direct physical interactions (solid gray lines) and functional association with transcription (dashed gray lines) are shown. Node style indicates association with additional relevant overrepresented functions ($P <$ 0.0001 by Benjamini-Hochberg–corrected hypergeometric test). Components of the PTW/PP1 phosphatase, Baf-type, and TFIID complexes are highlighted. (**E**) Western blot analysis of key network components using streptavidin pulldowns from biotinylated lysates of SCC FAK-WT IL-33 CRISPR cells expressing either BirA empty vector or IL-33–BirA fusion protein. (**F**) Representative Western blot of chromatin fractions and whole cell lysates from SCC FAK-WT, FAK-WT pLKO, and FAK-WT IL-33 shRNA1 cells. (**G**) Interrogation of the IL-33 BioID protein interaction network to identify potential upstream regulators of m*Ccl5* promoter associated transcription factors (taken from Qiagen ENCODE database). PP, protein-protein interaction; E, expression; PD, protein-DNA interaction; T, transactivation; A, activation. (**H**) Western blot analysis of IL-33:BRD4, IL-33:FAK, and IL-33:HDAC1 associations using streptavidin pulldowns from biotinylated lysates of FAK-WT IL-33–CRISPR SCC cells expressing either BirA empty vector or IL-33–BirA fusion protein. HDAC1, histone deacetylase 1. (**I**) qRT-PCR analysis of *Ccl5* expression in SCC FAK-WT cells treated with DMSO or JQ1 (200 nM for 48 hours). (**J**) qRT-PCR analysis of Ccl5 expression in FAK-WT SCC cells treated with DMSO or vorinostat (10 μM for 24 hours). Statistics in (I) and (J): ****$P \leq 0.0001$, **$P \leq 0.01$ by two-tailed unpaired *t* test. $n = 3$ for all experiments.

in common between the nuclear FAK and nuclear IL-33 interactomes, suggesting that these proteins may be part of the same molecular complexes that regulate *Ccl5* expression. Using streptavidin-coated beads, we isolated the IL-33 BioID fusion protein and confirmed that FAK and IL-33 exist in complex under steady-state conditions (Fig. 4H). Hence, we conclude that FAK binds to IL-33, and together, they complex with key *Ccl5*-regulatory transcription factors, to coregulate chemokine gene expression.

Besides TFIID, many of the IL-33–interacting partners converge on regulators of NF-κB, suggesting that NF-κB may be central to FAK and IL-33 regulation of chemokine expression. Notably, we showed that IL-33 interacts with the bromodomain protein BRD4 and the histone deacetylase HDAC1 (histone deacetylase 1; Fig. 4H). BRD4 is a member of the bromodomain and extraterminal domain (BET) family of transcriptional coactivators and elongation factors that recruit chromatin remodeling factors, including the SWI/SNF complex (*30*), to the promoters of genes via recognition of polyacetylated histone tails (*31*). Because IL-33 binds to both BRD4 and members of the Baf-type (SWI/SNF) complex, we hypothesize that IL-33 plays a role in formation of this complex at actively transcribing genes. It is known that BRD4 directly binds to acetylated p65 NF-κB, which leads to enhanced NF-κB transactivation activity (*32*), together suggesting a role for BRD4 in inflammatory transcriptional signaling. To support these conclusions, we treated FAK-WT SCC cells with the BET family inhibitor JQ1. This resulted in reduced *Ccl5* expression (Fig. 4I), implying a role for BET family proteins in the regulation of chemokine expression. In contrast, HDAC1 has been shown to negatively regulate NF-κB transcriptional activity via a direct interaction with p65 (RelA) (*33*). We used the HDAC inhibitor vorinostat and identified a clear induction of *Ccl5* expression upon HDAC inhibition (Fig. 4J). Collectively, our data support a model, whereby FAK binds to IL-33, which is a central component of a network of transcriptional regulators associated with the dynamic regulation of NF-κB–dependent chemokine transcription.

## DISCUSSION

Nuclear FAK is emerging as an important regulator of gene expression in cancer cells, controlling transcriptional networks that influence multiple cellular functions. For example, FAK is reported to interact with the transcription factors p53 and GATA4, resulting in their inactivation with effects on cell survival (*34*). We have shown that nuclear FAK regulates expression of chemokines and cytokines, including *Ccl5*, likely via interactions with transcription factors and transcriptional regulators (*9*). Here, we show that both IL-33 and sST2 are transcriptionally regulated by nuclear FAK in a kinase-dependent manner and that FAK interacts with transcription factors and transcriptional regulators linked to control of expression of *IL33* and *ST2*.

Depletion of IL-33 abundance in FAK-WT cells revealed that it is vital downstream of FAK in the regulation of chemokine expression, including that of *Ccl5*. We have previously identified a CCL5–CCR1/3/5 paracrine signaling axis between SCC FAK-WT cells and tumor-infiltrating $T_{reg}$ cells and have shown that CCL5 depletion results in FAK-WT tumor regression as a result of reduced tumor-infiltrating $T_{reg}$ cells (*9*). Our tumor growth studies here revealed that IL-33 depletion caused FAK-WT tumor regression, presumably because of IL-33–dependent regulation of *Ccl5* and other chemokines. Thus, IL-33 regulates proinflammatory gene programs downstream of FAK that we have shown to play an important role in defining the tumor-immune environment, affecting SCC tumor growth and survival.

sST2 functions as a decoy receptor that is secreted into the tumor environment, leading to competitive inhibition of IL-33–ST2 autocrine and paracrine signaling (*13*). Although IL-33 is not secreted by SCC cells, it can be secreted by macrophages and neutrophils (*35*), influencing the function of immune cell populations. ST2L is also present on activated $CD8^+$ T cells and natural killer cells, and IL-33 stimulation can increase IFN-γ expression (*14*) and cytotoxic activity (*18*). We identified ST2L on several immune cell types in the SCC tumor environment, including activated $CD8^+$ T cells. Depletion of sST2 in FAK-WT tumors largely resulted in $CD8^+$ T cell–dependent tumor regression, implying that sST2 contributes to inhibition of $CD8^+$ T cell–mediated immunity.

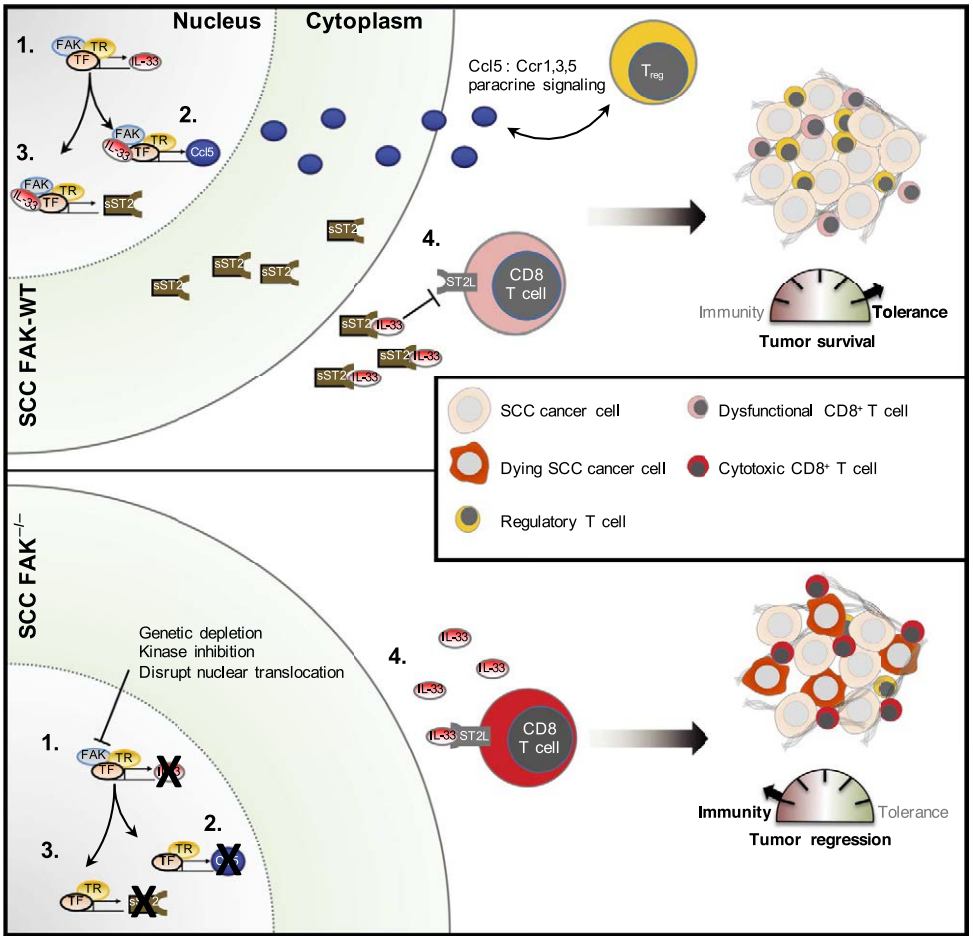


**Fig. 5. Nuclear FAK regulates IL-33/ST2 signaling to control the antitumor immune response.** Model of the mechanism. Nuclear FAK regulates *IL33* expression ("1") through interaction with transcription factors (TFs) and transcriptional regulators (TRs). Nuclear FAK and IL-33 cooperate to drive expression of *Ccl5* and *sST2* ("2" and "3," respectively) through interaction with transcription factors and transcriptional regulators. Ccl5 and sST2 are secreted from SCC cancer cells, promoting immune evasion. We have previously reported a CCL5-CCR1, 3, and 5 paracrine signaling axis between FAK-WT SCC cells and tumor-infiltrating regulatory T ($T_{reg}$) cells that contributes to immune evasion. We propose that sST2 contributes to immune evasion through competitive inhibition of IL-33/ST2 signaling on cytotoxic $CD8^+$ T cells ("4"), resulting in tumor tolerance.

Studies using an *ST2* knockout mouse have shown that host ST2 signaling is required for tumor regression to occur in response to overexpression of a secreted form of IL-33 (*14*). Therefore, we conclude that the presence of sST2 enables FAK-abundant tumors to benefit from nuclear IL-33 while counteracting the potential antitumor effects of secreted IL-33 (Fig. 5).

Nuclear IL-33 has been linked to regulation of transcription previously (*16*, *17*), although the precise mechanisms underpinning this are unknown. We confirmed that nuclear IL-33 interacts with chromatin, supporting its role in transcriptional regulation, and BioID proteomics identified proximal interactions with components of the Baf-type (SWI/SNF), PTW/PP1 phosphatase, and TFIID complexes. This implies that nuclear IL-33 functions in chromatin remodeling and transcriptional initiation. In support of this, we confirmed binding of WDR82, SMARCC1, TAF9, BRD4, and HDAC1 and showed that WDR82 was absent from chromatin after depletion of IL-33 from FAK-WT cells, showing that IL-33 is required to stabilize the WDR82 chromatin complex. WDR82 is a component of the PTW/PP1 phosphatase complex and is involved in regulating chromatin structure (*28*). It is also a core component of the mammalian Set1A/Set1B histone H3K4 methyltransferase complex that is associated with regulating H3K4 trimethylation, a key step in transcriptional activation (*36*).

Finally, we identified BRD4 and HDAC1 positive (*37*) and negative (*33*) regulators of NF-κB activity, respectively, as previously unknown nuclear IL-33–interacting proteins. BRD4 is also required for recruitment of the SWI/SNF complex to active promoters (*30*), and we have shown that IL-33 binds to several components of this complex. Therefore, IL-33 likely binds to BRD4, HDAC1, and other chromatin modifiers to control the dynamic expression of NF-κB target genes, such as *Ccl5* and other chemokines. Collectively, our data suggest that IL-33 acts to regulate chromatin organization and FAK-dependent transcription, promoting a proinflammatory gene program that enables evasion of the antitumor immune response.

## MATERIALS AND METHODS

### Cell lines

Isolation and generation of the FAK SCC cell model is described in detail by Serrels *et al.* (*12*). Briefly, SCC cells were induced in K14*Cre*ER *FAK*$^{flox/flox}$ mice on an FVB background using the dimethylbenz[*a*]anthracene/12-*O*-tetradecanoylphorbol 13-acetate two-stage skin chemical carcinogenesis protocol and cells isolated. After treatment with 4-hydroxytamoxifen, a FAK-null (*FAK*$^{-/-}$) cell clone was isolated, and retroviral transduction was used to stably reexpress FAK-WT and FAK mutant proteins. Phoenix Ecotropic cells were transfected with pWZL (Hygro) FAK using Lipofectamine 2000 (Thermo Scientific) according to the manufacturer's instructions. Twenty-four hours after transfection, cell culture supernatant was removed, filtered through a 0.45-μm Millex-HA filter (Millipore), diluted at a 1:1 ratio in normal SCC cell culture medium, supplemented with polybrene (5 μg/ml), and added to SCC FAK$^{-/-}$ cells for 24 hours. A total of two rounds of infection were performed to generate each cell line. Cells were cultured at 37°C in Glasgow minimum essential medium (MEM; Sigma-Aldrich) supplemented with 2 mM L-glutamine, MEM vitamins, 1 mM sodium pyruvate (all from Sigma-Aldrich), MEM amino acids, and 10% fetal bovine serum (FBS; both from Life Technologies), and maintained under selection using hygromycin (0.25 mg/ml). To overexpress IL-33 in *FAK*$^{-/-}$ SCC cells, the cells were transfected with 1.5 μg of IL-33 pcDNA3.1 (synthesized optimized sequence by Geneart, Life Technologies) using Lipofectamine 2000. Cells were selected in G418 (400 μg/ml), and overexpression of IL-33 was confirmed by Western blotting.

### shRNA-mediated ST2 and IL-33 knockdown

To generate lentiviral particles, $2 \times 10^6$ human embryonic kidney 293FT cells were transfected with a mixture of 2 μg of shRNA [RMM4534-EG77125 (IL-33) and RMM4534-EG17082 (ST2/IL1l1R); GE Healthcare], 0.5 μg of MDG2, and 1 μg of PAX2 plasmid DNA using Lipofectamine 2000 (Thermo Fisher Scientific) as per the manufacturer's guidelines. Forty-eight hours after transfection, medium was removed and filtered through a 0.45-μm Millex-AC filter (Millipore) and mixed at a 1:1 ratio with normal SCC growth medium, supplemented with polybrene (Millipore) to a final concentration of 5 μg/ml, and added to SCC cells for 24 hours. Cells were subjected to two rounds of lentiviral infection before selection in puromycin (2 μg/ml).

### siRNA-mediated knockdown of SP1 and RUNX1

To knockdown SP1 and RUNX1, FAK-WT SCC cells were transfected in 10 nmol of nontargeting siRNA SMARTpool, SP1 siRNA SMARTpool, or Runx1 siRNA SMARTpool (all from Dharmacon, siGenome), or a combination of 10 nmol of SP1 and RUNX1 siRNA SMARTpool using HyPerFect Transfection Reagent (Qiagen) as per the manufacturer's guidelines. Transfection was performed in serum-free medium for 24 hours, after which the medium was replaced with normal growth medium. Protein lysates were collected 48 hours after transfection.

### IL-33 CRISPR construct generation

Guide sequence oligonucleotides (forward: TTTCTTGGCTTTATATATCTTGTG GAAAGGACGAAACACCGTTCCTAGAA TCCCGTGGAT and reverse: GACTAGCCTTA TTTTAACTTGCTATTTCTAGCTCTAAAACATCCACGGGATTCTAGGAAC) including Eco RI restriction overhangs and a protospacer adjacent motif (PAM) sequence targeting exon 3 within *IL33* were annealed using Phusion High-Fidelity Polymerase [New England Biolabs (NEB)] according to the manufacturer's guidelines. Ten micromolar of each oligonucleotide was mixed with 25 mM $MgCl_2$, 2.5 mM deoxynucleotide triphosphate, 5X Phusion High-Fidelity Buffer, and Phusion Polymerase to a final volume of 50 μl. Cycling conditions were 98°C (30 s), 30 cycles of 98°C (10 s), 55°C (30 s), and 72°C (20 s), followed by a final incubation at 72°C (20 s). The final PCR product was analyzed by agarose gel electrophoresis. Annealed oligonucleotides were ligated into the gRNA_cloning vector (pCR-Blunt II-TOPO), a gift from G. Church (Addgene plasmid no. 41824). gRNA_cloning vector DNA (1.5 μg) was digested with 1.5 units of Afl II restriction enzyme (NEB) according to the manufacturer's guidelines and incubated for 1 hour at 37°C. Four nanograms of annealed oligonucleotides was ligated with 30 ng of linearized gRNA_ cloning vector using Gibson Assembly Master Mix (NEB) according to the manufacturer's guidelines and incubated for 1 hour at 50°C. Constructs were transformed into DH5α chemically competent cells and selected on agar plates containing kanamycin (50 μg/ml). To identify positive colonies, DNA was prepared and digested with Eco RI restriction enzyme (NEB).

### IL-33 CRISPR/Cas9 transfection and single-cell clone expansion

SCC-FAK-WT cells were seeded on a 100-mm tissue culture dish and grown until ~70% confluent. Cells were cotransfected with 3 μg of hCas9 and 3 μg of gRNA_cloning vector IL-33–specific guides, using

Lipofectamine 2000 (Thermo Scientific) according to the manufacturer's guidelines. IL-33 CRISPR knockout clones were isolated by dilution cloning; once cells reached confluence, they were trypsinized and resuspended in 10 ml of growth media. To ensure single-cell suspension, cells were passed through a cell strainer (Thermo Scientific), and 5 µl of the cell suspension was plated into a 15-cm plate. Several colonies were picked and expanded, and knockout of IL-33 was confirmed by quantitative PCR (qPCR) and Western blot. IL-33 primers used were forward: GGATCCGATTTTCGAGAGCTTAAACAT and reverse: GCGGCCGCATGAGACCTAGAATGAAGT. All primer sequences are detailed in table S2.

### Immunoblotting

Cells were washed twice in ice-cold phosphate-buffered saline (PBS) and lysed in radioimmunoprecipitation assay (RIPA) lysis buffer (50 mM tris-HCl at pH 7.4, 150 mM sodium chloride, 5 mM EGTA, 0.1% SDS, 1% NP-40, and 1% deoxycholate) supplemented with a protease and phosphatase inhibitor cocktail (mini cOmplete ULTRA Protease tablet and phosSTOP tablet from Roche). Lysates were clarified by high-speed centrifugation (16,000*g* for 15 min at 4°C). Protein concentration was measured using a Micro BCA Protein Assay (Thermo Scientific), and 10 to 20 µg of total protein were supplemented with 2X SDS sample buffer [tris (pH 6.8), 20% glycerol, 5% SDS, β-mercaptoethanol, and bromophenol blue) and boiled at 95°C for 5 min. Samples were separated by polyacrylamide gel electrophoresis using 4 to 15% Mini-PROTEAN TGX gels (Bio-Rad), proteins transferred to nitrocellulose, blocked [5% bovine serum albumin (BSA) in PBS–Tween 20 (BSA/PBS-T)], and probed with either anti–IL-33 (R&D Biosystems), anti–glyceraldehyde-3-phosphate dehydrogenase (GAPDH; Cell Signaling Technology), anti–phospho-FAK (Y397; Cell Signaling Technology), anti-FAK (Cell Signaling Technology), anti-WDR82 (Abcam), anti-TAF9 (Abcam), anti- SMARC C1 (Abcam), anti-BRD4 (Abcam), anti-HP1 α/β (Cell Signaling Technology), anti-SP1 (Abcam), anti-Runx1 (Cell Signaling Technology), or anti-HDAC1 Abs (Cell Signaling Technology; all 1:1000 in 5% BSA/PBS-T). Bound Ab was detected by incubation with anti-rabbit, anti-mouse, or streptavidin-conjugated horseradish peroxidase secondary Ab (Cell Signaling Technology) and visualized using the Bio-Rad ChemiDoc MP Imaging System.

### Chromatin preparation

Cells ($1.5 \times 10^6$) were plated in 100-mm dishes and, after 24 hours, washed twice in cold PBS. Cells were lysed in 400 µl of extraction buffer [10 mM Hepes (pH 7.9), 10 mM KCl, 1.5 mM $MgCl_2$, 0.34 M sucrose, 10% glycerol, and 0.2% NP-40 substitute) containing protease/phosphatase inhibitors (mini cOmplete ULTRA Protease tablet and phosSTOP tablet from Roche). Lysates were cleared at 6500*g* for 5 min at 4°C. The resulting nuclear pellet was washed in extraction buffer without NP-40 and centrifuged at 6500*g* for 5 min at 4°C. The pellet was resuspended in 400 µl of no-salt buffer [10 mM Hepes (pH 7.9), 3 mM EDTA, and 0.2 mM EGTA], incubated at 4°C for 30 min with agitation, and centrifuged at 6500*g* for 5 min at 4°C. The pellet was resuspended in 160 µl of high-salt solubilization buffer [50 mM tris-HCl (pH 8.0), 2.5 M NaCl, and 0.05% NP-40] vortexed briefly, incubated at 4°C for 30 min with agitation, and centrifuged at 16,000*g* for 10 min at 4°C. The supernatant containing chromatin fraction was collected, and trichloroacetic acid (TCA) precipitation was performed. TCA was added to a final volume of 10%, and samples were incubated for 15 min on ice. After centrifugation at 21,000*g* for 15 min, the resulting pellet was washed twice in 500 µl of cold acetone and then allowed to air-dry. The pellet was then resuspended in 20 µl of 2X SDS sample buffer [tris (pH 6.8), 20% glycerol, 5% SDS, β-mercaptoethanol, and bromophenol blue) and boiled at 75°C for 10 min. Samples were separated by polyacrylamide gel electrophoresis on a 12% Mini-PROTEAN TGX gel (Bio-Rad), transferred onto nitrocellulose membrane, blocked (5% BSA in BSA/PBS-T), and then incubated with primary and secondary Abs as above.

### sST2 and IL-33 ELISA

Cells ($2 \times 10^6$) were plated in a 100-mm tissue culture dish and left to adhere overnight. Medium was replaced with 4 ml of fresh complete growth medium and conditioned for 24 hours, collected, and spun at 1000 revolutions per minute (rpm) for 5 min to remove debris. Medium samples were analyzed for sST2 levels using a mouse ST2 Quantikine ELISA kit or mouse IL-33 Quantikine Elisa kit (R&D Systems). Cells adhered to the tissue culture dish were washed two times in ice-cold PBS and lysed in RIPA lysis buffer as above. Protein concentration was measured using Micro BCA Protein Assay, and protein quantities were used for normalization of ELISA values.

### qRT-PCR and NanoString

RNA was prepared from cells using the Qiagen RNeasy mini kit as per the manufacturer's instructions, inclusive of deoxyribonuclease (DNase) digestion. Final concentration of RNA was measured using a NanoDrop (Thermo Scientific). For qRT-PCR, 5 µg of total RNA was converted to complementary DNA (cDNA) using the SuperScript II cDNA Synthesis Kit (Thermo Fisher Scientific). For qRT-PCR, 62.5 ng of cDNA was added to SYBR Green (Applied Biosystems) and supplemented with 0.25 µl of 10 µM qPCR primers to a final reaction volume of 10 µl. IL-33 primers used were forward: GGATCCGATTTTCGAGAGCTTAAACAT and reverse: GCGGCCGCATGAGACCTAGAATGAAGT. ST2 primers used were forward: GCGGAGAATGGAAGCAACTA and reverse: AAGCAAGCTGAACAGGCAAT. Ccl5 primers used were forward: CCCTCACCATCATCCTCACT and reverse: CCTTCGAGTGACAAACACGA. qRT-PCR was performed on a StepOne Plus qRT-PCR instrument (Applied Biosystems). PCR conditions were as follows: 95°C (3 min), followed by 40 cycles of 95°C (5 s), 60°C (10 s), and 72°C (10 s). Melt curve analysis was performed after each qPCR reaction. Data were analyzed using the delta-delta cycle threshold (ddCT) method, and expression was calculated relative to GAPDH. For NanoString analysis, 150 ng of RNA was labeled with gene-specific bar codes as per the manufacturer's instructions and quantified using a NanoString nCounter DX. NanoString analysis was carried out by the Newcastle NanoString nCounter analysis service. Analysis was performed using nSolver analysis software (NanoString).

### Generation of IL-33–BirA–expressing SCC cell line

IL-33 cDNA was amplified by PCR using gene-specific primers (forward: GCAGCAGCGGCCGCATGAGACCTAGAATGAAGTATTCCAAC and reverse: TGCTGCGGATCCGATTTTCGAGAGCTTAAACATAATATTG) and subcloned into the Not1/BamH1 sites of pQCXIN-BirA-Myc. Specifically, 20 ng of pcDNA-3.1 IL-33 DNA template was mixed with 10 µM of each primer in PfuUltra Hotstart master mix (Stratagene) and subjected to PCR with cycle conditions as follows: 98°C (30 s; 30 cycles), 98°C (10 s), 60°C (30 s), and 72°C (1 min), followed by a final incubation at 72°C (10 min). After PCR, samples were gel-purified (Qiagen Gel Purification Kit) and eluted in 30 µl of nuclease-free water (NFW). The purified PCR product was incubated with 1 µl of BamH1 restriction enzyme, 1 µl of Not1 restriction enzyme, 5 µl of Buffer 3.1 (all from NEB) to a total of 20 µl, and incubated at 37°C

for 2 hours. One microgram of pQCXIN-BirA-Myc was incubated with 1 μl of BamH1 restriction enzyme, 1 μl of Not1 restriction enzyme, and 5 μl of Buffer 3.1 to a total of 20 μl and incubated at 37°C for 1 hour. After digestion, both the PCR product and digested vector were gel-purified and eluted in 30 μl of NFW. To ligate the digested IL-33 PCR product into the BamH1/Not1 sites of pQCXIN-BirA-Myc, a 1:4 ratio of digested vector to PCR product was used and incubated with 0.5 μl of T4 DNA ligase (NEB), along with DNA ligase buffer in a final reaction volume of 10 μl, and incubated for 2 hours at room temperature (RT). DH5α chemically competent cells (50 μl) (Life Technologies) were transformed with 5 μl of ligation reaction according to the manufacturer's guidelines and plated in agar plates containing ampicillin (100 μg/ml). Resulting colonies were checked for successful ligation using a diagnostic digest with BamH1 and Not1 restriction enzymes and, if positive, sequenced. Phoenix Ecotropic cells were transfected with empty vector–BirA or IL-33–BirA using Lipofectamine 2000 (Thermo Scientific) according to the manufacturer's guidelines. Forty-eight hours after transfection, cell culture supernatant was removed, filtered through a 0.45-μm Millex-HA filter (Millipore), diluted at a 1:1 ratio in normal SCC cell culture medium, supplemented with polybrene (5 μg/ml), and added to SCC FAK-WT IL-33–CRISPR cells for 24 hours. A total of two rounds of infection were performed to generate each cell line before selection in G418 (400 μg/ml).

### Proteomic analysis of the IL-33 interactome using BioID

Cells were incubated with 50 μM biotin (Sigma-Aldrich) in complete cell culture medium at 37°C for 24 hours, washed two times in ice-cold PBS, and lysed in RIPA lysis buffer as above. Cell lysates were sonicated using a Bioruptor (Diagenode) (30-s pulses with 30-s intervals over 5 min) and cleared by high-speed centrifugation (16,000*g* for 15 min at 4°C). Protein concentration was measured using Micro BCA Protein Assay (Thermo Scientific), and 1 mg of total cell lysate was incubated with 50 μl of streptavidin-C1 Dynabeads (Life Technologies) overnight at 4°C with agitation. Beads were washed using a magnetic tube rack three times with ice-cold RIPA buffer and two times with ice-cold PBS. Captured proteins (from experiments performed in biological triplicate) were subjected to on-bead proteolytic digestion, desalting, and liquid chromatography–tandem MS as described previously (*38*). Mean label-free MS intensities were calculated for each biological replicate. Peptide and protein false discovery rates were set to 1%. Proteins enriched from SCC-FAK-WT lL33-CRSIPR-IL-33–BirA cells by at least threefold when compared to SCC-FAK-WT IL-33–CRISPR-E.V.-BirA ($P < 0.05$) were considered specific. Proteomics analysis of nuclear FAK protein complexes is described in (*9*). All other protein interaction network analysis was performed using IPA (Qiagen). The IL-33 MS proteomics data have been deposited to the ProteomeXchange Consortium via the PRoteomics IDEntifications (PRIDE) database partner repository (*39*) with the data set identifier PXD007698.

### Interaction network analysis

Genes differentially expressed in $FAK^{-/-}$ SCC cells compared to FAK-WT SCC cells were extracted from microarray data (*9*) using rank product analysis. Significantly differentially expressed genes [$P < 0.0005$, percentage false-positives (*pfp*) < 0.05] were subjected to gene ontology enrichment analysis using DAVID Bioinformatics Resources (version 6.8) (*40*). Genes annotated with overrepresented top-level cellular component terms as determined by Benjamini-Hochberg–corrected hypergeometric test ($P < 0.05$) were used to seed a protein interaction network based on direct physical interactions constructed using the GeneMANIA plugin (version 3.4.1; mouse interactions) in Cytoscape (version 3.3.0) (*41*). The largest connected graph component was clustered using the Allegro Spring–Electric force–directed algorithm (Allegro Viva).

### Hierarchical cluster analysis

Unsupervised agglomerative hierarchical clustering was performed on the basis of Euclidean distance or Pearson correlation computed with an average-linkage or complete-linkage matrix using R or Cluster 3.0 (C Clustering Library, version 1.50) (*42*). Clustering results were visualized using R or Java TreeView (version 1.1.6) (*43*) and MultiExperiment Viewer (version 4.8.1) (*44*).

### Inhibitor treatment

FAK-WT SCC cells were treated with doses ranging from 50 to 250 nM VS4718 for 24 hours, 10 μM vorinostat for 24 hours, or 200 nM JQ1 for 48 hours, after which RNA or protein lysates were collected for qRT-PCR or Western blot analysis as described above. All inhibitors were obtained from Selleckchem.

### Subcutaneous tumor growth

All experiments involving animals were carried out in accordance with the UK Coordinating Committee on Cancer Research guidelines by approved protocol (Home Office Project License no. 60/4248). SCC cells ($1 \times 10^6$; defined earlier) were injected into both flanks of FVB mice, and tumor growth was measured twice weekly using calipers. Animals were sacrificed by cervical dislocation when tumors reached maximum allowed size (1.5 cm in diameter) or when signs of ulceration were evident. Group sizes ranged from three to five mice, each bearing two tumors, and tumor volume was calculated in Excel (Microsoft) using the formula $x - 4/3\pi r^3$. Statistics and graphs were calculated using Prism (GraphPad).

### $CD8^+$T cell depletion

Anti-mouse CD8 (clone 53-6.7) and appropriate isotype control Abs (rat immunoglobulin G 2a) were purchased from BioXcel. T cell depletion was achieved after intraperitoneal injection of 150 μg of depleting Ab (same for all Abs) into female age-matched FVB mice for three consecutive days and maintained by further intraperitoneal injection at 7-day intervals until the study was terminated. SCC FAK-WT ($1 \times 10^6$) or $FAK^{-/-}$ cells were injected subcutaneously into both flanks 6 days after initial Ab treatment, and tumor growth was measured twice weekly as described above.

### Fluorescence-activated cell sorting analysis of immune cell populations

Tumors established after injection of $1 \times 10^6$ SCC cells into both flanks of FVB mice were removed at day 12 into RPMI (Sigma-Aldrich) supplemented with 10% FBS (Life Technologies). Tumor tissue was mashed into a pulp using a scalpel and resuspended in Dulbecco's modified Eagle's medium (Sigma-Aldrich) supplemented with collagenase D (2 mg/ml) and DNase1 (200 U/ml; Roche). Samples were incubated for 30 min at 37°C with agitation, pelleted by centrifugation at 1600 rpm for 5 min at 4°C, resuspended in 5 ml of red blood cell lysis buffer (Pharm Lysing Buffer; Becton Dickinson) for 10 min at 37°C, pelleted by centrifugation at 1600 rpm for 5 min at 4°C, resuspended in PBS, and mashed through a 70-μm cell strainer. The resulting single-cell suspension pellet was pelleted by centrifugation at 1600 rpm for 5 min at 4°C and resuspended in PBS. This step was repeated a further time, and the

resulting cell pellets were resuspended in 100 µl of PBS containing e506 fixable viability dye (1:1000 dilution) and transferred into the well of a round-bottom 96-well plate. Samples were incubated at 4°C for 30 min. Cells were then pelleted by centrifugation at 1600 rpm for 5 min at 4°C and resuspended in fluorescence-activated cell sorting (FACS) buffer (PBS containing 1% FBS and 0.1% sodium azide). This step was repeated for a total of three times. Cell pellets were resuspended in 100 µl of Fc block [1:200 dilution of Fc Ab (eBioscience) in FACS buffer] and incubated for 15 min at RT. One hundred microliters of Ab mixture [1:200 dilution of Abs except anti-FoxP3, which was used at 1:100 (listed in fig. S3) in FACS buffer] was added to each well, and the samples were incubated for 30 min in the dark at 4°C. The plate was then centrifuged at 1600 rpm for 5 min at 4°C, and the cells were resuspended in FACS buffer. This step was repeated three times. Samples were analyzed using a BD Fortessa FACS Analyser. Data analysis was performed using FlowJo software. All Abs were from eBioscience. Statistics and graphs were calculated using Prism (GraphPad).

## SUPPLEMENTARY MATERIALS

www.sciencesignaling.org/cgi/content/full/10/508/eaan8355/DC1

Fig. S1. Identification of common upstream regulators of *IL33* and *ST2* promoter–associated transcription factors.

Fig. S2. CRIPSR knockout of *IL33* reduces *Ccl5* expression.

Fig. S3. Gene ontology enrichment analysis.

Table S1. Immune cell population markers.

Table S2. Primer sequences.

## REFERENCES AND NOTES


1. F. J. Sulzmaier, C. Jean, D. D. Schlaepfer, FAK in cancer: Mechanistic findings and clinical applications. *Nat. Rev. Cancer* **14**, 598–610 (2014).
2. H. M. Lightfoot Jr., A. Lark, C. A. Livasy, D. T. Moore, D. Cowan, L. Dressler, R. J. Craven, W. G. Cance, Upregulation of focal adhesion kinase (FAK) expression in ductal carcinoma in situ (DCIS) is an early event in breast tumorigenesis. *Breast Cancer Res. Treat.* **88**, 109–116 (2004).
3. A. L. Lark, C. A. Livasy, B. Calvo, L. Caskey, D. T. Moore, X. Yang, W. G. Cance, Overexpression of focal adhesion kinase in primary colorectal carcinomas and colorectal liver metastases: Immunohistochemistry and real-time PCR analyses. *Clin. Cancer Res.* **9**, 215–222 (2003).
4. M. Agochiya, V. G. Brunton, D. W. Owens, E. K. Parkinson, C. Paraskeva, W. N. Keith, M. C. Frame, Increased dosage and amplification of the focal adhesion kinase gene in human cancer cells. *Oncogene* **18**, 5646–5653 (1999).
5. G. W. McLean, N. H. Komiyama, B. Serrels, H. Asano, L. Reynolds, F. Conti, K. Hodivala-Dilke, D. Metzger, P. Chambon, S. G. N. Grant, M. C. Frame, Specific deletion of focal adhesion kinase suppresses tumor formation and blocks malignant progression. *Genes Dev.* **18**, 2998–3003 (2004).
6. H. Lahlou, V. Sanguin-Gendreau, D. Zuo, R. D. Cardiff, G. W. McLean, M. C. Frame, W. J. Muller, Mammary epithelial-specific disruption of the focal adhesion kinase blocks mammary tumor progression. *Proc. Natl. Acad. Sci. U.S.A.* **104**, 20302–20307 (2007).
7. G. H. Ashton, J. P. Morton, K. Myant, T. J. Phesse, R. A. Ridgway, V. Marsh, J. A. Wilkins, D. Athineos, V. Muncan, R. Kemp, K. Neufeld, H. Clevers, V. Brunton, D. J. Winton, X. Wang, R. C. Sears, A. R. Clarke, M. C. Frame, O. J. Sansom, Focal adhesion kinase is required for intestinal regeneration and tumorigenesis downstream of Wnt/c-Myc signaling. *Dev. Cell* **19**, 259–269 (2010).
8. J. K. Slack-Davis, E. D. Hershey, D. Theodorescu, H. F. Frierson, J. T. Parsons, Differential requirement for focal adhesion kinase signaling in cancer progression in the transgenic adenocarcinoma of mouse prostate model. *Mol. Cancer Ther.* **8**, 2470–2477 (2009).
9. A. Serrels, T. Lund, B. Serrels, A. Byron, R. C. McPherson, A. von Kriegsheim, L. Gómez-Cuadrado, M. Canel, M. Muir, J. E. Ring, E. Maniati, A. H. Sims, J. A. Pachter, V. G. Brunton, N. Gilbert, S. M. Anderton, R. J. B. Nibbs, M. C. Frame, Nuclear FAK controls chemokine transcription, $T_{regs}$, and evasion of anti-tumor immunity. *Cell* **163**, 160–173 (2015).
10. A. C. Cardoso, A. H. Pereira, A. L. Ambrosio, S. R. Consonni, R. Rocha de Oliveira, M. C. Bajgelman, S. M. G. Dias, K. G. Franchini, FAK forms a complex with MEF2 to couple biomechanical signaling to transcription in cardiomyocytes. *Structure* **24**, 1301–1310 (2016).
11. S.-T. Lim, N. L. G. Miller, X. L. Chen, I. Tancioni, C. T. Walsh, C. Lawson, S. Uryu, S. M. Weis, D. A. Cheresh, D. D. Schlaepfer, Nuclear-localized focal adhesion kinase regulates inflammatory VCAM-1 expression. *J. Cell Biol.* **197**, 907–919 (2012).
12. A. Serrels, K. McLeod, M. Canel, A. Kinnaird, K. Graham, M. C. Frame, V. G. Brunton, The role of focal adhesion kinase catalytic activity on the proliferation and migration of squamous cell carcinoma cells. *Int. J. Cancer* **131**, 287–297 (2012).
13. M. Milovanovic, V. Volarevic, G. Radosavljevic, I. Jovanovic, N. Pejnovic, N. Arsenijevic, M. L. Lukic, IL-33/ST2 axis in inflammation and immunopathology. *Immunol. Res.* **52**, 89–99 (2012).
14. X. Gao, X. Wang, Q. Yang, X. Zhao, W. Wen, G. Li, J. Lu, W. Qin, Y. Qi, F. Xie, J. Jiang, C. Wu, X. Zhang, X. Chen, H. Turnquist, Y. Zhu, B. Lu, Tumoral expression of IL-33 inhibits tumor growth and modifies the tumor microenvironment through $CD8^+$ T and NK cells. *J. Immunol.* **194**, 438–445 (2015).
15. Y. Zhang, C. Davis, S. Shah, D. Hughes, J. C. Ryan, D. Altomare, M. M. O. Peña, IL-33 promotes growth and liver metastasis of colorectal cancer in mice by remodeling the tumor microenvironment and inducing angiogenesis. *Mol. Carcinog.* **56**, 272–287 (2017).
16. S. Ali, A. Mohs, M. Thomas, J. Klare, R. Ross, M. L. Schmitz, M. U. Martin, The dual function cytokine IL-33 interacts with the transcription factor NF-κB to dampen NF-κB–stimulated gene transcription. *J. Immunol.* **187**, 1609–1616 (2011).
17. Y.-S. Choi, J. A. Park, J. Kim, S.-S. Rho, H. Park, Y.-M. Kim, Y.-G. Kwon, Nuclear IL-33 is a transcriptional regulator of NF-κB p65 and induces endothelial cell activation. *Biochem. Biophys. Res. Commun.* **421**, 305–311 (2012).
18. Q. Yang, G. Li, Y. Zhu, L. Liu, E. Chen, H. Turnquist, X. Zhang, O. J. Finn, X. Chen, B. Lu, IL-33 synergizes with TCR and IL-12 signaling to promote the effector function of $CD8^+$ T cells. *Eur. J. Immunol.* **41**, 3351–3360 (2011).
19. D. P. Lu, X. Y. Zhou, L. T. Yao, C. G. Liu, W. Ma, F. Jin, Y. F. Wu, Serum soluble ST2 is associated with ER-positive breast cancer. *BMC Cancer* **14**, 198 (2014).
20. D. O. Villarreal, D. B. Weiner, Interleukin 33: A switch-hitting cytokine. *Curr. Opin. Immunol.* **28**, 102–106 (2014).
21. A. A. Chackerian, E. R. Oldham, E. E. Murphy, J. Schmitz, S. Pflanz, R. A. Kastelein, IL-1 receptor accessory protein and ST2 comprise the IL-33 receptor complex. *J. Immunol.* **179**, 2551–2555 (2007).
22. A. Schmieder, G. Multhoff, J. Radons, Interleukin-33 acts as a pro-inflammatory cytokine and modulates its receptor gene expression in highly metastatic human pancreatic carcinoma cells. *Cytokine* **60**, 514–521 (2012).
23. D. Shao, F. Perros, G. Caramori, C. Meng, P. Dormuller, P.-C. Chou, C. Church, A. Papi, P. Casolari, D. Welsh, A. Peacock, M. Humbert, I. M. Adcock, S. J. Wort, Nuclear IL-33 regulates soluble ST2 receptor and IL-6 expression in primary human arterial endothelial cells and is decreased in idiopathic pulmonary arterial hypertension. *Biochem. Biophys. Res. Commun.* **451**, 8–14 (2014).
24. M. Canel, A. Byron, A. H. Sims, J. Cartier, H. Patel, M. C. Frame, V. G. Brunton, B. Serrels, A. Serrels, Nuclear FAK and Runx1 cooperate to regulate IGFBP3, cell-cycle progression and tumor growth. *Cancer Res.* **77**, 5301–5312 (2017).
25. C. Schiering, T. Krausgruber, A. Chomka, A. Fröhlich, K. Adelmann, E. A. Wohlfert, J. Pott, T. Griseri, J. Bollrath, A. N. Hegazy, O. J. Harrison, B. M. J. Owens, M. Löhning, Y. Belkaid, P. G. Fallon, F. Powrie, The alarmin IL-33 promotes regulatory T-cell function in the intestine. *Nature* **513**, 564–568 (2014).
26. L. Roussel, M. Erard, C. Cayrol, J.-P. Girard, Molecular mimicry between IL-33 and KSHV for attachment to chromatin through the H2A-H2B acidic pocket. *EMBO Rep.* **9**, 1006–1012 (2008).
27. K. J. Roux, D. I. Kim, M. Raida, B. Burke, A promiscuous biotin ligase fusion protein identifies proximal and interacting proteins in mammalian cells. *J. Cell Biol.* **196**, 801–810 (2012).
28. J.-H. Lee, J. You, E. Dobrota, D. G. Skalnik, Identification and characterization of a novel human PP1 phosphatase complex. *J. Biol. Chem.* **285**, 24466–24476 (2010).
29. J.-H. Lee, D. G. Skalnik, Wdr82 is a C-terminal domain-binding protein that recruits the Setd1A Histone H3-Lys4 methyltransferase complex to transcription start sites of transcribed human genes. *Mol. Cell. Biol.* **28**, 609–618 (2008).
30. J. Shi, W. A. Whyte, C. J. Zepeda-Mendoza, J. P. Milazzo, C. Shen, J.-S. Roe, J. L. Minder, F. Mercan, E. Wang, M. A. Eckersley-Maslin, A. E. Campbell, S. Kawaoka, S. Shareef, Z. Zhu, J. Kendall, M. Muhar, C. Haslinger, M. Yu, R. G. Roeder, M. H. Wigler, G. A. Blobel, J. Zuber, D. L. Spector, R. A. Young, C. R. Vakoc, Role of SWI/SNF in acute leukemia maintenance and enhancer-mediated *Myc* regulation. *Genes Dev.* **27**, 2648–2662 (2013).
31. S. Mujtaba, L. Zeng, M.-M. Zhou, Structure and acetyl-lysine recognition of the bromodomain. *Oncogene* **26**, 5521–5527 (2007).
32. B. Huang, X.-D. Yang, M.-M. Zhou, K. Ozato, L.-F. Chen, Brd4 coactivates transcriptional activation of NF-κB via specific binding to acetylated RelA. *Mol. Cell. Biol.* **29**, 1375–1387 (2009).
33. B. P. Ashburner, S. D. Westerheide, A. S. Baldwin Jr., The p65 (RelA) subunit of NF-κB interacts with the histone deacetylase (HDAC) corepressors HDAC1 and HDAC2 to negatively regulate gene expression. *Mol. Cell. Biol.* **21**, 7065–7077 (2001).
34. S.-T. Lim, X. L. Chen, Y. Lim, D. A. Hanson, T.-T. Vo, K. Howerton, N. Larocque, S. J. Fisher, D. D. Schlaepfer, D. Ilic, Nuclear FAK promotes cell proliferation and survival through FERM-enhanced p53 degradation. *Mol. Cell* **29**, 9–22 (2008).

35. E. Lefrancais, C. Cayrol, Mechanisms of IL-33 processing and secretion: Differences and similarities between IL-1 family members. *Eur. Cytokine Netw.* **23**, 120–127 (2012).
36. M. Wu, P. F. Wang, J. S. Lee, S. Martin-Brown, L. Florens, M. Washburn, A. Shilatifard, Molecular regulation of H3K4 trimethylation by Wdr82, a component of human Set1/COMPASS. *Mol. Cell. Biol.* **28**, 7337–7344 (2008).
37. Z. Zou, B. Huang, X. Wu, H. Zhang, J. Qi, J. Bradner, S. Nair, L.-F. Chen, Brd4 maintains constitutively active NF-κB in cancer cells by binding to acetylated RelA. *Oncogene* **33**, 2395–2404 (2014).
38. B. Turriziani, A. Garcia-Munoz, R. Pilkington, C. Raso, W. Kolch, A. von Kriegsheim, On-beads digestion in conjunction with data-dependent mass spectrometry: A shortcut to quantitative and dynamic interaction proteomics. *Biology (Basel)* **3**, 320–332 (2014).
39. J. A. Vizcaíno, A. Csordas, N. Del-Toro, J. A. Dianes, J. Griss, I. Lavidas, G. Mayer, Y. Perez-Riverol, F. Reisinger, T. Ternent, Q.-W. Xu, R. Wang, H. Hermjakob, 2016 update of the PRIDE database and its related tools. *Nucleic Acids Res.* **44**, 11033 (2016).
40. D. W. Huang, B. T. Sherman, R. A. Lempicki, Bioinformatics enrichment tools: Paths toward the comprehensive functional analysis of large gene lists. *Nucleic Acids Res.* **37**, 1–13 (2009).
41. P. Shannon, A. Markiel, O. Ozier, N. S. Baliga, J. T. Wang, D. Ramage, N. Amin, B. Schwikowski, T. Ideker, Cytoscape: A software environment for integrated models of biomolecular interaction networks. *Genome Res.* **13**, 2498–2504 (2003).
42. M. J. L. de Hoon, S. Imoto, J. Nolan, S. Miyano, Open source clustering software. *Bioinformatics* **20**, 1453–1454 (2004).
43. A. J. Saldanha, Java Treeview—Extensible visualization of microarray data. *Bioinformatics* **20**, 3246–3248 (2004).
44. A. I. Saeed, V. Sharov, J. White, J. Li, W. Liang, N. Bhagabati, J. Braisted, M. Klapa, T. Currier, M. Thiagarajan, A. Sturn, M. Snuffin, A. Rezantsev, D. Popov, A. Ryltsov, E. Kostukovich, I. Borisovsky, Z. Liu, A. Vinsavich, V. Trush, J. Quackenbush, TM4: A free, open-source system for microarray data management and analysis. *Biotechniques* **34**, 374–378 (2003).

**Acknowledgments:** We would like to thank the FACS facility at the Medical Research Council Centre for Inflammation Research, University of Edinburgh for their help with FACS analysis and the Central Biological Services animal technicians at Little France 2, University of Edinburgh for their assistance with biological work. **Funding:** This work was supported by Cancer Research UK (grant no. C157/A15703 to M.C.F.) and the European Research Council (grant no. 299440 Cancer Innovation to M.C.F.). A.V.K. is supported by a Cancer Research UK Edinburgh Centre grant. N.Q. is supported by the Wellcome Trust–University of Edinburgh ISSF2 programme. D.T. is supported by Cancer Research UK (grant no. C54352/A22011 awarded to S.M.A.). **Author contributions:** B.S., A.S., and M.C.F. devised and oversaw the project. B.S., A.S., N.M., A.B., S.M.A., and M.C.F. designed the experiments with contributions from M.C. and H.J.M. B.S., A.S., N.M., M.C., A.B., S.C.J., N.Q., and D.T. performed the experiments with contributions from A.V.K. B.S., A.S., N.M., M.C., A.B., N.Q., and S.C.J., analyzed the data. B.S. and A.B. performed the bioinformatics analysis. B.S., A.S., and M.C.F. wrote the manuscript with contributions from A.B. and N.M. All authors commented on and approved the final version. **Competing interests:** The authors declare that they have no competing interests. **Data and materials availability:** The MS proteomics data have been deposited to the ProteomeXchange Consortium via the PRIDE partner repository (data set identifier PXD007698).

Submitted 25 May 2017
Accepted 8 November 2017
Published 5 December 2017
10.1126/scisignal.aan8355

**Citation:** B. Serrels, N. McGivern, M. Canel, A. Byron, S. C. Johnson, H. J. McSorley, N. Quinn, D. Taggart, A. Von Kreigsheim, S. M. Anderton, A. Serrels, M. C. Frame, IL-33 and ST2 mediate FAK-dependent antitumor immune evasion through transcriptional networks. *Sci. Signal.* **10**, eaan8355 (2017).

# **Robotics** for Science, Science for **Robotics**

*Transforming the Future of Robotics in Research !*

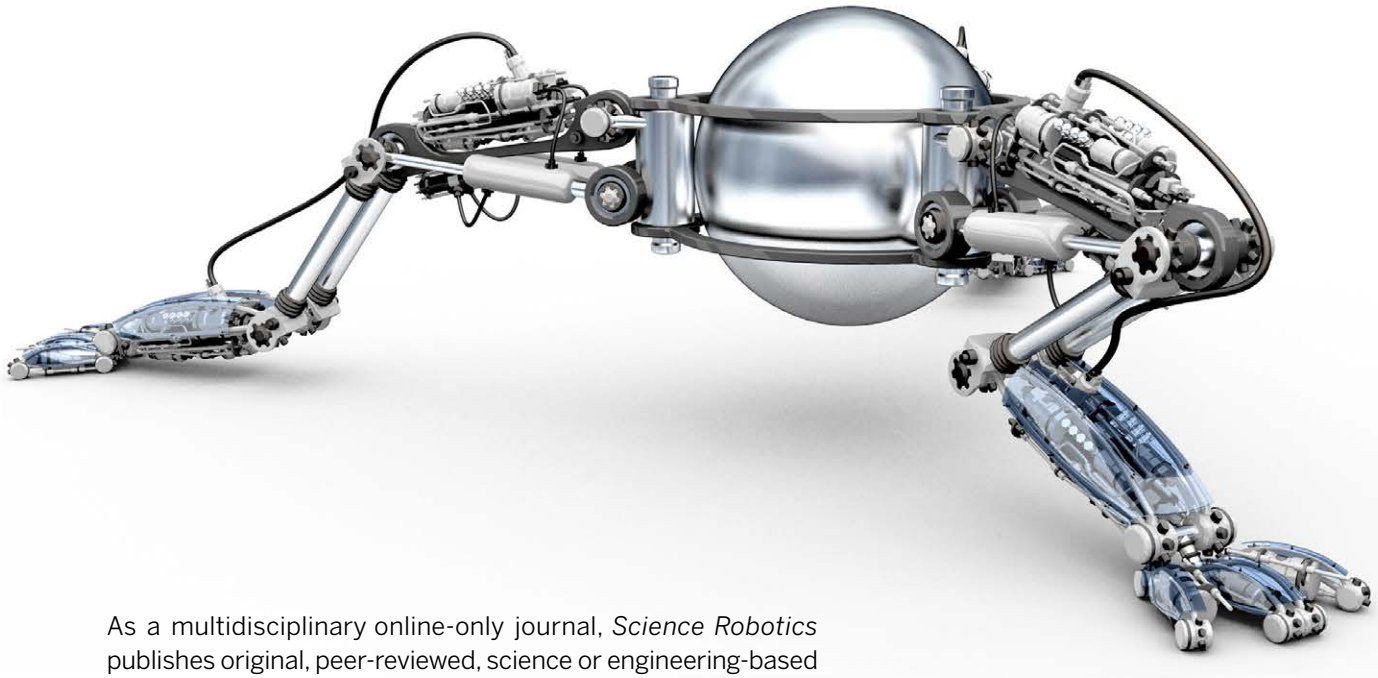

As a multidisciplinary online-only journal, *Science Robotics* publishes original, peer-reviewed, science or engineering-based research articles that advance the field of robotics. The journal provides a central forum for communication of new ideas, general principles, and original developments in research and field applications of robotics for all environments.

Science Robotics
AAAS

ScienceRobotics.org

ALLERGY

# A phenotypically and functionally distinct human $T_H2$ cell subpopulation is associated with allergic disorders

Erik Wambre,[1]* Veronique Bajzik,[1] Jonathan H. DeLong,[1] Kimberly O'Brien,[1] Quynh-Anh Nguyen,[1] Cate Speake,[1] Vivian H. Gersuk,[1] Hannah A. DeBerg,[1] Elizabeth Whalen,[1] Chester Ni,[1] Mary Farrington,[2] David Jeong,[2] David Robinson,[2] Peter S. Linsley,[1] Brian P. Vickery,[3] William W. Kwok[1,4]



**Allergen-specific type 2 helper T ($T_H2$) cells play a central role in initiating and orchestrating the allergic and asthmatic inflammatory response pathways. One major factor limiting the use of such atopic disease–causing T cells as both therapeutic targets and clinically useful biomarkers is the lack of an accepted methodology to identify and differentiate these cells from overall nonpathogenic $T_H2$ cell types. We have described a subset of human memory $T_H2$ cells confined to atopic individuals that includes all allergen-specific $T_H2$ cells. These cells are terminally differentiated $CD4^+$ T cells ($CD27^-$ and $CD45RB^-$) characterized by coexpression of $CRT_H2$, CD49d, and CD161 and exhibit numerous functional attributes distinct from conventional $T_H2$ cells. Hence, we have denoted these cells with this stable allergic disease–related phenotype as the $T_H2A$ cell subset. Transcriptome analysis further revealed a distinct pathway in the initiation of pathogenic responses to allergen, and elimination of these cells is indicative of clinical responses induced by immunotherapy. Together, these findings identify a human $T_H2$ cell signature in allergic diseases that could be used for response-monitoring and designing appropriate immunomodulatory strategies.**

## INTRODUCTION

As part of their specialization, $CD4^+$ effector T cells acquire functional and phenotypic characteristics to specifically respond against pathogens. Within different T helper ($T_H$) cell subsets, the $T_H2$ cell subset is characterized by the production of interleukin-4 (IL-4), IL-5, IL-9, and IL-13 cytokines, which promote both immunoglobulin E (IgE)– and eosinophil-mediated immune responses (*1*). Although $T_H2$ cells were initially considered to be a homogeneous subset, their functional heterogeneity is now appreciated, as is the fact that additional $T_H2$ subpopulations may determine $T_H2$-driven pathology (*2*–*4*). For example, a recent study revealed a subpopulation of human memory $T_H2$ cells that produces IL-17 along with cardinal $T_H2$ cytokines (*5*). Remarkably, the proportion of these circulating $T_H17/T_H2$ cells was extremely low in nonatopic individuals compared to patients with chronic severe asthma, suggesting a possible role in the pathogenesis and severity of the disease. Another source of heterogeneity among $CD4^+$ T cell subsets is at the level of T cell surface marker expression that determines their differentiation states, effector functions, and migratory capacity. With respect to the $T_H2$ cell subset, our group recently demonstrated that pathogenic allergen-specific T cells are highly matured effector $T_H2$ cells characterized by the lack of expression of CD27, a tumor necrosis factor receptor superfamily member of costimulatory molecules (*6*, *7*). Similarly, distinct subpopulations of $T_H2$ cells with enhanced function have been described in a murine model of allergic inflammation based on differential expression of CXCR3 and CD62L (*8*) or CCR8 (*9*) and in human allergic eosinophilic inflammatory diseases, according to the expression of the hematopoietic prostaglandin D synthase (hPGDS) (*10*) or IL-17RB (*11*). In these studies, the authors suggested that heterogeneity within $T_H2$-mediated immune responses plays differential roles in immunopathology. Hence, we surmise that allergic individuals have specific subpopulations of $T_H2$ cells associated with global atopic inflammatory disorders.

Until now, there has been no biological measurement to accurately reflect and quantify an underlying allergic disease process and ideally provide accurate surrogate end points to assess immunotherapy efficacy. A major impediment to the use of allergic disease–causing T cells as a therapeutic target and clinically useful biomarker is the lack of an accepted method to both identify these cells and differentiate them from the overall $T_H2$ cell types. Recent progress in peptide–major histocompatibility complex (MHC) class II (pMHCII) tetramer staining has allowed direct ex vivo visualization of allergen-specific $CD4^+$ T cells and enabled quantification and characterization of these cells in a setting closer to their natural physiological state (*7*, *12*). Description of a set of T cell surface markers that are differentially expressed in allergen-specific $T_H2$ cells as compared to classical $T_H2$ cells would allow this issue to be addressed.

Here, we describe an allergic T cell signature characterized by the coexpression of the chemoattractant receptor $CRT_H2$, the natural killer cell marker CD161, and the homing receptor CD49d in human terminally differentiated ($CD45RB^{low}$ $CD27^-$) $CD4^+$ T cells. The vast majority of allergen-specific T cells in allergic individuals with either food, pollen, pet's dander, mold, or house dust mite allergy fall into this subset and were preferentially deleted during allergen-specific immunotherapy (AIT). Hence, we have denoted this proallergic subpopulation of $T_H2$ cells, confined to atopic individuals, as the $T_H2A$ cell subset. Transcript analysis further highlights key functional differences between $T_H2A$ cells and conventional $T_H2$ cells, providing molecular signatures that suggest specific contribution of the $T_H2A$ cell subset to allergic disease. Together, these findings identify a pathogenic $T_H2$ cell signature unique to allergic individuals that could potentially be used as a clinically relevant biomarker and therapeutic target in atopic disorders.

## RESULTS

### Allergic disease–related phenotypic differences exist in the $T_H2$ cell subset

For many years, chemokine receptors and surface markers have been instrumental in the characterization of memory T cell subsets

[1]Benaroya Research Institute at Virginia Mason, Seattle, WA 98101, USA. [2]Virginia Mason Medical Center, Seattle, WA 98101, USA. [3]Aimmune Therapeutics, Brisbane, CA 94005, USA. [4]Department of Immunology, University of Washington, Seattle, WA 98195, USA.
*Corresponding author. Email: ewambre@benaroyaresearch.org

with distinct migratory capacity and effector functions. To determine whether a set of T cell surface markers can be differentially expressed in allergen-specific $T_H2$ cells, we undertook a detailed ex vivo phenotypic profiling of total $CD4^+$ T cells, conventional $T_H2$ cells, and allergen-specific $CD4^+$ T cells. Using alder pollen allergy as a model, freshly isolated peripheral blood mononuclear cells (PBMCs) from DR07:01- or DR15:01-restricted allergic individuals were stained with fluorescently labeled pMHCII tetramers, followed by magnetic column enrichment process to directly examine allergen-specific $CD4^+$ T cell phenotypic profiles. Among $T_H2$-associated surface markers, $CRT_H2$, the prostaglandin D2 receptor chemoattractant receptor–homologous molecule expressed on $T_H2$ cells, is reported as the most reliable marker to identify human $T_H2$ cells (*13*). As a control, we examined the ex vivo phenotypic profile of total $CRT_H2^+$ $CD4^+$ memory T cells to compare with the ex vivo enriched allergen-specific $CD4^+$ T cells. During these flow cytometric screen analyses, fluorochrome-conjugated antibodies directed against cell surface marker antigens were selected to elucidate the differentiation, maturation, activation, and homing properties of each group (fig. S1 and table S1). Variation in surface marker expression between groups is shown in fig. S2 (A and B). As expected, ex vivo enriched allergen-specific $CD4^+$ T cells from allergic individuals share numerous memory $T_H2$ cell features with the conventional $T_H2$ cell group featuring the expression of CD45RO, CCR4, CD200R, CD58, CD29, and $CRT_H2$. However, we identified an allergic T cell signature that includes two up-regulated (CD161 and CD49d) and four down-regulated (CD27, CD45RB, CCR7, and CD7) T cell surface markers with significant differential expression (greater than 20% change; $P < 0.001$) between groups (Fig. 1A). The $CD27^{low}$, $CCR7^{low}$, $CD7^{low}$, and $CD45RB^{low}$ phenotypes, which are associated with terminally differentiated memory $CD4^+$ T cells, likely reflect recurrent natural allergen exposure (*14*, *15*). This is consistent with previous findings by our group demonstrating a strong relationship between pathogenicity of allergen-specific $CD4^+$ T cells and the maturation stage of the cells (*7*, *16*). Although loss of CD27 expression within $CD4^+$ memory T cells is consistently associated with cells lacking CCR7 and CD7, we observed that $CD27^{low}$ $CD4^+$ T cell subset can be subdivided into two groups by CD45RB expression (fig. S3). Thus, to define a smaller set of surface markers, we chose CD27 and CD45RB as convenient down-regulated markers reflecting allergic features.

Another striking finding from this T cell profiling was the overexpression of the C-type lectin-like receptor CD161 (4.2-fold difference, $P < 0.001$) as part of the signature characterizing allergen-specific $T_H2$ cells. Expression of CD161 on $CD4^+$ T cells is typically associated with $T_H17$ responses (*17*, *18*), and like the conventional $T_H2$ cell subset ($CRT_H2^+$ $CD4^+$), allergen-specific $T_H2$ cells do not express the $T_H17$-associated chemokine receptor CCR6 (Fig. 1B). We next performed quantitative polymerase chain reaction (PCR) analysis on sorted cells from allergic donors and confirmed the higher expression of *CD161* mRNA in $CRT_H2$-expressing allergen-specific T cells compared to conventional $T_H2$ cells (Fig. 1C). However, although allergen-specific $T_H2$ cells express similar levels of *CD161* as the $T_H17$ cell subset ($CCR6^+$ $CXCR3^-$ $CD4^+$), these cells did not exhibit mRNA expression of $T_H17$ phenotypic markers such as *CCR6*, *IL23R*, and the transcription factor *RORC*. Together, these data indicate that allergic disease–related phenotypic differences (not related to a type 17 phenotype) occur in the $T_H2$ cell subset.

To demonstrate that our data were not restricted to tree pollen allergy, we next performed our ex vivo pMHCII tetramer approach to characterize allergen-specific $CD4^+$ T cells in patients with either food allergy (peanut), perennial allergy (cat and house dust mite), mold allergy (*Aspergillus* and *Alternaria*), or seasonal pollen allergy (alder and timothy grass). We also used nonallergic individuals as controls. Whatever the allergen tested in this study, IgE-mediated allergic diseases were characterized by high frequencies of allergen-specific $CRT_H2^+$ T cells, which were strictly absent in nonallergic subjects, suggesting that the presence of these $CD4^+$ effector T cells is necessary for allergy pathogenesis (Fig. 2A). In all allergic individuals tested, the vast majority of pMHCII tetramer–positive T cells were also characterized by the lack of CD27 expression along with expression of CD161 (Fig. 2B). Remarkably, $CRT_H2^+$ expression on

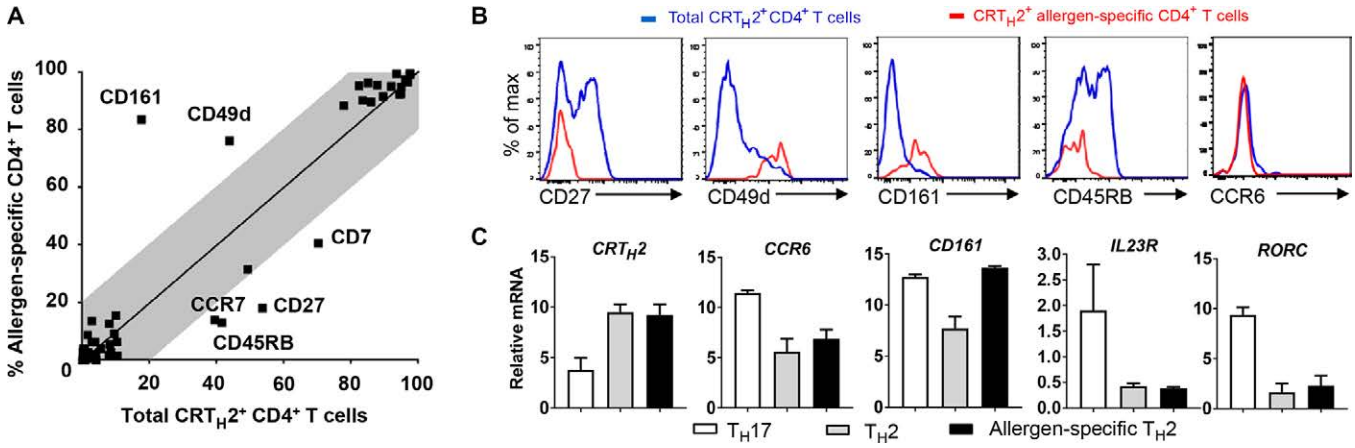


**Fig. 1. Allergic disease–related phenotypic differences emerged in the $T_H2$ cell subset.** (**A**) Fluorescence-activated cell sorting (FACS)–based T cell surface expression screening revealed up-regulated and down-regulated T cell surface markers in ex vivo magnetically enriched allergen-specific $CD4^+$ T cells compared to total $CRT_H2^+$ $CD4^+$ T cells. Average expression levels for each T cell surface marker in the allergen-specific $CD4^+$ T cell group and in total $CRT_H2^+$ $CD4^+$ T cell group are plotted against each other. Data are means from four allergic subjects per group. The gray field depicted less than 20% expression variation between groups. Differences between groups were analyzed using the Mann-Whitney *U* test. (**B**) Examples of intensity distributions of total $CRT_H2^+$ $CD4^+$ T cells (blue) and ex vivo magnetically enriched $CRT_H2^+$ allergen-specific $CD4^+$ T cells tracked by pMHCII tetramer (red) stained with candidate cell surface markers. Data are representative of at least three allergic donors. (**C**) Real-time PCR analysis confirms that allergen-specific $T_H2$ cells express *CD161* but are not related to a type 17 phenotype. Data are means ± SEM from at least three subjects per group.

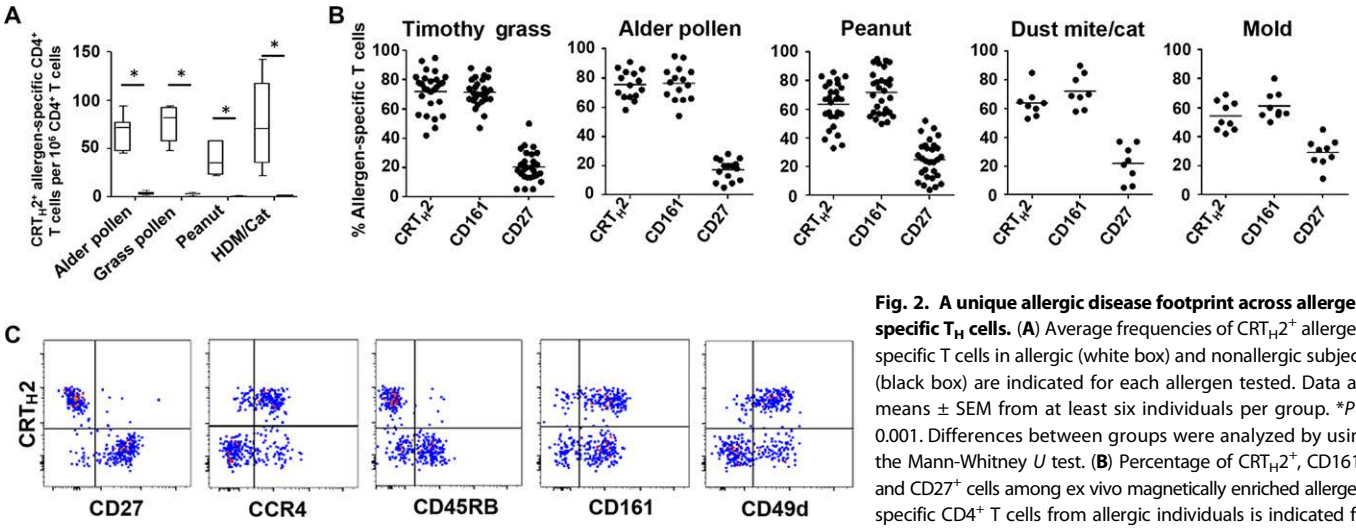


**Fig. 2. A unique allergic disease footprint across allergen-specific $T_H$ cells.** (**A**) Average frequencies of $CRT_H2^+$ allergen-specific T cells in allergic (white box) and nonallergic subjects (black box) are indicated for each allergen tested. Data are means ± SEM from at least six individuals per group. *$P$ < 0.001. Differences between groups were analyzed by using the Mann-Whitney $U$ test. (**B**) Percentage of $CRT_H2^+$, $CD161^+$, and $CD27^+$ cells among ex vivo magnetically enriched allergen-specific $CD4^+$ T cells from allergic individuals is indicated for each allergen tested. Each dot represents a single donor. (**C**) Plots show representative ex vivo profile of alder pollen–specific $CD4^+$ T cells in alder-allergic patient according to CD27, CCR4, CD45RB, CD161, CD49d, and $CRT_H2$ expression. Data are representative of at least three donors.

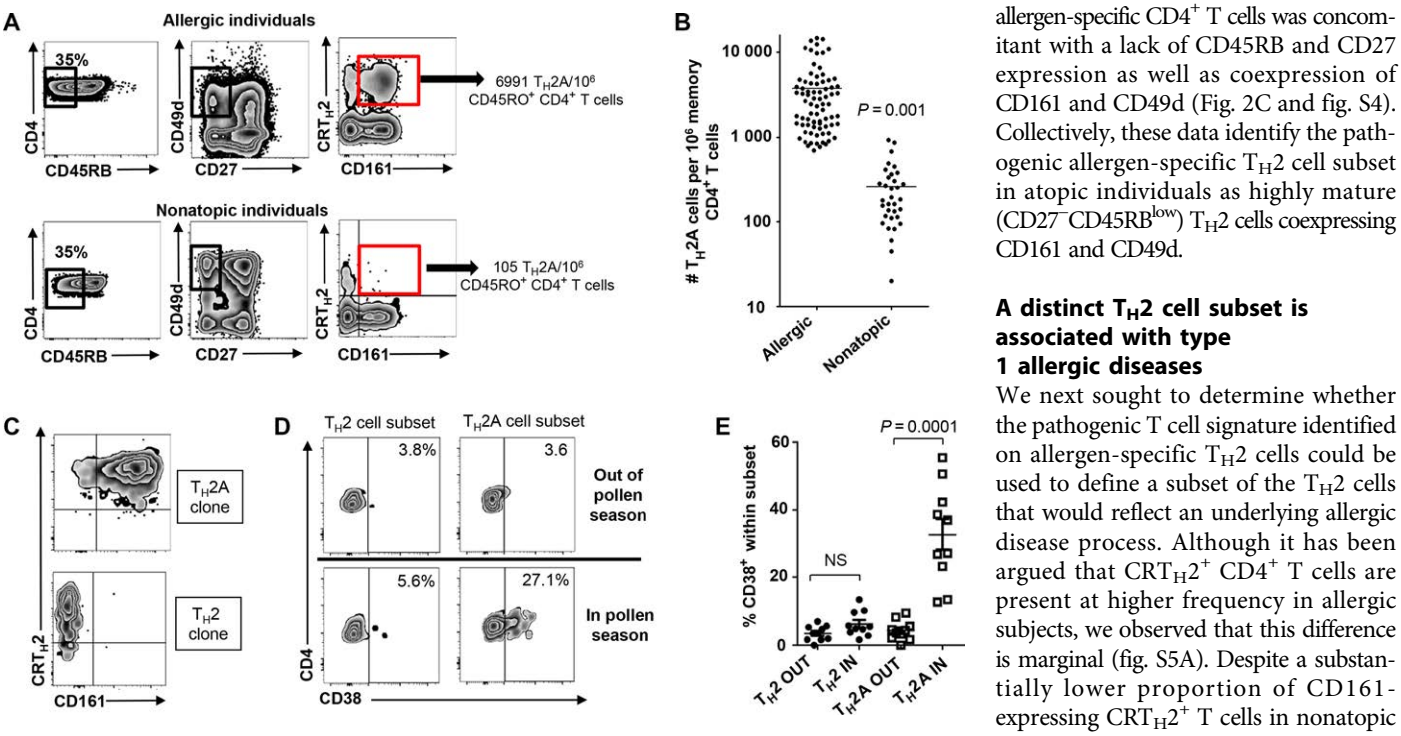


**Fig. 3. A distinct subset of $T_H2$ cells include pathogenic allergen-specific $CD4^+$ T cells.** (**A**) Gating strategy for defining proallergic $T_H2$ cells ($T_H2A$ cells). PBMCs were first gated according to their size, expression of CD4 and CD45RO, and after the exclusion of dead cells. Gates then identify $CD45RB^{low}$ cells among live memory ($CD45RO^+$) $CD4^+$ T cells, $CD27^-CD49d^+$ cell subset, and then $CRT_H2^+CD161^+$ T cell subset. Representative staining in allergic individual and nonatopic subject is shown. (**B**) Frequency of $CD45RB^{low}CD27^-CRT_H2^+CD161^+CD49d^+$ $CD4^+$ T cells ($T_H2A$) between allergic subjects ($n$ = 80) and nonatopic individuals ($n$ = 34). Each dot represents a single donor, and differences between groups were analyzed by using the Mann-Whitney $U$ test. (**C**) $T_H2$ and $T_H2A$ phenotype observed over a culture time of 6 weeks with subsequent T cell receptor (TCR) stimulations. (**D** and **E**) Percentage of $T_H2A$ and $T_H2$ cells expressing CD38 in and out grass pollen season in grass-allergic individuals. Data are representative of at least three donors (A, C, and D). Differences between groups were analyzed by using the Wilcoxon matched pairs test. NS, not significant.

allergen-specific $CD4^+$ T cells was concomitant with a lack of CD45RB and CD27 expression as well as coexpression of CD161 and CD49d (Fig. 2C and fig. S4). Collectively, these data identify the pathogenic allergen-specific $T_H2$ cell subset in atopic individuals as highly mature ($CD27^-CD45RB^{low}$) $T_H2$ cells coexpressing CD161 and CD49d.

## A distinct $T_H2$ cell subset is associated with type 1 allergic diseases

We next sought to determine whether the pathogenic T cell signature identified on allergen-specific $T_H2$ cells could be used to define a subset of the $T_H2$ cells that would reflect an underlying allergic disease process. Although it has been argued that $CRT_H2^+$ $CD4^+$ T cells are present at higher frequency in allergic subjects, we observed that this difference is marginal (fig. S5A). Despite a substantially lower proportion of CD161-expressing $CRT_H2^+$ T cells in nonatopic individuals, this subset was not restricted to allergic subjects. However, we observed that at least two markers (that is, CD161 and CR45RB or CD27) were needed to subset the $CRT_H2^+$ $CD4^+$ T cells to identify an allergy-prone $T_H2$ subset virtually absent in the nonatopic group, which includes the vast majority of allergen-specific T cells from allergic individuals (fig. S5, B and C). Using the gating strategy depicted in Fig. 3A, we

observed that all allergic individuals tested exhibited a significantly higher number ($n = 80$; mean ± SEM, 3766 ± 413 cells per $10^6$ memory $CD4^+$ T cells) of $CD45^{low}CD49d^+CD27^-$ $CRT_H2^+CD161^+$ cells relative to nonatopic individuals ($n = 34$; mean ± SEM, 259 ± 37 cells per $10^6$ memory $CD4^+$ T cells; $P < 0.0001$) (Fig. 3, A and B). Hence, we have named these proallergic $T_H2$ cells (which are unique to allergic individuals) the $T_H2A$ cell subset.

Remarkably, both conventional $T_H2$ and $T_H2A$ cell subsets retain their respective phenotype after long-term clonal expansion, suggesting that they did not differ in activation or maturation status and can thus be used as a stable and relevant surrogate marker (Fig. 3C). To confirm that the $T_H2A$ cell subset is specifically involved in type I allergic diseases, we next followed 10 grass pollen–allergic individuals before and during the grass pollen season (May to August), a window of time that correlates with increased allergy symptoms and with up-regulation of the activation marker CD38 within grass pollen–reactive $CD4^+$ T cells (*7*, *16*). Consistent with direct access to allergy-prone $T_H2$ cells according to $CRT_H2$, CD27, CD45RB, CD49d, and CD161 differential expression, we observed that CD38 expression was specifically up-regulated within the $T_H2A$ subset during grass pollen season but not within the conventional $T_H2$ cell subset or outside pollen season (Fig. 3, D and E). Collectively, our data demonstrate that the $T_H2A$ cell subset represents a phenotypically distinct $T_H2$ subpopulation, which may encompass the vast majority of pathogenic $T_H2$ cells involved in type I allergic diseases.

### The $T_H2A$ cell subset represents a suitable therapeutic target

To determine whether the $T_H2A$ cell subset constitutes a clinically relevant therapeutic target in the allergy context, we next performed a longitudinal study in a subset of peanut-allergic patients completing characterized oral desensitization immunotherapy (CODIT) with AR101, an experimental orally administered biological drug containing the antigenic profile found in peanuts. During this randomized, double-blinded, placebo-controlled trial (ARC001), coded samples from subjects were provided to the operator at baseline both before and after double-blind, placebo-controlled food challenges (DBPCFC) with peanut flour, as well as at the end of the maintenance visit before DBPCFC. The magnitude and quality of peanut-specific T cell responses were determined ex vivo using the CD154 up-regulation assay (*19*) after short restimulation of PBMCs with a pool of peanut peptides library derived from Ara h 1, Ara h 2, Ara h 3, Ara h 6, and Ara h 8 peanut-allergic components. As expected, the vast majority of peanut-reactive $CD4^+$ T cells were bona fide $T_H2A$ cells at baseline, and the DBPCFC protocol led to significant increased expression of the cell surface activation marker CD38 (Fig. 4A and fig. S6A), concomitant with an increased average frequency of these cells (Fig. 4B). Accordingly, only $T_H2A$ cells, and not conventional $T_H2$ cells, were specifically activated after peanut oral food challenge (OFC) (fig. S6B).

As reported elsewhere (*20*), 100 and 78% of patients who completed the active treatment regimen ($n = 23$) tolerated a cumulative amount of peanut protein of 443 and 1043 mg, respectively, compared to 19 and 0% in the placebo group ($n = 26$). In such a setting, we observed a direct correlation between decrease in peanut-specific $T_H2A$ cell frequency and achievement of peanut desensitization in the active group compare to placebo (Fig. 4, C and D, and fig. S6C). Together, our data demonstrate that $T_H2A$ cells play a critical role in allergic disease pathogenesis and reinforce previous data by our group that the allergen-specific $T_H2$ cell subset may represent a suitable therapeutic target and surrogate marker of clinical efficacy during AIT (*7*, *16*, *21*).

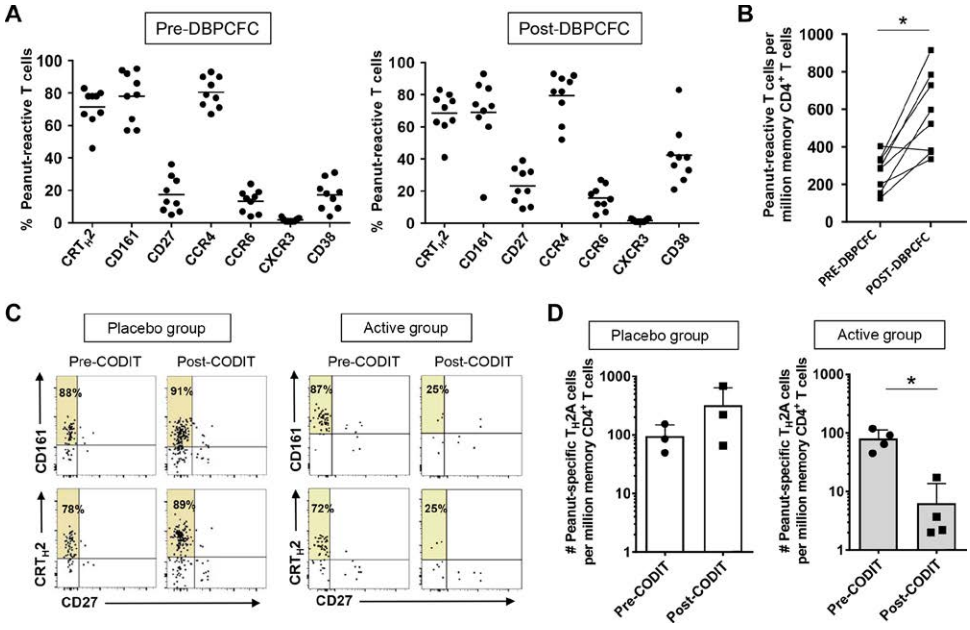


**Fig. 4. Peanut-specific $T_H2A$ cells are specifically targeted during immunotherapy.** (**A**) Ex vivo phenotype of peanut-reactive $CD4^+$ T cells before and after DBPCFC with peanut flour. Each dot represents a single donor. (**B**) Ex vivo frequency of peanut-reactive $CD4^+$ T cells before and after DBPCFC. (**C**) Plots show representative ex vivo profile of peanut-reactive $CD4^+$ T cells according to CD27, CD161, and $CRT_H2$ expression before and after CODIT both in placebo and active groups. Data are representative of at least three donors per group. Percentages of $CD27^-$ allergen-specific T cells expressing the given marker are indicated in the upper left quadrant. (**D**) Ex vivo peanut-specific $T_H2A$ cell frequencies before and after CODIT both in placebo ($n = 3$) and active ($n = 4$) groups. Differences between groups were analyzed by using the Wilcoxon matched pairs test (A and B) and unpaired *t* test (D). *$P < 0.05$.

### $T_H2A$ cells differentially contribute to $T_H2$-driven pathology

To determine whether allergic disease–related functional differences could be identified in the $T_H2A$ cell subset, freshly isolated $T_H2A$, $T_H2$ ($CD161^-CRT_H2^+CD27^-$), and $T_H1/T_H17$ ($CD161^+CRT_H2^-CD27^-$) cell subsets from allergic individuals were subjected to polychromatic intracellular cytokine profile analysis. After polyclonal activation with phorbol 12-myristate 13-acetate (PMA)/ionomycin, a significantly higher proportion of $T_H2A$ cells expressed IL-5 and IL-9 compared to conventional $T_H2$ cells (Fig. 5A). Conversely, interferon-γ (IFN-γ) and IL-17, the respective cytokines for $T_H1$ and $T_H17$ cell subsets, were restricted to the $CD161^+CRT_H2^-CD27^+$ $T_H$ cell population. The $T_H2A$ cell subset was also more polyfunctional, with a significantly greater proportion of cells producing simultaneously multiple $T_H2$ effector cytokines compared to conventional $T_H2$ cells (Fig. 5, B and C). As a comparison, expression of cardinal $T_H2$ cytokine was also investigated within ex vivo enriched allergen-specific $CD4^+$ T cells in allergic

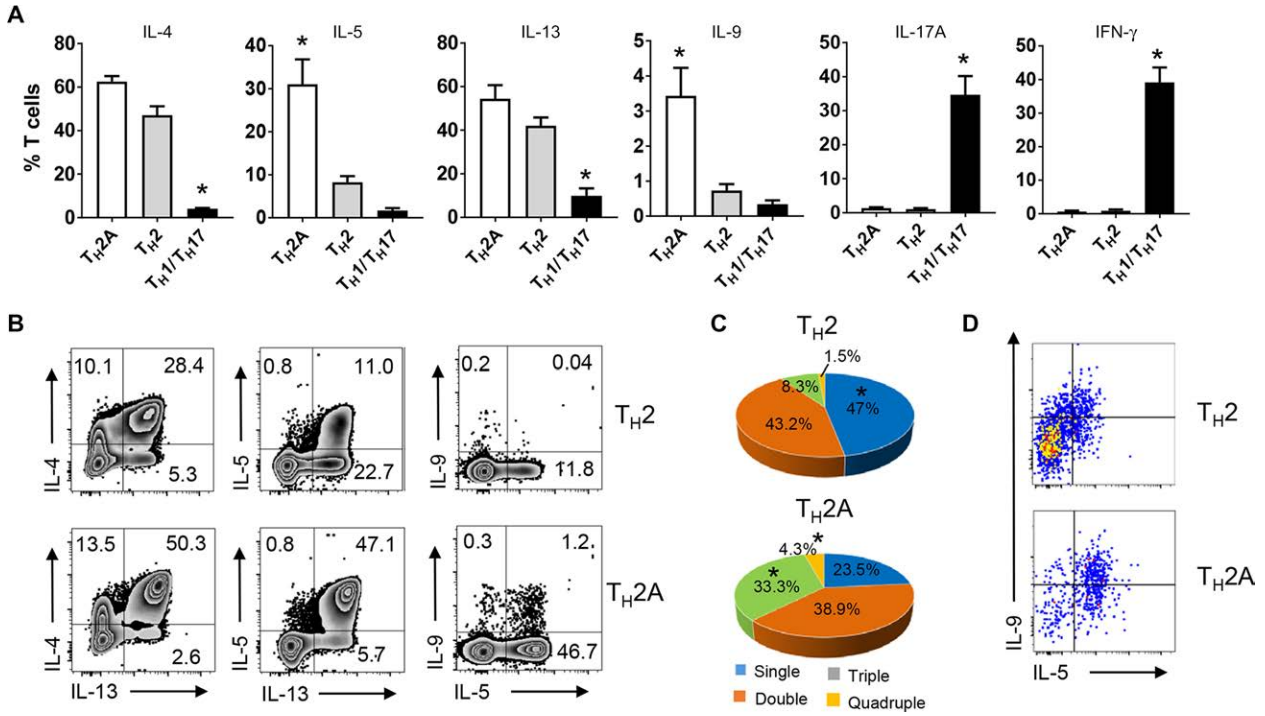


**Fig. 5. $T_H2A$ cell subset may differentially contribute to $T_H2$-driven pathology.** (**A**) Cytokine production by $T_H2A$ (white bar), conventional $T_H2$ (gray bar), and $T_H1/T_H17$ (black bar) cell subset. T effector cell subset from allergic individuals was sorted by FACS and stimulated for 5 hours with PMA/ionomycin in the presence of a protein transport inhibitor. Data are means ± SEM of four subjects per group. Differences between groups were analyzed by using the Mann-Whitney *U* test. *$P < 0.01$. (**B**) Plots show representative ex vivo intracellular cytokine staining for IL-4, IL-13, IL-5, and IL-9 in FACS-sorted $T_H2$ and $T_H2A$ subset. Numbers indicate relative percentages in each quadrant. (**C**) Pie charts show the proportion of cells producing simultaneously one, two, three, or four cardinal $T_H2$ cytokines (IL-4, IL-5, IL-9, and IL-13) after polyclonal activation. Data are mean percentage of cytokine-producing cells from four allergic donors. Comparisons between groups were performed using Kruskal-Wallis one-way analysis of variance (ANOVA) on ranks. *$P < 0.01$. (**D**) Plots show representative intracellular cytokine staining for IL-5 and IL-9 in $T_H2$ and $T_H2A$ cell clone from the same allergic individuals. Data are representative of at least three allergic donors (B and D).

individuals and found to be restricted to the $CD27^-CRTH2^+CD161^+$ allergen-specific $CD4^+$ T cell subset (fig. S7). Remarkably, the unique secretion pattern of $T_H2A$ cell lines was quite stable over time, even after multiple rounds of stimulations over sequential 6-week cultures (Fig. 5D). Thus, human circulating $T_H2A$ cells may contribute differently to $T_H2$-driven pathology than conventional $T_H2$ cells by simultaneously producing multiple cardinal $T_H2$ cytokines.

### Transcriptome analysis reveals unique pathway in $T_H2A$ cells

To further investigate the pathophysiologic meaning of the allergic T cell signature, we performed microarray analysis (Gene Expression Omnibus accession GSE93219) on freshly isolated $T_H2A$ cells compared to known T cell subsets (that is, $T_H1$, $T_H17$, and $T_H2$) from different donor pools, which contained blood from two to three donors. This was necessary to obtain sufficient numbers of cells for microarray experiments. From the data sets comparing $T_H2A$ with $T_H2$ cells, epithelium-derived cytokines receptors, such as the IL-25 receptor (*IL-17RB*), the IL-33 receptor (*IL1RL1*), and the thymic stromal lymphopoietin–receptor (*CLRF2*), which are well-known molecules involved in the allergic/asthmatic immune response (*22*–*24*), were more highly expressed in $T_H2A$ cells relative to conventional $T_H2$ cells (Fig. 6, A and B). In addition, we confirmed that $T_H2A$ cells produced more *IL-5* and *IL-9* relative to conventional $T_H2$ cells, whereas $T_H1$- and $T_H17$-related genes (*IFN-γ*, *IL-17*, *RORC*, *IL23-R*, and *CCL20*) were absent in $T_H2$ and $T_H2A$ cell subset (Fig. 6B). $T_H2A$ cells also highly expressed genes involved in arachidonic acid signaling that have previously been linked to allergic disease such as *hPGDS* (*10*), the prostaglandin synthase *PTGS2* (*25*, *26*), the short-chain free fatty acid receptor *GPR42* (*27*), and the peroxisome proliferator–activated receptor *PPARγ* (table S2) (*21*). Because of limitations of currently available anti-human ST2 and IL17RB reagents, we were unable to observe the differential expression of these two markers on the surface of peripheral $CD4^+$ T cells by using flow cytometry. Thus, we wished to determine whether up-regulation of *IL-17RB* and *IL1RL1* transcript identified in the $T_H2A$ cell subset was specifically observed on allergen-specific T cells from allergic individuals. To this aim, we performed a real-time PCR expression analysis on sorted pMHCII tetramer–positive T cells tracking peanut-specific $CD4^+$ T cells in peanut-allergic subjects and in nonatopic individuals. Sorted conventional $T_H2$ cells from the same allergic subjects were also used as control. As expected, we confirmed that gene transcripts, such as *CD161*, *IL1RL1*, and *IL17RB*, were expressed in allergen-specific $CD4^+$ T cells from allergic individuals but were absent both in conventional $T_H2$ cells and in allergen-specific T cells from nonallergic individuals (Fig. 6C). Although not causal, these data imply that pathological differences between $T_H2A$ and conventional $T_H2$ cells in allergic individuals are fundamental to disease development (fig. S8).

## DISCUSSION

Although antigen-specific $T_H2$ cells are at the core of the allergic process in atopic individuals, tracking and targeting these allergic

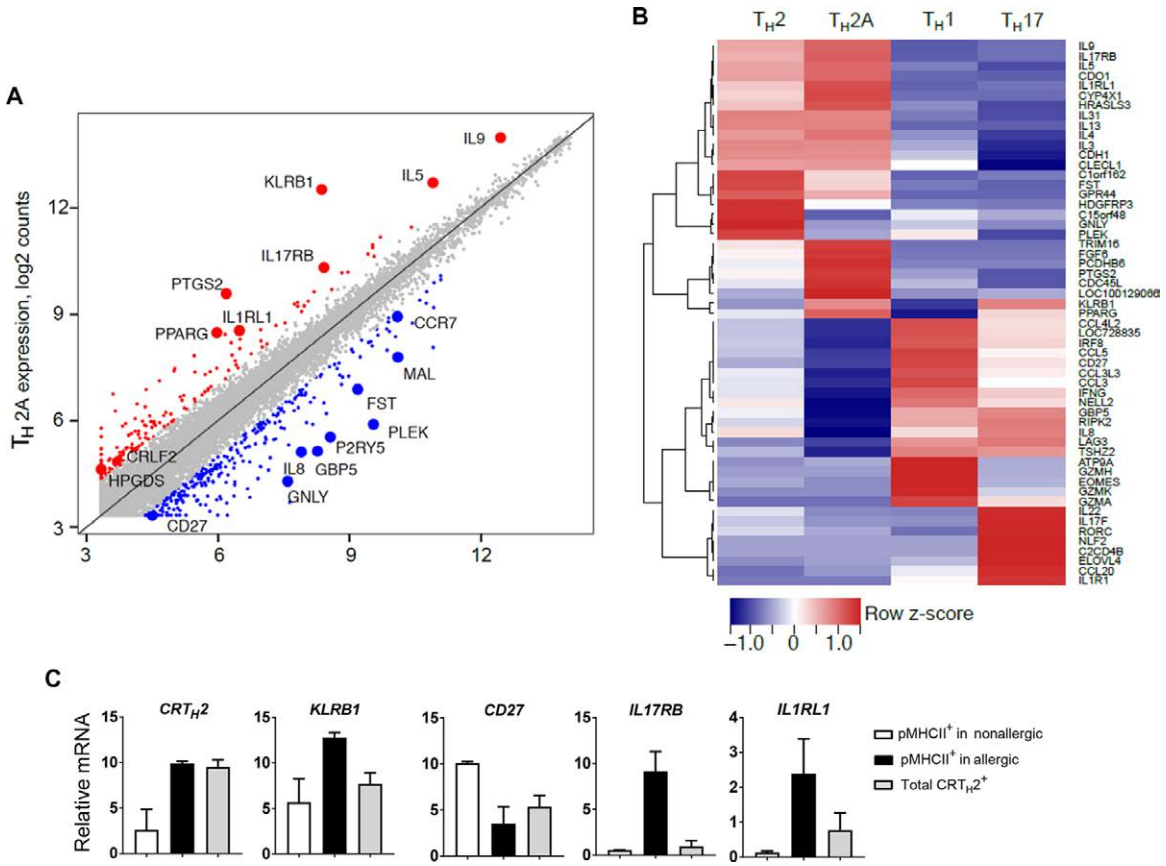


**Fig. 6. $T_H2A$ cell subset shows distinct gene expression patterns.** (**A**) Scatterplot of the average signal of $T_H2A$ versus conventional $T_H2$ cell gene expression microarray data. Shown are genes whose transcription has been up-regulated (red) or down-regulated (blue) by a factor of 2. Genes that have previously been linked to allergic diseases are listed. (**B**) Hierarchical clustering heat map of all genes with expression fold changes of eight in one cell subset relative to the other three subsets. Data are mean normalized raw gene expression values from two independent microarray experiments on cells sorted from different donor pools (each pool containing blood from two to three donors). (**C**) Real-time PCR analysis showing mRNA expression profile of the most relevant genes up-regulated in $T_H2A$ cell subset in total $CRT_H2^+$ T cells (gray) and in allergen-specific T cells from nonallergic individuals (white) or allergic subjects (black). Data are means ± SEM from at least three subjects per group.

disease–causing T cells without affecting other nonpathogenic $T_H2$ processes have been a challenge. Using an ex vivo pMHCII tetramer–based T cell profiling, we have shown that in all type 1 allergic individuals, the differential expression of at least three markers (that is, $CRT_H2$, CD161, and a differentiation stage marker such as CR45RB or CD27) is needed to define a pathogenic $T_H2$ cell subset that is allergen-specific and virtually absent in nonatopic individuals (denoted here as $T_H2A$ subset).

Multiples lines of evidence suggested the pathogenic potential of $T_H2A$ cell subset in settings of allergic inflammatory disease. First, we observed that allergen-specific $T_H2$ cells from allergic patients with either seasonal, perennial, fungus, or food allergy were virtually all contained in the terminally differentiated ($CD27^-$) memory $T_H$ cell subset that coexpresses $CRT_H2$ and CD161. Second, the overall number of cells from this subset was markedly higher in all allergic individuals as compared to nonatopic individuals. This particular proallergic $T_H$ cell subset is remarkable in that it can easily be detected directly ex vivo in every allergic individual due to its ability to include a broad array of allergen-specific $T_H2$ cells. Hence, our data demonstrate that during a natural allergen challenge, such as pollen season or a peanut challenge test, the $T_H2A$ cell subset was distinctively activated (*16*, *28*, *29*). Finally, our data highlight key functional and molecular differences between pathogenic and conventional $T_H2$ cells, recapitulating previous observation in their murine counterpart (*8*) and highlighting specific therapeutic targets.

CD161 expression has been described as a hallmark of human $T_H17$ cells (*17*, *18*). Therefore, its expression on a $T_H2$ cell subset that does not express CCR6, RORC, or IL-17 cytokine is of great interest. Given that lectin-like transcript 1, the CD161 ligand, is expressed on respiratory epithelial cells during respiratory virus infection (*30*), it likely indicates the specialized role of allergen-specific $T_H2$ cells and thus may be implicated in allergic pulmonary inflammation and asthma exacerbation. CD161 expression also provides gut-specific homing properties to T cells (*31*), and a higher proportion of $CD161^+$ circulating $CD4^+$ T cells have been previously described in allergic patients compared to nonatopic individuals (*10*, *32*). Expression of CD161 on $T_H2$ cells was also associated with IL-5–producing T effector cells associated with eosinophilic gastrointestinal disease (*3*). In support of these findings, our results show that IL-5 and IL-9 cytokines have some of the greatest fold changes of all up-regulated transcripts in the $T_H2A$ subpopulation compared with conventional $T_H2$ cells. Our functional analysis also confirmed that $T_H2A$ cells exhibited profoundly superior functional activity compared to conventional $T_H2$ cells, with individual cells capable of producing a larger amount of a broad spectrum of $T_H2$ cytokines upon TCR activation. Because each $T_H2$ cytokine has a well-defined and relatively

specific function, it is likely that $T_H2A$ cells have greater adverse activity relative to conventional $T_H2$ cells, which might reflect the wide array of clinical symptoms associated with allergic disorders (*10*, *33*–*35*).

Understanding why some individuals elicit a pathogenic $T_H2$ response to allergen might facilitate the development of improved vaccination strategies. It therefore raises the question of the origin of $T_H2A$ cells in atopic individuals. There is now growing evidence for a role of epithelium-derived cytokines in the differentiation of $T_H2$ cells and in the establishment of airway inflammation (*36*). IL-33 and IL-25 pathways have been also associated with the induction of both IL-9 and IL-5 production in human $T_H2$ cells that drive a cascade of downstream events (*37*–*40*). One possible mechanism to explain and integrate all these results into a cohesive schema is that upon allergen recognition, epithelial cells release cytokines that not only stimulate innate cell networks but may also act directly on $CD4^+$ T cells to confer memory $T_H2$ cell pathogenicity in atopic individuals, as recently suggested by Endo *et al.* (*39*). Whether local epithelial cytokines influence allergen-specific $T_H2$ cell response requires further study, but our finding that $T_H2A$ cells specifically express *IL-17RB* and *IL1RL1* supports the notion of a local checkpoint that restricts the optimal pathogenic $T_H2$ responses to sites of tissue distress (*10*, *41*). By establishing a clear link between the elimination of the allergen-specific $T_H2A$ cell subset in peanut-allergic patients and the clinical benefit induced by oral immunotherapy, our data reinforce previous reports by our group that the current immunotherapy approach, using crude preparation of intact allergens, restores a desensitization state in the allergic patients by means of preferential exhaustion/deletion of allergen-specific $T_H2$ cells (*7*, *16*, *42*). $T_H2A$ cell subset shares multiple functional features with $CCR8^+$ (*9*), $hPGDS^+$ (*10*), and $IL\text{-}17RB^+$ (*11*) pathogenic $T_H2$ cell subsets that have been recently described in chronic atopic dermatitis, eosinophilic gastrointestinal diseases, and eosinophilic chronic rhinosinusitis, respectively. Therefore, it seems likely that $T_H2A$ cell subset described in this study may encompass various types of pathogenic $T_H2$ cell populations involved in atopic diseases. Together, it supports the "disease induction model" proposed by Nakayama and colleagues (*43*–*45*), wherein the presence of a pathogenic $CD4^+$ T cell subset with distinct phenotypic and functional properties might be sufficient for the pathogenesis of an immune-mediated disease, regardless of the balance of other $T_H$ subsets.

In summary, we have identified a proinflammatory human $T_H2$ cell subpopulation unique to atopic individuals that is defined by stable coexpression of $CRT_H2$, CD161, and CD49d and low expression of CD45RB and CD27. We suggest that $T_H2A$ cells are important in the pathogenesis of allergic diseases and should facilitate the detailed analysis of allergen-specific $T_H2$ cell subset in allergic individuals. Therefore, further detailed studies focusing on the $T_H2A$ cell subset may prove useful in the diagnosis, molecular characterization, or the discovery of novel therapeutic targets to enhance the power of allergen vaccines.

## MATERIALS AND METHODS

### Study design

The main research objective of this study was to determine whether allergic individuals have specific subpopulations of $T_H2$ cells associated with global atopic inflammatory disorders. To investigate allergic-related differences in peripheral T cells from allergic individuals, the profile of allergen-specific $T_H2$ cell subset ex vivo using direct pMHCII tetramer staining was determined and compared to the profile of total $T_H2$ cell subset. Candidate signature-associated markers were then tested in allergic patients and in nonatopic individuals. To evaluate this signature in the context of clinical intervention, a longitudinal study was conducted in patients receiving oral immunotherapy. Sample size was determined on the basis of the availability of fresh blood samples and with the intention to include samples before and after OFC and before and after therapy, where possible. All data generated were included in the analysis. Researchers performing the measurements were blinded to the treatment group and sample identity. To further explore the pathophysiologic meaning of this allergic T cell signature, we used real-time PCR, intracellular cytokine analysis and microarray analysis. Replication numbers for experiments are listed in the figure legends. Primary data for experiments where $n < 20$ are shown in table S3.

### Subjects

Subjects were recruited at the Allergy Clinic at Virginia Mason Medical Center. All subjects were recruited with informed consent, and the study was approved by the Institutional Review Board of Benaroya Research Institute. Allergic subjects ($n = 80$) were selected on the basis of their clinical history, a positive prick test, and positive IgE reactivity to extract (test score, $\geq$0.35 kU/liter) using the ImmunoCAP test (Phadia AB). For subjects with no history of allergy ($n = 34$), the nonatopic status was confirmed by a lack of IgE reactivity and a negative in vitro basophil activation assay after stimulation with a pool of allergen extracts. All subjects were human leukocyte antigen (HLA)–typed by using sequence-specific oligonucleotide primers with UniTray SSP kits (Invitrogen).

### CODIT study design and participants

In ARC001 (*46*), a multicenter, randomized, double-blind, placebo-controlled study of efficacy and safety of CODIT (Aimmune Therapeutics Inc.), peanut-allergic subjects aged 4 to 26 years were enrolled on the basis of clinical history of allergy to peanut, a serum IgE to peanut of $\geq$0.35 kU/liter (UniCAP) or positive skin prick test to peanut of >3 mm compared to control, and an allergic reaction at or before 100 mg of peanut protein during a screening DBPCFC, conducted in accordance with PRACTALL (Practical Issues in Allergology, Joint United States/European Union Initiative) guidelines. Participants were randomly assigned (1:1) to active treatment with AR101 or matched placebo. Subjects initiated the study with a single dose of 0.5 mg of study product and escalated biweekly over the course of about 20 weeks to the target maintenance dose of 300 mg/day. The primary clinical efficacy end point was the proportion of subjects in each group who tolerated at least 300 mg (443 mg cumulative) of peanut protein with no more than mild symptoms at the exit DBPCFC. Of 55 subjects enrolled in the ARC001 study, 10 participants were consented for additional volume of blood (10 to 15 ml) to be collected before and after the screening DBPCFC, and 7 participants (3 placebo and 4 active) were consented for additional volume of blood to be collected before and after CODIT.

### Tetramer reagents

Biotinylated HLA-DR molecules were generated and purified as described (*47*). T cell epitopes were identified by tetramer-guided epitope mapping (table S4) (*48*). Epitope-specific pMHCII tetramer reagents were generated by loading specific peptides onto biotinylated soluble DR monomers and subsequently conjugated with phycoerythrin (PE)–streptavidin (*47*).

### Ex vivo analysis of allergen-specific CD4$^+$ T cells

Twenty million PBMCs in culture medium at a concentration of 150 million cells/ml were treated with dasatinib (*49*) for 10 min at 37°C, followed by staining with of PE-labeled pMHCII tetramers (20 μg/ml) at room temperature for 100 min. After tetramer staining, cells were then washed twice and incubated with anti-PE magnetic beads (Miltenyi Biotec) at 4°C for another 20 min. The cells were washed again and enriched using a magnetic column according to the manufacturer's instructions (Miltenyi Biotec). Frequency was calculated as previously described (*50*). For unbiased FACS screen analysis, $CRT_H2$-labeled PBMCs and cells in the tetramer-bound fractions were both stained with antibodies against markers of interest (table S1) or corresponding isotype-matched monoclonal antibodies. A combination of the vital dye Via-Probe (BD Pharmingen) as a viability marker, CD19 (eBioscience), and CD14 (eBioscience) was used to exclude dead cells, B cells, and monocytes from the analysis, respectively. A FACSAria II was used for multiparameter analysis, and data were analyzed with FlowJo software (Tree Star, Inc.).

### $T_H2A$ cell subset analysis

$T_H2A$ cells were defined as $CD4^+CD45RO^+CD27^-CD45RB^{low}CRTH2^+CD161^+CD49d^+$ T cell subset. The following antibodies were used in flow cytometric analysis: fluorescein isothiocyanate (FITC)–conjugated anti-CD45RB (clone MEM-55, AbD Serotec), phycoerythrin-Texas Red (ECD)–conjugated anti-CD45RO (clone UCHL1, Beckman Coulter), Alexa Fluor 647–conjugated anti-$CRT_H2$ (clone BM16, BD Biosciences), antigen-presenting cell (APC)–H7–conjugated anti-CD27 (clone M-T271, BD Biosciences), V450-conjugated anti-CD38 (clone HIT2, eBioscience), eFluor 650–conjugated anti-CD3 (clone OKT3, eBioscience), PE-conjugated anti-CD161 (clone HP-3G10, eBioscience), PE-Cy7–conjugated anti-CD49d (clone 9F10, BioLegend), and BV605-conjugated anti-CD4 (clone OKT4, BioLegend). $CD45RB^{low}$ cells were identified using a cutoff of 35% among live memory $CD4^+$ T cells.

### $T_H$ cell subset isolation

Freshly isolated PBMCs were labeled with V500-conjugated anti-CD4 (clone RPA-T4, BD Biosciences), Alexa Fluor 647–conjugated anti-$CRT_H2$ (clone BM16, BD Biosciences), PE-Cy7–conjugated anti-CCR6 (clone R6H1, BD Biosciences), AF488-conjugated anti-CXCR3 (clone 1C6/CXCR3, BD Biosciences), APC-H7–conjugated CD27 (clone M-T271, BD Biosciences), ECD-conjugated anti-CD45RO (clone UCHL1, Beckman Coulter), PE-conjugated anti-CD161 (clone HP-3G10, eBioscience), and eFluor 650–conjugated anti-CD3 (clone OKT3, eBioscience). A combination of the vital dye Via-Probe (BD Pharmingen) as a viability marker, CD19 (eBioscience), and CD14 (eBioscience) was used to exclude dead cells, B cells, and monocytes from the analysis, respectively. $T_H2A$ cells ($CD4^+CD45RO^+CD27^-CRT_H2^+CD161^+$), conventional $T_H2$ cells ($CD4^+CD45RO^+CD27^-CRT_H2^+CD161^-$), $T_H17$ cell subset ($CD4^+CD45RO^+CRT_H2^-CCR6^+CXCR3^-$), and $T_H1$ cells ($CD4^+CD45RO^+CRT_H2^-CCR6^-CXCR3^+$) were isolated to a purity over 96% using FACSAria II (BD Biosciences) (fig. S9).

### Intracellular cytokine staining

Intracellular staining was performed by using the Cytofix/Cytoperm buffer set (BD Biosciences) according to the manufacturer's instructions. Briefly, cells were incubated for 5 hours at 37°C with 5% $CO_2$ with PMA (50 ng/ml), ionomycin (500 ng/ml), and GolgiPlug (BD Biosciences), permeabilized with Cytofix/Cytoperm buffer, and stained with APC-conjugated anti-IL-5 (JES1-39D10, Miltenyi Biotec), FITC-conjugated anti–IL-4 (clone 8D4-8, eBioscience), PE-conjugated anti–IL-9 (clone MH9A4, BioLegend), PerCP/Cy5.5-conjugated anti–IL-13 (clone JES10-5A2, BioLegend), BV510-conjugated anti–IFN-γ (clone 4S.B3, BioLegend), and APC/Cy7-conjugated anti–IL-17 (clone BL168, BioLegend). After 30 min at 4°C, cells were washed and immediately analyzed by flow cytometry.

### Real-time PCR expression analysis

The Fluidigm BioMark 96.96 Dynamic Array (*51*) was used to measure the gene expression in small cell populations. Ten cells per well were sorted by FACS in quadruplicate into 96-well plates containing a reaction mix for reverse transcription (CellsDirect One-Step qRT-PCR kit, Invitrogen) and preamplification with 96 selected gene primer pairs (Delta Gene assays, Fluidigm Corp.). After sorting, samples were reverse-transcribed and preamplified for 18 cycles. Primers and deoxynucleotide triphosphates were removed by incubation with Exonuclease I (New England Biolabs), and samples were diluted (five times) with TE buffer and stored at −20°C. Samples and assays (primer pairs) were prepared for loading onto 96.96 Fluidigm Dynamic Arrays according to the manufacturer's recommendations. Briefly, the sample was mixed with 20× DNA binding dye sample loading reagent (Fluidigm Corp.) and 2× SsoFast EvaGreen Supermix with Low ROX (Bio-Rad). Assays were mixed with 2× assay loading reagent (Fluidigm Corp.) and TE buffer to a final concentration of 5 μM. The 96.96 Fluidigm Dynamic Arrays (Fluidigm Corp.) were primed and loaded on an IFC Controller HX (Fluidigm Corp.), and real-time PCR was run on a BioMark HD (Fluidigm Corp.). Data were collected and analyzed using Fluidigm Real-Time PCR analysis software (v4.1.2).

### Microarray analysis and data analysis

Conventional $T_H1$ cells, conventional $T_H17$ cells, $T_H2A$ cells, and conventional $T_H2$ cells were sorted from PBMCs of allergic subjects, as described above. Use of donor pools (each pool containing blood from two to three donors) was necessary to obtain sufficient numbers of cells for microarray experiments. Sorted $T_H$ subsets were stimulated for 6 hours with anti-CD3/CD28 beads (Life Technologies) or left unstimulated before extraction of RNA (RNeasy Mini kit, Qiagen). Replicates of RNA were obtained from each sample that passed quality control. Complementary RNA was prepared by amplification and labeling using the Illumina TotalPrep RNA Amplification kit (Life Technologies) and hybridized to human HT-12 Beadarray chips (Illumina). Beadchips were scanned on a HiScanSQ (Illumina). Background-subtracted data were generated using GenomeStudio software (Illumina). Data were processed by customized R/Bioconductor pipeline, including quantile normalization (*52*), flooring, $\log_2$ transformation, and PALO filtering (Present At Least Once; at least one sample must have had detection $P < 0.01$). Analyses were performed using R.

### Statistical analysis

Prism software (GraphPad) was used for statistical analysis of flow cytometry data. No randomization or exclusion of data points was used. The nonparametric Mann-Whitney *U* test was used for unpaired comparisons between groups, whereas the nonparametric Wilcoxon matched pairs test was used for paired comparison.

## SUPPLEMENTARY MATERIALS

www.sciencetranslationalmedicine.org/cgi/content/full/9/401/eaam9171/DC1

Fig. S1. Flow cytometric plots showing phenotyping of ex vivo enriched allergen-specific $CD4^+$ T cells in allergic subjects.

Fig. S2. Characteristics of allergic disease causing $CD4^+$ T cells.
Fig. S3. Allergen-specific $T_H2$ cells are highly mature cells.
Fig. S4. Allergen-specific $T_H2$ cells fall into the $CD27^-CD161^+CD45RB^-CD49d^+$ $CD4^+$ T cell subset.
Fig. S5. Discrimination between proallergic $T_H2A$ and conventional $T_H2$ cell subset.
Fig. S6. Influence of OFC and oral immunotherapy on peanut-specific $CD4^+$ T cells.
Fig. S7. Expression of $T_H2$ cytokines is restricted to the allergen-specific $T_H2A$ cell subset.
Fig. S8. Overview of $T_H2A$ phenotype.
Fig. S9. Gating strategy for $T_H$ cell subset isolation.
Table S1. List of antibodies used in this study for the allergen-specific $CD4^+$ T cell profiling.
Table S2. List of all up-regulated genes in the $T_H2A$ cell subset relative to conventional $T_H2$ cells.
Table S3. Primary data.
Table S4. List of pMHCII tetramer reagents used in this study.

## REFERENCES AND NOTES


1. S. Romagnani, T-cell responses in allergy and asthma. *Curr. Opin. Allergy Clin. Immunol.* **1**, 73–78 (2001).
2. B. Upadhyaya, Y. Yin, B. J. Hill, D. C. Douek, C. Prussin, Hierarchical IL-5 expression defines a subpopulation of highly differentiated human Th2 cells. *J. Immunol.* **187**, 3111–3120 (2011).
3. C. Prussin, Y. Yin, B. Upadhyaya, $T_H2$ heterogeneity: Does function follow form? *J. Allergy Clin. Immunol.* **126**, 1094–1098 (2010).
4. A. Wensky, M. C. G. Marcondes, J. J. Lafaille, The role of IFN-γ in the production of Th2 subpopulations: Implications for variable Th2-mediated pathologies in autoimmunity. *J. Immunol.* **167**, 3074–3081 (2001).
5. L. Cosmi, L. Maggi, V. Santarlasci, M. Capone, E. Cardilicchia, F. Frosali, V. Querci, R. Angeli, A. Matucci, M. Fambrini, F. Liotta, P. Parronchi, E. Maggi, S. Romagnani, F. Annunziato, Identification of a novel subset of human circulating memory $CD4^+$ T cells that produce both IL-17A and IL-4. *J. Allergy Clin. Immunol.* **125**, 222–230 (2010).
6. S. Gilles, C. Traidl-Hoffmann, CD27 expression on allergen-specific T cells: A new surrogate for successful allergen-specific immunotherapy? *J. Allergy Clin. Immunol.* **129**, 552–554 (2012).
7. E. Wambre, J. H. DeLong, E. A. James, R. E. LaFond, D. Robinson, W. W. Kwok, Differentiation stage determines pathologic and protective allergen-specific $CD4^+$ T-cell outcomes during specific immunotherapy. *J. Allergy Clin. Immunol.* **129**, 544–551 (2012).
8. Y. Endo, C. Iwamura, M. Kuwahara, A. Suzuki, K. Sugaya, D. J. Tumes, K. Tokoyoda, H. Hosokawa, M. Yamashita, T. Nakayama, Eomesodermin controls interleukin-5 production in memory T helper 2 cells through inhibition of activity of the transcription factor GATA3. *Immunity* **35**, 733–745 (2011).
9. S. A. Islam, D. S. Chang, R. A. Colvin, M. H. Byrne, M. L. McCully, B. Moser, S. A. Lira, I. F. Charo, A. D. Luster, Mouse CCL8, a CCR8 agonist, promotes atopic dermatitis by recruiting $IL\text{-}5^+$ $T_H2$ cells. *Nat. Immunol.* **12**, 167–177 (2011).
10. A. Mitson-Salazar, Y. Yin, D. L. Wansley, M. Young, H. Bolan, S. Arceo, N. Ho, C. Koh, J. D. Milner, K. D. Stone, S. A. Wank, C. Prussin, Hematopoietic prostaglandin D synthase defines a proeosinophilic pathogenic effector human $T_H2$ cell subpopulation with enhanced function. *J. Allergy Clin. Immunol.* **137**, 907–918 (2016).
11. E. P. S. Lam, H. H. Kariyawasam, B. M. J. Rana, S. R. Durham, A. N. McKenzie, N. Powell, N. Orban, M. Lennartz-Walker, C. Hopkins, S. Ying, J. Rimmer, V. J. Lund, D. J. Cousins, S. J. Till, IL-25/IL-33–responsive $T_H2$ cells characterize nasal polyps with a default $T_H17$ signature in nasal mucosa. *J. Allergy Clin. Immunol.* **137**, 1514–1524 (2016).
12. E. Wambre, E. A. James, W. W. Kwok, Characterization of CD4+ T cell subsets in allergy. *Curr. Opin. Immunol.* **24**, 700–706 (2012).
13. L. Cosmi, F. Annunziato, M. I. G. Galli, R. M. E. Maggi, K. Nagata, S. Romagnani, CRTH2 is the most reliable marker for the detection of circulating human type 2 Th and type 2 T cytotoxic cells in health and disease. *Eur. J. Immunol.* **30**, 2972–2979 (2000).
14. C. Tortorella, H. Schulze-Koops, R. Thomas, J. B. Splawski, L. S. Davis, L. J. Picker, P. E. Lipsky, Expression of CD45RB and CD27 identifies subsets of CD4+ memory T cells with different capacities to induce B cell differentiation. *J. Immunol.* **155**, 149–162 (1995).
15. R. D. Fritsch, X. Shen, G. P. Sims, K. S. Hathcock, R. J. Hodes, P. E. Lipsky, Stepwise differentiation of CD4 memory T cells defined by expression of CCR7 and CD27. *J. Immunol.* **175**, 6489–6497 (2005).
16. E. Wambre, J. H. DeLong, E. A. James, N. Torres-Chinn, W. Pfutzner, C. Möbs, S. R. Durham, S. J. Till, D. Robinson, W. W. Kwok, Specific immunotherapy modifies allergen-specific $CD4^+$ T-cell responses in an epitope-dependent manner. *J. Allergy Clin. Immunol.* **133**, 872–879 (2014).
17. L. Cosmi, R. De Palma, V. Santarlasci, L. Maggi, M. Capone, F. Frosali, G. Rodolico, V. Querci, G. Abbate, R. Angeli, L. Berrino, M. Fambrini, M. Caproni, F. Tonelli, E. Lazzeri, P. Parronchi, F. Liotta, E. Maggi, S. Romagnani, F. Annunziato, Human interleukin 17–producing cells originate from a $CD161^+CD4^+$ T cell precursor. *J. Exp. Med.* **205**, 1903–1916 (2008).
18. L. Maggi, V. Santarlasci, M. Capone, A. Peired, F. Frosali, S. Q. Crome, V. Querci, M. Fambrini, F. Liotta, M. K. Levings, E. Maggi, L. Cosmi, S. Romagnani, F. Annunziato, CD161 is a marker of all human IL-17-producing T-cell subsets and is induced by RORC. *Eur. J. Immunol.* **40**, 2174–2181 (2010).
19. M. Frentsch, O. Arbach, D. Kirchhoff, B. Moewes, M. Worm, M. Rothe, A. Scheffold, A. Thiel, Direct access to $CD4^+$ T cells specific for defined antigens according to CD154 expression. *Nat. Med.* **11**, 1118–1124 (2005).
20. J. A. Bird, J. M. Spergel, S. M. Jones, R. Rachid, A. H. Assa'ad, J. Wang, S. A. Leonard, S. S. Laubach, E. H. Kim, B. P. Vickery, B. Davis, J. Heimall, A. Cianferoni, A. J. MacGinnitie, E. Crestani, R. M. Elfont, H. A. Sampson, A. W. Burks, in *EAACI Congress*, A. W. Burks, Ed. (EAACI, 2015), vol. 70, p. 110.
21. M. Bonvalet, H. Moussu, E. Wambre, C. Ricarte, S. Horiot, A.-C. Rimaniol, W. W. Kwok, F. Horak, O. de Beaumont, V. Baron-Bodo, P. Moingeon, Allergen-specific $CD4^+$ T cell responses in peripheral blood do not predict the early onset of clinical efficacy during grass pollen sublingual immunotherapy. *Clin. Exp. Allergy* **42**, 1745–1755 (2012).
22. S. F. Ziegler, The role of thymic stromal lymphopoietin (TSLP) in allergic disorders. *Curr. Opin. Immunol.* **22**, 795–799 (2010).
23. M. A. Portelli, E. Hodge, I. Sayers, Genetic risk factors for the development of allergic disease identified by genome-wide association. *Clin. Exp. Allergy* **45**, 21–31 (2015).
24. Y. Matsumoto, E. Noguchi, Y. Imoto, K. Nanatsue, K. Takeshita, M. Shibasaki, T. Arinami, S. Fujieda, Upregulation of *IL17RB* during natural allergen exposure in patients with seasonal allergic rhinitis. *Allergol. Int.* **60**, 87–92 (2011).
25. I. H. S. Chan, N. L. S. Tang, T. F. Leung, S. L. Ma, Y. P. Zhang, G. W. F. Wong, C. K. Wong, C. W. K. Lam, Association of prostaglandin-endoperoxide synthase 2 gene polymorphisms with asthma and atopy in Chinese children. *Allergy* **62**, 802–809 (2007).
26. M. L. Fajt, S. L. Gelhaus, B. Freeman, C. E. Uvalle, J. B. Trudeau, F. Holguin, S. E. Wenzel, Prostaglandin $D_2$ pathway upregulation: Relation to asthma severity, control, and $T_H2$ inflammation. *J. Allergy Clin. Immunol.* **131**, 1504–1512 (2013).
27. H. L. Puhl III, Y.-J. Won, V. B. Lu, S. R. Ikeda, Human GPR42 is a transcribed multisite variant that exhibits copy number polymorphism and is functional when heterologously expressed. *Sci. Rep.* **5**, 12880 (2015).
28. M. Pepper, J. L. Linehan, A. J. Pagán, T. Zell, T. Dileepan, P. P. Cleary, M. K. Jenkins, Different routes of bacterial infection induce long-lived $T_H1$ memory cells and short-lived $T_H17$ cells. *Nat. Immunol.* **11**, 83–89 (2010).
29. J. Hendriks, Y. Xiao, J. Borst, CD27 promotes survival of activated T cells and complements CD28 in generation and establishment of the effector T cell pool. *J. Exp. Med.* **198**, 1369–1380 (2003).
30. S. Satkunanathan, N. Kumar, M. Bajorek, M. A. Purbhoo, F. J. Culley, Respiratory syncytial virus infection, TLR3 ligands, and proinflammatory cytokines induce CD161 ligand LLT1 expression on the respiratory epithelium. *J. Virol.* **88**, 2366–2373 (2014).
31. M. A. Kleinschek, K. Boniface, S. Sadekova, J. Grein, E. E. Murphy, S. P. Turner, L. Raskin, B. Desai, W. A. Faubion, R. de Waal Malefyt, R. H. Pierce, T. McClanahan, R. A. Kastelein, Circulating and gut-resident human Th17 cells express CD161 and promote intestinal inflammation. *J. Exp. Med.* **206**, 525–534 (2009).
32. Y. Gernez, R. Tirouvanziam, K. D. Nguyen, L. A. Herzenberg, A. M. Krensky, K. C. Nadeau, Altered phosphorylated signal transducer and activator of transcription profile of $CD4^+CD161^+$ T cells in asthma: Modulation by allergic status and oral corticosteroids. *J. Allergy Clin. Immunol.* **120**, 1441–1448 (2007).
33. Y.-H. Wang, K. S. Voo, B. Liu, C.-Y. Chen, B. Uygungil, W. Spoede, J. A. Bernstein, D. P. Huston, Y.-J. Liu, A novel subset of $CD4^+$ $T_H2$ memory/effector cells that produce inflammatory IL-17 cytokine and promote the exacerbation of chronic allergic asthma. *J. Exp. Med.* **207**, 2479–2491 (2010).
34. Y. Wang, P. Angkasekwinai, W. Spoede, D. Huston, Y. Liu, Proinflammatory stimuli induce the generation of IL-17-producing $T_H2$ memory cells that is associated with exacerbated allergic diseases. *J. Allergy Clin. Immunol.* **123**, S143 (2009).
35. H. A. Brough, D. J. Cousins, A. Munteanu, Y. F. Wong, A. Sudra, K. Makinson, A. C. Stephens, M. Arno, L. Ciortuz, G. Lack, V. Turcanu, IL-9 is a key component of memory $T_H$ cell peanut-specific responses from children with peanut allergy. *J. Allergy Clin. Immunol.* **134**, 1329–1338 (2014).
36. K. R. Bartemes, H. Kita, Dynamic role of epithelium-derived cytokines in asthma. *Clin. Immunol.* **143**, 222–235 (2012).
37. L. Blom, B. C. Poulsen, B. M. Jensen, A. Hansen, L. K. Poulsen, IL-33 induces IL-9 production in human $CD4^+$ T cells and basophils. *PLOS ONE* **6**, e21695 (2011).
38. M. Kurowska-Stolarska, P. Kewin, G. Murphy, R. C. Russo, B. Stolarski, C. C. Garcia, M. Komai-Koma, N. Pitman, Y. Li, W. Niedbala, A. N. J. McKenzie, M. M. Teixeira, F. Y. Liew, D. Xu, IL-33 induces antigen-specific $IL\text{-}5^+$ T cells and promotes allergic-induced airway inflammation independent of IL-4. *J. Immunol.* **181**, 4780–4790 (2008).
39. Y. Endo, K. Hirahara, T. Iinuma, K. Shinoda, D. J. Tumes, H. K. Asou, N. Matsugae, K. Obata-Ninomiya, H. Yamamoto, S. Motohashi, K. Oboki, S. Nakae, H. Saito, Y. Okamoto,

T. Nakayama, The interleukin-33-p38 kinase axis confers memory T helper 2 cell pathogenicity in the airway. *Immunity* **42**, 294–308 (2015).
40. J.-B. Lee, C.-Y. Chen, B. Liu, L. Mugge, P. Angkasekwinai, V. Facchinetti, C. Dong, Y.-J. Liu, M. E. Rothenberg, S. P. Hogan, F. D. Finkelman, Y.-H. Wang, IL-25 and CD4$^+$ $T_H2$ cells enhance type 2 innate lymphoid cell–derived IL-13 production, which promotes IgE-mediated experimental food allergy. *J. Allergy Clin. Immunol.* **137**, 1216–1225 (2016).
41. S. J. Van Dyken, J. C. Nussbaum, J. Lee, A. B. Molofsky, H.-E. Liang, J. L. Pollack, R. E. Gate, G. E. Haliburton, C. J. Ye, A. Marson, D. J. Erle, R. M. Locksley, A tissue checkpoint regulates type 2 immunity. *Nat. Immunol.* **17**, 1381–1387 (2016).
42. E. Wambre, Effect of allergen-specific immunotherapy on CD4+ T cells. *Curr. Opin. Allergy Clin. Immunol.* **15**, 581–587 (2015).
43. T. Nakayama, K. Hirahara, A. Onodera, Y. Endo, H. Hosokawa, K. Shinoda, D. J. Tumes, Y. Okamoto, Th2 cells in health and disease. *Annu. Rev. Immunol.* **35**, 53–84 (2016).
44. Y. Endo, K. Hirahara, R. Yagi, D. J. Tumes, T. Nakayama, Pathogenic memory type Th2 cells in allergic inflammation. *Trends Immunol.* **35**, 69–78 (2014).
45. K. Hirahara, T. Nakayama, CD4$^+$ T-cell subsets in inflammatory diseases: Beyond the Th1/Th2 paradigm. *Int. Immunol.* **28**, 163–171 (2016).
46. Aimmune Therapeutics, Developing an orally administered biologic immunotherapy for the treatment of peanut allergy (Aimmune Therapeutics, 2017); www.aimmune.com/clinical-trials/ar101-for-peanut-allergy/.
47. E. J. Novak, A. W. Liu, G. T. Nepom, W. W. Kwok, MHC class II tetramers identify peptide-specific human CD4$^+$ T cells proliferating in response to influenza A antigen. *J. Clin. Invest.* **104**, R63–R67 (1999).
48. E. J. Novak, A. W. Liu, J. A. Gebe, B. A. Falk, G. T. Nepom, D. M. Koelle, W. W. Kwok, Tetramer-guided epitope mapping: Rapid identification and characterization of immunodominant CD4$^+$ T cell epitopes from complex antigens. *J. Immunol.* **166**, 6665–6670 (2001).
49. A. Lissina, K. Ladell, A. Skowera, M. Clement, E. Edwards, R. Seggewiss, H. A. van den Berg, E. Gostick, K. Gallagher, E. Jones, J. J. Melenhorst, A. J. Godkin, M. Peakman, D. A. Price, A. K. Sewell, L. Wooldridge, Protein kinase inhibitors substantially improve the physical detection of T-cells with peptide-MHC tetramers. *J. Immunol. Methods* **340**, 11–24 (2009).
50. W. W. Kwok, M. Roti, J. H. Delong, V. Tan, E. Wambre, E. A. James, D. Robinson, Direct ex vivo analysis of allergen-specific CD4$^+$ T cells. *J. Allergy Clin. Immunol.* **125**, 1407–1409 (2010).
51. L. Warren, D. Bryder, I. L. Weissman, S. R. Quake, Transcription factor profiling in individual hematopoietic progenitors by digital RT-PCR. *Proc. Natl. Acad. Sci. U.S.A.* **103**, 17807–17812 (2006).
52. B. M. Bolstad, R. A. Irizarry, M. Astrand, T. P. Speed, A comparison of normalization methods for high density oligonucleotide array data based on variance and bias. *Bioinformatics* **19**, 185–193 (2003).

**Acknowledgments:** We thank K. Gilroy, S. Posso, G. Marchesini, and T.-S. Nguyen for the help with subject recruitment. We thank K. Arumuganathan for the expert advice on flow cytometry. We thank C. Cousens-Jacobs for the excellent secretarial assistance. We thank G. T. Nepom and J. Buckner for the comments on the manuscript. pMHCII reagents are available from the Tetramer Core under a material transfer agreement with the Benaroya Research Institute. **Funding:** This work was supported by the NIH (grant R01AI108839 to E. Wambre, grant DP3DK110867 to P.S.L., and grant HHSN272200700046C to W.W.K.). Food Allergy Research and Education (FARE) contributed supplemental support to the Wambre Laboratory. Immune Tolerance Networks (ITN) and Aimmune Therapeutics provided support to the Benaroya Research Institute for the pilot experiments on samples from Aimmune's clinical trial. **Author contributions:** E. Wambre designed the study, planned and performed the experiments, analyzed the data, and wrote the manuscript. V.B., J.H.D., K.O., Q-A.N., and C.S. performed the experiments, analyzed the data, and reviewed the manuscript. M.F., D.J., D.R., and B.P.V. participated in patient recruitment, clinical data, and biological sample collection. B.P.V. directed the ARC001 study and provided coded biological sample from ARC001 study. E. Whalen, V.H.G., C.N., H.A.D., and P.S.L. statistically analyzed the microarray and PCR data and reviewed the manuscript. W.W.K. provided advice and technical support, analyzed the data, and reviewed the manuscript. E. Wambre, P.S.L., and W.W.K. raised the funding and supervised the project. **Competing interests:** E. Wambre and W.W.K. are inventors on patent/patent application (EP 2681555 A1) held/submitted by the Benaroya Research Institute that covers "$T_H2$A analysis: Detection of an immune response." All other authors declare that they have no competing interests.

Submitted 15 May 2015
Resubmitted 3 February 2017
Accepted 31 May 2017
Published 2 August 2017
10.1126/scitranslmed.aam9171

**Citation:** E. Wambre, V. Bajzik, J. H. DeLong, K. O'Brien, Q.-A. Nguyen, C. Speake, V. H. Gersuk, H. A. DeBerg, E. Whalen, C. Ni, M. Farrington, D. Jeong, D. Robinson, P. S. Linsley, B. P. Vickery, W. W. Kwok, A phenotypically and functionally distinct human $T_H2$ cell subpopulation is associated with allergic disorders. *Sci. Transl. Med.* **9**, eaam9171 (2017).

CANCER

# Eradication of spontaneous malignancy by local immunotherapy

Idit Sagiv-Barfi,[1] Debra K. Czerwinski,[1] Shoshana Levy,[1] Israt S. Alam,[2] Aaron T. Mayer,[2] Sanjiv S. Gambhir,[2] Ronald Levy[1]*



**It has recently become apparent that the immune system can cure cancer. In some of these strategies, the antigen targets are preidentified and therapies are custom-made against these targets. In others, antibodies are used to remove the brakes of the immune system, allowing preexisting T cells to attack cancer cells. We have used another noncustomized approach called in situ vaccination. Immunoenhancing agents are injected locally into one site of tumor, thereby triggering a T cell immune response locally that then attacks cancer throughout the body. We have used a screening strategy in which the same syngeneic tumor is implanted at two separate sites in the body. One tumor is then injected with the test agents, and the resulting immune response is detected by the regression of the distant, untreated tumor. Using this assay, the combination of unmethylated CG–enriched oligodeoxynucleotide (CpG)—a Toll-like receptor 9 (TLR9) ligand—and anti-OX40 antibody provided the most impressive results. TLRs are components of the innate immune system that recognize molecular patterns on pathogens. Low doses of CpG injected into a tumor induce the expression of OX40 on $CD4^+$ T cells in the microenvironment in mouse or human tumors. An agonistic anti-OX40 antibody can then trigger a T cell immune response, which is specific to the antigens of the injected tumor. Remarkably, this combination of a TLR ligand and an anti-OX40 antibody can cure multiple types of cancer and prevent spontaneous genetically driven cancers.**

## INTRODUCTION

T cells that recognize tumor antigens are present in the tumor microenvironment, and their activity is modulated through stimulatory and inhibitory receptors. Once cancer is well established, the balance between these inputs is tipped toward immunosuppression (*1*, *2*). The inhibitory signals on T cells are delivered through molecules such as cytotoxic T lymphocyte–associated protein 4 (CTLA4) and programmed cell death protein 1 (PD1) by interaction with their respective ligands expressed on cancer cells and/or antigen-presenting cells (APCs). However, these same tumor-reactive T cells express stimulatory receptors including members of the tumor necrosis factor receptor (TNFR) superfamily. Therefore, many attempts are being made to relieve the negative checkpoints on the antitumor immune response and/or to stimulate the activation pathways of the tumor-infiltrating effector T cells ($T_{effs}$).

Here, we conducted a preclinical screen to identify candidate immunostimulatory agents that could trigger a systemic antitumor T cell immune response when injected locally into one site of tumor. We found that Toll-like receptor 9 (TLR9) ligands induce the expression of OX40 on CD4 T cells in the tumor microenvironment. OX40 is a costimulatory molecule belonging to the TNFR superfamily, and it is expressed on both activated $T_{effs}$ and regulatory T cells ($T_{regs}$). OX40 signaling can promote $T_{eff}$ activation and inhibit $T_{reg}$ function.

The addition of an agonistic anti-OX40 antibody can then provide a synergistic stimulus to elicit an antitumor immune response that cures distant sites of established tumors. This combination of TLR9 ligand and anti-OX40 antibody can even treat spontaneous breast cancers, overcoming the effect of a powerful oncogene. This in situ vaccine maneuver is safe because it uses low doses of the immunoenhancing agents and practical because the therapy can be applied to many forms of cancer without prior knowledge of their unique tumor antigens.

[1]Division of Oncology, Department of Medicine, Stanford University, Stanford, CA 94305, USA. [2]Department of Radiology, Molecular Imaging Program at Stanford (MIPS), Stanford University, Stanford, CA 94305, USA.
*Corresponding author. Email: levy@stanford.edu

## RESULTS

### In situ vaccination with a TLR9 ligand induces the expression of OX40 on intratumoral CD4 T cells

TLRs are known to signal the activation of a variety of cells of the innate and adaptive immune system. To exploit this for cancer therapy, we subcutaneously implanted a tumor into syngeneic mice, and after the tumor had become established, we injected a CpG oligodeoxynucleotide—a ligand for TLR9—into the tumor nodule. We then analyzed the intratumoral T cells for their expression of inhibitory and activation markers. Before treatment, we observed that OX40 was expressed on CD4 cells in the tumor microenvironment (Fig. 1A, top) and that this was restricted mainly to the $T_{regs}$, as has been previously reported (*3*–*5*) (Fig. 1B, top). After intratumoral injection of CpG, there was up-regulation of OX40 on CD4 T cells (Fig. 1A, middle), mostly among the effector CD4 cells that greatly outnumber the $T_{regs}$ (Fig. 1, A and B, bottom). This inductive effect was specific to the activating receptor OX40 and did not occur for inhibitory T cell checkpoint targets such as CTLA4 and PD1 (fig. S1A). Moreover, this OX40 up-regulation on CD4 cells also occurred in a patient with follicular lymphoma that had been treated with low-dose radiation and intratumoral injection of CpG (Fig. 1C) and in tumor-infiltrating cell populations from lymphoma patients' samples that were exposed to CpG in vitro (Fig. 1, D and E, and fig. S2). In these human cases, the enhancement of OX40 expression was observed on both $T_{effs}$ and $T_{regs}$ (Fig. 1D). All of these changes occurred only in the tumor that was injected with CpG and not in the tumor at the untreated site (fig. S1B).

#### *CpG induces OX40 as revealed by in vivo imaging*

The enhancement of OX40 expression by intratumoral injection of CpG could be visualized in mice by whole-body small-animal positron emission tomography (PET) imaging after tail-vein administration

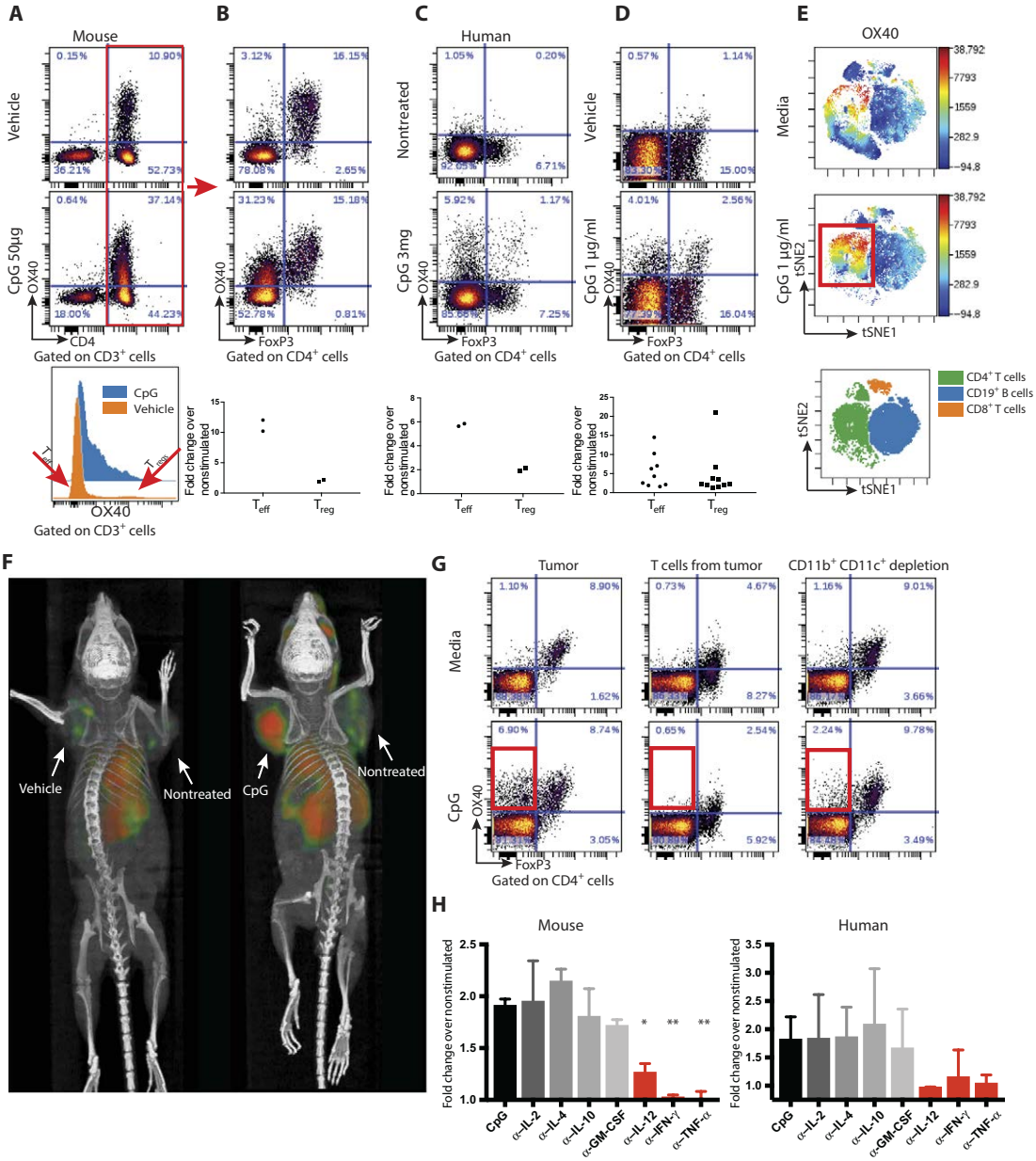


**Fig. 1. CpG induces the expression of OX40 on CD4 T cells.** (**A**) A20 tumor–bearing mice were treated either with vehicle (top) or CpG (middle). Forty-eight hours later, tumors were excised and a single-cell suspension was stained and analyzed by flow cytometry. (**B**) OX40 expression within the $CD3^+CD4^+$ subset was separately analyzed for FoxP3-negative [effector T cell ($T_{eff}$)] and FoxP3-positive [regulatory T cell ($T_{reg}$)] subsets. Fold changes of $OX40^+$ cells were calculated according to their frequencies in the vehicle versus CpG treatment ($n = 2$). (**C**) Fine needle aspirates from CpG-injected and noninjected tumors of a follicular lymphoma patient were obtained 22 hours after treatment. Fluorescence-activated cell sorting (FACS) plots of OX40 expression within the $CD4^+$ subset after a 24-hour rest in media. Top: Nontreated lesion. Bottom: CpG-treated site ($n = 2$). (**D**) Single-cell suspensions from biopsy specimens of human lymphoma (five mantle cell lymphomas and five follicular lymphomas) were exposed in vitro to CpG for 48 hours and analyzed for OX40 expression as in (B). (**E**) CpG-stimulated human lymphoma–infiltrating $CD4^+$ T cells, $CD8^+$ T cells, and $CD19^+$ B cells were gated and visualized in tSNE (t-Distributed Stochastic Neighbor Embedding) space using Cytobank software. The viSNE map shows the location of each $CD4^+$, $CD19^+$, and $CD8^+$ cell population (green, blue, and orange, respectively; bottom). Cells in the viSNE maps were colored according to the intensity of OX40 expression. CpG up-regulation of OX40 expression on a subset of $CD4^+$ T cells is highlighted by a red box. (**F**) BALB/c mice were implanted subcutaneously with A20 lymphoma cells ($5 \times 10^6$) on both the right and left shoulders. When tumors reached between 0.7 and 1 cm in the largest diameter (typically on days 8 to 9 after inoculation), phosphate-buffered saline and CpG (50 μg) were injected into one tumor site (left tumor). Sixteen hours later, $^{64}$Cu-DOTA-OX40 was administered intravenously via the tail vein. Positron emission tomography imaging of mice was performed 40 hours after in situ treatment. Left: Vehicle-treated. Right: CpG-treated. These images are representative of six mice per group. (**G**) Fresh A20 tumors were excised from animals (typically 5 to 6 days after inoculation), and either whole tumors (left), T cells purified from the tumor (middle), or whole tumor depleted of CD11b- and CD11c-expressing cells (right) were treated for 48 hours with media (top) or CpG (bottom) and were analyzed for their expression of OX40 by flow cytometry. (**H**) Left: A20 tumors were excised as in (F). Right: Single-cell suspensions from biopsy specimens of human follicular lymphoma. Tumors were treated for 48 hours with media and CpG with or without antibodies (1 μg/ml) to interleukin-2 (IL-2), IL-4, IL-10, granulocyte-macrophage colony-stimulating factor (GM-CSF), IL-12, interferon-γ (IFN-γ), or tumor necrosis factor–α (TNF-α) and were analyzed for their expression of OX40 by flow cytometry. α–IL-12, $^*P = 0.0144$; α–IFN-γ, $^{**}P = 0.0032$; α–TNF-α, $^{**}P = 0.008$, unpaired *t* test, either depleting antibody versus CpG alone.

of an anti-OX40 antibody labeled with $^{64}$Cu (Fig. 1F). Remarkably, the systemically injected antibody revealed that OX40 was induced in the microenvironment of the injected tumor, as opposed to a second noninjected tumor site in the same animal. This result indicates that the effect of CpG at this low dose to up-regulate OX40 expression is predominately local.

***CpG induces cytokine secretion by myeloid cells which in turn induces OX40 expression on T cells***

Purified tumor-infiltrating T cells do not up-regulate OX40 when exposed to CpG in vitro (Fig. 1G). The T cells within whole tumor cell populations similarly fail to up-regulate OX40 after depletion of macrophages and dendritic cells (Fig. 1G). From these results, we conclude that myeloid-derived cells communicate the CpG signal to T cells. Therefore, we tested for the role of several cytokines in this cellular cross-talk. In human and mice tumors, antibody neutralization of interleukin-12 (IL-12), interferon-γ (IFN-γ), and TNF-α each prevented the CpG-induced up-regulation of OX40 on T cells in these tumor cell populations (Fig. 1H). In contrast, neutralization of IL-2, IL-4, IL-10, and granulocyte-macrophage colony-stimulating factor (GM-CSF) had no effect (fig. S3).

## In situ vaccination with a TLR ligand and anti-OX40 antibody induces T cell immune responses that cure established cancers

On the basis of the results above, we hypothesized that an agonistic anti-OX40 antibody could augment CpG treatment and help to induce antitumor immune responses. To test this hypothesis, we implanted mice with A20 B cell lymphoma tumors at two different sites in the body, allowed the tumors to become established, and then injected a TLR agonist together with a checkpoint antibody into only one tumor site (Fig. 2A). The animals were then monitored for tumor growth at both the injected and the distant sites (Fig. 2B). The tumors of vehicle-treated mice grew progressively at both sites. CpG caused complete regression of tumors at the local injected site but had only a slight delay in growth of the distant nontreated tumor. The anti-OX40 antibody alone induced a slight delay in growth of both the treated and nontreated tumors. However, the combination of CpG and anti-OX40 resulted in complete regression of both injected and noninjected tumors. Consistent with the time needed to induce an adaptive T cell response, the kinetics of regression at the two sites was different, with the distant site following the local site by several days (fig. S1C). Tumor regressions in response to the combined treatment were long-lasting and led to cure of most of the mice (Fig. 2B, bottom).

The systemic antitumor response required the presence of both $CD4^+$ and $CD8^+$ T cells because mice treated with the corresponding depleting antibodies were unable to control tumor growth (Fig. 2C). $CD8^+$ T cells derived from mice treated with both CpG and anti-OX40 antibody responded to tumor cells in vitro as measured by IFN-γ production (Fig. 2D). $CD4^+$ T cells from mice treated by the combination also responded to tumors in vitro but with a lesser magnitude (fig. S4). Immediately after CpG and anti-OX40 injection, the proportion of the CD4 effector/memory T cell subset increased at the treated site. Twenty-four hours later, this subset increased in the spleen, and 5 days later, the same occurred at the distant, nontreated site (fig. S5).

Distant tumors occasionally did recur in mice treated with the effective combination (3 of 90 mice), and interestingly, these late recurring tumors were sensitive to retreatment by anti-OX40 and CpG (fig. S6). An alternative TLR agonist, resiquimod (R848), a ligand for TLR7/8, in combination with anti-OX40 induced a similar systemic antitumor immune response (fig. S7A). Anti-OX40 antibody was especially effective compared to other immune checkpoint antibodies, such as anti-PD1 and anti–PDL1 (programmed death-ligand 1) (fig. S7B), which delayed tumor growth in the nontreated site but were not curative.

In situ vaccination with CpG and anti-OX40 was effective not only against lymphoma but also against tumors of a variety of histologic types, such as breast carcinoma (4T1), colon cancer (CT26), and melanoma (B16-F10) (fig. S8, A to C). In all these tumor models, the systemic therapeutic effects were induced by extremely low doses of both the CpG (typically 50 μg) and the anti-OX40 antibody (typically 8 μg) or even lower (fig. S9). However, the TLR agonist worked best when it was injected directly into the tumor, consistent with its action to up-regulate the OX40 target in the T cells of the tumor microenvironment. Similar systemic effects were obtained when the OX40 antibody was given systemically, rather than into the tumor, but at higher doses (fig. S10).

## In situ vaccination protects animals genetically prone to spontaneous breast cancers

Female FVB/N-Tg(MMTV-PyVT)634Mul/J mice (also known as PyVT/PyMT) develop highly invasive mammary ductal carcinomas that give rise to a high frequency of lung metastases (*6*). By 6 to 7 weeks of age, all female carriers develop the first palpable mammary tumor (*7*), and eventually, tumors develop in all of their 10 mammary fat pads. This provided an opportunity for therapeutic intervention in a spontaneous tumor model where the site of tumor development is known and accessible for in situ vaccination.

Young mice were observed, and as their first tumor reached 50 to 75 $mm^3$, we injected it with CpG and anti-OX40 antibody (Fig. 3A). In some cases, a second tumor was present at the beginning of therapy, and in these mice with coincident tumors, treatment at a single tumor site with CpG and anti-OX40 led to significant retardation of growth of the contralateral tumor (Fig. 3B), establishing the combination as a therapy for established and disseminating tumors. The injected and the noninjected tumors regressed, and remarkably, the treated mice were protected against the occurrence of independently arising tumors in their other mammary glands (Fig. 3C). The treated mice had significantly lower eventual total tumor burdens (Fig. 3, C and D) and developed far fewer lung metastases (Fig. 3E). This in situ vaccination with CpG and anti-OX40 not only caused tumor regression and reduced tumor incidence but also had a major effect on the survival of these cancer-prone mice (Fig. 3F). After CpG and anti-OX40 treatment, these mice developed antitumor CD8 T cells in their spleens as indicated by their ability to produce IFN-γ when exposed in vitro to autologous tumor cells from the noninjected tumor site (Fig. 3G). These results establish that the antitumor immune response was elicited against tumor antigens shared by all the independently arising tumors in these mice, rather than antigens unique to the injected tumor, and accounted for the impressive therapeutic effects seen.

## Therapeutic effect of in situ vaccination is antigen-specific and triggered at the site of local injection

The results of cross-protection against independently arising tumors in the spontaneous breast cancer model raise the question of antigen specificity. We approached this question using two different tumors that are antigenically distinct. Mice cured by in situ vaccination of the A20 lymphoma were immune to rechallenge with the same tumor (A20) but not to a different tumor (CT26) (fig. S11). Conversely, mice cured of the CT26 tumor were immune to rechallenge with CT26 but not with A20. Therefore, these two tumors are antigenically distinct.

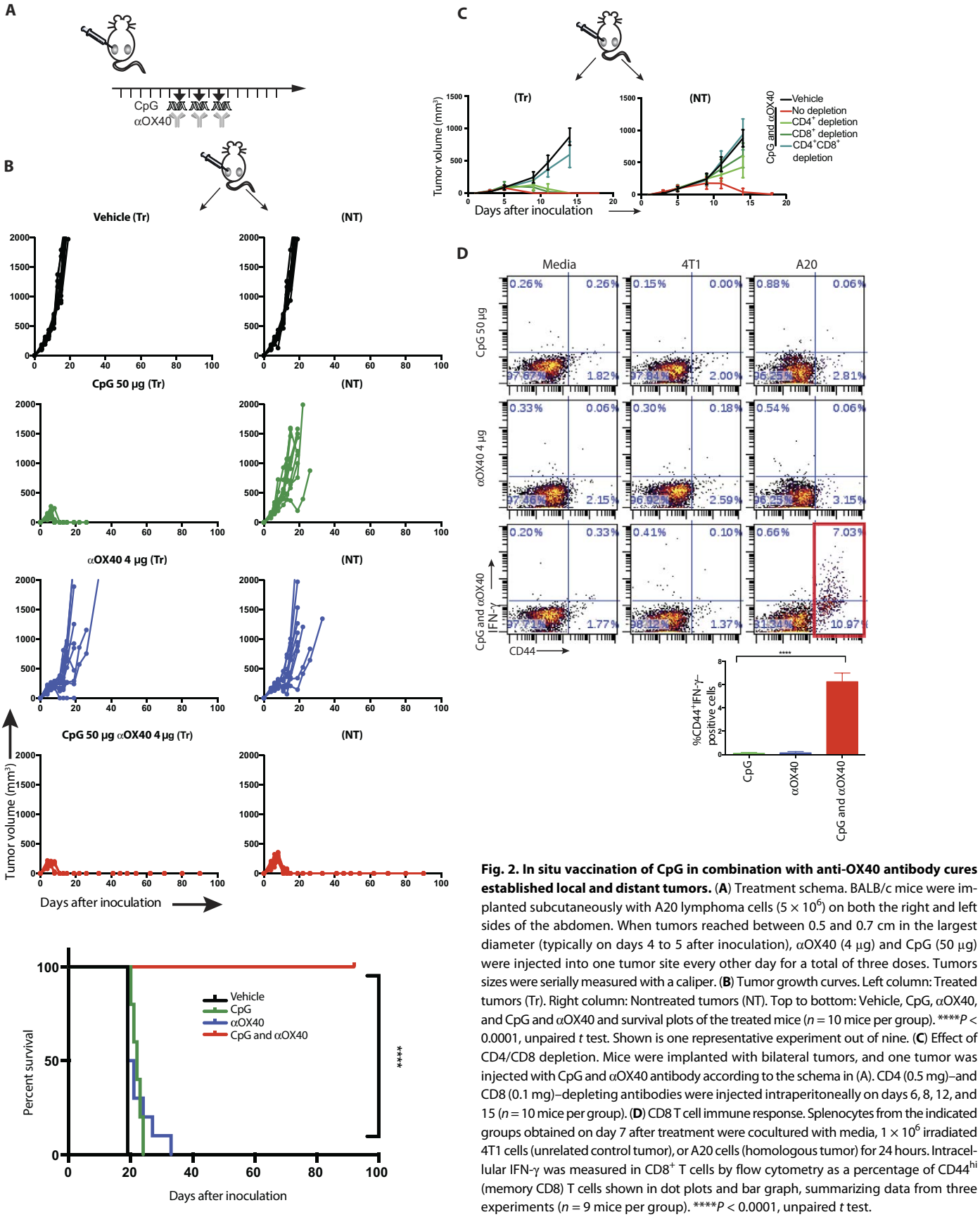


**Fig. 2. In situ vaccination of CpG in combination with anti-OX40 antibody cures established local and distant tumors.** (**A**) Treatment schema. BALB/c mice were implanted subcutaneously with A20 lymphoma cells ($5 \times 10^6$) on both the right and left sides of the abdomen. When tumors reached between 0.5 and 0.7 cm in the largest diameter (typically on days 4 to 5 after inoculation), αOX40 (4 μg) and CpG (50 μg) were injected into one tumor site every other day for a total of three doses. Tumors sizes were serially measured with a caliper. (**B**) Tumor growth curves. Left column: Treated tumors (Tr). Right column: Nontreated tumors (NT). Top to bottom: Vehicle, CpG, αOX40, and CpG and αOX40 and survival plots of the treated mice ($n = 10$ mice per group). ****$P <$ 0.0001, unpaired $t$ test. Shown is one representative experiment out of nine. (**C**) Effect of CD4/CD8 depletion. Mice were implanted with bilateral tumors, and one tumor was injected with CpG and αOX40 antibody according to the schema in (A). CD4 (0.5 mg)–and CD8 (0.1 mg)–depleting antibodies were injected intraperitoneally on days 6, 8, 12, and 15 ($n = 10$ mice per group). (**D**) CD8 T cell immune response. Splenocytes from the indicated groups obtained on day 7 after treatment were cocultured with media, $1 \times 10^6$ irradiated 4T1 cells (unrelated control tumor), or A20 cells (homologous tumor) for 24 hours. Intracellular IFN-γ was measured in $CD8^+$ T cells by flow cytometry as a percentage of $CD44^{hi}$ (memory CD8) T cells shown in dot plots and bar graph, summarizing data from three experiments ($n = 9$ mice per group). ****$P < 0.0001$, unpaired $t$ test.

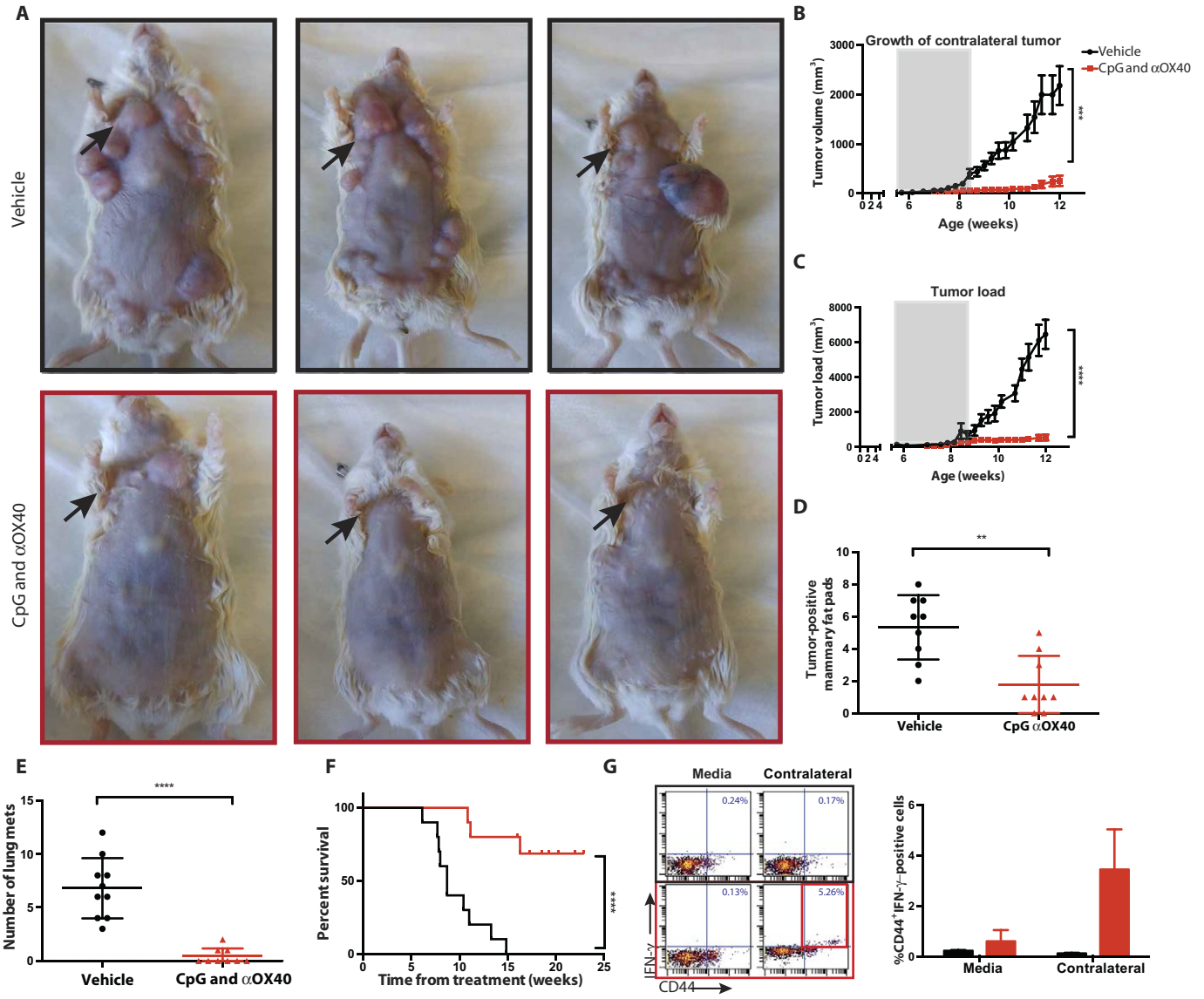


**Fig. 3. In situ vaccination with CpG and anti-OX40 is therapeutic in a spontaneous tumor model.** (**A**) MMTV-PyMT transgenic female mice were injected into the first arising tumor (black arrow) with either vehicle (top) or with CpG and αOX40 (bottom); pictures were taken on day 80. (**B**) CpG and αOX40 decrease the tumor size of a nontreated contralateral tumor. Growth curves represent the volume of a contralateral (untreated) tumor in mice that had two palpable tumors at the beginning of treatment. Mice treated by in situ vaccination (red; $n = 6$) or vehicle (black; $n = 6$). ***$P = 0.0008$, unpaired $t$ test. (**C**) CpG and αOX40 decrease the total tumor load. Growth curves represent the sum of the volume of 10 tumors from the different fat pads of each mouse, measured with calipers ($n = 10$ mice per group), and the window of treatment is indicated by the gray bar. ****$P < 0.0001$, unpaired $t$ test. (**D**) Time-matched quantification of the number of tumor-positive mammary fat pads. **$P = 0.011$, unpaired $t$ test ($n = 9$ mice per group). (**E**) Mice were sacrificed at the age of 80 days, and lungs were excised and analyzed ex vivo for the number of metastases (mets). ****$P < 0.0001$, unpaired $t$ test ($n = 10$ mice from vehicle-treated group; $n = 9$ mice with CpG and αOX40). (**F**) Survival plots of the treated mice. ****$P < 0.0001$. Data are means ± SEM ($n = 10$ mice per group). (**G**) CD8 T cell immune response. Splenocytes from the indicated groups obtained on days 7 to 15 after treatment were cocultured for 24 hours with either media or $1 \times 10^6$ irradiated tumor cells taken from an independent contralateral site on the body. Intracellular IFN-γ was measured in $CD8^+$ T cells by flow cytometry as shown in dot plots and bar graph, summarizing data as a percentage of $CD44^{hi}$ (memory CD8) T cells ($n = 3$ mice per group).

To further demonstrate the specificity of the antitumor response, we implanted tumors into mice at three different body sites: two with the A20 and one with CT26 (Fig. 4A). One A20 tumor site was then injected with CpG and anti-OX40 antibody. Both A20 tumors, the injected one and the noninjected one, regressed but the unrelated CT26 tumor continued to grow (Fig. 4A). In a reciprocal experiment, we injected mice with two CT26 tumors and one A20 tumor and treated one CT26 tumor. Once again, only the homologous distant tumors (in this case, CT26) regressed but not the unrelated A20 tumor (Fig. 4B). This result confirmed that the immune response induced by the therapy was tumor-specific. Furthermore, it demonstrated that in situ vaccination with these low doses of agents works by triggering an immune response in the microenvironment of the injected site rather than by diffusion of the injected agents to systemic sites.

Naturally arising tumors can show intratumoral antigenic heterogeneity. To test whether CpG and anti-OX40 treatment can trigger an

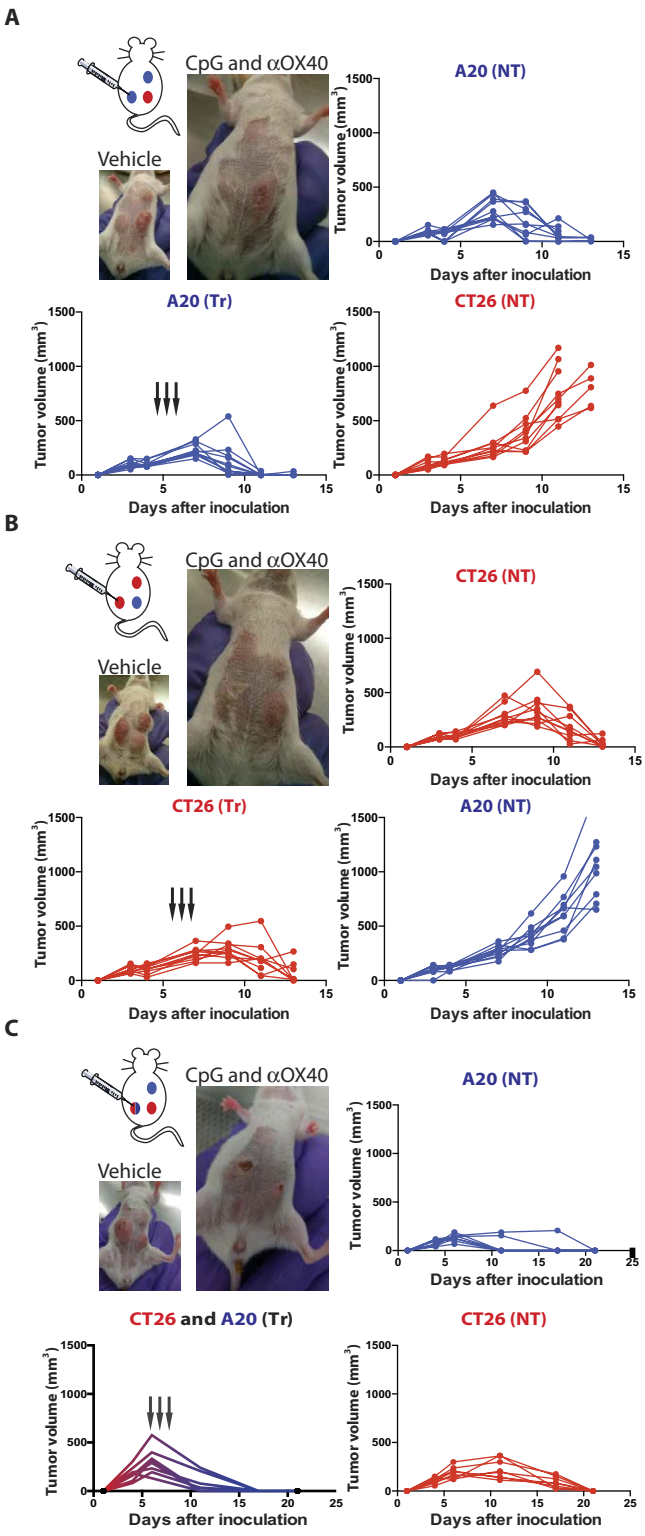


**Fig. 4. Immunizing effects of intratumoral CpG and anti-OX40 are local and tumor-specific.** (**A**) Three-tumor model. Each mouse was challenged with three tumors, two of them A20 lymphoma (blue) and one CT26 colon cancer (red). Mice were treated at the indicated times (black arrows). Tumor growth curves of the treated tumor (bottom left), the homologous nontreated A20 tumor (top right), and the heterologous CT26 tumor (bottom right). Photos of a representative mouse at day 11 after tumor challenge from the vehicle-treated group and from the group with A20 tumors treated with intratumoral CpG and αOX40 ($n$ = 10 mice per group) are shown. (**B**) Reciprocal three-tumor model with two CT26 tumors and one A20 tumor. Treatment was given to one CT26 tumor, and growth curves are shown for the treated CT26 tumor site (bottom right), the nontreated homologous CT26 tumor site (top right), and the heterologous A20 tumor (bottom right). Photos of a representative mouse from this experiment ($n$ = 10 mice per group) are shown. (**C**) Mixed three-tumor model. Each mouse was challenged with three tumors: one A20 (blue, top right abdomen), one CT26 (red, bottom right abdomen), and one mixture of A20 and CT26 tumor cells (blue and red gradient, left abdomen). Mice were treated only in the mixed tumor at the indicated times (black arrows). Tumor growth curves of the treated tumor (bottom left), the nontreated A20 tumor (top right), and the nontreated CT26 tumor (bottom right). Photos of a representative mouse at day 11 after tumor challenge from the vehicle-treated group (top) and at day 17 from the intratumoral CpG and αOX40 ($n$ = 8 mice per group) are shown.

immune response against multiple different tumor antigens at the same time, we injected mice with a mixture of A20 and CT26 tumor cells at one site, treated that site with local CpG and anti-OX40 antibody, and monitored two additional sites of tumor containing each of the single tumor cells (A20 and CT26, respectively). In situ vaccination of the mixed tumor site simultaneously induced immune responses protective of each of the respective other two pure tumor sites (Fig. 4C). These results demonstrate the power of in situ vaccination to simultaneously immunize against a panoply of different tumor antigens.

## Fc competency is required for efficacy of the anti-OX40 antibody

OX40 is expressed on both intratumoral FoxP3$^+$ $T_{regs}$ and activated $T_{effs}$ (Fig. 1B). The immunoenhancing activity of the anti-OX40 antibody could therefore be mediated by inhibition/depletion of $T_{regs}$, by stimulation of $T_{effs}$, or by a combination of both. We tested the anti-OX40 $T_{reg}$ depletion hypothesis by replacing it with an antibody against folate receptor 4 (FR4), a $T_{reg}$-depleting agent (fig. S12A) (*8*). $T_{regs}$ were partially depleted (43% reduction) by the anti-FR4 in combination with CpG, but no distant therapeutic effect occurred (Fig. 5A). We further investigated this question using mice genetically engineered to express diphtheria toxin under the FoxP3 promoter (*9*, *10*). Injection of diphtheria toxin led to complete $T_{reg}$ depletion in these mice (fig. S12B). However, when combined with intratumoral CpG, no distant therapeutic effect was observed (Fig. 5B). As others have shown, stimulation of $T_{regs}$ through OX40 can impair their function (*4*, *11*, *12*), which we confirm here (fig. S13, A and B). Therefore, we conclude that $T_{reg}$ stimulatory impairment but not depletion is involved in the mechanism of therapeutic synergy with CpG. To dissect the mechanism of these potent therapeutic effects, we compared two different forms of the anti-OX40 antibody that differ in their ability to bind to CD16: the activating Fc receptor on natural killer (NK) cells and macrophages. When used in combination with CpG, the native, Fc-competent version of anti-OX40 antibody induced systemic antitumor immunity, whereas the Fc-mutant version did not (Fig. 5A). We repeated the in situ vaccination experiment in mice deficient in the Fc common γ chain, a component of the activating Fc γ receptors I, III, and IV (*13*). Once again, in the absence of Fc receptor interaction, this time at the level of the host, the effect of in situ vaccination with CpG and anti-OX40 antibody was lost (fig. S14). These results could implicate ADCC (antibody-dependent cellular cytotoxicity) function of the antibody or alternatively an Fc-dependent agonistic action of the anti-OX40 antibody (*14*, *15*).

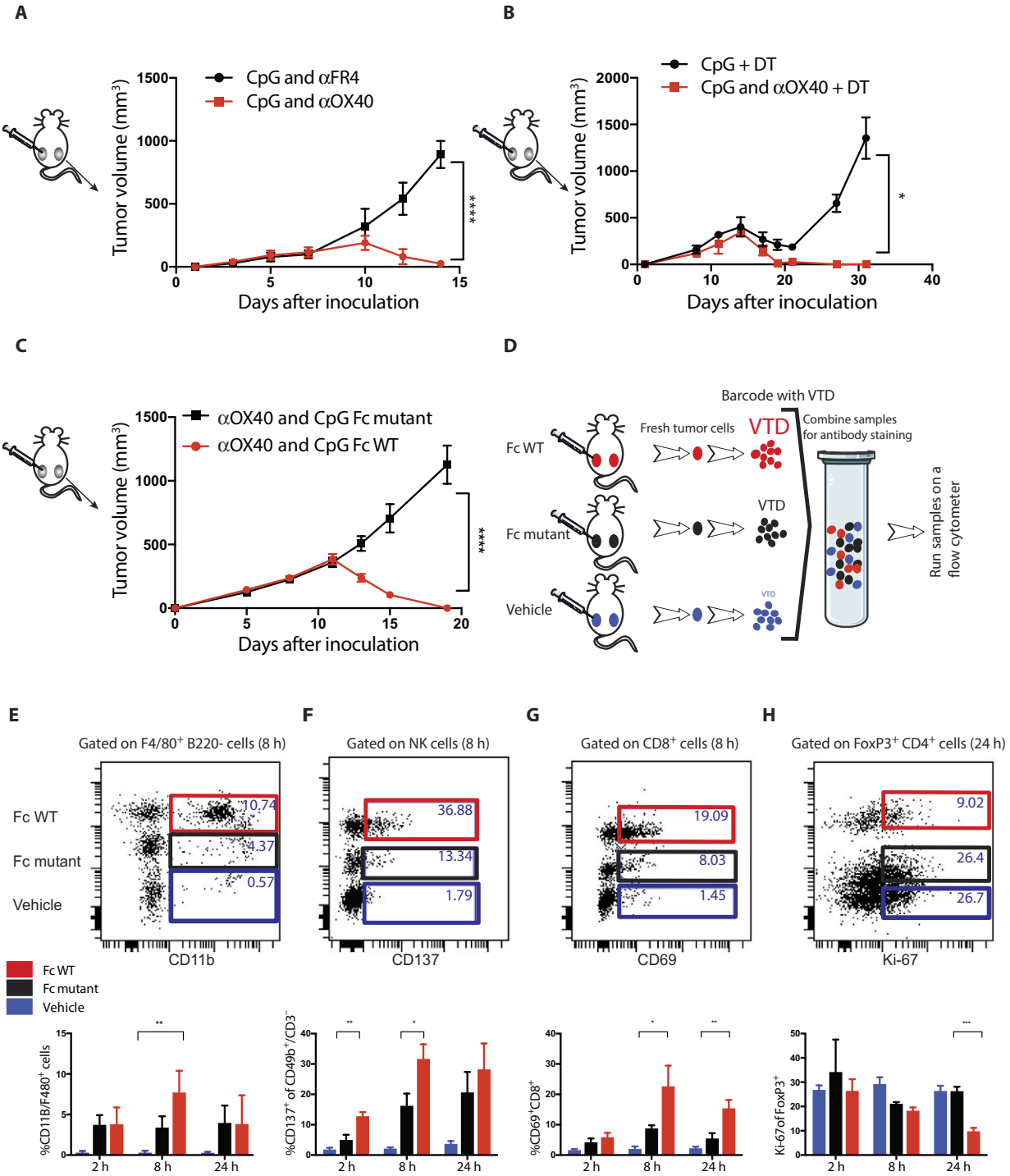


**Fig. 5. A competent Fc is required for the antitumor immune response.** (**A** and **B**) Effect of $T_{reg}$ depletion. (A) Tumors were implanted according to the schema in Fig. 2A. Mice were treated with either CpG and anti–folate receptor 4 (FR4) antibody (15 μg) or CpG and αOX40 as described in Fig. 2A, and the NT was measured over time. ****$P <$ 0.0001, unpaired *t* test ($n = 10$ mice per group). (B) DEREG mice were implanted with B16-F10 melanoma cells ($0.05 \times 10^6$) on both the right and left sides of the abdomen. Diphtheria toxin (DT; 1 μg) was injected intraperitoneally on days 1, 2, 7, and 14. CpG or combination of CpG and anti-OX40 was given on days 7, 9, and 11. The NT was measured over time. *$P = 0.0495$, unpaired *t* test ($n = 4$ mice per group). (**C**) A20 cells were inoculated and treated as described in Fig.2A, tumor volumes were measured after treatment of CpG with either αOX40 rat immunoglobulin G1 (IgG1) (red) or αOX40 rat IgG1 Fc mutant (black). ****$P < 0.0001$, unpaired *t* test ($n = 10$ mice per group). WT, wild type. (**D**) Tumors from control and treated mice were excised at the indicated times after a single treatment, and the cell populations from the different groups were differentially labeled (barcoded) with two different levels of violet tracking dye (VTD) and mixed together, stained, and analyzed as a single sample [$n = 3$ mice per group (C to F)]. (**E** to **H**) Dot plots for single time point and bar graphs for replicates of multiple time points. (E) Number of F4/80 $CD11b^+$ myeloid cells. **$P = 0.009$ (8 h), Fc WT versus vehicle. (F) CD137 expression on natural killer (NK) cells. **$P = 0.0035$ (2 h), *$P = 0.0343$ (8 h), unpaired *t* test, Fc WT versus Fc mutant. (G) CD69 expression on $CD8^+$ T cells. *$P = 0.025$ (8 h), **$P = 0.0064$ (24 h), unpaired *t* test, Fc WT versus Fc mutant. (H) $T_{reg}$ cell proliferation. ***$P = 0.0003$ (24 h), unpaired *t* test, Fc WT versus Fc mutant.

Therefore, we examined immune cells in the tumor microenvironment during the early phases of treatment with intratumoral CpG and compared the changes induced with the Fc-competent to those induced by the Fc-mutant version of the anti-OX40 antibody. Early after in situ vaccination, within 24 hours, the tumor-infiltrating cell populations from animals treated with Fc-competent or Fc-mutant antibodies were barcoded (*16*), pooled, and then costained by a panel of antibodies to identify subsets of immune cells and their activation states (Fig. 5B). The cell populations derived from the different treatment groups were then separately identified by their barcodes. In response to the anti-OX40 antibody with the native Fc, there was an increase in myeloid cell infiltration (Fig. 5C), a cell population important in the cross-talk between CpG and the T cells (see above; Fig. 1, F and G). NK cells showed an Fc-dependent up-regulation of their CD137 activation marker (Fig. 5D). In addition, the Fc-competent but not the Fc-mutant antibody induced activation of a population of CD8 T cells, as indicated by increased CD69 expression (Fig. 5E). $T_{regs}$ were inhibited in their proliferation by comparison to those exposed to the antibody with the mutated Fc region (Fig. 5F). Neither $T_{regs}$ nor $T_{effs}$ were killed by the Fc-competent antibody (fig. S15). These early cellular changes occurred only in the tumor microenvironment of the treated site and were not evident at other sites throughout the mouse (fig. S1B). These results imply that anti-OX40 antibodies, in conjunction with TLR ligands, can induce therapeutic systemic antitumor immune responses by a combination of NK cell activation, $T_{reg}$ inhibition, and $T_{eff}$ activation, all at the treated tumor site.

## DISCUSSION

We have developed a practical strategy for immunotherapy of cancer. It takes advantage of the preexisting T cell immune repertoire within the tumor microenvironment. The combination of a TLR agonist and an activating antibody against OX40 amplifies these antitumor T cells and induces their action throughout the body against tumor at nontreated sites. This in situ vaccination does not require knowledge of the tumor antigens. Potential drawbacks include reliance on adequate immune infiltrates and the availability of a suitable injectable site of tumor.

After screening a series of immune activators and checkpoint antibodies, we identified the combination of CpG oligodeoxynucleotide (TLR9 ligand) and anti-OX40 antibody to be the most potent form of in situ vaccination in multiple mouse models. TLR7/8 agonists could substitute for CpG, but checkpoint antibodies against PD1, PDL1, or CTLA4 could not substitute for anti-OX40.

The synergistic therapeutic effect between locally injected CpG and anti-OX40 antibodies is explained by the fact that CpG induced the expression of the OX40 target on $CD4^+$ T cells in the tumor microenvironment. CpG also induced OX40 in $CD4^+$ T cells in the tumor microenvironment of human lymphoma tumors, and therefore, our results are likely to translate to human cancer.

It has been reported that local intratumoral administration of CpG together with systemic antibody against IL-10R leads to rejection of the injected tumor and distant metastases (*17*, *18*). This combination was shown to deflect M2 to M1 macrophages in the tumor microenvironment (*19*). Therefore, we examined the requirement for induction of OX40 expression on CD4 T cells by CpG in our system. We found that it was dependent on cytokines secreted by myeloid cells, including IL-12, IFN-γ, or TNF-α but not IL-2, IL-4, IL-10, and GM-CSF.

The therapeutic effect at the distant sites was specific for antigens expressed by the tumor at the injected site that were shared with the tumor cells at the distant sites. This result not only established the tumor specificity of the immunization but also proved that it was the local effect of the injected agents in the tumor microenvironment rather than their systemic delivery that triggered the systemic antitumor immune response.

Autoimmune toxicities are a common complication of systemically administered immune checkpoint antibodies (*20*–*24*). In contrast, direct injection of the antibodies into the tumor at very low doses can avoid these side effects (*25*, *26*). In our experiments, in situ injection of microgram quantities of immune stimulants and checkpoint antibodies proved to be sufficient to induce the required local immune modulation, resulting in a systemic antitumor immune response.

A major challenge in tumor immunotherapy lies in breaking tumor immune tolerance. In a previous report, we showed that depletion of tumor-specific $T_{regs}$ by the addition of anti-CTLA4 antibody was associated with enhanced antitumor efficacy (*27*). However, we find here that activating antibody against OX40 is sufficient. It is known that OX40 is expressed on both $T_{regs}$ and $T_{effs}$ in the tumor microenvironment, and as we now realize, OX40 can be further induced on $CD4^+$ T cells in response to CpG. Modulating both $T_{effs}$ and $T_{regs}$ is essential to obtain therapeutic effect (*28*–*30*). Antibodies to OX40 costimulate $T_{effs}$ (*31*–*37*), and they also inhibit the function of $T_{regs}$ (*12*, *27*, *38*–*40*).

Having demonstrated the potent therapeutic efficacy of in situ immunotherapy in several different transplanted tumor types, we assessed this form of therapy in a spontaneous arising tumor. The MMTV-PyMT mouse model recapitulates several of the characteristics of virulent human breast cancer, among them showing histology similarity, having loss of estrogen and progesterone receptors, and overexpressing ErbB2/Neu and cyclin D1 (*6*, *41*, *42*). Although the tumors within a mouse arise independently in different mammary glands, they all share the expression of the PyMT antigen (*43*). Injection of CpG and anti-OX40 antibody into the first tumor to occur in each mouse resulted in reduced tumor load in the other mammary fat pads and prevented lung metastases. These results demonstrate the potency of the in situ vaccine maneuver in a situation of spontaneous cancer-driven by a strong oncogene, suggesting the possibility of a direct application to human cancer. By analogy to the genetically prone mice, we can imagine administering an in situ vaccine at the site of the primary tumor before surgery in patients at high risk for the occurrence of metastatic disease and/or in patients genetically prone to develop second primary cancers, such as those with inherited mutation in the BRCA genes.

The CpG used here, SD-101, is currently being tested in patients as a single agent and in combination with other therapeutic modalities (NCT02927964, NCT02266147, NCT01745354, NCT02254772, and NCT02521870). Anti-OX40 antibody is also currently being studied in phase 1 clinical trials (NCT02559024, NCT01644968, NCT02221960, NCT02318394, NCT02274155, NCT01862900, NCT01303705, and NCT02205333). The results from our current preclinical studies provide strong rationale for combining CpG with agonistic anti-OX40 antibodies in a therapeutic format of in situ vaccination in patients with lymphoma and solid tumors. As we have shown, CpG and anti-OX40 antibodies work locally at very low doses that should provide the advantage of avoiding toxicities that occur with their systemic administration.

## MATERIALS AND METHODS

### Study design

Our objective was to develop a new immunotherapy for cancer by using the tumor itself as a source of antigen, of immune reactive cells and as a site for injecting immune activating agents—in situ vaccination. Our general strategy was to implant the same syngeneic tumor at two separate sites in the body of mice. One tumor was then injected with the test agents, and tumor size was measured in both the treated and nontreated sites. Using this assay for abscopal therapeutic effects, we identified the combination of unmethylated CG–enriched oligodeoxynucleotide (CpG)—a TLR9 ligand—and an agonistic antibody against OX40 as the most promising immunostimulatory regimen.

Because transplanted syngeneic tumor models lack certain aspects of naturally occurring tumors, we also studied the effects of our combination in a spontaneous model of breast cancer. This model is driven by the polyoma middle T oncogene under the control of the MMTV promoter, and the female mice develop independently arising breast cancers in all of their mammary glands between 5 and 14 weeks of age.

We observed the mice, and when their first breast cancer tumor arose, we injected it with our combination of CpG and anti-OX40 antibody. Each mouse was then monitored for the regression of simultaneously present second tumors, for the occurrence of newly arising tumors, for metastatic disease in their lungs, and for their survival. Data were analyzed by Kaplan-Meier curves with events scored as the time to reach 2 cm in the largest diameter at which time the mouse was sacrificed. Data were analyzed using the log-rank test.

We studied the mechanism of the therapy by examining the requirement for T cells and their subsets, including $T_{regs}$, and by the requirement for Fc function of the anti-OX40 antibody. These requirements were tested by depleting specific T cells and by substituting an Fc mutant for the native anti-OX40 antibody.

In all therapy experiments, to ensure similar tumor sizes in all treatment groups, mice were randomized only after tumors were established. To ensure statistical power, experimental groups were typically composed of 10 animals each. For each experiment, mice numbers, statistical tests, and numbers of experimental replicates are described in the figure legends. Data include all outliers. Investigators were not blinded during evaluation of the in vivo experiments. Raw data for all therapy experiments are provided in table S1.

### Reagents

CpG SD-101 was provided by Dynavax Technologies. Anti-mouse CD8a (clone 2.43) and anti-mouse CD4 (clone GK1.5) antibodies were purchased from BioXCell. Anti-OX40 (CD134) monoclonal antibody (mAb) [rat immunoglobulin G1 (IgG1), clone OX86; European Collection of Cell Cultures], isotype control rat hybridoma, SFR8-B6 [American Type Culture Collection (ATCC) HB-152] were produced as ascites in severe combined immunodeficient mice by Bionexus. Fc-silent Anti-OX40 (CD134) mAb was purchased from Absolute Antibody.

The following mAbs were used for flow cytometry: CD4-PerCP (peridinin chlorophyll protein) Cy5.5, CD3-PerCP Cy5.5, or BV786; CD4-BV650, CD8a–FITC (fluorescein isothiocyanate), or APC (allophycocyanin) H7; CD44-APC, IFN-γ–PE (phycoerythrin), B220-PerCP Cy5.5, CD49b-PE CY7, CD69-BV605, CD137-PE, and ICOS (CD278)–PE Cy7; FoxP3-PE; and Ki-67–BV711. These antibodies and their isotype controls were purchased from BD Biosciences, BioLegend, or eBioscience.

### Cell lines and mice

A20 B cell lymphoma, B16-F10 melanoma, and CT26 colon carcinoma lines were obtained from ATCC, and 4T1-Luc breast carcinoma cell line was a gift from the S. Strober laboratory and the C. Contag laboratory (both at Stanford University). Tumor cells were cultured in complete medium (RPMI 1640; Dulbecco's modified Eagle's medium for B16-F10; Cellgro) containing 10% fetal bovine serum (FBS; HyClone), penicillin (100 U/ml), streptomycin (100 μg/ml), and 50 μM 2-mercaptoethanol (Gibco). Cell lines were routinely tested for mycoplasma contamination.

Six- to 8-week-old female BALB/c and C57BL/6 were purchased from Charles River (www.criver.com). FVB/N-Tg(MMTV-PyVT)634Mul/J male FVB/NJ females [C57BL/6-Tg(Foxp3-DTR/EGFP)23.2Spar; also known as DEREG mice] were purchased from The Jackson Laboratory (http://jaxmice.jax.org/). Mice were housed in the Laboratory Animal Facility of the Stanford University Medical Center (Stanford, CA). All experiments were approved by the Stanford administrative panel on laboratory animal care and conducted in accordance with Stanford University animal facility guidelines.

### Tumor inoculation and animal studies

A20, CT26, 4T1, and B16-F10 tumor cells ($5 \times 10^6$, $0.5 \times 10^6$, $0.01 \times 10^6$, and $0.05 \times 10^6$, respectively) were injected subcutaneously at sites on both the right and left sides of the abdomen. When tumor size reached 0.5 to 0.7 cm in the largest diameter, mice were randomized to the experimental groups. CpG and anti-OX40 were injected into the tumor only on the right side of the animals in a volume of 50 μl. Tumor size was monitored on both sides of the animals with a digital caliper (Mitutoyo) every 2 to 3 days and expressed as volume (length × width × height). Mice were sacrificed when tumor size reached 1.5 cm in the largest diameter as per guidelines. All mice that developed tumors on both sides of the abdomen were included in the experiments. The investigator was not blinded to the group allocation during the experiment and/or when assessing the outcome.

4T1 tumor–challenged mice were analyzed for lung metastasis by injecting India ink through the trachea after euthanasia. Lungs were then excised, washed once in water, and fixed in Fekete's solution (100 ml of 70% alcohol, 10 ml of formalin, and 5 ml of glacial acetic acid) at room temperature. Surface metastases subsequently appeared as white nodules at the surface of black lungs and were counted under a microscope.

DEREG mice were implanted with B16-F10 tumor cells as described above. Diphtheria toxin (1 μg; Sigma-Aldrich) was injected intraperitoneally on days 1, 2, 7, and 14 after tumor implantations. CpG or combination of CpG and anti-OX40 was given on days 7, 9, and 11 after tumor implantations.

### Flow cytometry

Cells were surface-stained in phosphate-buffered saline (PBS), 1% bovine serum albumin, and 0.01% sodium azide, fixed in 2% paraformaldehyde, and analyzed by flow cytometry on a FACSCalibur or LSR II (BD Biosciences). Data were stored and analyzed using Cytobank (www.cytobank.org).

### Multiplex flow cytometry—fluorescent cell barcoding

Excised tumors from mice treated with an Fc-competent OX40 antibody, an Fc-silent OX40 antibody (Absolute Antibody), or saline were mechanically processed into single-cell suspensions and barcoded using three different concentrations of CellTrace Violet Proliferation

reagent (Life Technologies) ranging from 5 to 0.1 μM. Once barcoded, equal numbers of cells from each group were combined and stained with LIVE/DEAD Fixable Green Dead Cell Stain (Life Technologies) followed by antibodies against surface antigens to determine populations of interest such as tumor (B220), T cells (CD3, CD4, and CD8), and NK cells (CD56) as well as those to look at activation (CD69, CD137, and ICOS). Cells were then fixed and permeabilized (eBioscience), stained for FoxP3 ($T_{regs}$) and Ki-67 (proliferation), and analyzed by flow cytometry.

### IFN-γ production assay

Single-cell suspensions were made from spleens of treated mice (on day 7 after treatment), and red cells were lysed with ammonium chloride and potassium buffer (Quality Biological). Splenocytes were then cocultured with $1 \times 10^6$ irradiated A20 or 4T1 cells for 24 hours at 37°C and 5% $CO_2$ in the presence of 0.5 μg of anti-mouse CD28mAb (BD Pharmingen). Monensin (GolgiStop; BD Biosciences) was added for the last 5 to 6 hours. Intracellular IFN-γ expression was assessed using BD Cytofix/Cytoperm Plus Kit as per the manufacturer's instructions.

### Depletion of CD4 and CD8 T cells

Anti-CD4 (clone GK1.5, rat IgG2b) and anti-CD8 (clone 2.43, rat IgG2b) mAbs (BioXCell) were injected 2 days and 1 day before therapy, on the day therapy was begun, and at 5, 8, and 19 days after the beginning of therapy at a dose of 0.5 or 0.1 mg per injection for CD4 and CD8, respectively. The depletion conditions were validated by flow cytometry of blood showing specific depletion of more than 95% of each respective cell subset.

### In vitro assessment of OX40 expression

Fresh tumor cells were excised from mice, processed into single-cell suspensions, and incubated for 48 hours with CpG (1 μg/ml). Cells were then stained for the surface antigens CD3, CD4, CD8, and OX40. They were then fixed and permeabilized using reagents from eBioscience, followed by FoxP3 staining. T cell isolation and depletion of T cells and CD11b- and CD11c-expressing cells from tumors used kits from Miltenyi Biotec.

### Tetramer staining

PE-conjugated H-2Ld tetramer to peptide SPSYVYHQF (MuLV env gp70, 423 to 431) was purchased from ProImmune, and PE-conjugated H-2Ld tetramer to peptide IASNENMETMESSTLE (influenza nucleoprotein 365 to 380) was a gift from the M. Davis laboratory (Stanford University). Antibodies were used at 5 μg/ml, and tetramer staining was performed in fluorescence-activated cell sorting buffer for 10 min at room temperature and followed by surface staining on ice for 20 min.

### Activation and suppression assay

#### *T cell activation assay*

C57BL/6 splenocytes were isolated, violet tracking dye (VTD)–labeled, and incubated in the presence of anti-CD3 antibody (0.05 μg/ml) for 72 hours with or without anti-OX40 antibodies. T cell activation and proliferation were determined by VTD dilution and the expression of the activation marker CD69.

#### *$T_{reg}$ suppression assay*

To determine the impact of OX40 antibodies on $T_{reg}$ activity, VTD-labeled splenic cells were cocultured with OX40–KO (knockout) $T_{regs}$ [OX40 wild-type (WT) splenocytes/OX40 KO $T_{reg}$ = 1:1]. Cells were cocultured in 96-well plate in the presence of anti-CD3 and anti-CD28 beads (Thermo Fisher Scientific) for 96 hours with or without anti-OX40 antibody (1 μg/ml). Proliferation of the WT-labeled $T_{effs}$ was measured by flow cytometry and calculated by VTD dilution. $T_{regs}$ were isolated using kits from Miltenyi Biotec.

### PET imaging

PET imaging of mice was performed using the microPET/CT hybrid scanner (Inveon, Siemens). PET images were reconstructed using 2 iterations of three-dimensional ordered subset expectation maximization (3DOSEM) algorithm (12 subsets) and 18 iterations of the accelerated version of 3D-MAP (that is, FASTMAP)—matrix size of 128 × 128 × 159. Computed tomography (CT) images were acquired just before each PET scan to enable attenuation correction of the PET data set and provided an anatomic reference for the PET image. Mice were anesthetized using isoflurane gas (2.0 to 3.0% for induction and 2.0 to 2.5% for maintenance). $^{64}$Cu-DOTA-OX40 (80 to 110 μCi; radiochemical purity of 99% as determined by thin-layer chromatography; and specific activity is 185 MBq/mg) was administered intravenously via the tail vein 16 hours after CpG and vehicle intratumoral injections. Static PET scans (10 min) were acquired 16 hours after intravenous administration of $^{64}$Cu-DOTA-OX40 (40 hours after intratumoral injections). Once reconstructed using a 3DOSEM algorithm, PET images were coregistered with CT images to generate figures using the IRW (Inveon Research Workplace) image analysis software (version 4.0; Siemens).

### Up-regulation of OX40 on CD4 T cells infiltrating human B cell tumors

Tumor samples from patients with Follicular and Mantle Cell B cell lymphoma who were part of ongoing clinical trials [Stanford International Review Board (IRB) protocols IRB-31224, IRB-36750, and IRB-5089] were available for in vitro analysis. Single-cell suspensions were incubated for either 24 or 48 hours in RPMI medium containing 5% FBS (HyClone), penicillin (100 U/ml), and streptomycin (100 μg/ml) and then stained for T cell surface antigens including CD3, CD4, CD8, and OX40. They were also fixed and permeabilized using reagents from eBioscience and then stained for FoxP3. For in vitro stimulation studies, CpG at a concentration of 1 μg/ml was added to the medium.

For response of tumor-infiltrating cells to CpG in vivo, a sample was obtained from a site of tumor that had been injected with CpG (3 mg) 24 hours before and compared to a site of tumor that had not been injected. Both of these sites shared as part of the clinical protocol an exposure to low-dose radiation (2 grays on each for two successive days). Single-cell suspensions were rested in the medium with no further exposure to CpG for 24 hours before analysis of OX40 expression by flow cytometry.

### Statistical analysis

Prism software (GraphPad) was used to analyze tumor growth and to determine statistical significance of differences between groups by applying an unpaired Student's *t* test. *P* values <0.05 were considered significant. The Kaplan-Meier method was used for survival analysis. *P* values were calculated using the log-rank test (Mantel-Cox).

## SUPPLEMENTARY MATERIALS

www.sciencetranslationalmedicine.org/cgi/content/full/10/426/eaan4488/DC1

Fig. S1. In situ vaccination with a TLR9 ligand induces the local expression of OX40 but not that of PD1 or CTLA4.

Fig. S2. CpG induces the expression of OX40 on CD4 T cells.

Fig. S3. Cytokines are playing a role in the CpG T cell cross-talk.
Fig. S4. Intracellular IFN-γ production of $CD4^+$ cells.
Fig. S5. Frequency of T cell subsets.
Fig. S6. Tumor recurrence is sensitive to treatment with anti-OX40 and CpG.
Fig. S7. Resiquimod (R848) in combination with anti-OX40 and anti-PD1/PDL1 in combination with CpG.
Fig. S8. In situ vaccination with CpG and anti-OX40 is effective against breast carcinoma, colon cancer, and melanoma.
Fig. S9. Dose de-escalation of CpG and αOX40 antibody.
Fig. S10. Systemic administration of anti-αOX40 antibody.
Fig. S11. Long-term memory in cured mice.
Fig. S12. Confirmation of $T_{reg}$ depletion from the tumor.
Fig. S13. Anti-OX40 antibody stimulates $T_{effs}$ and inhibits function of $T_{regs}$.
Fig. S14. Requirement for Fc competency of the anti-OX40 antibody.
Fig. S15. Neither $T_{regs}$ nor $T_{effs}$ are depleted by anti-OX40 antibody.
Table S1. Primary data.

## REFERENCES AND NOTES


1. E. M. Sotomayor, I. Borrello, E. Tubb, F.-M. Rattis, H. Bien, Z. Lu, S. Fein, S. Schoenberger, H. I. Levitsky, Conversion of tumor-specific $CD4^+$ T-cell tolerance to T-cell priming through in vivo ligation of CD40. *Nat. Med.* **5**, 780–787 (1999).
2. K. Staveley-O'Carroll, E. Sotomayor, J. Montgomery, I. Borrello, L. Hwang, S. Fein, D. Pardoll, H. Levitsky, Induction of antigen-specific T cell anergy: An early event in the course of tumor progression. *Proc. Natl. Acad. Sci. U.S.A.* **95**, 1178–1183 (1998).
3. T. So, M. Croft, Cutting edge: OX40 inhibits TGF-beta- and antigen-driven conversion of naive CD4 T cells into $CD25^+Foxp3^+$ T cells. *J. Immunol.* **179**, 1427–1430 (2007).
4. M. D. Vu, X. Xiao, W. Gao, N. Degauque, M. Chen, A. Kroemer, N. Killeen, N. Ishii, X. C. Li, OX40 costimulation turns off $Foxp3^+$ Tregs. *Blood* **110**, 2501–2510 (2007).
5. J. D. Fontenot, J. P. Rasmussen, L. M. Williams, J. L. Dooley, A. G. Farr, A. Y. Rudensky, Regulatory T cell lineage specification by the forkhead transcription factor Foxp3. *Immunity* **22**, 329–341 (2005).
6. E. Y. Lin, J. G. Jones, P. Li, L. Zhu, K. D. Whitney, W. J. Muller, J. W. Pollard, Progression to malignancy in the polyoma middle T oncoprotein mouse breast cancer model provides a reliable model for human diseases. *Am. J. Pathol.* **163**, 2113–2126 (2003).
7. C. T. Guy, R. D. Cardiff, W. J. Muller, Induction of mammary tumors by expression of polyomavirus middle T oncogene: A transgenic mouse model for metastatic disease. *Mol. Cell. Biol.* **12**, 954–961 (1992).
8. T. Yamaguchi, K. Hirota, K. Nagahama, K. Ohkawa, T. Takahashi, T. Nomura, S. Sakaguchi, Control of immune responses by antigen-specific regulatory T cells expressing the folate receptor. *Immunity* **27**, 145–159 (2007).
9. K. Lahl, T. Sparwasser, In vivo depletion of $FoxP3^+$ Tregs using the DEREG mouse model. *Methods Mol. Biol.* **707**, 157–172 (2011).
10. K. Lahl, C. Loddenkemper, C. Drouin, J. Freyer, J. Arnason, G. Eberl, A. Hamann, H. Wagner, J. Huehn, T. Sparwasser, Selective depletion of $Foxp3^+$ regulatory T cells induces a scurfy-like disease. *J. Exp. Med.* **204**, 57–63 (2007).
11. K. S. Voo, L. Bover, M. L. Harline, L. T. Vien, V. Facchinetti, K. Arima, L. W. Kwak, Y. J. Liu, Antibodies targeting human OX40 expand effector T cells and block inducible and natural regulatory T cell function. *J. Immunol.* **191**, 3641–3650 (2013).
12. Y. Bulliard, R. Jolicoeur, J. Zhang, G. Dranoff, N. S. Wilson, J. L. Brogdon, OX40 engagement depletes intratumoral Tregs via activating FcγRs, leading to antitumor efficacy. *Immunol. Cell Biol.* **92**, 475–480 (2014).
13. F. Nimmerjahn, J. V. Ravetch, Fcγ receptors as regulators of immune responses. *Nat. Rev. Immunol.* **8**, 34–47 (2008).
14. F. Li, J. V. Ravetch, Inhibitory Fcγ receptor engagement drives adjuvant and anti-tumor activities of agonistic CD40 antibodies. *Science* **333**, 1030–1034 (2011).
15. D. Zhang, M. V. Goldberg, M. L. Chiu, Fc engineering approaches to enhance the agonism and effector functions of an anti-OX40 antibody. *J. Biol. Chem.* **291**, 27134–27146 (2016).
16. P. O. Krutzik, G. P. Nolan, Fluorescent cell barcoding in flow cytometry allows high-throughput drug screening and signaling profiling. *Nat. Methods* **3**, 361–368 (2006).
17. A. Burocchi, P. Pittoni, A. Gorzanelli, M. P. Colombo, S. Piconese, Intratumor OX40 stimulation inhibits IRF1 expression and IL-10 production by Treg cells while enhancing CD40L expression by effector memory T cells. *Eur. J. Immunol.* **41**, 3615–3626 (2011).
18. A. P. Vicari, C. Chiodoni, C. Vaure, S. Ait-Yahia, C. Dercamp, F. Matsos, O. Reynard, C. Taverne, P. Merle, M. P. Colombo, A. O'Garra, G. Trinchieri, C. Caux, Reversal of tumor-induced dendritic cell paralysis by CpG immunostimulatory oligonucleotide and anti–interleukin 10 receptor antibody. *J. Exp. Med.* **196**, 541–549 (2002).
19. C. Guiducci, A. P. Vicari, S. Sangaletti, G. Trinchieri, M. P. Colombo, Redirecting in vivo elicited tumor infiltrating macrophages and dendritic cells towards tumor rejection. *Cancer Res.* **65**, 3437–3446 (2005).
20. S. N. Gettinger, L. Horn, L. Gandhi, D. R. Spigel, S. J. Antonia, N. A. Rizvi, J. D. Powderly, R. S. Heist, R. D. Carvajal, D. M. Jackman, L. V. Sequist, D. C. Smith, P. Leming, D. P. Carbone, M. C. Pinder-Schenck, S. L. Topalian, F. S. Hodi, J. A. Sosman, M. Sznol, D. F. McDermott, D. M. Pardoll, V. Sankar, C. M. Ahlers, M. Salvati, J. M. Wigginton, M. D. Hellmann, G. D. Kollia, A. K. Gupta, J. R. Brahmer, Overall survival and long-term safety of nivolumab (anti–programmed death 1 antibody, BMS-936558, ONO-4538) in patients with previously treated advanced non-small-cell lung cancer. *J. Clin. Oncol.* **33**, 2004–2012 (2015).
21. D. F. McDermott, C. G. Drake, M. Sznol, T. K. Choueiri, J. D. Powderly, D. C. Smith, J. R. Brahmer, R. D. Carvajal, H. J. Hammers, I. Puzanov, F. S. Hodi, H. M. Kluger, S. L. Topalian, D. M. Pardoll, J. M. Wigginton, G. D. Kollia, A. Gupta, D. McDonald, V. Sankar, J. A. Sosman, M. B. Atkins, Survival, durable response, and long-term safety in patients with previously treated advanced renal cell carcinoma receiving nivolumab. *J. Clin. Oncol.* **33**, 2013–2020 (2015).
22. E. Gonzalez-Rodriguez, D. Rodriguez-Abreu; Spanish Group for Cancer Immuno-Biotherapy, Immune checkpoint inhibitors: Review and management of endocrine adverse events. *Oncologist* **21**, 804–816 (2016).
23. L. Kottschade, A. Brys, T. Peikert, M. Ryder, L. Raffals, J. Brewer, P. Mosca, S. Markovic; Midwest Melanoma Partnership, A multidisciplinary approach to toxicity management of modern immune checkpoint inhibitors in cancer therapy. *Melanoma Res.* **26**, 469–480 (2016).
24. A. Sgambato, F. Casaluce, P. C. Sacco, G. Palazzolo, P. Maione, A. Rossi, F. Ciardiello, C. Gridelli, Anti PD-1 and PDL-1 immunotherapy in the treatment of advanced non-small cell lung cancer (NSCLC): A review on toxicity profile and its management. *Curr. Drug Saf.* **11**, 62–68 (2016).
25. M. F. Fransen, T. C. van der Sluis, F. Ossendorp, R. Arens, C. J. M. Melief, Controlled local delivery of CTLA-4 blocking antibody induces $CD8^+$ T-cell–dependent tumor eradication and decreases risk of toxic side effects. *Clin. Cancer Res.* **19**, 5381–5389 (2013).
26. A. Marabelle, H. Kohrt, R. Levy, Intratumoral anti-CTLA-4 therapy: Enhancing efficacy while avoiding toxicity. *Clin. Cancer Res.* **19**, 5261–5263 (2013).
27. A. Marabelle, H. Kohrt, I. Sagiv-Barfi, B. Ajami, R. C. Axtell, G. Zhou, R. Rajapaksa, M. R. Green, J. Torchia, J. Brody, R. Luong, M. D. Rosenblum, L. Steinman, H. I. Levitsky, V. Tse, R. Levy, Depleting tumor-specific Tregs at a single site eradicates disseminated tumors. *J. Clin. Invest.* **123**, 2447–2463 (2013).
28. S. Piconese, B. Valzasina, M. P. Colombo, OX40 triggering blocks suppression by regulatory T cells and facilitates tumor rejection. *J. Exp. Med.* **205**, 825–839 (2008).
29. J. Ziai, G. Frantz, L. Zhang, C. Kozlowski, H. Gilbert, J. Smith, M. Kowanetz, J. M. Kim, M. Huseni, Prevalence analysis of OX40-positive cell populations in solid tumors. *J. Immunother. Cancer* **3** (suppl. 2), P113 (2015).
30. S. Mallett, S. Fossum, A. N. Barclay, Characterization of the MRC OX40 antigen of activated CD4 positive T lymphocytes—A molecule related to nerve growth factor receptor. *EMBO J.* **9**, 1063–1068 (1990).
31. K. Sugamura, N. Ishii, A. D. Weinberg, Therapeutic targeting of the effector T-cell co-stimulatory molecule OX40. *Nat. Rev. Immunol.* **4**, 420–431 (2004).
32. T. A. Triplett, C. G. Tucker, K. C. Triplett, Z. Alderman, L. Sun, L. E. Ling, E. T. Akporiaye, A. D. Weinberg, STAT3 signaling is required for optimal regression of large established tumors in mice treated with anti-OX40 and TGFβ receptor blockade. *Cancer Immunol. Res.* **3**, 526–535 (2015).
33. K. A. Murphy, M. G. Lechner, F. E. Popescu, J. Bedi, S. A. Decker, P. Hu, J. R. Erickson, M. G. O'Sullivan, L. Swier, A. M. Salazar, M. R. Olin, A. L. Epstein, J. R. Ohlfest, An in vivo immunotherapy screen of costimulatory molecules identifies Fc-OX40L as a potent reagent for the treatment of established murine gliomas. *Clin. Cancer Res.* **18**, 4657–4668 (2012).
34. S. Murata, B. H. Ladle, P. S. Kim, E. R. Lutz, M. E. Wolpoe, S. E. Ivie, H. M. Smith, T. D. Armstrong, L. A. Emens, E. M. Jaffee, R. T. Reilly, OX40 costimulation synergizes with GM-CSF whole-cell vaccination to overcome established $CD8^+$ T cell tolerance to an endogenous tumor antigen. *J. Immunol.* **176**, 974–983 (2006).
35. A. Curti, M. Parenza, M. P. Colombo, Autologous and MHC class I–negative allogeneic tumor cells secreting IL-12 together cure disseminated A20 lymphoma. *Blood* **101**, 568–575 (2003).
36. A. Song, J. Song, X. Tang, M. Croft, Cooperation between CD4 and CD8 T cells for anti-tumor activity is enhanced by OX40 signals. *Eur. J. Immunol.* **37**, 1224–1232 (2007).
37. D. Hirschhorn-Cymerman, S. Budhu, S. Kitano, C. Liu, F. Zhao, H. Zhong, A. M. Lesokhin, F. Avogadri-Connors, J. Yuan, Y. Li, A. N. Houghton, T. Merghoub, J. D. Wolchok, Induction of tumoricidal function in $CD4^+$ T cells is associated with concomitant memory and terminally differentiated phenotype. *J. Exp. Med.* **209**, 2113–2126 (2012).
38. M. J. Gough, C. E. Ruby, W. L. Redmond, B. Dhungel, A. Brown, A. D. Weinberg, OX40 agonist therapy enhances CD8 infiltration and decreases immune suppression in the tumor. *Cancer Res.* **68**, 5206–5215 (2008).
39. N. Kitamura, S. Murata, T. Ueki, E. Mekata, R. T. Reilly, E. M. Jaffee, T. Tani, OX40 costimulation can abrogate $Foxp3^+$ regulatory T cell-mediated suppression of antitumor immunity. *Int. J. Cancer* **125**, 630–638 (2009).

40. B. Valzasina, C. Guiducci, H. Dislich, N. Killeen, A. D. Weinberg, M. P. Colombo, Triggering of OX40 (CD134) on $CD4^+CD25^+$ T cells blocks their inhibitory activity: A novel regulatory role for OX40 and its comparison with GITR. *Blood* **105**, 2845–2851 (2005).
41. R. G. Lapidus, S. J. Nass, N. E. Davidson, The loss of estrogen and progesterone receptor gene expression in human breast cancer. *J. Mammary Gland Biol. Neoplasia* **3**, 85–94 (1998).
42. S. Ménard, E. Tagliabue, M. Campiglio, S. M. Pupa, Role of HER2 gene overexpression in breast carcinoma. *J. Cell. Physiol.* **182**, 150–162 (2000).
43. J. E. Maglione, D. Moghanaki, L. J. T. Young, C. K. Manner, L. G. Ellies, S. O. Joseph, B. Nicholson, R. D. Cardiff, C. L. MacLeod, Transgenic Polyoma middle-T mice model premalignant mammary disease. *Cancer Res.* **61**, 8298–8305 (2001).

**Funding:** This work is supported by grants from the NIH (R01 CA188005), the Leukemia and Lymphoma Society (TAP-120921), and the Boaz and Varda Dotan and the Phil N. Allen foundations. **Author contributions:** I.S.-B., D.K.C., I.S.A., and A.T.M. designed and performed all experiments. I.S.-B., S.L., S.S.G., and R.L. wrote the paper. **Competing interests:** S.S.G. is founder and equity holder of CellSight Inc. that develops and translates multimodality strategies for imaging cell trafficking/transplantation. All other authors declare that they have no competing interests. **Data and materials availability:** CpG SD-101 is available from Dynavax Technologies under a material transfer agreement.

Submitted 13 April 2017
Resubmitted 13 September 2017
Accepted 13 December 2017
Published 31 January 2018
10.1126/scitranslmed.aan4488

**Citation:** I. Sagiv-Barfi, D. K. Czerwinski, S. Levy, I. S. Alam, A. T. Mayer, S. S. Gambhir, R. Levy, Eradication of spontaneous malignancy by local immunotherapy. *Sci. Transl. Med.* **10**, eaan4488 (2018).

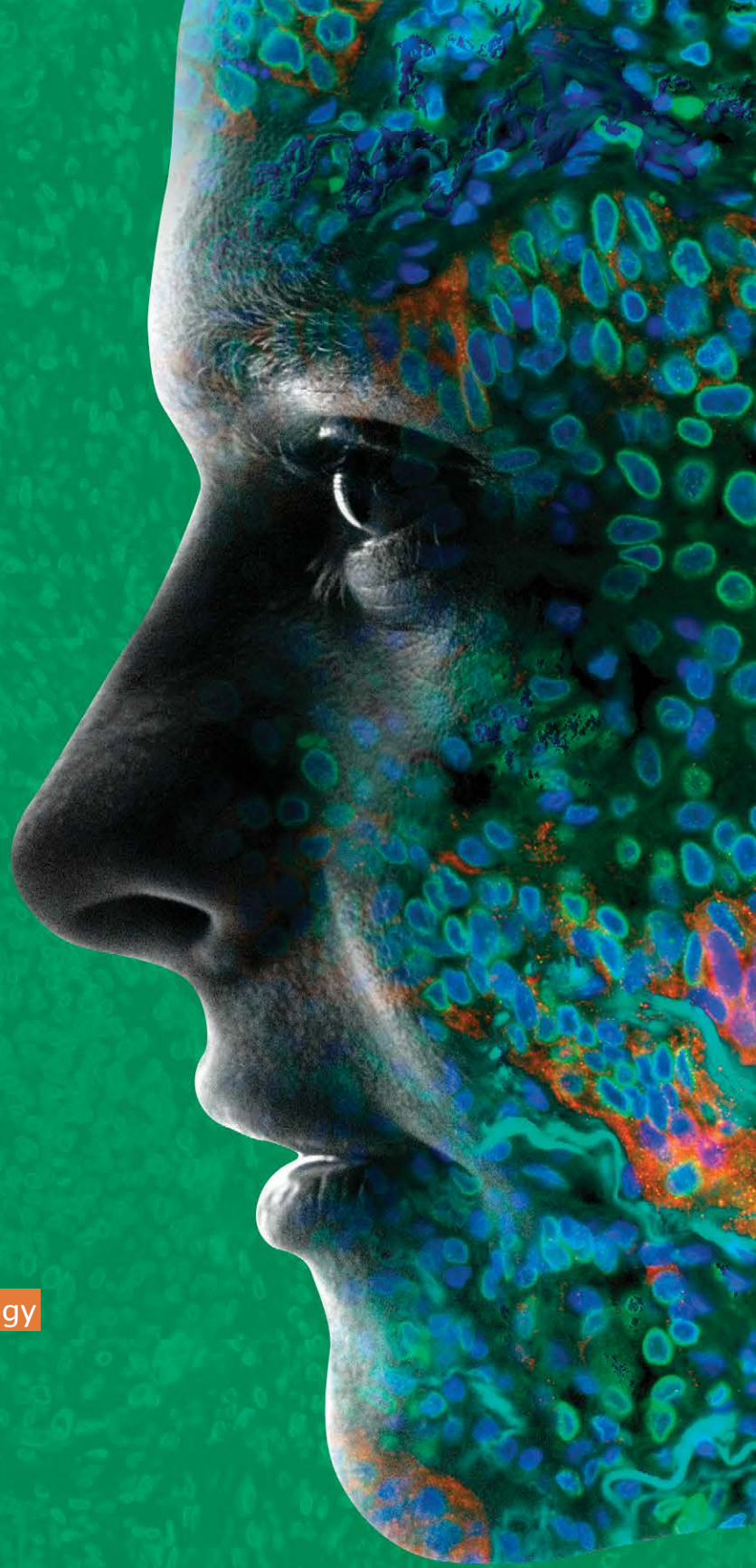

# Light your way.

## Get the full picture with trusted tumor immune response results from our in-house validated antibodies.

When it comes to your tumor immune response research, blind spots are unacceptable. Independent testing has demonstrated that 75% of antibodies in today's market are non-specific or simply do not work at all.* But at Bethyl, we've manufactured and validated every antibody we make on site to ensure target specificity and sensitivity. All to guarantee our antibodies will function as designed in your assay 100% of the time. More than 10,000 independent citations over the past 15 years have proven that, at Bethyl, we put a lot in every drop.

See our data at bethyl.com/immuno-oncology

**Weller, MG, Analytical Chemistry Insights:11, 21-27 (2016).*

Antibodies shown: Rabbit anti-PD-L1 (red, A700-020) & Lamin-A/C (green, A303-430A) in FFPE lung.


BETHYL
LABORATORIES, INC

Really Good Antibodies